ADVANCED IMAGE ANALYSIS AND TECHNIQUES FOR DEGRADATION
CHARACTERIZATION OF AGGREGATES

BY

MAZIAR MOAVENI

DISSERTATION

Submitted in partial fulfillment of the requirements
for the Degree of Doctor of Philosophy in Civil Engineering
in the Graduate College of the
University of Illinois at Urbana-Champaign, 2015

Urbana, Illinois

Doctoral Committee:

Professor Erol Tutumluer, Chair
Professor Marshal R. Thompson
Professor Christopher P. L. Barkan
Professor Jeffery R. Roesler
Assistant Professor Enad Mahmoud, University of Texas - Pan American

ABSTRACT

Morphological or shape properties of virgin and recycled aggregate sources are known to affect pavement and railroad track mechanistic behavior and performance significantly in terms of strength, modulus and permanent deformation. Under repeated traffic loading aggregate particles used in construction of pavement and railroad track are routinely subjected to degradation through attrition, impact, grinding and polishing type mechanisms, which result in altering their shape and size properties. The recent advances in digital image acquisition and processing techniques have the potential to be used for objective and accurate measurement of aggregate particle size and shape properties in a rapid, reliable and automated fashion both in the laboratory and in the field. The primary focus of this dissertation includes the design, manufacturing, calibration and validation of different hardware and software components of an Enhanced-University of Illinois Aggregate Image Analyzer (E-UIAIA) with many improvements over the first generation device. A new fully automated color image segmentation algorithm was developed as part of this research which showed excellent performance in detecting aggregate particles with different sizes and natural colors. Customized Look Up Tables (LUTs) were developed to enhance the Hue (H) and Saturation (S) representations of dark and bright aggregate images which improved the thresholding results. The different binary image processing modules available in the original UIAIA device for computing size and shape properties of aggregate particles were updated and merged into a single user friendly interface. Moreover, a new processing algorithm for image arithmetic operations and thresholding was developed and validated for computing the percentages of asphalt coating on Reclaimed Asphalt Pavement (RAP) aggregates.

The research findings presented in this dissertation include the implementation of newly developed E-UIAIA in capturing the rate and magnitude of changes in shape and size properties of aggregate particles caused by abrasion, polishing and breakage actions at different degradation levels. The standard laboratory degradation test results including Los Angeles Abrasion (LAA) and Micro-Deval (MD) were combined with imaging based particle

shape indices to successfully classify different aggregate sources according to their resistance to degradation.

As a step forward for bringing the advances in aggregate imaging methods to project sites and quarries, this dissertation introduces a field aggregate image acquisition and processing procedure. Advanced image analysis and segmentation techniques that combine a Markov Random Field (MRF) approach for image modeling, graph cut for optimization and user interaction for enforcing hard constraints were used. The developed algorithm was utilized for extraction and analyses of individual aggregate particle size and shape properties from 2D field images of multi-aggregate particles captured in a single frame using a Digital Single Lens Reflex (DSLR) camera. The developed field imaging and segmentation methodology showed satisfactory performance in two case studies involving quantification of size and shape properties of large size aggregate sources as well as railroad ballast samples collected from various ballast depths in a mainline freight railroad track. The image acquisition and processing methodologies presented in this dissertation hold the potential to provide optimized aggregate resource selection, better aggregate quality control and quality assurance (QC/QA) as well as improved material specifications.

ACKNOWLEDGEMENTS

TABLE OF CONTENTS

CHAPTER 1:
INTRODUCTION

1.1 Introduction

Aggregate materials are used as the main component of road subbase/base, riprap, cement concrete, asphalt concrete and railroad ballast. Since transportation infrastructure continues to age and expand in size, the need for repair, maintenance and reconstruction grows. As a result, the demand for aggregates increases. On the other hand, high quality aggregate materials are becoming increasingly scarce and expensive in many parts of the country because gravel mines and rock quarries are being lost to other land uses. Aggregate materials are characterized for uses and applications in construction projects according to specifications that are often not directly linked to their performance. For example, current revisions of Super Performing Asphalt Pavements (Superpave) and American Railway Engineering and Maintenance-of-way Association (AREMA) design specifications suggest that aggregate materials need to be characterized from three main perspectives including "consensus or physical properties", "soundness or chemical properties" and "gradation or particle size distributions" [1, 2]. In these two important specifications, the history of the development of recommended standard aggregate testing methods, e.g., evaluating particle shape properties, often goes back more than half a century. Considering the recent advances in data acquisition, sensor technology, control systems and computer signal processing, there is a need to review the current conventional aggregate testing procedures with the goal of developing new techniques. Improvements to be made in performance-based testing procedures by implementing new technologies result in characterizing aggregate materials accurately and objectively.

During the last decade, machine vision technology and image analysis has been utilized as an objective and accurate inspection system for quantifying the aggregate particle size and shape properties in a rapid, reliable and automated fashion when compared to traditional manual methods [3]. Three-dimensional laser scanning techniques combined

with optical equipment have also been used to develop computational programs for shape and size characterization of aggregates [4, 5]. These approaches hold the potential to be applied in the field and automatically control the size and shape properties of construction aggregate materials in the job sites and quarries to evaluate the influences of different quarry operations such as crushing method and/or crusher arrangements. Additionally, proper packing of aggregate particles as a granular layer would maximize the level of internal friction angle and number of contact forces which all depend on the aggregate shape properties. Implementation of these computer vision based technologies therefore provides the opportunity for optimized aggregate selection/utilization and significant economic benefits with sustainable uses of aggregate resources in building transportation infrastructure. Objective measurement of aggregate shape properties needs to be considered as an essential component in designing layered pavement and railroad track structures. In recent years, the shape or morphological properties of construction aggregates have been successfully correlated to the improved properties and performances of transportation facilities in terms of strength, modulus and deformation characteristics [6, 7, 8, 9].

1.2 Shape Properties of Construction Aggregates

The mineralogy and geological origin of a rock source primarily affect the shape properties of aggregates during the crushing operation in quarries [10]. There are three basic types of rocks that exist on planet earth; igneous rocks, sedimentary rocks and metamorphic rocks. Granite as an igneous rock and limestone as a sedimentary rock, for example, are widely used in highway and railroad track construction.

The chemical composition and shape of rock's crystals controls the level of brittleness and how it fractures during crushing operation [11]. Limestone with "aphinitic" or fine grained crystals tends to be more brittle and fractures into more Flat and Elongated (F&E) particles [10]. Brown and Marek [12] reported that the shape of aggregate particle is a function of mineralogical composition of the source rock.

In terms of method of crushing in the quarry, Kojovic [13] suggests running the crusher with a full or choked feed cavity and crusher operation in closed circuits to improve the shape of the produced aggregate particles. Brown and Marek [12] also showed that jaw

or gyratory type crushers as compression type machines when used as primary crushers tend to produce more F&E particles in comparison to impact type crushers.

Figure 1.1 illustrates the key physical shape properties of an aggregate particle. At the scale of macro level, angularity is generally defined as a measure of crushed faces and sharpness of the corners in an aggregate particle. In general, using aggregate sources with equidimensional (cubical) and angular particle shapes are preferred in comparison to flat, thin, or elongated particles [14]. The level of internal shear resistance in the particulate medium is highly influenced by the particle angularity. Consequently, rounded or uncrushed aggregates increase the rutting susceptibility at the construction stage during compaction operations [15]. Furthermore, Perdomo [16] observed that using rounded particles is one of the chief asphalt mixture deficiencies that contribute to low rutting resistance.

Roughness or irregularities at micro level on the surface of the aggregate is called surface texture of the aggregate. This aggregate property is the main factor which controls the magnitude of frictional resistance (micro texture) of road surface [17]. Aggregate surface texture can also affect the deformational properties of granular layers under repeated loading. In a research study by Thom and Brown [18], the visible surface roughness of aggregate particles was reported to primarily affect the base layer permanent deformation.
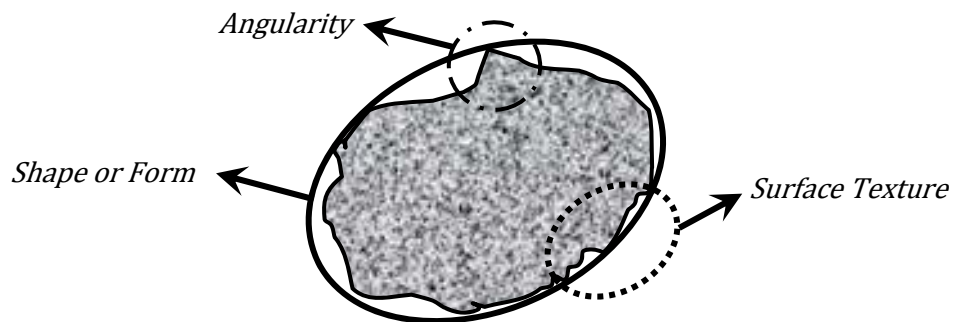
Figure 1.1 Illustration of Shape Properties for an Aggregate Particle

The dimensional ratio of an aggregate particle is generally referred to F&E ratio or form property. Superpave asphalt concrete mixture design specifications use this aggregate shape property to identify aggregate sources that may have tendency to impede the compaction process or might not satisfy the Voids in Mineral Aggregate (VMA)

3

requirements. These type of particles are more susceptible to breakage during the compaction process and under the service loads. As a result, particle size distribution that is used in the design phase deviates from the target gradation [19].

Currently there are only a few standard testing procedures to measure aggregate shape properties. ASTM D3398, "Index of Aggregate Particle Shape and Texture", provides a combined assessment of particle shape and texture. In this testing method, voids in aggregate layers compacted at different levels of compaction energy is used as an indirect indicator of angularity and/or roughness of particles. ASTM D5821, "Test Method for Determining the Percentage of Fractured Faces in Coarse Aggregate", is defined as the percentage (by mass) of aggregates larger than No.4 sieve (4.75 mm) with one or more fractured faces. ASTM C1252 "Uncompacted Void Content of Fine Aggregates" is used for an indirect measurement of particle shape and surface texture of aggregate smaller than No.8 sieve (2.36 mm). ASTM D4791 "Flat or Elongated Particles in Coarse Aggregates" is used to determine the percentage by mass of coarse aggregates that have a maximum to minimum dimension ratio greater than five. In this method, a standard caliper device is used to measure the dimensional ratio of particles.

1.3 Application of Machine Vision in Evaluating Aggregate Shape Properties

Standard test methods described in the previous section use indirect indicators for evaluating aggregate shape properties. These methods have several shortcomings including being laborious and subjective with low repeatability. Thus, the results from these tests often lack a direct linkage to accurate measurements of strength and permanent deformation characteristics of constructed aggregate layers.

Computer vision or Machine Vision (MV) is the technology that mimics the human vision sense and is used to develop imaging based systems for applications such as automated inspection systems, process control and robot guidance. Digital image processing techniques such as morphological filtering, thresholding, pattern recognition and segmentation are used to process the acquired images in imaging systems [20]. Digital cameras can also be used to capture the vertical laser plane images generated by laser

4

scanners. The three-dimensional laser scanner data can be converted into gray-scale digital images such that a pixel intensity is the representation of the height of each data point.

In many cases, machine learning is combined with computer vision to make decisions or perform actions. In a computer vision problem, there are typically six stages that need to be followed to interact with the available knowledge and finally generate the output results (see Figure 1.2). Many different approaches and processing methods have already been developed and are available to use in each of these stages.
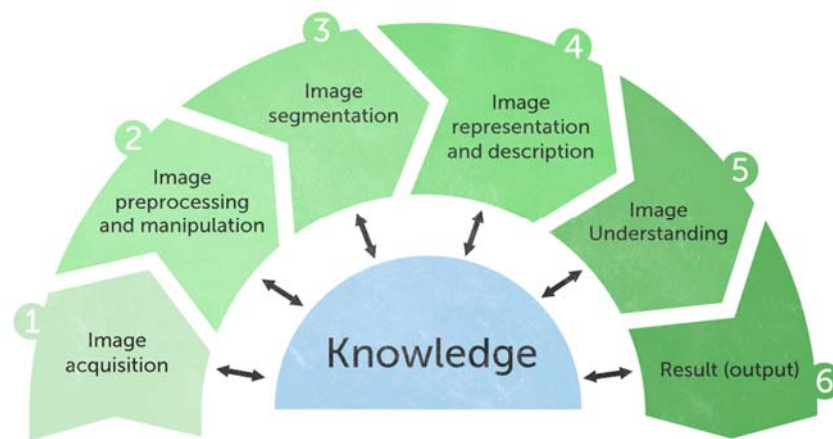
Figure 1.2 Stages in Solving a Problem with Computer Vision Approach [21]

During the last two decades, researchers and practitioners in the field of civil engineering have started to take advantage of machine vision approaches for a multitude of applications such as tracking construction site resources [22], inspection of railroad track [23] and measuring in-situ displacement of unsaturated soils [24]. Generally, the efficiency of these methods is evaluated by comparing the MV based results and the results obtained from conventional computer modeling or laboratory testing. MV based approaches are known for their accuracy, reliability, speed and repeatability.

Machine vision technology has also been utilized to develop imaging systems for direct and objective measurement of aggregate size and shape properties. These systems have different capabilities and features in terms of hardware and software components.

5

Masad et al. [25] studied the capabilities and concepts as well as advantages and disadvantages of these aggregate imaging systems. In addition to the need for appropriate hardware selection, the main challenge in developing these aggregate imaging systems is to define a proper mathematical based aggregate shape index associated with the digital image of an aggregate particle captured by one or more cameras. Different image processing approaches such as binary image morphology, image Fourier analysis and wavelet decomposition have been incorporated into these systems. Validating these imaging systems in terms of accuracy, repeatability and/or precision includes the ability to detect particle shape variations between crushed versus uncrushed aggregate sources, unpolished versus polished aggregate particles and correlating the shape indices with the field or laboratory performance. More information related to aggregate imaging systems will be provided in Chapter 2 of this dissertation.

1.4 Research Approach

1.4.1 Background

The commonly used aggregate property, which makes a certain aggregate material to pass any agency's specifications for construction and field utilization in transportation infrastructure, has typically been the particle size distribution or gradation. Certainly, gradation is an important property that influences the loss in performance with usage or degradation patterns of aggregates in bound/unbound layers of road pavements and railroad tracks. To assess aggregate degradation, loss in mass and the related change in gradation is currently used as the only indicator of aggregate resistance to abrasion and polishing as well as breakage during laboratory durability tests such as Los Angeles Abrasion (LAA) and Micro-Deval (MD). In addition to gradation, particle shape also degrades and needs to be considered when it comes to sustainable and mechanistic based designs of pavements and railroad track structures.

As aggregates undergo degradation due to traffic loading and environmental conditions, both the size and shape properties deteriorate. Systematic registration of the magnitude and rate of this change can be used in the assessment of life cycle analysis which is essentially linked to the development of performance models. Due to lack of a unifying and

advanced standard method to efficiently quantify aggregate shape properties, the degradation behavior of aggregates with respect to change in particle shape has not been properly considered in transportation geotechnics field and needs further research and investigation.

As described in the previous section, computer vision technology has been applied to develop aggregate imaging systems and imaging based shape indices for efficient measurement of the shape of aggregate particles. These aggregate imaging systems typically use mathematical algorithms for identifying a numerical shape index to compute form, angularity and surface texture properties of aggregates. Among many imaging based shape indices, summarized by Al-Rousan et al. [3], Flat and Elongated Ratio (F&E Ratio), Angularity Index (AI) and Surface Texture Index (STI) measured by the University of Illinois Aggregate Image Analyzer (UIAIA) were recommended as promising key indices from the findings of national studies [26, 27, 28].

Figure 1.3 illustrates the UIAIA system featuring an individual aggregate particle with three orthogonal views captured using three progressive scan digital cameras. In this system, monochrome digital images of three views of aggregate particles are captured. The corresponding binary images are then generated through an image processing technique called "thresholding". Extracting the pixel coordination of the boundaries of an aggregate particle therefore makes it possible to define the mathematical based shape indices and quantify the morphological properties through the use of AI, STI and F&E Ratio of the particles.

Recent research findings at the University of Illinois showed that adequately quantifying aggregate F&E Ratio, AI and STI improved considerably the ability of the regression based predictive models in estimating the modulus and strength properties of commonly used aggregates in highway pavement construction [29]. Such predictive equations can be used more commonly to generate reasonable default mechanistic design input properties for aggregates received from certain rock quarries, gravel pits and other commercial aggregate sources throughout the country. Another important conclusion of this study was that locally available aggregate sources even with marginal level of quality could

be used to satisfy mechanistic-empirical pavement design requirements considering optimizing gradation and particle shapes [30].
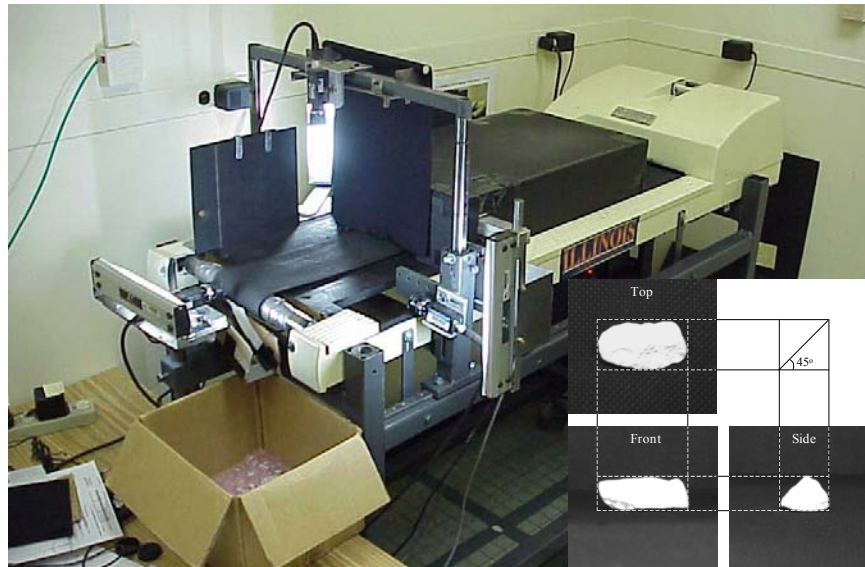
Figure 1.3 University of Illinois Aggregate Image Analyzer (UIAIA) [31]

In a recent study by Wnek et al. [9], aggregate shape properties identified by UIAIA were linked to strength properties of different railroad ballast density groups. The authors were able to show that higher angularity generally resulted in higher ballast strength properties. Depending on aggregate mineralogy, certain aggregates could also yield high fouling susceptibility and increased breakage potential in railroad ballast field application.

1.4.2 Research Need Statement

Mineralogy and chemical compositions are primary factors that affect aggregate particle color [32]. Many sources of construction aggregates such as basalt and peridotite or in general "trap rocks" include a high portion of dark colored particles. It is important to note that capturing good quality images in any type of aggregate imaging system is an essential step for successful computation of imaging based shape properties of aggregates. According to Rao [31], a minimum contrast level needs to be achieved between an aggregate particle and the black background surfaces used in UIAIA. It is beyond the capability of image processing algorithm incorporated in UIAIA to distinguish the particles from the background if the aggregate color is as dark as or darker than the background. This deficiency can be

8

particularly problematic when it comes to identifying the shape of Reclaimed Asphalt Pavement (RAP) type recycled aggregates. Processed RAP produces particles that are coated with some percentages of asphalt and are very hard to be distinguished if placed on a black background. Another limitation of the original UIAIA system was the low resolution cameras limited to 640×480 pixels and also the non-adjustable focal lengths of the lenses. These two fixed parameters limit the field of view of the cameras and cause difficulties when capturing the images of large size railroad ballast particles which can have sizes up to 3 in. (76.2 mm). Therefore, an improved image acquisition and processing interface with advanced hardware and software components had to be developed to overcome these problems and enhance the capabilities of UIAIA.

A basic technique for image segmentation is "thresholding". The thresholding technique seeks to find boundaries between different regions in the image according to the differences in pixel intensities/colors. Usually, the threshold value(s) are either preset or adaptively (automatically and iteratively) chosen and used to partition pixels into different sets based on their intensities/colors [33]. Advanced methods in color image thresholding holds the potential to be implemented in a new image acquisition and processing interface to improve the efficiency of capturing and analyzing the images of aggregates with different color variations.

During the last decade, researchers have started to take advantage of imaging based measurement of aggregate shape properties combined with laboratory testing methods to quantify the magnitude and trend of aggregate degradation. UIAIA has been combined with Los Angeles Abrasion (LAA) apparatus (ASTM C535) to measure the effect of abrasion and impact forces on changing aggregate shape properties during degradation process [34]. More recent studies have shown the successful application of imaging techniques to evaluate the level of aggregate degradation on the job site by measuring the shape properties of the aggregate samples collected from asphalt plants or in-service unbound aggregate layers [35, 36]. Therefore, the development of a second generation of UIAIA with enhanced capabilities will make it possible to efficiently capture the changes in the validated imaging based shape indices for all sources of aggregate materials including the railroad ballast and the RAP aggregate with darker colors. Detecting the magnitude and rate of these changes can

be used to develop performance models and better classify aggregate sources in terms of their resistance to polishing, abrasion and breakage.

RAP materials include recycled aggregate with varying degrees of asphalt coating. The asphalt coating percentage on RAP particles, which is a function of particle size, binder content and method of RAP production, is an important characteristic of the different RAP materials. According to NCHRP 452 report [37], the binder content and physical properties of RAP aggregates including particle shape, texture and angularity need to be determined for their proper use in the desired mixture design. These factors also control the performance of RAP in terms of stiffness, crack resistance, modulus and deformation characteristics. The digital raw and processed images of RAP particles generated by an improved generation of UIAIA holds the potential to be used in the development of a post image processing algorithm for evaluating the level of asphalt coating on particles. Implementation of this technology provides the opportunity for optimized RAP selection and utilization which will provide sustainability benefits to the transportation infrastructure.

Although imaging techniques have been recognized as an improvement for quantifying aggregate shape properties, there are still some difficulties in implementing this method by DOTs and highway agencies. This includes aggregate sampling in job sites/quarries for shipping to laboratory and one at a time single particle image scanning and processing which makes the process tedious and time consuming. Recently, low cost, powerful high-resolution digital cameras have been available for everyday use by practitioners. A fast, simple and cost effective field imaging procedure with user friendly hardware and software components can also be developed to facilitate quantifying aggregate shape properties in the job sites/quarries using high resolution color images captured by digital cameras available in the market.

1.4.3 Research Objectives

The development of an "Enhanced" version of the University of Illinois Aggregate Image Analyzer (E-UIAIA) with hardware and software improvements including color image acquisition and processing capability to distinguish dark colored aggregates is the main objective of this research. As was discussed before, the three cameras used in UIAIA have a sensor resolution of 640×480 pixels and are capable of taking only monochrome images.

Since the distance between the cameras and the aggregate particles are fixed and the focal length of the camera lenses are also fixed, the UIAIA is only capable of capturing images with 160 pixels/inch (0.1875 mm/pixel) spatial resolution. Therefore, capturing the images of large aggregate particles with sizes greater than 1.5 in. (38.1 mm) would be very challenging in this system. Additionally, Rao [31] found that the number of pixels required to represent a 1 in. (25.4 mm) length measurement is inversely proportional to size of the object. This simply means that using cameras with higher sensor resolution will improve the accuracy of size measurement since higher number of pixels can be allocated to smaller particles. Thus, the E-UIAIA needs to be equipped with cameras with higher sensor resolution and lenses with variable focal lengths. E-UIAIA will be calibrated using several calibration sphere balls with known diameters and shape properties. Considering the final arrangement of the cameras, different spatial resolutions will be identified to capture the images of aggregate particles with sizes from No.4 sieve (4.75 mm) to 3 in. (76.2 mm). The E-UIAIA will be validated by the use of UIAIA and its well established imaging based particle size and shape indices for individual measurement of Volume (V), F&E Ratio, AI, STI and Surface Area (SA). The performance of the new system in characterizing several aggregate sources as well as its repeatability and precision will be studied as part of this PhD dissertation. The development of a robust and accurate post image processing algorithm to quantify the asphalt coating percentages of RAP particles is another scope of this research. A combination of image processing and enhancement techniques, including histogram-based image thresholding, binary image morphology analysis and arithmetic image operation will be used to segment the asphalt coating from the RAP images captured by the E-UIAIA.

A second objective of this research is the implementation of E-UIAIA to quantify and link the extent of coarse aggregate degradation as determined in the laboratory with MD and LAA type test procedures. A statistical evaluation of the shape property results will be performed to develop regression based models. These models are used to describe the degradation behavior of individual aggregate sources in terms of the loss in AI and STI. Furthermore, material weight loss at different MD and LAA degradation cycles will be correlated with the percentage of change in shape properties in order to verify the

applicability of imaging based methods in characterizing the resistance of aggregates to degradation.

Third objective of this research is the development and implementation of a customized machine vision system to acquire and process the images of a group of aggregate particles in the field. Field imaging involves capturing color photos of multiple aggregate particles in a single 2D image using a high-resolution Digital Single Lens Reflex (DSLR) camera. Separate images of single aggregate particles are then automatically extracted by applying the appropriate image segmentation techniques including Markov Random Field (MRF) and graph cut segmentation methods. The size and shape properties of each particle are subsequently analyzed based on image processing algorithms of the E-UIAIA. This technology will be evaluated using two case studies to assess the effectiveness of the developed method. In the first case study, the size and shape of aggregate particles collected from three depths of an in-service railroad ballast layer will be evaluated. This includes capturing the size and shape variations at different depths under the effect of ballast degradation caused by repeated train loading. The second case study includes characterizing size and shape properties of large size aggregate particles with sizes up to 6 in. (152.4 mm) used as aggregate subgrade materials. Due to large size of these aggregates, laboratory sieve analysis is unable to identify the particle size distribution. Therefore, the developed field imaging methodology would be a good alternative to be used as a control quality tool to measure the size and shape properties of these large sized particles.

1.5 Dissertation Outline

This dissertation has been divided into eight chapters. An overview of upcoming chapters is presented in this section.

Chapter 2 includes an overview and operational principles related to UIAIA and its imaging based shape indices. A literature review is provided on the influence of aggregate shape properties and their impact on the design and performance of asphalt concrete mixtures, cement concrete, subbase/base unbound layers and railroad ballast. Additionally, a brief background is provided in this chapter on the degradation mechanisms of aggregates, testing procedures to assess aggregate degradation, digital image segmentation, color

thresholding as well as image acquisition and processing using National Instrument (NI) LabView platform.

Chapter 3 includes comprehensive information and discussions related to the design and development of E-UIAIA. The camera and conveyor selection as well as design and manufacturing stages for different hardware components of E-UIAIA are described. The improved NI LabView based image acquisition, image calibration and image processing software interfaces including color thresholding in Hue, Saturation, Intensity (HSI) representation and innovative software camera triggering features of E-UIAIA are introduced. Furthermore, the calibration procedure using calibration spheres and identification of required spatial resolution for capturing images of particles with different sizes is explained in detail. This chapter also includes the description of a validation and comparison study to ensure that E-UIAIA generates accurate and repeatable measurements of size and shape properties similar to UIAIA.

Chapter 4 of this dissertation includes laboratory testing and image analysis results which demonstrate the applicability of E-UIAIA in evaluating aggregate resistance to degradation through LA-Abrasion tests. Image acquisition and processing procedures as well as the statistical analysis results for fourteen sources of railroad ballast are provided in this chapter. Additionally, regression based degradation models are established and presented based on the rate and magnitude of change in morphological properties captured by E-UIAIA. Finally, LA-Abrasion testing results combined with developed degradation models are used to classify ballast sources into different categories considering their resistance to abrasion, breakage and polishing forces.

Chapter 5 of this dissertation presents the laboratory testing and image analysis results to demonstrate the applicability of E-UIAIA in evaluating aggregate resistance to degradation through MD testing. Eleven sources of single size aggregates from the state of Illinois that are used for surface asphalt mixes are studied. Similar to Chapter 4, this chapter also includes the regression based degradation models based on MD testing results as well as rate and magnitude of change in particle shape properties. MD testing results combined with developed degradation models are used to classify these aggregate sources into different zones considering their resistance to abrasion, breakage and polishing forces.

Chapter 6 focuses on the application of E-UIAIA to determine the imaging based size and shape indices of RAP aggregates from six different sources such that the influence of asphalt coating in altering morphological properties is studied. The development and validation of an image processing algorithm which is able to estimate the percentages of asphalt coating on RAP aggregates is also presented in this chapter.

Chapter 7 of this dissertation elaborates on the development of an image acquisition and processing methodology for shape and size characterization of a group of aggregate particles captured in the field. The observations and analysis results from two case studies for the implementation of this field imaging technology are presented in this chapter

The summary of the findings and conclusions related to this PhD research are provided in Chapter 8. Recommendations for future research and further development in this area are also given at the end of this chapter.

CHAPTER 2:
LITERATURE REVIEW

2.1 Aggregate Imaging Systems

As part of NCHRP 4-30 research project, several different aggregate imaging systems and their associated imaging based shape indices were comprehensively studied [25]. In total, eight different imaging systems equipped with one to three cameras were evaluated in terms of the characteristics of the image acquisition procedure and the accuracy of the image analysis methods. Table 2.1 lists the names and features of each of these systems.

Table 2.1 Aggregate Imaging Systems and their Salient Features [25]

Name of Imaging System	Analysis Concept	Measured Aggregate Shape Properties
VDG – 40 Videograder	Uses one camera to capture image and evaluate particles as they fall in front of a backlight	Form / Size
Computer Particle Analyzer (CPA)		Form / Size
Micromeritics OptiSizer PSDA		Form / Size
Buffalo Wire Works PSSDA		Form / Size
Camsizer	Uses two cameras to capture image and evaluate particles as they fall in front of a backlight	Form / Size Angularity
WipShape	Uses two cameras to capture image of aggregates passing on a mini conveyor system	Form / Size Angularity
University of Illinois Aggregate Image Analyzer (UIAIA)	Uses three cameras to capture three projections of a particle moving on a conveyor belt	Form / Size Angularity Surface Texture Volume Surface area
Aggregate Imaging System (AIMS)	Uses one camera and autofocus microscope to measure the characteristics of coarse and fine aggregates	Form / Size Angularity Surface Texture

In this section a brief description is provided regarding each of these systems. It needs to be noted that none of these imaging systems have been currently approved as a standard procedure for characterizing the shape properties of aggregates. However, the findings of

NCHRP 4-30 research project indicated that UIAIA and Aggregate Imaging System (AIMS) could be considered as the two most reliable imaging systems to evaluate the shape and size properties of aggregates. For each system the relevant references are provided here for further information. Since the main focus of this dissertation relates to the development of a new generation of UIAIA, more detailed descriptions are provided about this device.

2.1.1 VDG – 40 Videograder

French public works laboratory (LCPC) has developed VDG-40 Videograder. An electromagnetic vibrator is used in this device to extract the constituents of the sample in a hopper which directs them along a feed channel toward separator drum. Using the separator drum, the aggregate particles are oriented toward the falling plane at the desired speed. A line scan Charge-Couple Device (CCD) camera acquires the images of aggregate particles as they fall in front of a backlight. Each particle's third dimension is computed from 2D projection image based on the assumption of elliptical particles. Therefore, this system is capable of measuring the particle size distribution, flatness (VDG-40 FLAT) and slenderness ratios (VDG-40 SLEND). Figure 2.1 illustrates VDG-40 Videograder and a schematic of image capturing procedure of falling aggregates. Further information related to VDG-40 can be found elsewhere [38].

Figure 2.1 Components of VDG-40 Videograder and Image Acquisition of Falling Aggregates [25]

2.1.2 Computer Particle Analyzer (CPA)

Similar to VDG-40, this device also uses a line-scan CCD camera and a backlight surface to capture the images of particles as they fall. This device can be used in the

laboratory or as a continuous scanner of a product stream. 2D projection image of an aggregate particle is used to reproduce an idealized 3D shape. Therefore, this system is capable of generating the particle size and form distribution for aggregate samples. Further technical information about this system is provided elsewhere [39]. This device and the size related properties of a particle are shown in Figure 2.2.
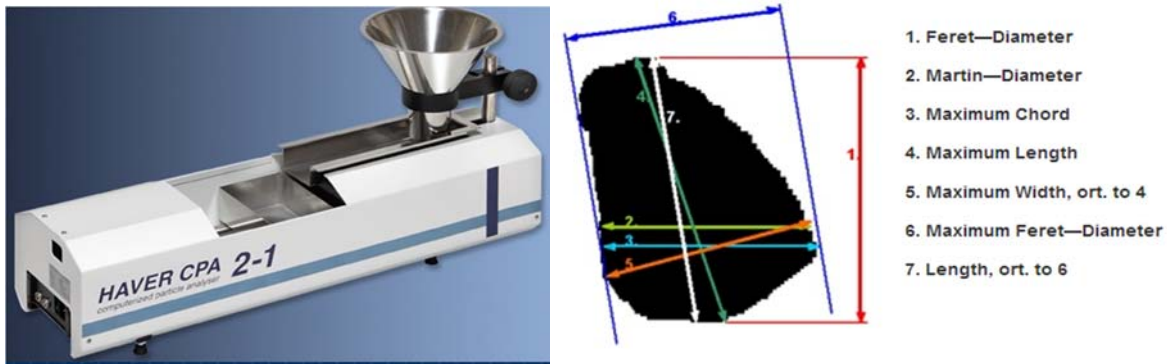
Figure 2.2 Components of Computer Particle Analyzer and Associated Particle Size Properties [40]

2.1.3 Micromeritics OptiSizer (PSDA)

This device also uses a line scan CCD camera to capture image and evaluate particles ae they fall in front of a backlight. The 2D binary projected images are used to measure the size properties. Similar to the method described in CPA, these values will be later used to represent the ideal 3D shapes of particles. This device can be used to measure the gradation and form of aggregate particles [38]. PSDA device is shown in Figure 2.3

Figure 2.3 Micromeritics OptiSizer (PSDA) [25]

2.1.4 Buffalo Wire Works (PSSDA)

This device has been developed by Dr. Penumadu at the University of Tennessee. This system operates very similar to VDG-40 and captures images of particles as they fall in front of the backlight. The system provides information about gradation and form of particles. All analysis and data reporting are performed in a custom software package [38]. Two experimental test devices that have the same analysis concept are developed. These devices are called PSSDA-Large and PSSDA-Small. PSSDA-Large is used for analyzing coarse aggregate particles while PSSDA-Small is used for analysis of fine aggregates. Figure 2.4 shows both of these systems.

Figure 2.4 Buffalo Wire Works (PSSDA) System for Evaluating Size/Form for Coarse (Left-Side Picture) and Fine (Right-Side Picture) Aggregates [38]

2.1.5 Camsizer

Camsizer system uses two optically matched cameras to capture images of fine and coarse aggregate particles at different resolution. Individual particles exit the hopper to a vibrating feed channel and fall between the light source and the camera. Particles are detected as projected surfaces and are digitized in the computer. This system can measure the size and form as well as a convexity based angularity index for the particles. More information related to hardware and software components of this system can be found elsewhere [25]. Figure 2.5 shows an overall view of the Camsizer.

2.1.6 WipShape

Dr. Maerz at the University of Missouri was the developer of Wipshape system. Two orthogonal oriented synchronized cameras are used in this system to capture images of coarse aggregate particles. Coarse aggregates are placed on a rotary backlight tray while a second backlight surface provides the background for the front camera. Therefore, both the top and front cameras can easily capture the silhouette of the particles. This system can measure the aggregate shape and gradation. WipShape uses the minimum average curve radius method to quantify the aggregate angularity. More detailed information about the hardware and technical background related to WipShape can be found elsewhere [41]. Figure 2.6 shows the WipShape system.
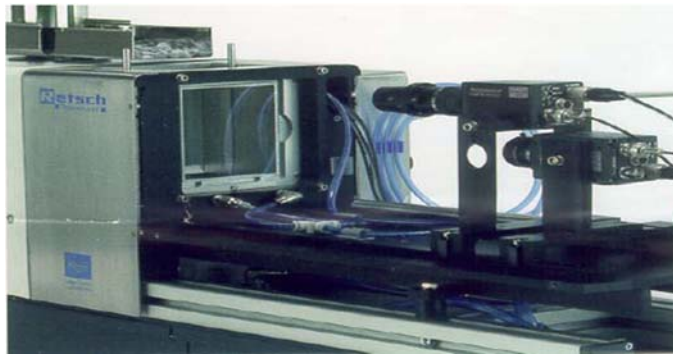
Figure 2.5 Overall View of Camsizer Imaging System [25]
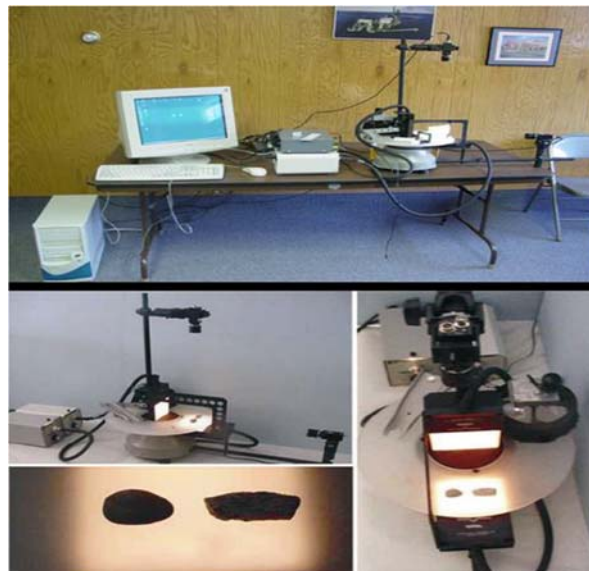
Figure 2.6 WipShape System [42]

2.1.7 Aggregate Image Measurement System (AIMS)

This system has been originally designed and manufactured by Dr. Eyad Masad at Texas A&M University. Two modules are incorporated in this system. The first module is for the analysis of fine aggregates; black and white images are captured using a video camera and a microscope. The second module is used for the analysis of coarse aggregate; grayscale images as well as black and white images are captured. Fine aggregates are analyzed for shape and angularity, while coarse aggregates are analyzed for shape, angularity and texture. A video microscope is used to determine the depth of particles, while the images of 2D projections provide the other two dimensions. These three dimensions quantify the shape of particle. Additionally, angularity is determined using gradient method by analyzing the black and white images, while texture is determined by analyzing the grayscale images using wavelet image processing technique [43].

Recently, a second generation of this imaging system, AIMS2, has been developed and commercialized in the US as part of a national initiative sponsored by the Federal Highway Administration under the Highways for LIFE program [44], The improvements in the new system includes a variable magnification microscope-camera system and two different lighting configurations to capture aggregate images for analysis. Additionally, the entire system is placed inside a box with a door to reduce the effect of ambient light on the quality of captured images.
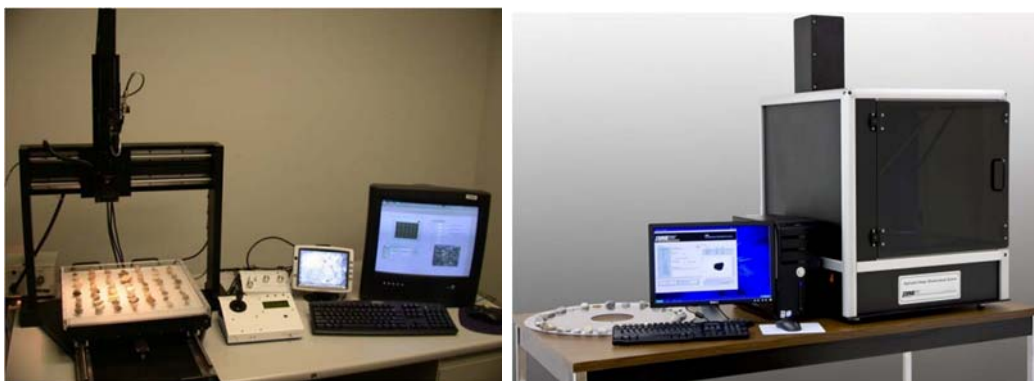
Figure 2.7 AIMS First Generation (Left-Side Picture) and the Second Generation AIMS-II (Right-Side Picture) [44]

It needs to be noted that the maximum particle size that can be scanned with this system is 1 in. (25.4 mm). Therefore, the shape properties of railroad ballast particles with

sizes above 1 in. (25.4 mm) cannot be evaluated with this system. The first and second generation of AIMS is shown in Figure 2.7.

2.1.8 University of Illinois Aggregate Image Analyzer (UIAIA)

Rao and Tutumluer [27, 31] developed University of Illinois Aggregate Image Analyzer (UIAIA) to automate the process of measuring the shape and size properties of coarse aggregates. This section briefly describes the image acquisition and processing features of this system. UIAIA uses three Charge Couple Device (CCD) cameras with sensor resolution of 640 x 480 pixels to capture images of aggregate particles from top, side and front views. Using these three orthogonally views, the Volume (V), Surface Area (SA), Surface Texture Index (STI), Angularity Index (AI) and size of each aggregate particle are evaluated. Figure 2.8 shows a schematic of UIAIA describing different parts of this machine. Infrared and fiber optic sensors detect the location of the particles on the conveyor and they send a signal to trigger three cameras. 1/30th of a second delay between detecting a particle and camera triggering lets the particle to move into the field of view of three cameras.
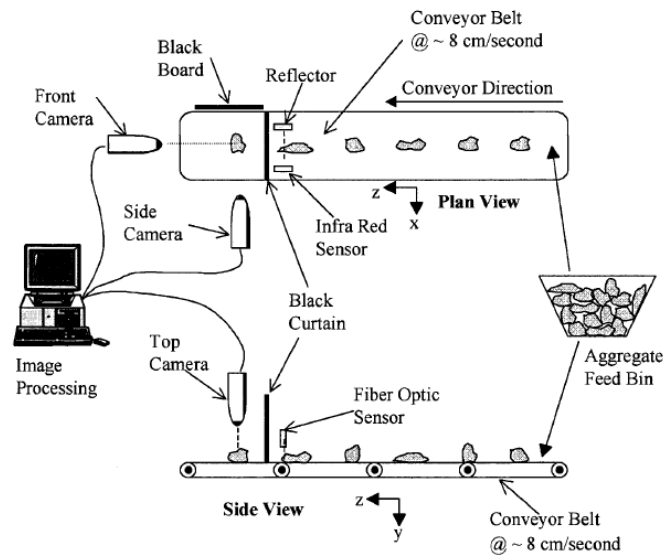
Figure 2.8 Illustration of UIAIA Components [31]

Three fluorescent lights and three black backgrounds are provided to capture the monochrome images of bright colored aggregates. Progressive scan cameras with higher shutter speeds are used in this system to address the motion blur caused by the moving

nature of aggregate particles on the conveyor. National Instrument Image Acquisition (NI-IMAQ) acts as an interface between the PCI 1408 frame grabber board and the LabView 2006 programming environment as the acquisition software. Captured digital images of aggregate particles are converted to array of pixels. Then, inter-class variance thresholding operation [45] is performed on individual greyscale images to generate the corresponding binary images. After assigning a threshold value to each image, all pixels with gray levels below this threshold value are reduced to '0' (black) while all pixels with gray levels greater than threshold value are made equal to '255' (white) (see Figure 2.9).
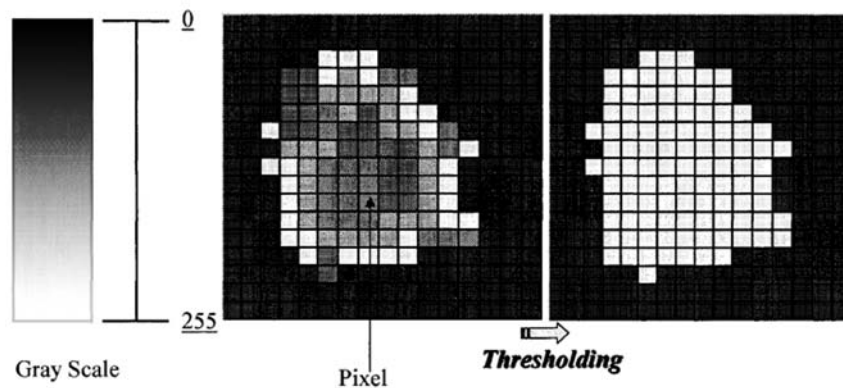
Figure 2.9 Grayscale Image Thresholding in UIAIA [46]

Obviously, successful thresholding operation is highly dependent on the particle color as well as the level of contrast between the object and background. Five modules that use post-processing particle morphology analysis on binary images have been developed to quantify the main aggregate shape properties. The outputs of these modules are particle volume, particle sieve size, flat and elongated ratio, angularity index, surface texture index and surface area [46]. A brief background is provided here about the methodology that is used for computation of these shape indices. More detailed description about UIAIA and its shape indices can be found elsewhere [27, 31]

(1) Volume computation

The 3D equivalent of a pixel, a pixel cube, is termed as voxel [47]. 3D reconstruction method that is used in UIAIA to calculate the volume of each particle is basically counting the number of these voxels belonging to an aggregate particle. Initially, grayscale image

thresholding, conversion of image to array and particle subset array selection are performed to identify the domain of an aggregate particle. Then, the volume computation algorithm examines each voxel that belongs to the domain of the particle image. Corresponding three pixels in xy, yz and zx planes are counted as part of the particle if they have the threshold pixel intensity equal to 255. Finally, total number of cubic pixels that satisfy this condition give the volume of an aggregate particle in terms of number of voxels. The UIAIA is adjusted for a calibration factor of 1 in. (25.4 mm) = 158.6 pixels or 1 pixel = 0.006305 in. (0.160147 mm). Therefore, Equation 2.1 can be used to calculate the particle volume:

Particle Volume (in³) = number of counted voxels × (0.006305)³   2.1

Rao [31] was able to verify and validate this volume computation technique by comparing the imaging based volume results with the weights of particles for a known specific gravity (G_s). The capability of UIAIA to estimate the volumes of particles improves the accuracy of this system in measuring the particle size distribution comparable with laboratory sieve analysis. This point will be later discussed in this chapter. Figure 2.10 illustrates the 3D reconstruction and voxel based volume computation of an aggregate particle.
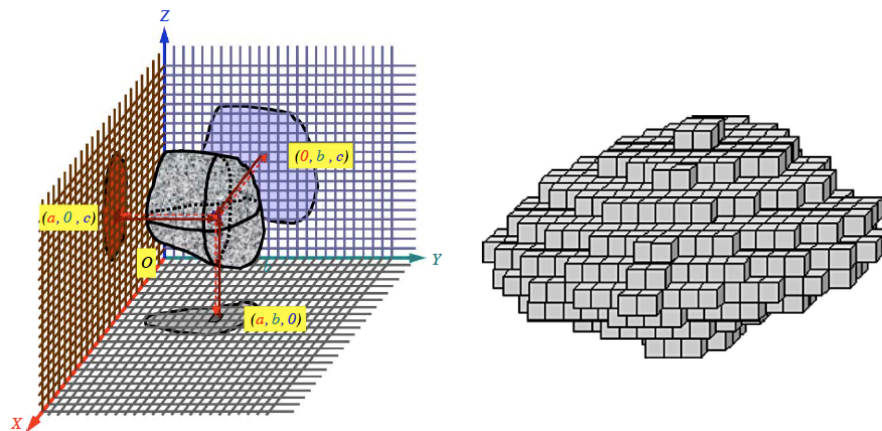
Figure 2.10 Projected Images of an Aggregate Particle in Cartesian Planes and 3D Volume Reconstruction by Voxel Counting [48]

23

(2) *Flat and Elongated Ratio (F&E)*

According to ASTM D 4791, the F&E Ratio of an aggregate particle is defined as the ratio of the maximum dimension of the particle to the minimum dimension. First, the maximum intercept which is the longest segment in the particle in all possible directions of projection is identified. Then, the dimension that is perpendicular to the maximum intercept is determined. After detecting the maximum intercept and the perpendicular dimension of each of the three views of an aggregate particle, the six dimensions are sorted to determine the maximum and minimum values. Finally, the ratio of the maximum dimension to the minimum dimension gives the desired F&E Ratio. (see Figure 2.11)

Longest Dimension
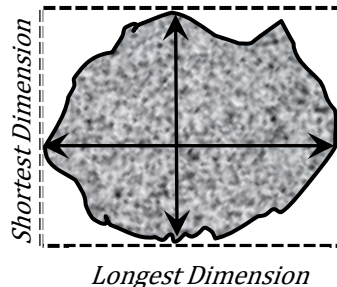
Figure 2.11 F&E Ratio Measurement of an Aggregate Particle in UIAIA

(3) *Particle Size Distribution (Sieve Analysis)*

Rao [31] suggests that for identifying the particle size distribution using UIAIA, the intermediate imaging based size for each aggregate particle needs to be determined. The lowest of the three maximum intercept values computed from the three captured views is chosen as the intermediate aggregate particle dimension. Accordingly, if this dimension is smaller than the diagonal length of the square mesh/opening in a desired laboratory sieve, the particle passes through that given sieve. Rao [31] was able to show that gradation curves developed based on this described imaging approach matched very closely with laboratory mechanical sieve analysis results obtained from ASTM C136 testing procedure.

(4) *Angularity Index*

Rao [31] developed the image processing algorithm for evaluating the angularity of aggregate particles in UIAIA. To approximate the profile of each 2D image of a particle, the coordinates of the particle profile are initially extracted. Then, the outline is approximated

24

by an n-sided polygon as shown in Figure 2.12. An optimum "n" value of 24 was found to give the best results in terms of separating crushed particles from uncrushed gravel [27]. The angle α subtended at each vertex of the polygon is computed next.
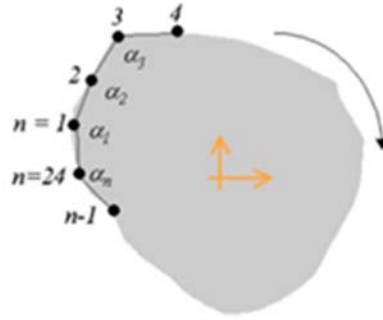
Figure 2.12 Replacing an Aggregate Particle with an n-Sided Polygon [27]

A relative change in slope of the n sides of the polygon is subsequently estimated by computing the change in angle α at each vertex with respect to the angle in the preceding vertex. The frequency distribution of the changes in the vertex angles is established in 10-degree class intervals. The number of occurrences in a certain interval and the magnitude are then related to the angularity of the particle profile. Equation 2.2 is used for calculating angularity of each projected image.

$$Angularity = \sum_{e=0}^{170} e \times P(e) \qquad\qquad 2.2$$

In this equation, e is the starting angle value for each 10-degree class interval and P(e) is the probability that change in angle α has a value in the range of e to (e+10). From its definition as given in Equation 2.2, the angularity has units of degree. Therefore, the angularity for a circle will be 0. The AI of a particle is then determined by averaging the angularity values calculated from all three views when weighted by their corresponding areas as given in Equation 2.3.

$$AI = \frac{\sum_{i=1}^{3} Angularity(i) \times Area(i)}{\sum_{i=1}^{3} Area(i)} \qquad\qquad 2.3$$

25

In this equation, i takes values from 1 to 3 for top, front and side orthogonal views. The final AI for the entire aggregate sample can be represented as the average or the distribution curve for all the particles.

(5) *Surface Texture Index*

The STI measurement in UIAIA is performed based on a familiar concept in binary image morphology analysis that is called "erosion and dilation." [46]. One erosion cycle processes each 2D image by removing boundary pixels of an object surface to leave the object less dense along its outer boundary. However, dilation is the reverse process of erosion and a single dilation cycle increases the particle shape or image dimension by the same pixels around its boundary. Erosion cycles followed by the same number of dilation cycles tend to smoothen the surface of a particle by trimming the peaks and corners and patching the sharp dents on the boundary (see Figure 2.13). The difference in area in terms of pixel counts for 2D images before and after equal number of erosion and dilation is directly related to the surface micro-irregularities [46]. Equation 2.4 defines the STI for each particle image.

$$Surface\ Texture\ Index = \frac{A_1 - A_2}{A_1} \times 100 \qquad\qquad 2.4$$

where,

A_1 = Area (in pixels) of the 2D image before applying erosion and dilation;

A_2 = Area (in pixels) of the 2D image after applying a sequence of "n" cycles of erosion followed by "n" cycles of dilation.

Before Erosion & Dilation   *After Erosion & Dilation*

Figure 2.13 Smoothing the Surface of a Particle Image Linking to Surface Texture Before and After Cycles of Erosion and Dilation [46]

Pan [46] was able to show that in order to set up an index independent of particle size, the optimum number of cycles of erosion and dilation or "n" needs to be identified using the Equation 2.5.

$$n = \frac{L}{\beta}$$ 2.5

where,

L = Longest or maximum intercept of the particle image;

β = Scaling factor for erosion and dilation operations.

The optimal n value was determined as 20 at which STI of a set of smooth surface coarse aggregates such as river gravel was recognized as significantly different from the STI of a set of rough surface coarse aggregates [46]. The final STI value is a weighted average value of its individual image STI values determined from three views (front, top, side images).

(6) Surface Area

Pan [46] developed an algorithm for surface area computation using images captured by UIAIA. Surface area calculation of an aggregate particle with irregular shape requires representation of the entire surface of an aggregate particle with self-oriented small 2D plane elements or ΔS_i. Basically, voxel elements that are used in 3D volume reconstruction and are located on the surface of the particle and stablish these surface elements. Finally, Equation 2.6 is used to calculate the surface area of each particle. The solution to this double integration is estimated by summation of ΔS_i series over the domain of the particle in Euclidian coordinate system while the ΔS_i elements are sufficiently small [27].

$$\iint_{\Sigma} ds = \lim_{n \to \infty} \sum_{i=1}^{n} \Delta S_i$$ 2.6

Each of these 2D ΔS_i elements on the surface of the particle have different orientation and therefore contribute with different magnitude to the total surface area. Since the projections of each 2D ΔS_i element contained in a voxel are three pixels in the three coordinate planes, the magnitude of a 2D ΔS_i element can be determined by its orientation as devoted by three directional cosines as described in Equation 2.7.

$$\Delta S_i = \frac{Area_{pixel}}{\cos(\phi_{ij})}$$ 2.7

where, ϕij is the directional normal angle of each area element ΔS_i wih respect to the three coordinate planes (j=1, 2, 3) respectively.

It needs to be noted that this approach do not consider that curvature exists on the surface of a real aggregate particle. Later, Pan et al. [48] were able to show that because surface curvature is a function of particle angularity, a correction factor (see Equation 2.8) can be considered to improve the accuracy of surface area estimation.

$$Surface\ Area = \frac{\Delta S_{Total}}{1+(0.2291-0.0004AI)} \qquad\qquad 2.8$$

where, ΔS_{Total} is the area summation of all the 2D ΔS_i elements in terms of in.^{2} or m^2 and AI is the angularity index for the aggregate particle.

2.2 Laser Based Systems for Evaluating Aggregate Shape Properties

In addition to camera based imaging systems, laser scan technology has also been used to characterize the shape and size properties of aggregate particles. Pan [46] used a Roland LPX-1200 3D laser scanner to verify the accuracy of surface area measurements performed by UIAIA. Figure 2.14 shows this laser system which is set up to scan an aggregate particle.

Figure 2.14 Roland LPX-1200 3D Laser Scanner [49]

He was able to show that measured surface areas with UIAIA matched very closely with surface area measurements by laser scanner. Pan [46] observed that scanning one aggregate particle with laser scanner took almost 90 minutes while he was able to capture

the images of 1000 aggregate particles in only 70 minutes with UIAIA. Considering the significant variability in particle shapes in a given aggregate sample, it is important to use an efficient system which can capture statistically sufficient number of scans/images in a reasonable amount of time. Later, Anochie-Boateng et al. [50] combined the aforementioned laser scanner with developed analysis techniques to quantify the sphericity and F&E Ratio related to different aggregate samples. They reported that approximately 30 minutes was required to scan a 0.75 in. (19 mm) aggregate particle.

Recently, as part of NCHRP 4-43 research project, Wang et al. [4] developed a 3D aggregate characterization system and analysis method using Laser Detection and Ranging (LADAR) approach. LADAR is a remote sensing technology that measures distance by illuminating a target with a laser and analyzing the reflected light. This system is called Fourier Transform Interferometry (FTI) which acquires 3D surface coordinates of the particles using the combination of laser and imaging. A fiber optic switch is adopted in FTI to adjust the input of laser signals from two sources with wavelengths of 675 nm and 805 nm, respectively. The image of the aggregate surface in the mirror is later captured by a CCD camera and analyzed using the Fourier transform to represent the surface profile of the particle. Figure 2-15 shows a picture of the FTI aggregate imaging system.

Figure 2.15 FTI Aggregate Image System [4]

Morphological properties of particles including form, angularity, surface texture and surface area are analyzed using Fourier transform signal processing method. As part of

NCHRP 4-43 research effort, Wang et al. [4] compared the FTI results with those from AIMS-II and UIAIA systems. They concluded that when angularity and texture between two aggregate sources are significantly different, these three imaging systems may be sensitive enough to differentiate them with similar order of ranking. Major safety concern incurred by the users of FTI system is the risk of eye damage associated with the laser source. The risk of ocular damage can be managed by limiting the power of the laser source for the interferometer. Additionally, surface area and volume computation of the particles is reported to be very time consuming with this system.

In summary, the reviewed literature shows that laser based systems are capable of generating promising results and certainly need to be considered as an alternative for further research and development in aggregate shape characterization area. However, these systems are still associated with several disadvantages and concerns including the length of time required to scan each particle, the high initial cost of laser device as well as safety risks.

2.3 Influence of Aggregate Shape Properties on Performance

The morphological or shape properties of aggregate particles significantly affect the performances of the unbound/bound layers of highway and airfield pavements as well as railroad ballast under dynamic traffic loading. These constructed aggregate layers are evaluated in terms of shear strength, modulus and permanent deformation characteristics [6, 7, 8, 51]. Additionally, road safety from the perspective of frictional resistance of the pavement surface is a function of pavement micro-texture, which is highly influenced by the magnitude of aggregate surface texture and angularity [17, 52, 53].

According to laboratory and field performances and numerical modeling results such as from Discrete Element Method (DEM), ballast layers in railroad track that are constructed with angular aggregate particles possess higher strength properties and thus improved lateral track stability when compared to rounded aggregate particles [54]. Uthus [55] studied the deformational properties of unbound granular aggregates used as railroad ballast. She concluded that aggregate shape properties strongly influenced the internal friction angles and therefore the shear strength properties of ballast layers. Recently, Huang [54] used DEM ballast computer modeling and considered the effect of individual particle

size and shape properties on railroad ballast strength, lateral stability and settlement potentials. The findings of Huang's study confirmed that ballast with angular aggregate particles had higher strength and lateral stability in comparison to rounded particles due to better aggregate interlock.

Han [56] developed a railroad ballast quality evaluation computer model which considered particle characteristics including shape, angularity, surface texture, gradation and specific gravity. He was able to evaluate the model using field data related to ballast layer track performance. The findings showed that particle shapes were indeed an important factor and had to be considered in design.

Rao et al. [27] demonstrated that the AI values measured with UIAIA for 50-50 blends of the crushed stone and gravel samples correlated well with the shear strength properties from triaxial tests. Later, Pan et al. [28] studied the effects of particle angularity and surface texture for 21 blends of uncrushed and crushed aggregate sources on the resilient modulus and permanent deformation behavior of unbound granular material samples in the laboratory. They concluded that both AI and STI were closely linked to modulus and deformation properties of aggregate sources.

Quiroga et al. [57] studied the effect of aggregate shape, texture and gradation on the performance of fresh concrete. They observed that aggregate blends with cubical shape, rounded and smooth particles required less paste at a given slump as opposed to blends with flat, elongated, angular and rough-surfaced particles. On the other hand, uniform size distribution with sufficient amounts of each size resulted in aggregate blends with improved aggregate packing and low water demand. Recently, Polat et al. [58] investigated the effects of shape properties of aggregates quantified by digital image processing on the compressive strength properties of cement concrete. They were able to show that spherical particles were desirable for increased compressive strength, unit weight and slump values.

A comprehensive research project sponsored by Iowa Department of Transportation investigated the effects of aggregate shape properties on the volumetric properties of Hot Mix Asphalt (HMA), particularly Voids in Mineral Aggregates (VMA). Statistical regression based analyses showed that the combination of the maximum aggregate size and gradation in addition to particle shape and texture properties influenced the volumetric conditions of

HMA mixtures at the stable-unstable threshold. Based on the findings of this study, a new paradigm to volumetric mix design was developed which is capable of considering the aggregate shape factors including gradation, shape and texture in the mixture design [59]. Recently, Prowell et al. [10] studied the aggregate properties and the performance of Superpave designed HMA as part of the NCHRP 9-35 research project. The outcome of this study showed that increasing coarse aggregate fractured faces or "angularity" increased rutting resistance. Additionally, increased particle index value or uncompacted voids in coarse aggregates also provided increased rutting resistance. The latter combines the effect of form, angularity and surface texture associated with each particles.

As part of NCHRP IDEA Project 114, Masad et al. [60] conducted a comprehensive study investigating the relationship of aggregate surface texture to asphalt pavement skid resistance using image analysis. The findings of this project verified that skid resistance was not only related to the average aggregate surface texture, but also to the texture distribution within an aggregate sample. They suggested that aggregate surface texture distribution could be considered in developing more accurate performance models to predict asphalt pavement skid resistance.

2.4 Degradation Mechanism of Aggregates

According to Tolppanen [61], the most important factors which cause in-service aggregate degradation include: a) material source properties including mineralogy and petrography, b) shape of aggregate particles, c) initial size distribution and arrangement of particles, d) force concentration on particle surfaces and e) aggregate layer maintenance operations and environmental conditions.

Since the energy required to crush aggregate particles is a function of the amount of created new surface areas, Moavenzadeh et al. [62] used the concept of an increase in surface area of particles as a tool in measuring the magnitude of degradation in an aggregate matrix. They showed that in a uniform as opposed to a dense graded aggregate mixture, the number of contact forces were fewer and particles were subjected to higher contact pressures which in turn causes much more breakage and degradation. Increasing the average grain size of the particle chain transmitting the load increased the force required to break particles. However,

by increasing grain size, the contact point between particles becomes fewer which eventually increases the forces acting on contact surfaces. Nurmikolu [63] states that "*The breakage of the particles is compounded by the fact that a particle needs to transmit the same load after having been broken and is increasingly susceptible to breakage due to its smaller size*". Several types of forces such as attrition, impact and grinding are imposed on the aggregate particles at different stages of degradation including production at the quarry/plant [64], transporting to job site and compaction during construction. All of these factors in addition to in-service dynamic traffic loading as well as environmental effects cause "aggregate degradation" or deviating the aggregate structure from its target condition in terms of both size and shape of particles.

As mentioned before, the initial shape distribution of particles can also affect the aggregate degradation. Raymond [65] investigated the performance of a thin layer of granular material when acting as a foundation material under repeatedly loaded surface footing. Raymond observed negligible to zero breakdown when rounded aggregates were used while particle breakdown, including powdering, was noticeable after testing the crushed particles as the foundation layer.

Several studies in the literature investigated the characterization of aggregate degradation and its effects on the bearing capacity of unbound/bound layer from the perspective of change in size distribution or decrease in coarse to fine fraction ratio [66, 67, 68]. It is important to note that aggregate degradation can cause abrasion which results in particles to lose their angularity and surface texture or become more rounded and spherical. Aggregate degradation changes the void ratio or packing properties and ultimately influences the performance. On the other hand, aggregate particles after breakage possess fresh surfaces which might have sharp edges and rougher surface texture.

2.5 Evaluation of Aggregate Resistance to Degradation

Several standards and test procedures such as Los Angeles Abrasion (LAA), Mill Abrasion (MA), Deval Abrasion (DA) and Micro-Deval (MD) have been developed to evaluate the resistance of aggregates to degradation. In these laboratory tests, aggregate particles are subjected to different levels and combinations of abrasion or attrition, impact and grinding

forces for a certain time or number of revolutions. Occasionally, water may be added to the specimen to consider the effect of moisture during degradation process. At the end of each test, loss of material's mass in terms of percentage relative to the original mass is considered as the degradation evaluation criteria. Tables 2.2 and 2.3 summarize the American and European standard procedures for evaluating aggregate resistance to degradation based on LAA and MD methods. Note that ASTM method is not currently available for performing MA, DA and MD on railroad ballast.

Table 2.2 ASTM Standard Procedures for LAA and MD Laboratory Tests

Standard number	ASTM C131	ASTM C535	ASTM D6928
Description	LAA on regular size aggregate	LAA on railroad ballast	MD on regular size aggregate
Action imposed on aggregate	Abrasion or attrition - Impact - Grinding	Abrasion or attrition - Impact - Grinding	Abrasion and grinding in the presence of water
Size of aggregate	4 gradations covers 1 in. (25 mm) to No.8 sieve	3 gradations covers 2.5 in. (63 mm) to 0.75 in. (19 mm)	3 gradations covers 0.75 in. (19 mm) to No.4 sieve
Mass of sample	11 lbs. (5000 gr)	22 lbs. (10000 gr)	3.3 lbs. (1500 gr)
Charge type	Steel spheres with Dia. = 1.84 in. (46.8 mm)	Steel spheres with Dia. = 1.84 in. (46.8 mm)	Steel spheres with Dia. = 0.374 in. (9.5 mm)
Amount of charge	6 to 12 steel balls based on aggregate grading	12 steel balls	5000 gr of balls and 2 Liters of water
Number of revolutions	500 @ 30 rpm	1000 @ 30 rpm	95 min to 120 min depending on gradation @100 rpm
Degradation criteria	Loss as a percentage of original mass after wash sieving through No.12 sieve	Loss as a percentage of original mass after wash sieving through No.12 sieve	Loss as a percentage of original mass after wash sieving through No.16 sieve

DA was initially used in England to measure the quality of highway aggregate materials. Later, British Rail (BR) used a modified version of this test to assess the minimum durability of ballast life. This test can be conducted in dry and wet conditions. The dimensions of cylinder in the DA testing machine is 7.87 in. (200 mm) diameter and 13.38 in. (340 mm) depth. The cylinder shall be mounted on a shaft at an angle of 30 degrees with

the axis of rotation of the shaft. Depending on the maximum particle size and gradation of the sample, 6 to 12 standard steel spheres with approximately 1.89 in. (48 mm) diameter are charged to the cylinder and the machine starts to rotate for 10,000 revolutions at 33 rpm. After finishing the test, the weight of the material passing through No.8 sieve or No.12 sieve, depending on sample gradation, divided by the initial weight of material is considered as the degradation criteria [69].

Table 2.3 European Standard Procedures for LAA and MD Laboratory

Standard number	EN 1097-2	EN 1097-2 Annex "A" or EN 13450 Annex "C"	EN 1097-1	EN 1097-1 Annex "A" or EN 13450 Annex "E"
Description	LAA on regular size aggregate	LAA on railroad ballast	MD on regular size aggregate	MD on railroad ballast
Action imposed on aggregate	Resistance to fragmentation - Different test for Impact	Resistance to fragmentation - Different test for Impact	Resistance to wear	Resistance to wear
Size of aggregate	Covers 0.55 in. (14mm) to 0.4 in. (10mm) *	Covers 2 in. (50mm) to 1.2 in. (31.5mm)	Covers 0.55 in. (14mm) to 0.4 in. (10mm) **	Covers 2 in. (50mm) to 1.2 in. (31.5mm)
Mass of sample	5000 gr	10000 gr	1000 gr	10000 gr
Charge	Steel spheres with D = 46.8 mm and weight of 400 gr	Steel spheres with D = 46.8 mm and weight of 400 gr	Steel spheres with D = 9.5 mm	No steel ball used
Amount of charge	11 steel balls	12 steel balls	5000 gr of balls and 2.5 Liters of water	No steel ball and 2 Liters of water
Number of revolutions	500 @ 30rpm	1000 @ 30 rpm	120 min @100 rpm	140 min @100 rpm
Degradation criteria	Loss as a percentage of original mass after wash sieving through No.12 (1.7 mm)	Loss as a percentage of original mass after wash sieving through No.12 (1.7 mm)	Loss as a percentage of original mass after wash sieving through No.12 (1.7 mm)	Loss as a percentage of original mass after wash sieving through No.12 (1.7 mm)

MA is a wet abrasion test which needs 6.6 lbs (3 kg) of railroad ballast material with specified gradation. The MA procedure includes revolving the sample without charging any steel spheres around the longitudinal axis of a 9 in. (229 mm) external diameter porcelain jar for 10,000 revolution at 33 rpm. The MA value is the amount of material passing No.200

sieve relative to the original mass of the sample [70]. Note that although DA and MA methods have been common in the past, currently Superpave mix design procedure and American Railway Engineering and Maintenance-of-Way Association (AREMA) both recommend LAA method to evaluate the resistance of aggregate to degradation. Additionally, most state DOT's use MD method to evaluate the properties of highway aggregates related to polishing and frictional resistance.

In addition to aforementioned tests, some other standard procedures have been developed for assessing aggregate resistance to degradation. Aggregate Impact Value (AIV) and Aggregate Crushing Value (ACV) are the two indices that are also used by practitioners to evaluate the breakage susceptibility of aggregates. British Standards, BS 812-112 and BS 812-110 describe the laboratory procedure related to these two laboratory tests. In terms of evaluating the influence of environmental conditions on aggregate degradation, "sodium and magnesium sulfate soundness" tests (AASHTO T 104) is generally considered [15].

According to findings from NCHRP 4-23 research project [71], LAA and MD were considered among the most important tests which influence the performance of aggregates used in unbound pavement layers. Wu et al. [72] compared several abrasion/degradation testing procedures with the objective of correlating the laboratory testing results with the field performance of asphalt pavement. They reported that Micro-Deval and magnesium sulfate soundness tests showed the best correlation with field performance.

As part of NCHRP Project 4-20C, Folliard et al. [73] listed LAA and MD as the required tests at level 1 design category. They reported that abrasion and polishing resistance of aggregates evaluated by these two tests are among the properties that most affect the performance parameters of concrete pavements.

Using the results of a comprehensive railway ballast survey performed by CP Rail, Clifton et al. [74] proposed a method to predict the service life of ballast layer by relating the train traffic in terms of Million Gross Tons (MGT) with abrasion and degradation properties of aggregates considering particle size distribution. Recently, Boler et al. [34] conducted LAA laboratory testing with different number of turns applied on limestone and granite ballast sources to simulate the particle breakage under track usage. They reported that at around 400 LAA turns the original uniform ballast gradation generally become "well-graded".

Furthermore, using ballast shear box test results they observed decreasing trends in shear strength with decreasing the AI and F&E Ratio of the particles. Klassen et al. [75] suggested the Abrasion Number (AN) for railroad ballast as the sum of LAA and five times MA values. Later, Raymond & Bathurst [76] reported that AN showed good correlations with ballast permanent deformation properties under cyclic triaxial testing.

The degradation process that happens in a granular medium under field conditions is an extremely complicated mechanism. By the time of writing this dissertation, no standard laboratory test has been developed that can fully simulate degradation of unbound aggregate layers under the effect of variable field environmental conditions and repeated traffic loading. Deep understanding of aggregate performance associated with its life cycle and degradation patterns in terms of particle abrasion and breakage requires accurate and systematic measurement of both particle size and shape properties at different deterioration levels.

2.6 Introduction to Machine Vision

Machine vision aims to create a model of the real world using digital images [77]. In other words, the ability of a computer to "see and compute differences" is called machine or computer vision. The main components of any machine vision system include: problem definition, image acquisition and image processing including segmentation as well as interpretation of the extracted features. Human eyes can only detect the electromagnetic wavelengths ranging from 390 to 770 nanometers (nm). However, the video cameras can be sensitive to a much wider wavelengths which make them an efficient tool for many industrial and medical applications such as handwriting recognition, material inspection, medical image analysis and pattern recognition [78].

In this section, a brief overview related to color image processing and color thresholding is provided. Later, this concept will be implemented in the development of image acquisition and processing of E-UIAIA. Additionally, a short introduction related to image acquisition and processing using National Instrument (NI) Lab View and its graphical or "G" programing interface is provided.

2.6.1 Color Image Processing

An image that is acquired by a camera generally needs to be pre-processed to gain compatibility with the desired vision processing method. Poor contrast, random variation in intensity or "noise" and insufficient illuminations need to be addressed using image enhancement methods during the early phase of image processing. Histogram modification and linear filters such as mean filtering, median filtering, look up tables and Gaussian smoothing are generally used to remove these noises and enhance the image. The human eye can distinguish thousands of different color shades and intensities but only around 100 shades of grey. Therefore, a great amount of information can be found in the color image and this extra information helps to improve image analysis tasks such as object identification and extraction based on color [79]. Figure 2.16 shows the range of wavelengths for the main three Red, Green and Blue (RGB) colors.
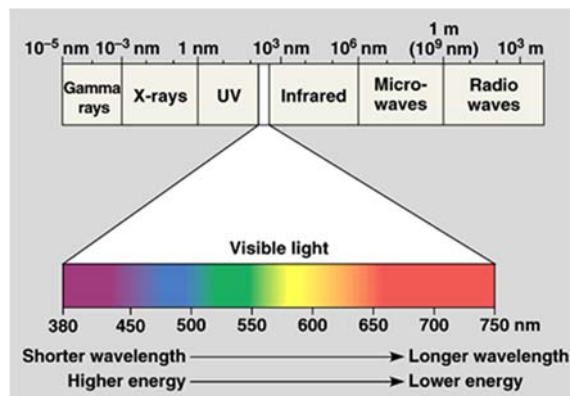
Figure 2.16 The Visible Spectrum and Colors [80]

There are three types of cones in human retina which respond differently to incident light associated with the three main colors. Figure 2.17 shows responses of these cones as a function of wavelength.

In computer vision, there are different ways to represent a color image. These alternatives are called "Color Models". Red, Green, Blue (RGB) and Hue, Saturation, Intensity (HSI) are the two most important color models that are further described in this section.
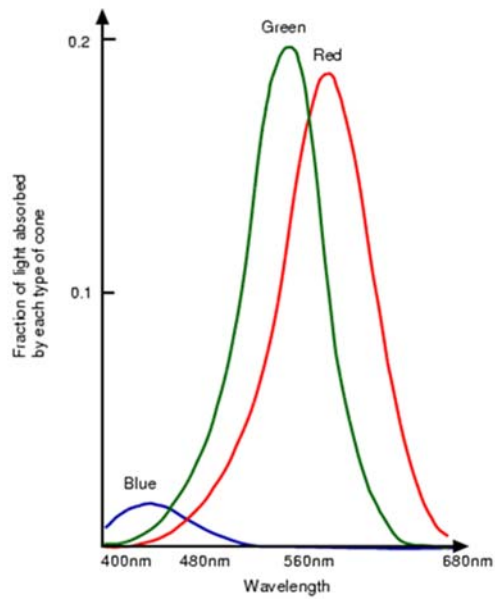
Figure 2.17 Spectral Responses for Each Cone Type in Human Eye [79]

In the RGB model, an image consists of three independent image planes, one in each of the primary colors: red, green and blue. Figure 2.18 shows the geometry of the RGB color model for specifying colors.
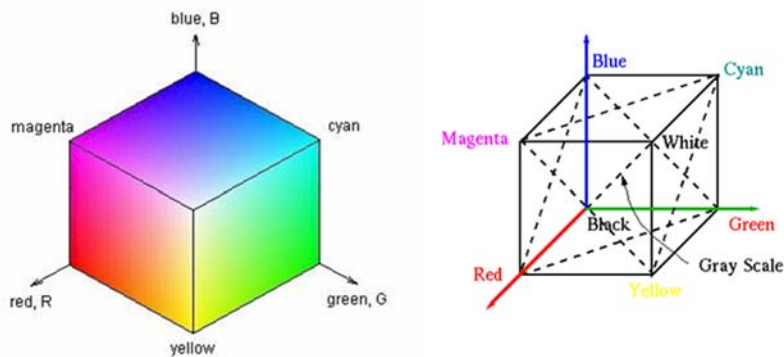
Figure 2.18 RGB Color Cube [79]

The color image also can be specified by three quantities including Hue, Saturation and Intensity. The entire space of colors can be represented in HSI model as shown in Figure 2.19.
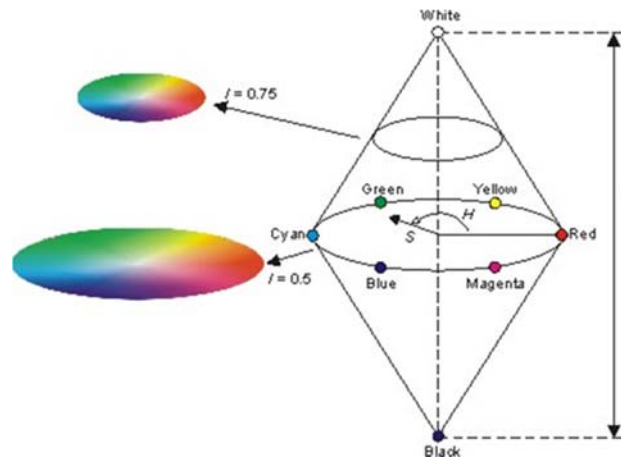
Figure 2.19 HSI Color Model [81]

RGB and HSI color representation models can be converted to each other. The HSI color space is very attractive color model for image processing applications since it represents colors similarly to how the human eye senses colors. Therefore, HSI is generally considered as the preferred color model when it comes to color image processing. Many image processing techniques that are available for gray scale images are applicable to individual color planes to enhance a particular channel so that the desired features or objects in the image stand out. These enchantments help to achieve more accurate results after applying segmentation/thresholding.

2.6.2 Image Segmentation and Color Image Thresholding

The process of partitioning an image into different areas/zones is called image segmentation. As an initial post-processing step in image segmentation, "image thresholding" is generally used to determine boundaries between different regions in the image according to the differences in intensity and color. The result of this analysis is called binarization results. In many cases, thresholding can effectively be applied to images that have "bimodal histograms". These type of histograms are associated with images that include objects and background having significantly different average brightness. The main goal in many applications is solving the problem of separating the background and the foreground.

Finding the correct approach and parameters to threshold an image can be very challenging. Bovic [82] states that "Direct human operator intervention is generally needed

40

to get successful binarization results. However, even with human picking a visually *optimal* value for thresholding, the results are rarely *perfect*. There is nearly always some misclassification of object as background and vice versa". Therefore, innovative approaches and algorithms called "region correction methods" are generally developed to correct these misclassification errors.

Color image thresholding can be performed on RGB or HSI representation of an image. This technique performs image enhancement on each individual channel and then provides the final output with combining the results from desired channels. Several researchers have applied HSI color thresholding and concluded that this method gives better results in comparison to RGB color thresholding [83]. Clustering is a widely used technique for image segmentation [84, 85]. In this technique, a feature vector, which records pertinent information about the pixel such as its spatial coordinates, intensity/color, gradient and so on, is first generated for each pixel in the image. Thus, the image is segmented according to the clusters in the high dimensional feature vector space. Another major technique in image segmentation is region growing [86]. This technique begins with a selection of a set of seed pixels by the user. After that, comparison tests are performed in order to determine pixels bearing similarity to the seed pixels. The process is then iterated until convergence. Region growing techniques provide users with better control of the process and output segmented regions that the users define with clear edges.

Graph based approaches are also popular for image segmentation and thresholding. A graph is constructed where every pixel corresponds to a node and every pair of neighboring pixels is connected by an (weighted) edge. The technique then aims to cut the graph into certain connected components so that the total weight of the edges that are cut is minimal. Many cutting algorithms are suggested in the literature, such as, the graph-cuts algorithm [87] and normalized-cuts algorithm [88]. Note that the graph-cut techniques are minimizing an underlying energy/cost functional. There is a multitude of other segmentation techniques that are also based on the minimization of a suitable cost functional. As part of graph-cut segmentation, The Markov Random Field (MRF) technique [89] is widely used for pixel labeling problems in computer vision. When only two labels exist, they are labeled as "foreground" and "background". Pixels that belong to the foreground (object) are usually

labeled as 1 while pixels that belong to background are labeled as 0. This technique will be further discussed in chapter 7 of this dissertation.

2.6.3 Image Acquisition and Processing Using National Instrument (NI) LabView

Laboratory Virtual Instrument Engineering Workbench (LabView) developed by National Instrument Corporation in Austin, TX is a graphical programming language that is widely used in different fields of research. Using its graphical programming interface, called "G", the programs or Virtual Instruments (VIs) can be designed as graphical block diagrams for data acquisition, control and processing. The interactive user interface of each VI is called front panel which includes all the indicators and controls as well as display windows for input and processed images. The user can enter the parameters and input values in this panel. NI Vision Image Acquisition Software (NI-IMAQ) makes it possible to communicate with different types of frame grabbers and cameras to acquire, save and display images. NI Vision Development Module provides a comprehensive library with many imaging and machine vision functions. These functions as readily programmed algorithms called "Sub VIs", which can be used for many image processing operations such as converting images with different formats to arrays, image enhancements and filtering, segmentation and thresholding as well as morphological binary image processing. The processed images as well as the quantitative values of the measured features can be stored in the hard disk for further post-processing and analysis. Vision Assistant, another software product from NI, allows the user to quickly prototype and test different image processing approaches to determine the best alternative for a desired purpose. Figure 2.20 illustrates different parts of a processing window in Vision Assistant.

NI Vision VIs are divided into three main categories including: Vision Utilities, Image Processing and Machine Vision. Vision utilities are used for image manipulation and management tasks such as reading, writing and displaying the images with BMP, TIFF, JPEG, PNG and AIPD formats. Image processing category allows the user to perform wide range of processing operations such as pixel comparison, frequency analysis by 2D Fast Fourier Transform (FFT) and computing the histogram of an image. Finally, machine vision module can be employed to perform common machine vision inspection tasks such as checking for the presence or absence of a part in an image and measuring dimensions [82].
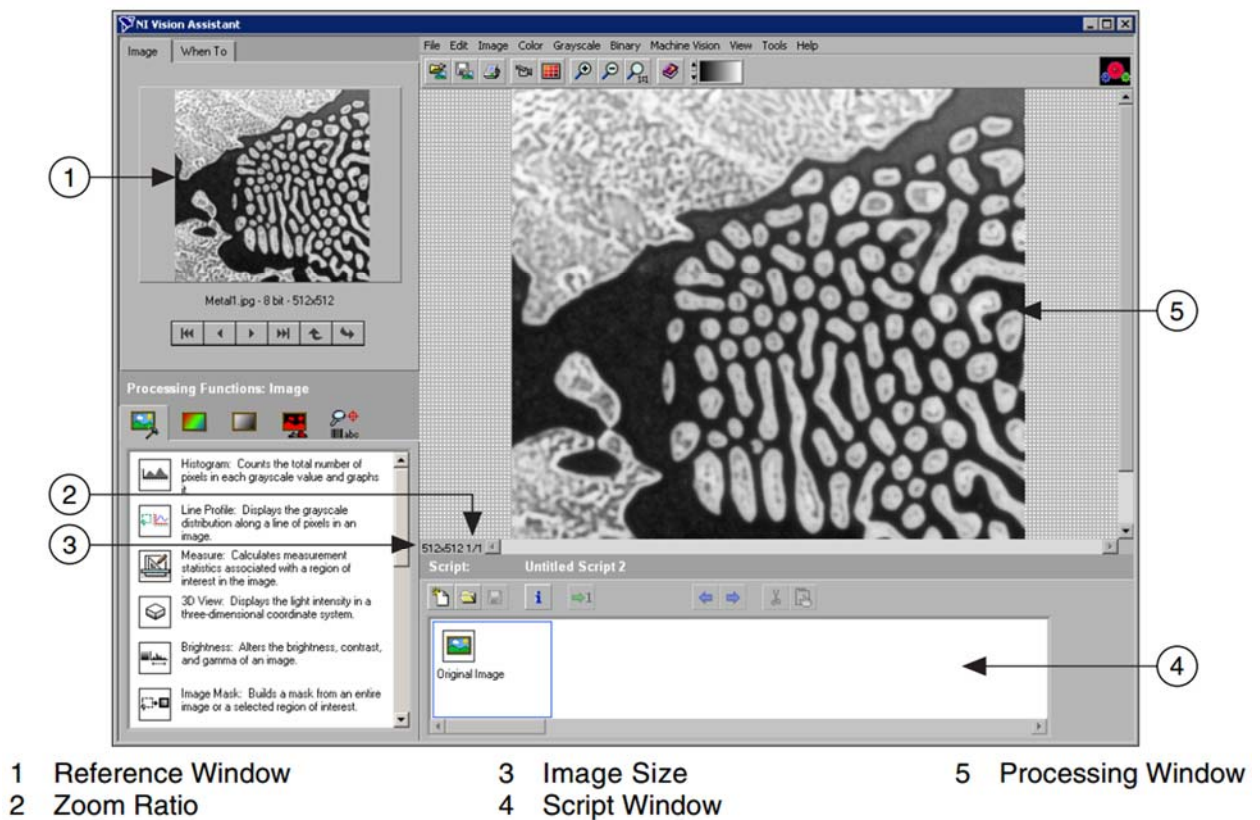
Figure 2.20 NI Vision Assistant Processing Window [90]

The challenging part in developing any robust algorithm using NI Vision is discovering the appropriate combinations and arrangements of these three main categories of VIs, or in other words, laying out the "architectural configuration of the graphical code". As an example, Figure 2.21 shows the block diagram of a simple VI which reads an RGB color image and extracts and displays the corresponding intensity plane. The aforementioned features of NI Vision will be implemented in this research for the development of an improved image acquisition, image calibration and image processing interface in E-UIAIA. For further information regarding image processing with LabView please refer to [91].
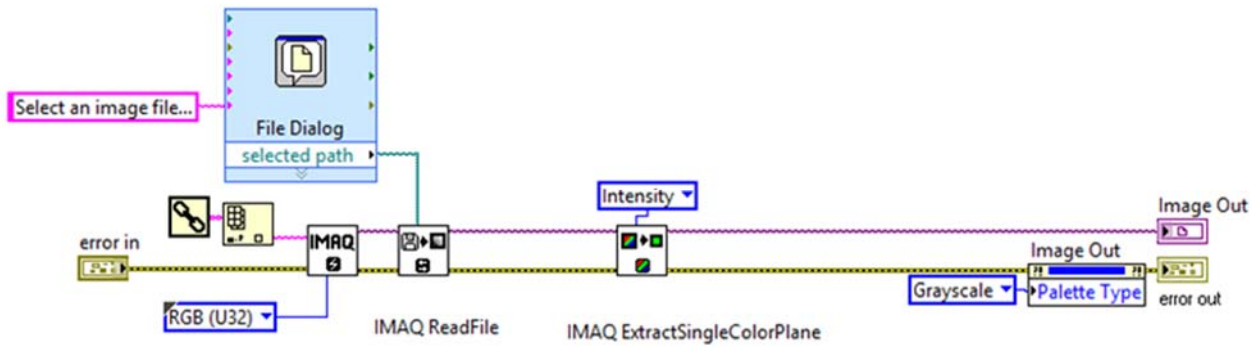
Figure 2.21 Block Diagram of a Sample VI for Reading an Image, Extracting Intensity Channel and Displaying the Results

2.7 Summary

A brief and technical background related to aggregate imaging system and their associated shape/size indices was provided in this chapter. The advantages and disadvantages of laser based systems in comparison to imaging based systems was also discussed. Additionally, available laboratory testing methods for evaluating resistance of aggregate particles to degradation was reviewed in more details. A comprehensive literature review was performed regarding the effect of aggregate shape and size properties in controlling the performance of unbound/bound layers of highway pavement as well as railroad ballast. By looking into several research projects and reports during the past two decades, it cannot be overstated that aggregate shape properties need to be considered as a critical factor which influence the laboratory and in-service performance of different aggregate construction materials. Therefore, advanced and unified testing methods are needed to efficiently and objectively characterize the shape properties of aggregate particles.

Reviewing the literature showed that the degradation behavior with focus on recording the change in particle shape distributions has not been well understood yet. Therefore, this topic needs to be systematically studied to assist in quality control and development of improved methods for classifying aggregate sources and predicting their performances.

CHAPTER 3:

DEVELOPMENT OF ENHANCED UNIVERSITY OF ILLINOIS AGGREGATE IMAGE ANALYZER

This chapter provides detailed information on the different design and manufacturing stages including the calibration phase for the development of Enhanced University of Illinois Aggregate Image Analyzer (E-UIAIA).

3.1 Selection, Manufacturing, and Assembly of Hardware Components

The initial efforts for the development of E-UIAIA started in September 2011. After consulting with Graftek Imaging Inc., different alternatives for proper selection of main components of the imaging system including camera, LED lights, cables, laser sensor and frame grabber were discussed. It was decided that a Dorner 2200 Series small belt conveyor with aluminum frame with flat belt and drive would be considered as the main frame of E-UIAIA. Note that a modified treadmill conveyor belt was originally used in UIAIA. The heavy weight and large dimensions of this treadmill conveyor limited the portability of UIUIA. The Dorner 2200 small belt conveyor is made out of aluminum which makes it light weight and easy to move. Appropriate dimensions for the belt, 12 in. (304.8 mm) width by 42 in. (1066.8 mm) length, provided enough room for the aggregate particles and also mounting three cameras. An adjustable support stand and a motor with variable speed control were also added to the conveyor system. Further information related to the conveyor belt system can be found elsewhere [92].

In the preliminary design of E-UIAIA, it was first envisioned to use black and white cameras to capture monochrome images similar to UIAIA. To address the problem in capturing the images of dark aggregate particles, it was originally decided to consider using one belt with black color and another belt with white color. Although this approach could resolve the issue in regard to imaging the dark colored particles, it could cause other difficulties. Furthermore, two separate image processing modules would then be needed to

segment aggregate particles placed on backgrounds with black or white colors. It means that each time the operator had to visually inspect the aggregate sample and make a decision regarding which color of background to use. Additionally, the belt had to be switched every time to provide the desirable background considering the color of aggregate particles in the sample. Although switching the belt and finding the proper background color could be done in a reasonable amount of time, it would not be practical and causes delay and difficulties in aggregate image acquisition stage.

The machine shop services in the Civil and Environmental Engineering (CEE) Department at the University of Illinois were rendered to manufacture the camera mounts, light mounts as well as installing a metal background for side and front cameras. In the original design of UIAIA, the front and side cameras were orthogonal to each other in a way that it required using two separate backgrounds for side and front cameras. However, in the improved design of E-UIAIA, it was decided to rotate both front and side cameras up to exactly 45 degrees while still keeping them orthogonal. This improvement in the design, eliminates the need for using two separate backgrounds. Note that the background for front and side cameras needed to be replaced with white color in case of imaging dark colored aggregates. Originally, three LED lights were used in E-UIAIA. The front and side lights were positioned vertically and perpendicular relative to the surface of the belt. Furthermore, the top LED light was positioned perpendicular to the background surface. It was observed that capturing the images of aggregates with these light arrangements caused considerable amount of shadow around the aggregate particle in the image. Figure 3.1 shows the initial assembly of E-UIAIA with black and white cameras. This figure shows the shadow in the top image of aggregate particle.

Considering the aforementioned limitations, it was finally decided to use color cameras and a blue background for E-UIAIA. A custom designed non-reflective blue belt was ordered. The blue color was chosen to assure achieving the best contrast between the aggregate particles with all possible natural colors (except blue) and the background. Additionally, a blue metal sheet was installed along the conveyor belt to provide a continuous and consistent blue color background for side and front cameras.
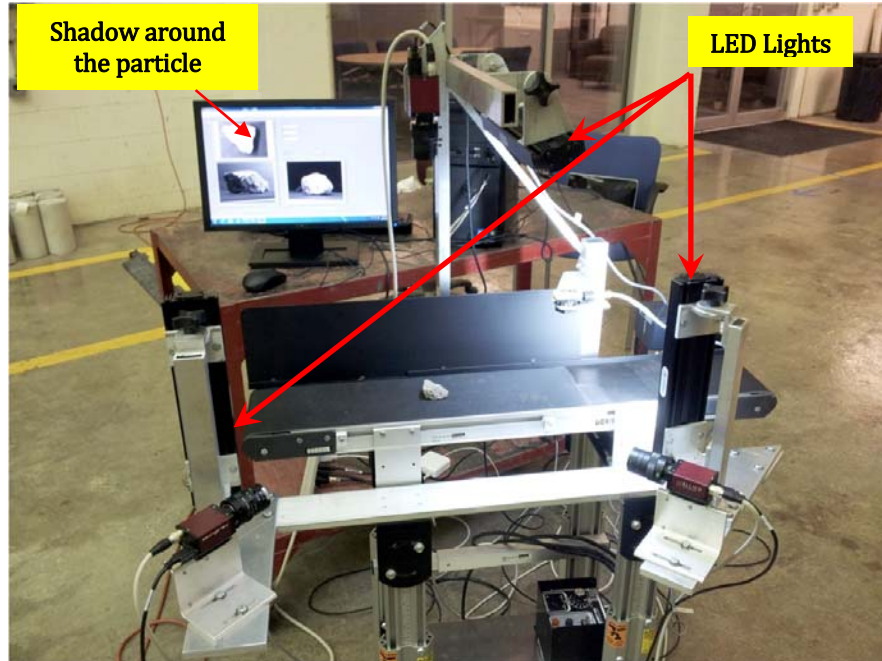
Figure 3.1 Initial Assembly of E-UIAIA with Black and White Cameras

One of the shortcomings of UIAIA was its using a fixed focal length type of lens for the cameras. Considering that the distance between the cameras and the object was fixed, the system would be limited to capture images at a fixed spatial resolution of 160 pixels per inch (ppi). Since the sensor resolution of the cameras in UIAIA were fixed at 640 × 480 pixels, capturing the images of large size aggregate particles such as railroad ballast, with sizes above 2.5 in. (63.5 mm), would be very challenging with this system. After extensive research during the design phase of E-UIAIA, it was decided to use AVT Stingray CCD progressive scan color cameras with 1292 × 964 pixel sensor resolution and using variable focal length lenses. Therefore, considering the 12-36 mm variability in focal length and keeping a fixed distance between cameras and the particles at 18 in. (457.2 mm), it would be possible to capture the images of aggregate particles with sizes from 0.187 in. (4.75 mm) up to 3 in. (76.2 mm)

The associated variable image calibration interface of E-UIAIA will be described later in this chapter. Noted that considering the moving nature of aggregate particles on the belt and the variability of the location of particles when the cameras are triggered, there should be enough room in the image frame for the particle to always stay in the field of view of the

47

cameras. Considering the focal length of the used lenses and the fixed distance between the cameras and the object as described above, the minimum spatial resolutions to capture images of aggregate particles can be identified and are recommended as listed in Table 3.1.

Table 3.1 Recommended Spatial Resolutions for Imaging of Aggregates with Different Sizes

Aggregate size	Target spatial resolution (ppi)
2 in. (50.8 mm) and above	160
1 in. (25.4 mm) and 1.5 in. (38.1 mm)	230
0.5 in. (12.7 mm) and 0.75 in. (19.05 mm)	330
0.187 in. (4.75 mm) and 0.375 in. (9.525 mm)	430

As it was discussed earlier, using three vertical LED lights were found to cause shadows around the particle. Therefore, it was decided to use four High Intensity Advanced Illumination White 24V LED lights and mount them horizontally relative to the belt at left, right, front and top with dimmer controls to assure sufficient and uniform light distribution all around the aggregate particle. Through extensive trials and errors, the optimum locations and angles of these LED lights were finalized to minimize reflection on the belt as well as shadows around the rock. The improved illumination design would make the operator capable of achieving images with best contrast considering the natural color variations in the aggregate particles. A TDK-Lambda AC-DC 24V@25A power supply was installed on the conveyor to provide the required power for four LED lights as well as the laser sensor. Note that the cameras are powered up directly from the computer using the PCI card.

Since the resolution of the captured images in E-UIAIA are almost four times higher than UIAIA, a fast and reliable 1394b Dual Bus PCI Express Card with Four ports was used to transfer the acquired images to the computer at high speed rate. This card is compatible with progressive scan CCD cameras and offers good reliability for real time image acquisition and processing. In order to trigger the cameras at the right moment while the particle is moving on the belt, a Banner Q30 Diffuse-Mode Laser Sensor was mounted on top of the conveyor. All the three cameras were connected to this laser sensor using a I/O 12 pin Hirose to open end cable. Note that a software triggering module was designed to automatically (without the need for laser sensor) save the right image frame while the cameras are in live or real

time acquisition mode and recording up to 30 frames/second. This feature of E-UIAIA will be further explained in this chapter. The speed of the conveyor belt is adjustable with a dimmer control. The hardware triggering control of the E-UIAIA is designed to adjust the delay in triggering the cameras according to the speed of the conveyor belt. Four swivel casters were also assembled on the conveyor belt to facilitate moving the E-UIAIA and improve the portability of the system. A Vostro 260 Mini Tower Dell Personal Computer was selected to control the system. The important specifications of this computer includes an Intel i5 Processor with 3.1 GHz and 6 MB Cache as well as 8 GB Dual Channel DDR3 SDRAM and 500 GB Hard Drive space. Table 3.2 summarizes all the final hardware components of E-UIAIA. More details regarding the electrical wiring drawing for connecting different parts can be found in Appendix A of this dissertation.

The assembly and mounting the parts on the conveyor was accomplished around July 2012. Two more prototypes of E-UIAIA were manufactured in 2013 and were delivered to two industry partners. Figure 3.2 shows the final assembly of E-UIAIA with all of its components.
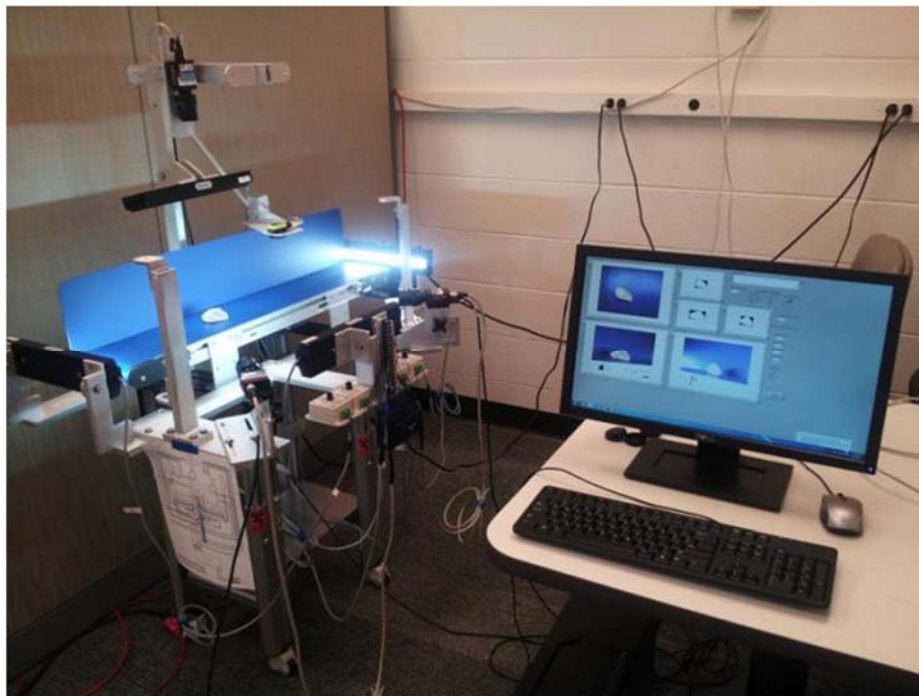

Figure 3.2 Final Assembly of E-UIAIA with Color Cameras and Blue Background

Table 3.2 Description of Hardware Components of E-UIAIA

Hardware Part	Manufacturer	Important Features & Descriptions
Conveyor	Dorner	2200 Series - Flat End Belt Drive - Aluminum Frame
Blue Belt	Dorner (Special order)	1G - Color Contrasting - Urethane Material
CCD Camera	Allied Vision Technology	F-125 Color- Progressive Scan - 1292 x 964 Resolution 30 Frames/Sec
Laser Sensor	Banner	Q30LDLQ Model - Diffuse Mode - Class 2 Static/Dynamic/Single Point
I/O Cable	Allied Vision Technology	Compatible with AVT IEEE 1394 Cameras - 8 pin Hirose Female to Open End
PCI Express Card	Allied Vision Technology	1394 Dual Bus Adaptor with Four Ports Up to 800 Mb/Sec Transfer Rate
IEEE 1394 Cable	Allied Vision Technology	Compatible with AVT IEEE 1394 Cameras - b to b Cable - 9 pin - Screw Lock
LED Light	Advanced Illumination	LL6212-WHI24HD- High Intensity Line light With Diffuser White Color
Camera Lens	Computar	M3Z1228CMP-Manual Variable 12-36 mm Focal Length Max Aperture Ratio 1:2:8
Personal Computer	Dell	Vostro 260 Mini Tower - Intel Core i5 Processor 3.1 GHz 6MB Cache - 8GB DDR3 - 500 GB Hard Disk
LED Dimmer	Super Bright Leds	LDK-8A-DC 24V LED – Output 192 Watts - Max load 8 Amps
Power Supply	TDK-Lambda	DSP60-24 – AC/DC 24V @ 2.5A
Calibration Balls	Hoover Precision	Derlin Material – 2",2.25", and 3" Diameters -Special Grade

3.2 Improved Software Design

Graphical programming in LabView 2012 platform was used to develop VIs to capture and process the images of aggregate particles from three views. The main task in developing the control software for E-UIAIA was establishing an efficient color thresholding algorithm to be able to automatically segment the aggregate particles with both dark and bright colors from the blue background and convert them into their corresponding black and white binary images. The color threshloding scheme is not only used in aggregate shape property image processors but also is applied in hardware and software triggering image acquisition module as well as image calibration interfaces. Therefore, this algorithm will be initially discussed in more detail in this section.

3.2.1 Color Thresholding Scheme in E-UIAIA using HSI Image Representation

As already discussed in Chapter 2, any color image can be represented in different color spaces and channels. In a color image, each pixel has three intensity values corresponding to Red, Green and Blue components. Each channel of a color image is basically a gray scale image with pixel values from 0 to 255. Therefore, grayscale image processing methods can also be applied into individual components of a color image. Figure 3.3 illustrates how the pixels from an RGB color image are formed from corresponding pixels of three channels.
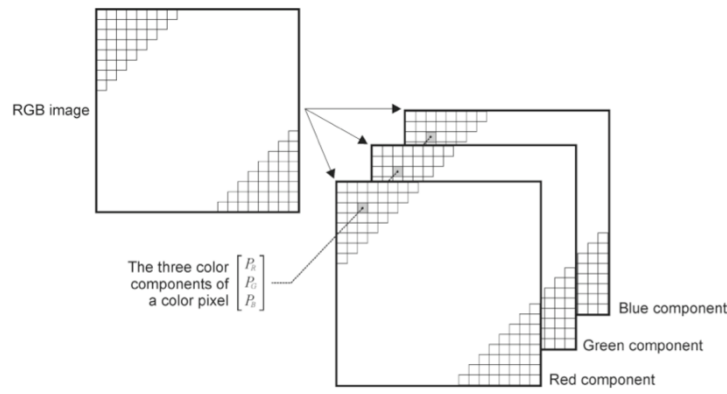
Figure 3.3 Three Color Components of an RGB Image [93]

The RGB color image can be represented in Hue (H), Saturation (S), and Intensity (I) channels using Equations from 3.1 to 3.3. In these equations, it is assumed that RGB pixel values have been normalized to the range between 0 and 1 [93].

$$H = \begin{cases} \theta & if \ B \leq G \\ 360 - \theta & if \ B > G \end{cases} \quad when \quad \theta = \cos^{-1} \left\{ \frac{0.5\left[(R-G)+(R-B)\right]}{\left[(R-G)^2 + (R-B)(G-B)\right]^{1/2}} \right\} \qquad 3.1$$

$$S = 1 - \frac{3}{(R+G+B)}\left[\min(R,G,B)\right] \qquad 3.2$$

$$I = \frac{1}{3}(R+G+B) \qquad 3.3$$

Gray scale images and their corresponding pixel intensity histogram distribution related to RGB and HSI channels of several bright colored and dark colored aggregates were inspected carefully. Two examples of these distribution analysis are shown in Tables 3.3 and 3.4. Table 3.3 shows how dark particle bi-modal image histograms could be achieved in saturation channel. According to Table 3.4, bi-modal histograms were observed in all the channels of RGB and HSI. As discussed in Chapter 2, generally the image histograms with bi-modal shapes are related to images with good contrast between foreground and background. One of the common challenges in segmenting an image into foreground and background is the determination of a proper threshold value. This happens when the background and the object have very similar pixel intensity values, which results in unimodal or multimodal shapes of image histograms. In these cases, it would be very important to choose the correct channel and also identify the appropriate threshold values which can give the best results.

In cases where sufficient contrast does not exist between the background and the foreground, image manipulation techniques such as image filtering and applying Look UP Tables (LUT) to the pixel values are used to enhance the image and facilitate the image segmentation. LUT method will be further discussed in this chapter since it is used in the image processing algorithm of E-UIAIA. Achieving binary images of aggregate particles with minimum amount of noise is the final goal in developing a robust image processing algorithm. Image thresholding is the operation which is used to generate binary images. In a binary image, the pixel values can have only two values which are 0 (black) or 1 (white).

Global thresholding which is the automatic clustering threshold function in LabView was applied to generate the binary black and white images. All automatic thresholding functions that are available in LabView use the histogram of an image to identify the threshold. Figure 3.4 shows a bimodal image histogram. In this figure, i presents the gray level value and h(i) shows the frequency related to each pixel value. The task is to determine a proper threshold value k to divide the histogram into classes 0 and 1. Accordingly, the following iterative procedure is the approach used to determine the threshold value. This method is known as clustering with K-Means variations [93]:

1. Select an initial estimate for the global threshold, k;

Table 3.3 RGB and HSI Representation of a Dark Aggregate Particle and Histograms
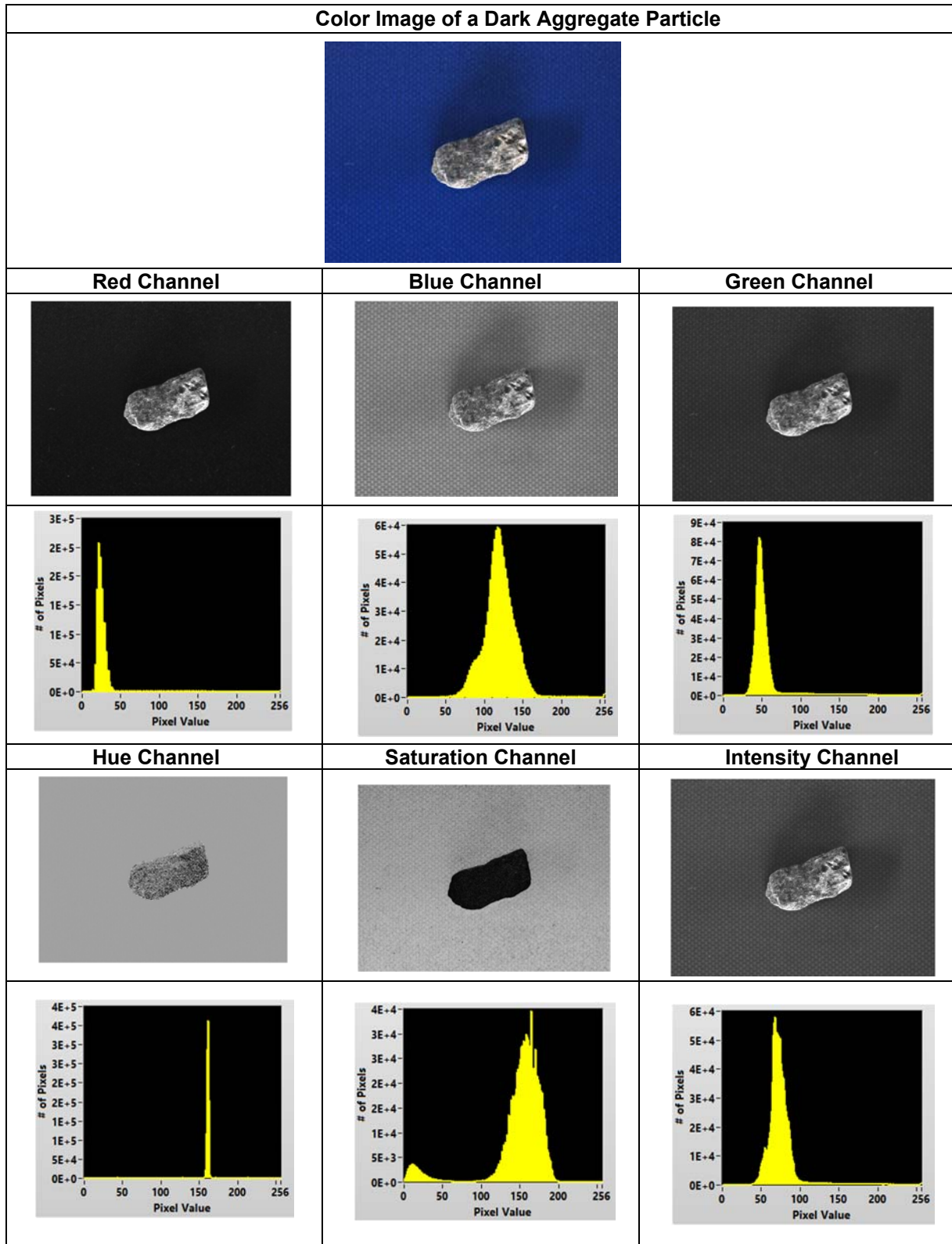
Table 3.4 RGB and HSI Representation of a bright Aggregate Particle and Histograms
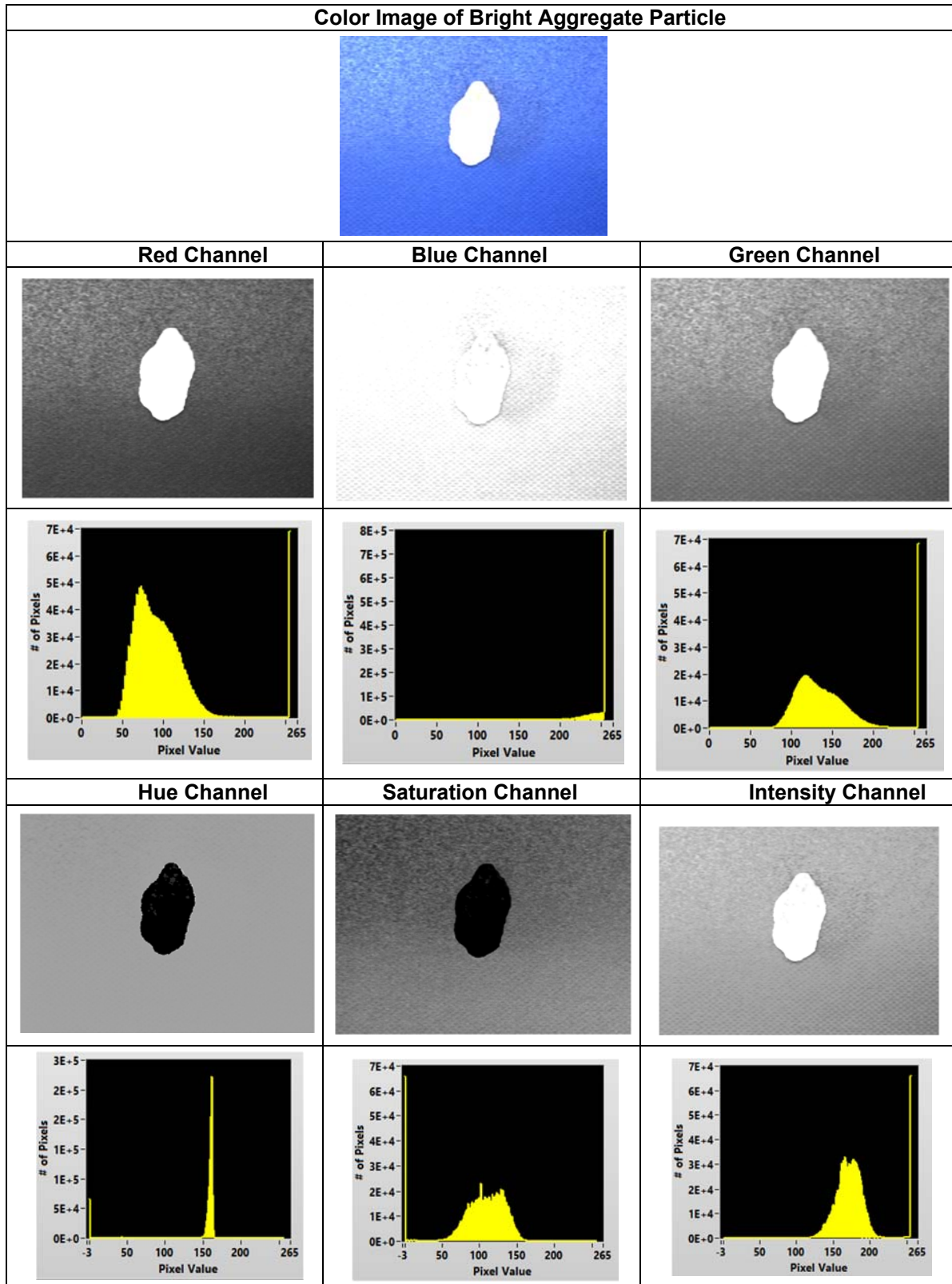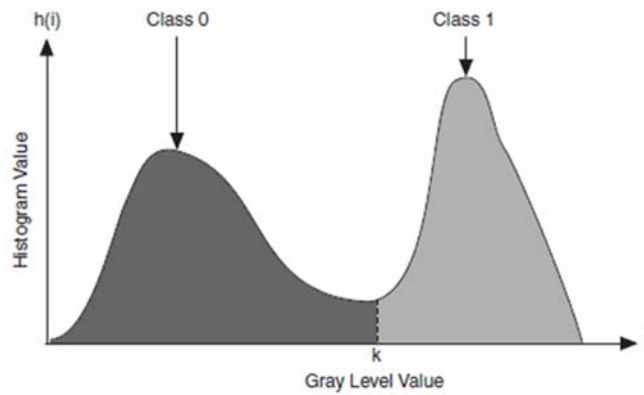
Figure 3.4 Typical Shape of a Bimodal Histogram of an Image

2. Segment the image using k. This will produce two classes of pixels: class 0 includes all the pixels with intensity values less than k and class 1 includes all the pixels with intensity values greater than k;

3. Calculate the average intensity values m_1 and m_2 for the pixels in regions class 0 and class 1, respectively;

4. An updated threshold value is computed according to Equation 3.4;

$$k = \frac{1}{2}(m_1 + m_2)$$ 3.4

5. Steps 2 through 4 are repeated until the difference in k in successive iterations is smaller than a predefined value which is generally considered as 0.5.

To identify the best channels for representing the color images of aggregates, the described clustering thresholding method was applied to RGB and HSI channels of both dark and bright color aggregates shown in Tables 3.2 and 3.3. The output binary images corresponding to each channel is shown in Table 3.5 and 3.6. By visual inspection and comparing these binary images in terms of level of noise after thresholding, it was decided to select Hue and Saturation channels. Note that these two channels were selected since automatic thresholding algorithm showed more or less satisfactory performance in separating the background and the particle without pre-processing of the image. In the next section, the image manipulation and enhancement operations that are used to further reduce the noise in binary images are described.

55

Table 3.5 Clustering Threshold Performance on RGB and HSI Channel on a Dark Aggregate
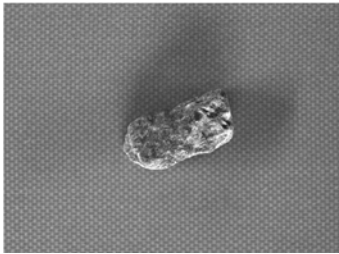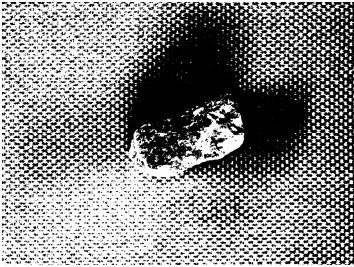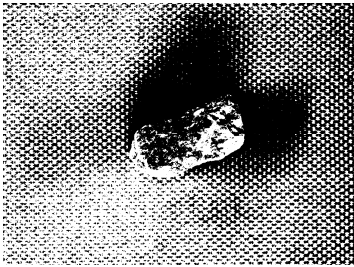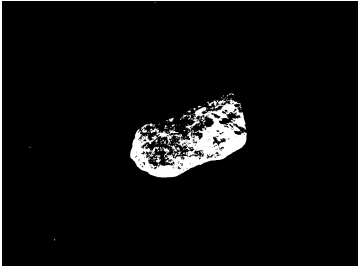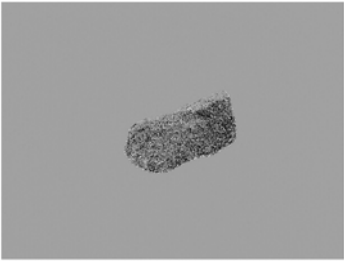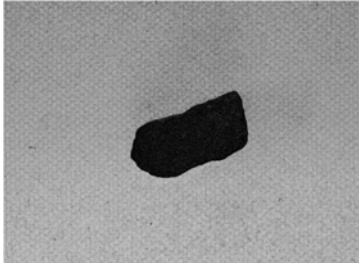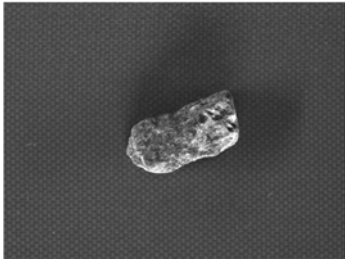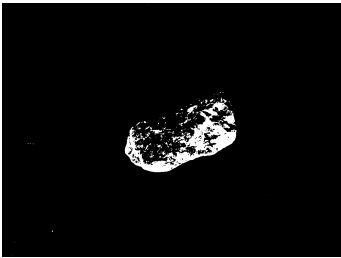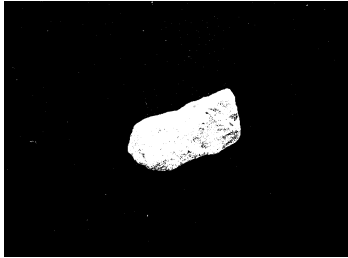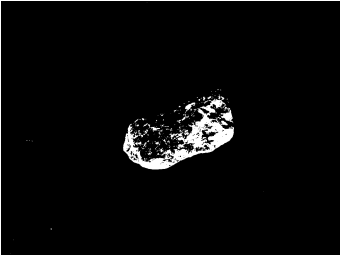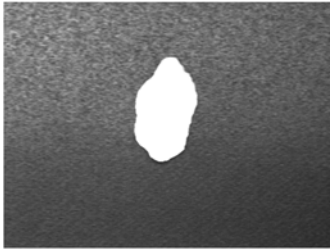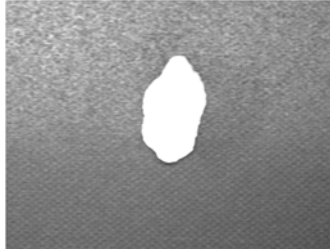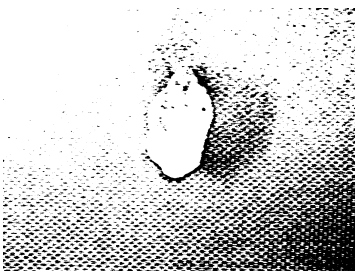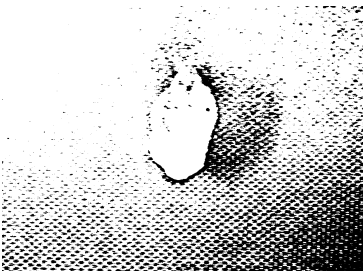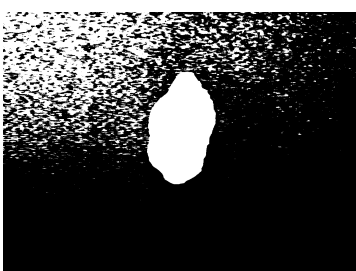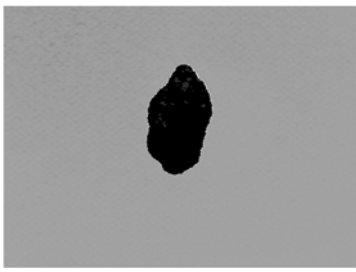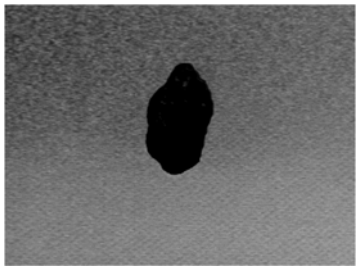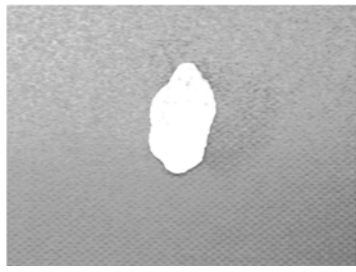
Color Image of a Dark Aggregate Particle		
Red Channel	Blue Channel	Green Channel
Red Thresholded	Blue Thresholded	Green Thresholded
Hue Channel	Saturation Channel	Intensity Channel
Hue Thresholded	Saturation Thresholded	Intensity Thresholded

Table 3.6 Clustering Threshold Performance on RGB and HSI Channel on a Bright Aggregate

Color Image of Bright Aggregate Particle		
Red Channel	Blue Channel	Green Channel
Red Thresholded	Blue Thresholded	Red Thresholded
Hue Channel	Saturation Channel	Intensity Channel
Hue Thresholded	Saturation Thresholded	Intensity Thresholded

(1) Look Up Table (LUT)

Similar to adjusting the brightness and contrast levels while displaying an image on a digital monitor, the goal of image manipulation is generally providing a "better" image. This can be achieved by a function f(g) where g values are the pixels for the original image. This function assigns a new value to each pixel. The process can be shown in Equation 3.5 [90].

$$s_{out}(x, y) = f(s_{in}(x, y)) \hspace{4cm} 3.5$$

In this equation, S_{in} function incudes the original pixel values and S_{out} function the resulting values. The input range obviously spans discrete values between 0 to 255 and the output pixel values can be projected to the same range or can be normalized to a desired range. The function f(g) is often identified by a table including 256 values. This table is called "Look Up Table".

Two customized LUTs were developed as part of color thresholding algorithm for E-UIAIA to enhance the Hue and Saturation channels. These two LUTs project the pixel intensities into a normalized range between 0 (black) to 16 (white) for both Hue and Saturation Channels. Figure 3.5 illustrates these two LUTs.
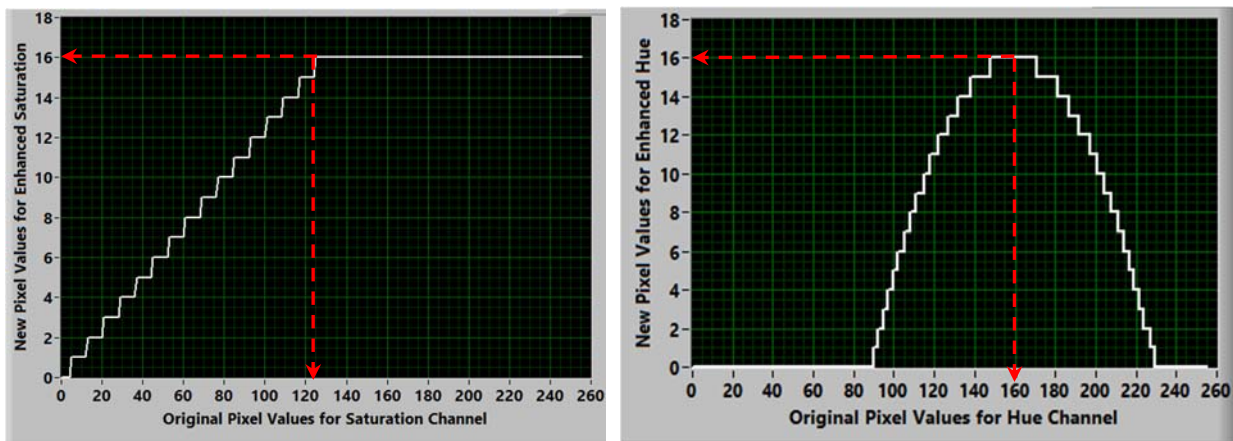
Figure 3.5 Look Up Tables for Enhancing Saturation and Hue Channels

According to Figure 3.5, the pixel values between 0 and 120 in Saturation channel are converted to values between 0 and 16 by a linear step function. Any pixel with intensity above 120 will take 16 as the new pixel value. The maximum Saturation intensity was

selected as 120 based on the observed bi-modal shape of pixel histograms corresponding to Saturation channel for both dark and bright aggregate particles (see Tables 3.3 and 3.4). By inspecting the Saturation histograms it can be observed that pixels with intensities below 120 most probably belong to the particle and the pixels with intensities above 120 belong to background. It is a reasonable assumption to consider that the pixels with intensities closer to 0 (black) belong to the particle with a higher chance. Likewise, all the pixel values above 120 will be returned to 16 which means they will be considered as background. Therefore, the linear step function was selected to improve the contrast between particle and background with a primary focus on highlighting the pixels that belong to aggregate particle.

Inspecting the image histograms related to Hue channel for both dark and bright particle shows that these histograms have uni-modal shape. However, a clear peak is observed in both of the histograms which reflects the effect of background. A conservative assumption through trial and error was made to select the pixels with intensities in the range of 90 to 160 and project them to the range of 0 and 16. It means that pixels with intensities closer to 90 will belong to particle with a higher chance while the pixel with values closer to 160 most probably belong to the background. A similar approach was applied to the pixels with values between 160 and 230. Therefore, a step quadratic function was used to uniformly project the pixel values between 90 and 230 to 0 and 16. The pixels with values below 90 and above 230 were returned to 0 since it was assumed that most probably they belong to particle.
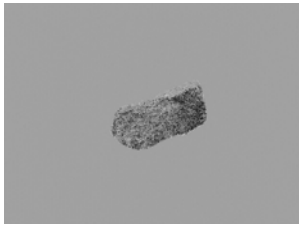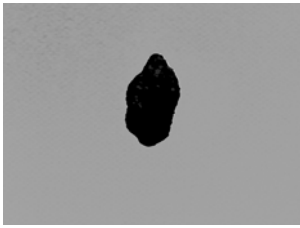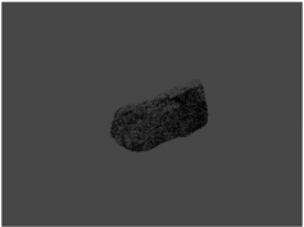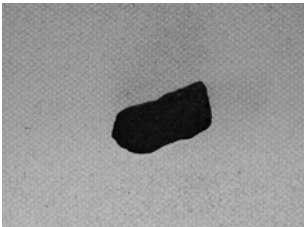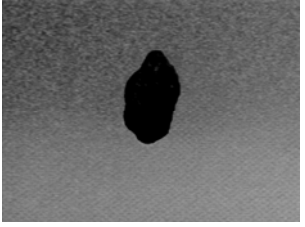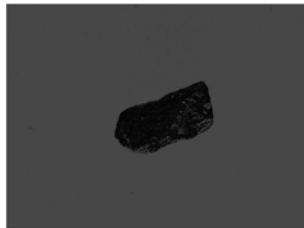
Considering the assumptions that were described above, the enhanced images in Hue and Saturation channels were generated and are shown in Table 3.7. Note that pixel intensities in these manipulated images are between 0 and 16.

(2) Pointwise Image Multiplication

The enhanced images for Hue and Saturation channels were multiplied by each other in order to bring the pixel intensities back to values between 0 and 255. According to the definition regarding pointwise image multiplication, the product image Q can be obtained from images P_1 and P_2 based on Equation 3.6.

$$Q(i, j) = P_1(i, j) \times P_2(i, j) \hspace{4cm} 3.6$$

Table 3.7 Presentation of Enhanced-Hue and Enhanced-Saturation Channels after Applying LUT

Dark Aggregate Particle	Bright Aggregate Particle
Hue Channel	Hue Channel
Enhanced-Hue Channel After LUT	Enhanced-Hue Channel After LUT
Saturation Channel	Saturation Channel
Enhanced- Saturation Channel After LUT	Enhanced-Saturation Channel After LUT

Multiplication of two enhanced images by each other will result in generating a greyscale image with significant improvement in terms of level of contrast between aggregate particle and the background. Therefore, applying the clustering threshold operation on the product of the enhanced Hue and Saturation image, gives clear and noiseless binary images which yield satisfactory segmentation process. The product image

and the corresponding binary image after thresholding is shown in Table 3.8 for both dark and bright aggregate particles.

Table 3.8 Product Image and Corresponding Thresholded Binary Images for Dark and Bright Aggregate Particles

Dark Aggregate Particle	Bright Aggregate Particle
Product Image from Multiplying Enhanced Hue and Enhanced Saturation	**Product Image from Multiplying Enhanced Hue and Enhanced Saturation**
Thresholded Product Image	**Thresholded Product Image**

(3) _IMAQ Fill Hole_

As the final stage in color thresholding process, IMAQ Fill Hole function in LabView [90] was applied on the thresholded images shown in Table 3.7 in order to improve the quality and reduce the noise in the binary images. This function finds and fills all the holes (white pixels) inside the particle by replacing their pixel values with 0.

The performance of the described color thresholding algorithm in segmenting the aggregate particles with different colors are shown in Table 3.9. According to this table, visual inspection of the generated binary images confirms the satisfactory performance of the developed method in thresholding the black and grey particles. Note that the images were captured at 200 ppi spatial resolution to

61

The LabView block diagram related to color thresholding method is provided in Appendix B of this dissertation.

Table 3.9 Segmentation of Aggregate Particles with Different Natural Colors

Aggregate Color Image					
Aggregate Natural color	Pink	Gray	Light brown	White	Black
Binary Image					

3.2.2 Camera Setup and Calibration Interface

According to Figure 3.6, the main user interface of the control software in E-UIAIA includes four different sections. All of the four main modules can be controlled using this interface.
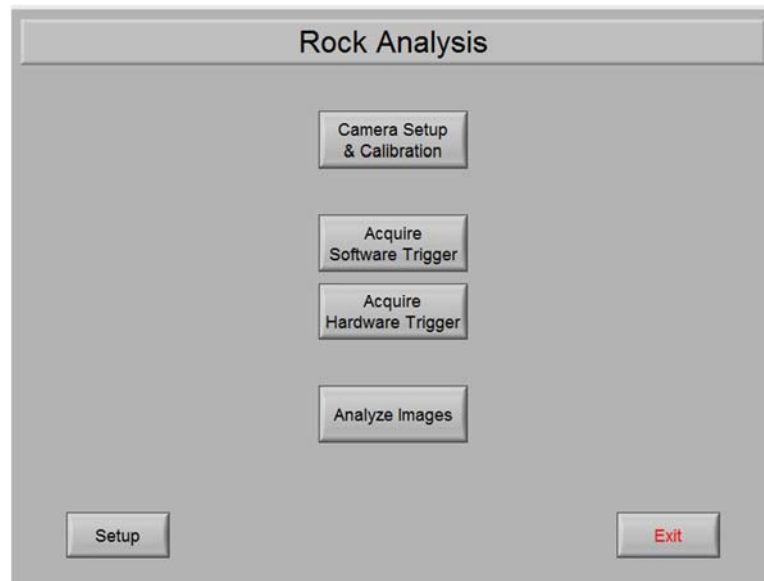
Figure 3.6 Main User Interface of the Software in E-UIAIA

The "setup" button in the main user interface is used to assign the cameras to each view as well as selecting the desired folder in the hard disk for saving the images, calibration

files and the analysis results. The first important step in successful measurement of aggregate shape properties is accurate and consistent image calibration. As discussed in section 3.1, using the camera setup and calibration module and the variable focal lengths of the camera lenses, the operator is able to adjust the system to capture images at 160 ppi to 430 ppi spatial resolution by taking into account the size of the aggregate particles. The white spherical calibration balls with known diameters are used to verify the achieved number of pixels per inch for each of the three cameras.

Additionally, camera setup and calibration module allows the operator to adjust the gain levels for each camera. This feature helps to numerically control the intensity of illumination that will be experienced by camera sensors. In other words, controlling the camera gains make it possible to determine the optimum digital illumination levels associated with the natural color variation of aggregate sources.

During the calibration process, all the three cameras are in continuous image acquisition mode. Thus, a real time color thresholding scheme, as described in section 3.2.1, assists the operator to observe the effect of change in illumination levels on the generated black and white binary images for both aggregate particles and calibration balls. Figure 3.7 shows the block diagram for continuous image acquisition and display mode used in the calibration module of E-UIAIA. NI-Vision Acquisition Software in LabView was used to design this feature.

After final adjustment of all three cameras and achieving desired identical number of pixels per inch in addition to identifying camera gain levels, "save calibration" controller on the front panel is used to save the associated calibration file. The system records and saves the calibrated values in a text file named "calibration". This calibration file is later used in image analysis module to convert the size, surface area and volume of aggregate particles into real engineering units in terms of in., in.^{2} and in.^{3} respectively.

Figure 3.8 shows a screen shot of the calibration interface in E-UIAIA. Verifying and evaluating the accuracy of the system in identifying size and shape properties of calibration spheres will be presented later in this chapter.
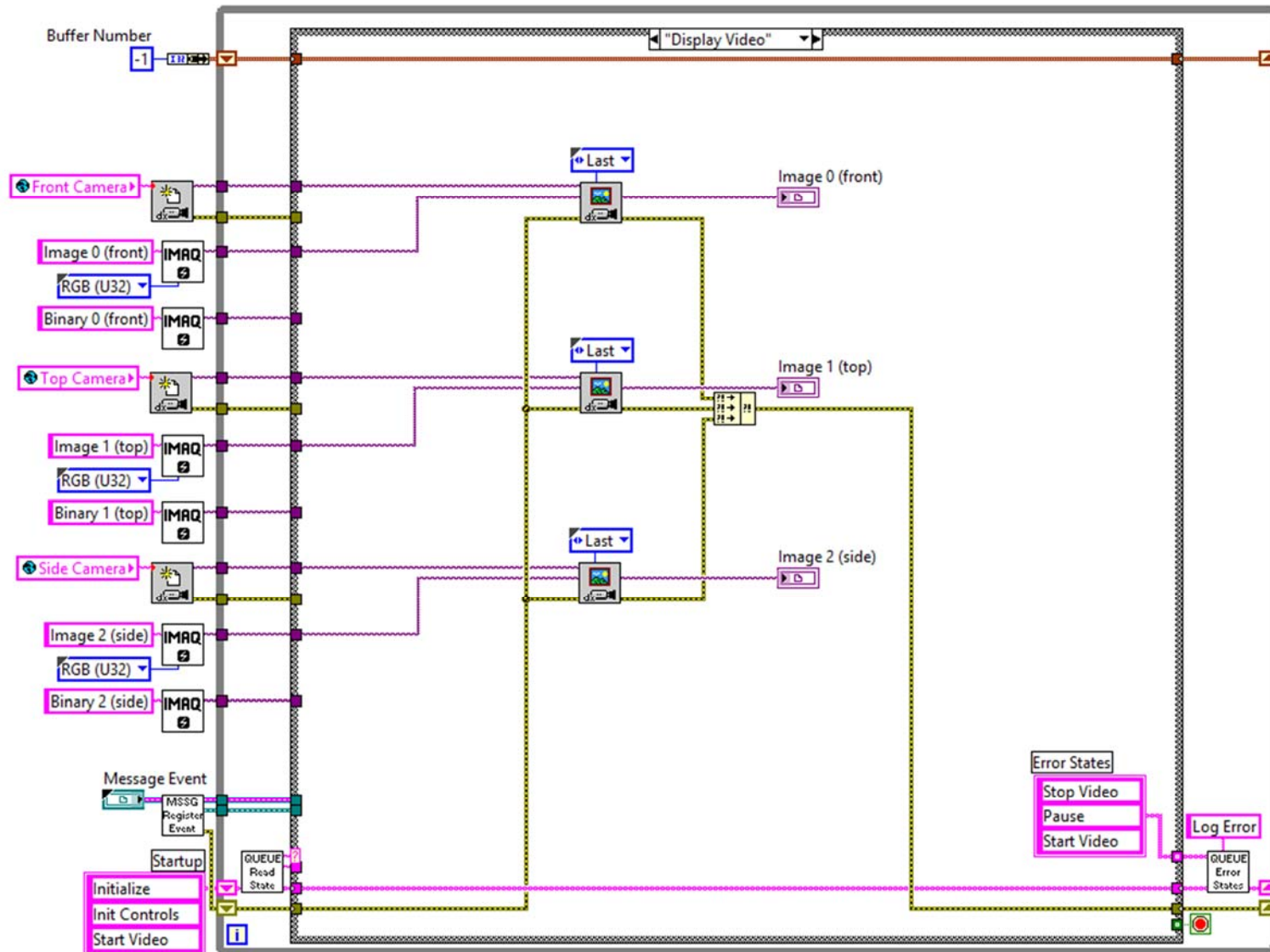
Figure 3.7 Block Diagram for Continuous Vision Acquisition and Display in E-UIAIA
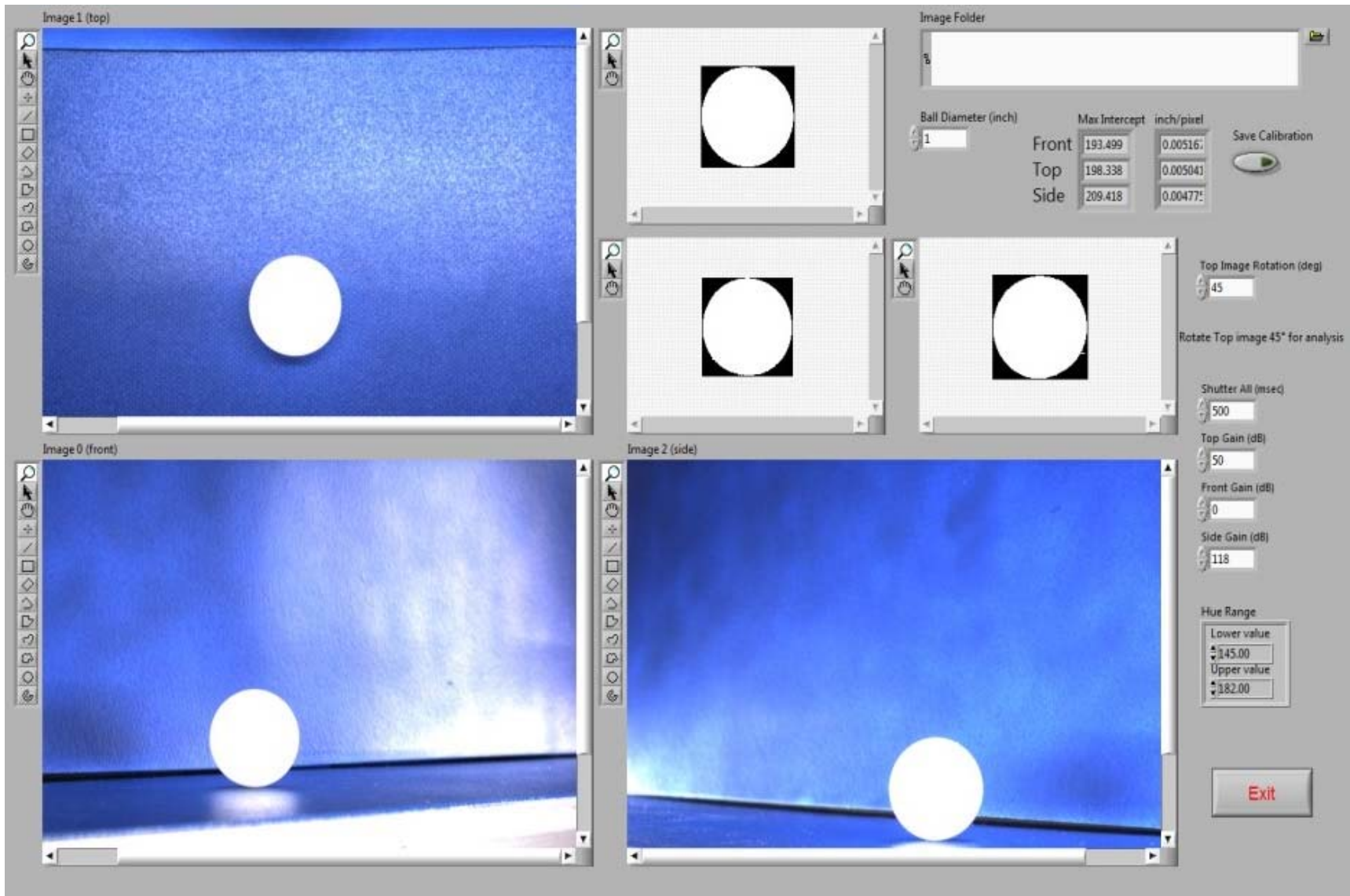
Figure 3.8 Camera Setup and Image Calibration User Interface in E-UIAIA

3.2.3 Aggregate Image Acquisition in Hardware and Software Modes

After calibration of all three cameras, the operator can decide between two alternatives to start acquiring the images of aggregate particles. If "Acquiring Hardware Trigger" mode is selected, the conveyor belt speed, camera delay and the laser sensor need to be adjusted relative to each other so that the cameras can be triggered at the right moment to save the images of particles when the aggregates are both in the field of view of the cameras and in the middle of the captured frame. The camera delay controller on the front panel can control all the three cameras. This method, which was originally used in UIAIA, has several drawbacks. For example, increasing or decreasing the conveyor belt's speed will require the operator to re-adjust the camera delays and reprogram the laser sensor. Additionally, the particles may not be positioned exactly on the center of the belt which may prevent the laser sensor to detect them. The need to adjust these parameters during image acquisition reduces the productivity of the system in terms of accuracy and scanning speed. Moreover, identifying the correct parameters can be a time-consuming and tedious process.

Therefore, an innovative live image acquisition and automatic real-time binary image processor/displayer was developed and a new module was added to E-UIAIA. If "Acquiring Software Trigger" mode is selected, all three cameras are set at the image capturing rate of 30 frames/second at shutter speed of 500 milliseconds. The captured frames are stored in the temporary memory and continuously inspected to check the existence/nonexistence of the particles. When the particle arrives to the center of field of view of the three cameras, the captured frame is saved and sent to the hard disk. Also, the color thresholding scheme generates the corresponding black and white binary image which is displayed on the front panel of user interface. Therefore, the software triggering module makes it possible to bypass the laser sensor and trigger the cameras based on the location of the particles in the image. This facilitates the process of image acquisition and also increases the scanning speed. A screen shot of the control software while acquiring three images of an aggregate particle with pink color at software triggering mode is shown in Figure 3.9. It needs to be added that Region of Interest (ROI) tools in LabView was used to focus the segmentation operation on just the aggregate particle and not the metal parts of the conveyor which might be visible in the side and front views.

66
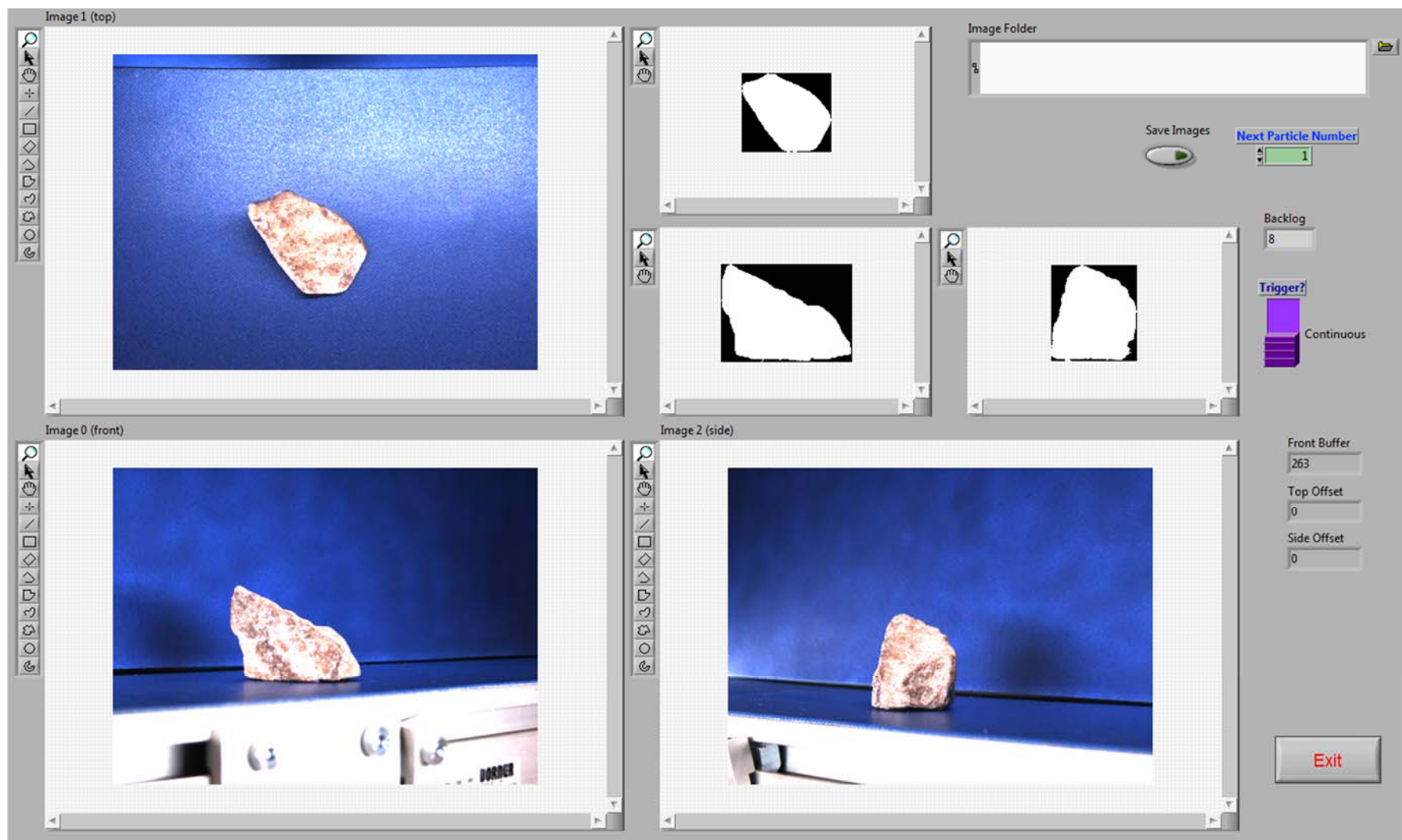
Figure 3.9 Software Triggering Module in E-UIAIA

3.2.4 "Analyze Images" Interface

The first stage in developing the "Analyze Images" module of E-UIAIA was carefully inspecting the current VIs used in UIAIA for calculating the shape properties of aggregates. Note that UIAIA was programmed based on LabView 2006 platform and calculating the shape properties require running separate VIs to compute each imaging based index. Additionally, a few programming errors or "bugs" were found in the current VIs that were corrected. In the angularity index VI, last angle measurement on the boundary of particle skipped a point and considered 23 points around the particle. According to angularity index definition given in [31] and described in Chapter 2, the algorithm was supposed to use 24 points on the boundary of aggregate particle to measure the angle at each vertex. Therefore, measuring 23 angles instead of 24 angles resulted in over estimating the angularity index values. The related numerical error will be discussed later in the validation section of this chapter.

Additionally, it was observed that an error in surface area VI resulted in over estimating the surface area of calibration spheres with known surface area values. Therefore, all of the VIs were reprogrammed using 2012 LabView version following the mathematical definitions of individual shape indices as described in [31, 46]. The block diagram of these new reprogrammed VIs for calculating the imaging based shape indices are included in Appendix B of this document. Finally, all of the VIs were combined into one master VI in a way that each shape index could be called as a "sub VI" when needed.

All of the shape indices can be computed simultaneously in the image analysis interface of E-UIAIA. The calibration file reader as well as color thresholding sub VI were also added to the master VI. Consequently, this module is capable of accepting color or black and white binary images for processing and returning the indices in engineering units. Using "Analyze Images" module, the operator can select the folder that includes the acquired images and the associated calibration file is automatically loaded (see Figure 3.10). After loading the acquired images, if the operator pushes "start analysis" controller on the front panel, the shape properties are computed and the numerical results are stored in an MS Excel file for further statistical post-processing analysis.
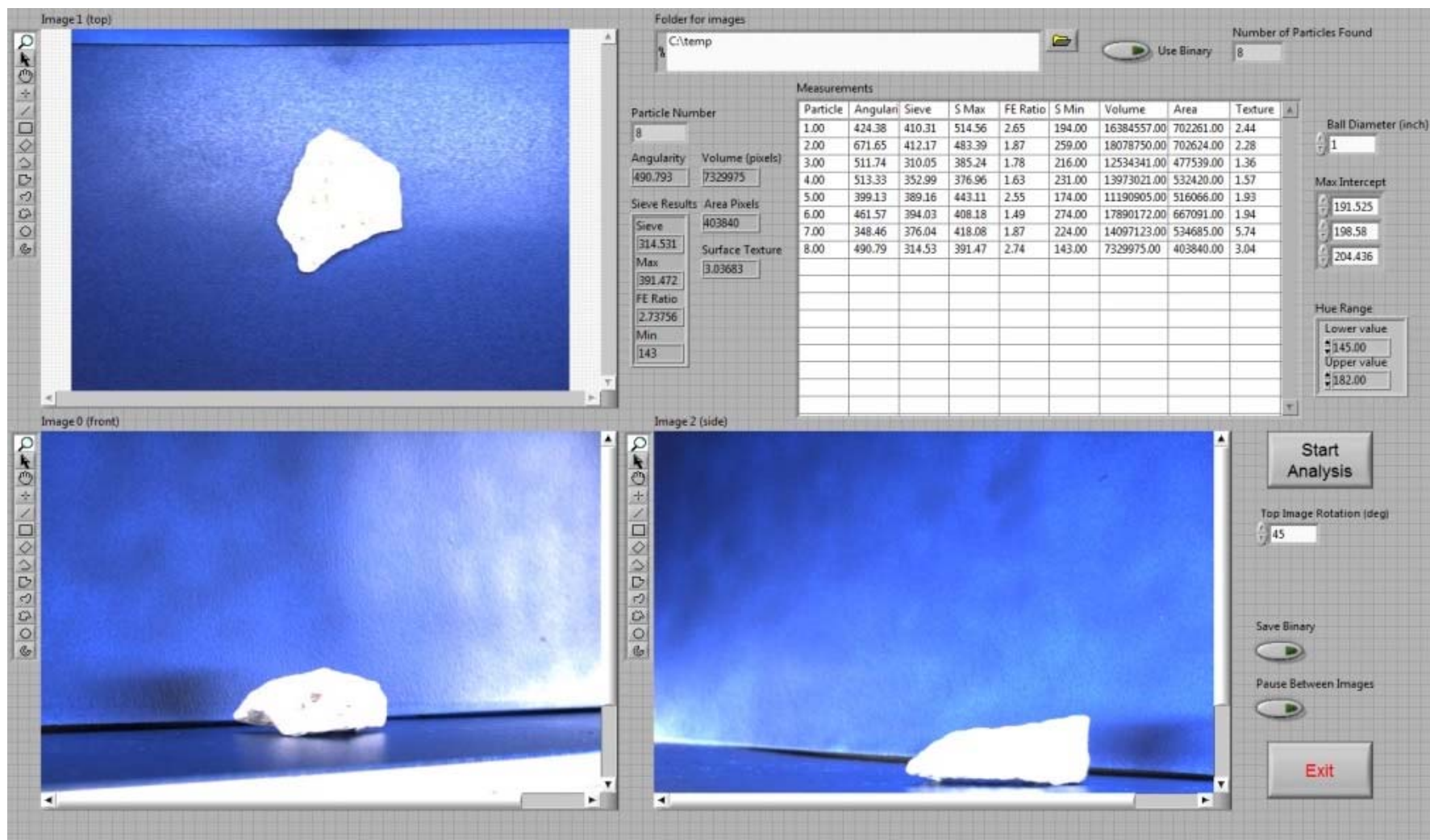
Figure 3.10 Analyze Image Module in E-UIAIA

Finally, the most important hardware and software modifications and advantages of E-UIAIA in comparison to UIAIA are summarized in Table 3.10.

Table 3.10 Comparison of UIAIA and E-UIAIA

Feature Description	UIAIA	E-UIAIA
Thresholding scheme	Black and white	Color-HSI Multichannel with Image Enhancement
Image processing speed	1 particle/second - Binary	20 particles/second - RGB & Binary
Camera sensor resolution	640 × 480	1292 × 964
Image format	bmp / monochrome	png / color
Light intensity control	Constant	Dimmer control/Camera gain control
Focal length	Constant	Variable with 12-36 mm
Spatial resolution	160 pixels/inch (0.1875 mm/pixels)	Variable 160-430 pixels/inch (0.1875-0.0564 mm/pixels)
Calibration method	Constant	Variable for each aggregate size
Camera triggering method	Laser sensor	Live video (30 frames/second) -Automatic simultaneous frame grabber

3.3 Validation of E-UIAIA

This section includes the final stage in the development of the E-UIAIA. This task was accomplished by evaluating the performance of the E-UIAIA system in generating repeatable and accurate measurements of imaging based shape indices.

3.3.1 Validation in Calibration Interface with Calibration Balls

Image calibration is used to convert the measurements made in terms of number of pixels into engineering units. Generally, calibration objects with known dimensions are used in image calibration to evaluate the accuracy of the measurements in the system. Measurement error in imaging systems is called "digitization error" which is a function of several factors including the sensitivity of the camera sensor to temperature and illumination in addition to magnitude of existing lens distortion. These factors not only vary from sensor to sensor but also vary from pixel to pixel in the same sensor. These effects may corrupt the intensity levels represented in every pixel of the image which influences the measurement accuracy. Fortunately, these errors can be significantly decreased by using

simple and frequent calibration operation on an imaging system to ensure the accuracy of the measurements and monitor the errors.

Four calibration spherical balls with 1 in. (25.4 mm), 0.75 in. (19.05 mm), 0.625 in. (15.875 mm), and 0.5 in. (12.7 mm) diameters have been originally used in calibrating the UIAIA. Since E-UIAIA is capable of capturing the images of particles with sizes up to 3 in. (76.2 mm), three additional calibrations spheres with 3 in. (76.2 mm), 2.75 in. (69.85 mm) and 1.5 in. (38.1 mm) were provided to achieve the average measurements for all sizes as well as finding the most accurate calibration factors at all levels of spatial resolution. These calibration balls are shown in Figure 3.11. Additionally, their expected shape and size indices are presented in Table 3.11. Note that the surfaces of these spheres are fully polished; therefore, their expected surface texture index would be close to zero.
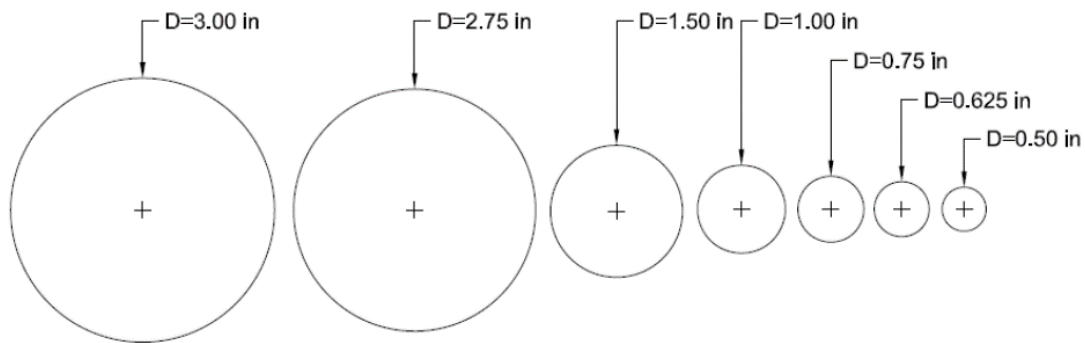
Figure 3.11 Calibration Spheres Used for Calibrating E-UIAIA
(Drawn to Relative Scale of 1:2)

Table 3.11 Expected Shape and Size Indices for Calibration Spheres

Calibration Sphere	Expected Theoretical Shape and Size Indices					
	Sieve size (in)	Area (in^2)	Volume (in^3)	Angularity Index (Degrees)	Surface Texture Index	F&E Ratio
3 in. diameter sphere	3.00	28.2743	14.1372	0	0	1
2.75 in. diameter sphere	2.75	23.7583	10.8892	0	0	1
1.5 in. diameter sphere	1.50	7.0686	1.7671	0	0	1
1 in. diameter sphere	1.00	3.1416	0.5236	0	0	1
0.75 in. diameter sphere	0.75	1.7671	0.2209	0	0	1
0.625 in. diameter sphere	0.625	1.2272	0.1278	0	0	1
0.5 in. diameter sphere	0.50	0.7854	0.0654	0	0	1

In Table 3.11 and other sections of this chapter, sieve size, area and volume are reported in terms of US measurement system because both UIAIA and E-UIAIA are calibrated based on the number of pixels per inch. According to Rao [31], the calibration factor as 1 in. =158.6 pixels is recommended for images that are captured by UIAIA. The size and shape properties of calibration balls measured by UIAIA in addition to their associated error values are summarized in Table 3.12. Note that measurement errors for calibration balls are calculated by comparing the size and shape values measured by UIAIA with their corresponding expected values listed in Table 3.11. The effect of new software and hardware components used in E-UIAIA on the reported imaging based shape indices will be further discussed in this chapter.

Table 3.12 Measurements and Errors Achieved with UIAIA at 158.6 ppi Calibration Factor [31]

Object	Measurement with UIAIA					
	Sieve size (in)	Area (in²)	Volume (in³)	Angularity Index (Degrees)	Surface Texture Index	F&E Ratio
1 in. diameter sphere	1.002	83.368	0.544	49.942	0.071	1.078
0.75 in. diameter sphere	0.741	34.776	0.229	39.442	0.084	1.107
0.625 in. diameter sphere	0.627	19.599	0.130	62.940	0.156	1.060
0.5 in. diameter sphere	0.516	10.805	0.073	119.518	0.216	1.059
Object	Measurement Errors (%)					
	Sieve size	Area	Volume	Angularity Index	Surface Texture Index	F&E Ratio
1 in. diameter sphere	0.197	2553.699	3.807	6.936	1.183	1.300
0.75 in. diameter sphere	-1.266	1867.892	3.756	5.478	1.400	1.783
0.625 in. diameter sphere	0.382	1497.075	1.994	8.742	2.600	1.000
0.5 in. diameter sphere	3.135	1275.738	11.037	16.600	3.600	0.983
Average Error for all sizes	*0.612*	*1798.6*	*5.149*	*9.439*	*2.196*	*1.267*

It was observed that the highest errors belong to angularity index and surface area measurements. As it was discussed earlier, these errors were partially due to "programming bugs" and therefore, malfunctioning the associated VIs. Table 3.12 also lists how the error values in measuring the surface texture index are increasing for smaller size spheres.

This can be related to using fixed spatial resolution in UIAIA and increasing noise levels in capturing and processing the images of smaller size objects. Nevertheless, Table 3.12 shows that the average error values for size, volume, surface texture and F&E Ratio for all sizes are less than 10%.

E-UIAIA was calibrated at four different target spatial resolutions according to Table 3.13 using the variable focal length capability of the lenses. Table 3.13 shows the average of achieved maximum intercept for all the three orthogonal views that are normalized to 1 inch. Note that 5 trials for individual sizes were used and the average of measurements are reported in Table 3.13. Since the fields of view of cameras decrease by increasing the focal length of lenses, capturing images of 3 in. and 2.75 in. calibration spheres at the spatial resolutions above 160 ppi was not possible. Therefore, the average captured values for all available sizes and for all the three cameras in E-UIAIA are used to convert the measurements into engineering units and also calculating the errors.

Table 3.13 Average of Achieved 1 in. Normalized Maximum Intercept in E-UIAIA

Object	Target Spatial Resolution (ppi)			
	160.00	230.00	330.00	430.00
3 in. diameter sphere	169.34	N/A	N/A	N/A
2.75 in. diameter sphere	168.13	N/A	N/A	N/A
1.5 in. diameter sphere	163.78	234.77	335.93	436.91
1 in. diameter sphere	164.60	233.80	333.84	434.54
0.75 in. diameter sphere	167.68	236.30	334.42	436.43
0.625 in. diameter sphere	168.41	237.24	334.46	432.29
0.5 in. diameter sphere	170.24	237.90	335.72	436.98
Average of all sizes	*167.46*	*236.00*	*334.88*	*435.43*

The measured shape indices for calibration spheres and error values in E-UIAIA are summarized in Table 3.14, 3.15 and 3.16 at different spatial resolutions. The following points can be concluded by comparing these results with those given in Table 3.12:

1- The average error related to surface area has significantly decreased. The reprogrammed VI follows the exact procedure developed by Pan [46] for calculating the surface area.

Table 3.14 Measurements and Errors Achieved with E-UIAIA at 160 ppi

Object	Measurement with E-UIAIA @ 160 ppi					
	Sieve size (in)	Area (in^2)	Volume (in^3)	Angularity Index (Degrees)	Surface Texture Index	F&E Ratio
3 in. diameter sphere	2.937	32.789	14.814	0.000	0.133	1.052
2.75 in. diameter sphere	2.694	27.357	11.373	0.000	0.092	1.046
1.5 in. diameter sphere	1.451	7.760	1.730	0.000	0.080	1.022
1 in. diameter sphere	0.970	3.434	0.509	3.978	0.190	1.032
0.75 in. diameter sphere	0.731	1.981	0.219	43.054	0.154	1.060
0.625 in. diameter sphere	0.612	1.359	0.127	45.348	0.102	1.050
0.5 in. diameter sphere	0.494	0.889	0.066	74.078	0.144	1.050
Object	Measurement Errors @ 160 ppi (%)					
	Sieve size	Area	Volume	Angularity Index	Surface Texture Index	F&E Ratio
3 in. diameter sphere	-2.114	15.967	4.568	0.000	2.222	0.861
2.75 in. diameter sphere	-2.054	15.146	4.250	0.000	1.533	0.767
1.5 in. diameter sphere	-3.271	9.784	-2.175	0.000	1.333	0.367
1 in. diameter sphere	-3.036	9.320	-2.881	0.553	3.167	0.533
0.75 in. diameter sphere	-2.492	12.086	-0.722	5.980	2.567	1.000
0.625 in. diameter sphere	-2.065	10.737	-0.541	6.298	1.700	0.833
0.5 in. diameter sphere	-1.125	13.186	0.141	10.289	2.400	0.833
Average Error for all sizes	*-2.308*	*12.318*	*0.377*	*3.303*	*2.132*	*0.742*

2- The average error related to angularity index has decreased as a result of debugging the associated VI as well as using higher spatial resolution for smaller objects.

3- The average error related to flat & elongated ratio has decreased.

4- The average error values related to volume, surface texture and size are all less than 6% which confirms accurate imaging based measurement at different spatial resolutions.

Note that the errors in surface area and volume increased up to 1-2% at higher spatial resolutions. This finding might be related to "optical distortion." Optical distortion is caused by the optical design of lenses and is also called "lens distortion."

Table 3.15 Measurements and Errors Achieved with E-UIAIA at 230 ppi

| Object | Measurement with E-UIAIA @ 230 ppi | | | | | |
	Sieve size (in)	Area (in²)	Volume (in³)	Angularity Index (Degrees)	Surface Texture Index	F&E Ratio
3 in. diameter sphere	1.452	8.033	1.783	0.000	0.118	1.036
2.75 in. diameter sphere	0.984	3.571	0.536	0.000	0.130	1.020
1.5 in. diameter sphere	0.740	2.007	0.227	13.334	0.094	1.028
1 in. diameter sphere	0.621	1.390	0.132	8.588	0.232	1.026
0.75 in. diameter sphere	0.500	0.897	0.067	60.984	0.254	1.022
Object	Measurement Errors @ 230 ppi (%)					
	Sieve size	Area	Volume	Angularity Index	Surface Texture Index	F&E Ratio
3 in. diameter sphere	-3.200	13.645	0.924	0.000	1.967	0.600
2.75 in. diameter sphere	-1.579	13.660	2.278	0.000	2.167	0.333
1.5 in. diameter sphere	-1.274	13.596	2.737	1.852	1.567	0.467
1 in. diameter sphere	-0.687	13.274	3.000	1.193	3.867	0.433
0.75 in. diameter sphere	0.064	14.181	3.094	8.470	4.233	0.367
Average Error for all sizes	*-1.335*	*13.671*	*2.407*	*2.303*	*2.760*	*0.440*

Increasing the level of distortion at higher focal length values is a known concept in computational photography. Further information regarding this fact can be found in [94]. Note that higher spatial resolution in E-UIAIA was achieved by using camera lens zoom and without physically moving the cameras closer to the object. Since the error values caused by lens distortion did not have a significant effect in increasing the errors on the shape indices, it was decided to fix the location of the cameras in order to facilitate easier operation of E-UIAIA. Note that the hardware design of E-UIAIA provides the possibility to adjust the positions of all cameras.

In general, the findings of the calibration experiment showed that E-UIAIA could successfully identify the known shape indices for spherical calibration balls. The overall measurement errors were found to be in reasonable ranges. Therefore, it was concluded that the established configuration of hardware and the features of the developed software were efficient enough for accurate measurements of shape indices. Further validation of the system is discussed next.

Table 3.16 Measurements and Errors Achieved with E-UIAIA at 330 ppi and 430 ppi

Object	Measurement observed with E-UIAIA @ 330 ppi					
	Sieve size (in)	Area (in²)	Volume (in³)	Angularity Index (Degrees)	Surface Texture Index	F&E Ratio
1.5 inch diameter sphere	1.471	8.132	1.865	0.000	0.108	1.022
1 inch diameter sphere	0.990	3.616	0.553	0.000	0.110	1.030
0.75 inch diameter sphere	0.747	2.045	0.236	0.000	0.120	1.020
0.625 inch diameter sphere	0.620	1.405	0.135	0.000	0.106	1.020
0.5 inch diameter sphere	0.498	0.901	0.069	5.334	0.102	1.020
Object	Measurement Errors @ 330 ppi (%)					
	Sieve size	Area	Volume	Angularity Index	Surface Texture Index	F&E Ratio
1.5 inch diameter sphere	-1.960	15.043	5.565	0.000	1.800	0.367
1 inch diameter sphere	-0.993	15.101	5.553	0.000	1.833	0.500
0.75 inch diameter sphere	-0.416	15.738	6.696	0.000	2.000	0.333
0.625 inch diameter sphere	-0.722	14.530	5.248	0.000	1.767	0.333
0.5 inch diameter sphere	-0.464	14.680	5.940	0.741	1.700	0.333
Average Error for all sizes	*-0.911*	*15.019*	*5.800*	*0.148*	*1.820*	*0.373*
Object	Measurement observed with E-UIAIA @ 430 ppi					
	Sieve size (in)	Area (in²)	Volume (in³)	Angularity Index (Degrees)	Surface Texture Index	F&E Ratio
1.5 inch diameter sphere	1.471	8.132	1.865	0.000	0.108	1.022
1 inch diameter sphere	0.990	3.616	0.553	0.000	0.110	1.030
0.75 inch diameter sphere	0.747	2.045	0.236	0.000	0.120	1.020
0.625 inch diameter sphere	0.620	1.405	0.135	0.000	0.106	1.020
0.5 inch diameter sphere	0.498	0.901	0.069	5.334	0.102	1.020
Object	Measurement Errors @ 430 ppi (%)					
	Sieve size	Area	Volume	Angularity Index	Surface Texture Index	F&E Ratio
1.5 inch diameter sphere	-1.960	15.043	5.565	0.000	1.800	0.367
1 inch diameter sphere	-0.993	15.101	5.553	0.000	1.833	0.500
0.75 inch diameter sphere	-0.416	15.738	6.696	0.000	2.000	0.333
0.625 inch diameter sphere	-0.722	14.530	5.248	0.000	1.767	0.333
0.5 inch diameter sphere	-0.464	14.680	5.940	0.741	1.700	0.333
Average Error for all sizes	*-0.911*	*15.019*	*5.800*	*0.148*	*1.820*	*0.373*

3.3.2 Validation of VIs for Computing Shape Indices – Comparison Study with UIAIA

An aggregate imaging database that was used back in 2005 in a validation study on UIAIA [46] was used in this research to evaluate the performances of improved VIs used in E-UIAIA to calculate shape and size properties similar to UIAIA. This imaging database includes the binary images for more than 15,000 aggregate particles from different sources. State highway agencies from South Carolina, Mississippi, Alabama, Georgia, Kentucky and Tennessee provided these aggregate samples with a wide range of shape and size properties. These aggregate materials were used in constructing different sections of a test track at the National Center for Asphalt Technology (NCAT) in Auburn, Alabama. The names, sources, and types of these aggregate samples can be found in Table 3.17.

Table 3.17 NCAT Aggregate Materials and Number of Aggregate Particles Analyzed with UIAIA and E-UIAIA

Aggregate Sample	Source	Material Type	Number of Particles Scanned
Blacksburg 67	South Carolina	Granite	497
Blacksburg 78M	South Carolina	Granite	1030
Blain 1/2 crushed gravel	Mississippi	Gravel	1404
Blain 3/4 crushed gravel	Mississippi	Gravel	814
Calera 67	Alabama	Limestone	539
Calera 7	Alabama	Limestone	1593
Columbus 6	Georgia	Granite	306
Columbus 7	Georgia	Granite	1098
Gadsden slag 78	Alabama	Slag	1390
Gilbertsville 57	Kentucky	Limestone	363
Gordonville 78	Tennessee	Limestone	1670
Jemison 1/2 crushed gravel	Alabama	Gravel	1809
Jemison 1/2 crushed gravel	Alabama	Gravel	1843
Lithia Springs 7	Georgia	Granite	1199

In this section, the imaging based shape and size indices generated from image processing algorithms used in both UIAIA and E-UIAIA are presented and differences in measurement in terms of percentage of errors between these two systems are further discussed. Noted that in the study by Pan [46] all of these aggregate sources were initially selected with bright natural colors. As it was discussed previously, it is beyond the capability

of UIAIA to capture high quality images from dark color aggregates as well as thresholding and generating associated binary images. Therefore, the performances of UIAIA and E-UIAIA imaging systems in acquiring and processing the images of dark color aggregate particles are the subject of discussion in the next section. The imaging based indices for volume weight prediction, angularity index, surface texture index, F&E Ratio and average sieve size results from both systems are presented in Tables 3.18 to 3.22 respectively.

According to Table 3.18, both UIAIA and E-UIAIA systems were able to estimate the actual weights of 14 aggregate samples with less than 10% error for both of the trials. In fact, the measurement difference between the two systems were observed to be less than 3%.

Table 3.18 UIAIA and E-UIAIA Weight Predictions Based on Imaging Based Volume Measurements

Aggregate Sample	Specific Gravity	Actual Weight (gr)	UIAIA Estimated Weight (gr)	E-UIAIA Estimated Weight (gr)	UIAIA Error (%)	E-UIAIA Error (%)	Error Difference (%)
Blacksburg 67	2.747	1176.1	1177.585	1189.725	0.126	1.158	-1.032
Blacksburg 78M	2.690	535.03	508.54	511.336	-4.951	-4.429	-0.523
Blain 1/2 crushed gravel	2.429	1278	1364.58	1366.266	6.775	6.907	-0.132
Blain 3/4 crushed gravel	2.442	1513.9	1514.53	1518.057	0.042	0.275	-0.233
Calera 67	2.690	1868.4	1840.17	1845.618	-1.511	-1.219	-0.292
Calera 7	2.752	1237.7	1343.56	1345.818	8.553	8.735	-0.182
Columbus 6	2.670	1937.9	1799.91	1854.783	-7.121	-4.289	-2.832
Columbus 7	2.611	1354.5	1308.77	1335.984	-3.376	-1.367	-2.009
Gadsdenslag 78	2.270	982.1	1033.51	1053.378	5.235	7.258	-2.023
Gilbertsville 57	2.651	1602.1	1579.44	1588.176	-1.414	-0.869	-0.545
Gordonville 78	2.735	1711.2	1860.75	1861.839	8.739	8.803	-0.064
Jemison 1/2 crushed gravel	2.548	986.3	1037.2	1038.142	5.161	5.256	-0.096
Jemison 3/8 crushed gravel	2.546	986.4	1037.7	1038.794	5.201	5.312	-0.111
Lithia Springs 7	2.558	1774.3	1872.35	1892.338	5.526	6.653	-1.127
Average of Percentage Error Difference in Weight Estimation Between UIAIA & E-UIAIA							*-0.800*

It needs to be added that the weights were calculated based on volume measurement with assuming a constant specific gravity value for all the particles. The weight measurement results confirm the accuracy of the new VI incorporated in E-UIAIA for repeatable volume

computation and verify that the new and old VIs return almost identical volume and weight values.

Based on angularity index measurements listed in Table 3.19, the average angularity index measurement difference for all the 14 aggregate samples between UIAIA and E-UIAIA was found to be around 10%. It was observed that E-UIAIA was consistently reporting lower angularity values and in one case even up to 23% lower in comparison to UIAIA. According to what was discussed previously regarding the debugged and improved angularity index VI used in E-UIAIA, this finding could be expected. However, both of the systems are capable of generating repeatable angularity index values. Note that in most cases lower standard deviation values were observed in AI measurement with E-UIAIA.

Table 3.19 UIAIA and E-UIAIA Imaging based Angularity Index for NCAT Aggregates

Aggregate Sample	UIAIA				E-UIAIA				Measurement Difference (%)		Ave. Diff. (%)
	Trial1		Trial2		Trial1		Trial2				
	Ave.	Std. Dev	Ave.	Std. Dev	Ave.	Std. Dev	Ave.	Std. Dev	Trial1	Trial2	
Blacksburg 67	441	82	418	70	421	86	396	71	4.425	5.190	4.81
Blacksburg 78M	439	73	436	76	387	64	385	68	11.845	11.697	11.77
Blain 1/2 crushed gravel	400	78	396	76	363	69	358	68	9.250	9.596	9.42
Blain 3/4 crushed gravel	405	85	407	87	374	84	378	86	7.654	7.125	7.39
Calera 67	392	70	395	69	370	64	372	63	5.730	5.899	5.81
Calera 7	393	65	395	66	354	55	357	58	9.997	9.667	9.83
Columbus 6	453	86	459	97	452	103	461	117	0.144	-0.497	-0.18
Columbus 7	515	97	523	89	433	97	436	100	15.964	16.604	16.28
Gadsdenslag 78	477	86	473	88	427	82	417	80	10.400	11.839	11.12
Gilbertsville 57	415	71	405	76	392	76	388	74	5.592	4.320	4.96
Gordonville 78	477	86	473	88	367	60	367	60	23.073	22.507	22.79
Jemison 1/2 crushed gravel	380	78	362	82	328	67	326	65	13.786	10.041	11.91
Jemison 3/8 crushed gravel	375	84	371	88	330	71	329	73	11.893	11.260	11.58
Lithia Springs 7	432	72	428	73	401	70	398	71	7.145	7.026	7.09
Average of Average Percentage Difference for Angularity Index Between UIAIA & E-UIAIA											*9.61*

Surface texture measurements for both UIAIA and E-UIAIA are reported in Table 3.20 which shows that there is a very good match between these two systems for this shape index.

The average recorded surface texture index difference between the two systems was found to be less than 1%. Therefore, these result confirm that the new VI for computing surface texture index in E-UAIA is capable of generating repeatable texture results similar to UIAIA.

Table 3.20 UIAIA and E-UIAIA Imaging Based Surface Texture Index for NCAT Aggregate

Aggregate Sample	UIAIA				E-UIAIA				Measurement Difference (%)		Ave. Diff. (%)
	Trial1		Trial2		Trial1		Trial2		Trial1	Trial2	
	Ave.	Std. Dev	Ave.	Std. Dev	Ave.	Std. Dev	Ave.	Std. Dev			
Blacksburg 67	2.453	1.75	1.943	1.37	2.449	1.750	1.945	1.372	0.158	-0.080	0.04
Blacksburg 78M	1.741	1.41	1.662	1.28	1.738	1.409	1.659	1.282	0.179	0.159	0.17
Blain 1/2 crushed gravel	1.152	0.59	1.114	0.53	1.150	0.589	1.112	0.532	0.133	0.194	0.16
Blain 3/4 crushed gravel	1.333	0.79	1.285	0.75	1.333	0.789	1.281	0.751	0.021	0.307	0.16
Calera 67	1.291	0.67	1.297	0.67	1.292	0.665	1.291	0.674	-0.098	0.460	0.18
Calera 7	1.192	0.61	1.231	0.73	1.194	0.607	1.228	0.735	-0.144	0.264	0.06
Columbus 6	2.145	1.55	2.199	1.88	2.141	1.554	2.191	1.882	0.175	0.357	0.27
Columbus 7	1.947	1.34	1.876	1.24	1.939	1.339	1.870	1.243	0.425	0.338	0.00
Gadsdenslag 78	1.414	0.65	1.443	1.34	1.408	0.655	1.440	1.410	0.426	0.208	0.32
Gilbertsville 57	1.593	0.89	1.634	1.19	1.588	0.893	1.605	1.186	0.313	1.804	0.00
Gordonville 78	1.461	1.06	1.361	0.95	1.465	1.060	1.362	0.952	-0.258	-0.071	0.00
Jemison 1/2 crushed gravel	1.098	0.7	1.156	0.88	1.086	0.700	1.103	0.881	1.073	4.569	0.00
Jemison 3/8 crushed gravel	1.145	0.94	1.154	0.87	1.140	0.938	1.153	0.872	0.431	0.129	0.00
Lithia Springs 7	1.712	1.07	1.412	0.85	1.704	1.069	1.413	0.850	0.481	-0.100	0.00
Average of Average Percentage Difference for Surface Texture Index Between UIAIA & E-UIAIA											*0.10*

According to Table 3.21, a very good match was observed for flat & elongated ratio measurements between UIAIA and E-UIAIA. The average of measurement differences between the two systems for this shape index was less than 1%. Therefore, these results confirm the validity and repeatability of the new flat and elongated ratio VI in E-UIAIA for repeatable estimation of the aggregate form and aspect ratios of particles.

Table 3.21 UIAIA and E-UIAIA Imaging Based Flat & Elongated Ratio for NCAT Aggregates

Aggregate Sample	UIAIA				E-UIAIA				Measurement Difference (%)		Ave. Diff. (%)
	Trial1		Trial2		Trial1		Trial2				
	Ave.	Std. Dev	Ave.	Std. Dev	Ave.	Std. Dev	Ave.	Std. Dev	Trial1	Trial2	
Blacksburg 67	3.006	1.000	2.826	0.938	3.086	1.060	2.841	0.943	-2.656	-0.545	-1.60
Blacksburg 78M	2.512	0.768	2.632	1.768	2.517	0.767	2.644	1.866	-0.182	-0.454	-0.32
Blain ½ crushed gravel	2.085	0.502	2.106	0.516	2.094	0.504	2.116	0.519	-0.437	-0.458	-0.45
Blain 3/4 crushed gravel	2.031	0.511	2.093	0.558	2.049	0.518	2.104	0.561	-0.856	-0.480	-0.67
Calera 67	2.372	0.760	2.402	0.749	2.381	0.767	2.412	0.753	-0.375	-0.413	-0.39
Calera 7	2.415	0.748	2.409	0.871	2.431	0.754	2.417	0.889	-0.657	-0.367	-0.51
Columbus 6	2.207	0.701	2.213	0.695	2.218	0.715	2.225	0.703	-0.503	-0.520	-0.51
Columbus 7	2.304	0.671	2.327	0.687	2.323	0.681	2.338	0.691	-0.822	-0.484	-0.65
Gadsdenslag 78	1.871	0.389	1.890	0.456	1.879	0.393	1.889	0.391	-0.455	0.056	-0.20
Gilbertsville 57	2.558	0.818	2.572	0.828	2.573	0.823	2.581	0.836	-0.587	-0.355	-0.47
Gordonville 78	2.316	0.795	2.387	1.314	2.334	0.800	2.400	1.370	-0.762	-0.569	-0.67
Jemison 1/2 crushed gravel	2.179	0.718	2.211	0.735	2.184	0.718	2.217	0.738	-0.226	-0.287	-0.26
Jemison 3/8 crushed gravel	2.243	0.745	2.219	0.742	2.249	0.752	2.221	0.739	-0.264	-0.124	-0.19
Lithia Springs 7	2.099	0.605	2.173	0.627	2.126	0.616	2.179	0.627	-1.280	-0.279	-0.78
Average of Average Percentage Difference for Flat & Elongated Ratio Between UIAIA & E-UIAIA											*-0.55*

Finally, the average sieve size measurements for UIAIA and E-UIAIA are presented in Table 3.22, which shows a very good match between these two systems. According to what was discussed in Chapter 2, the lowest of the three maximum intercept values computed from the three captured views is chosen as the intermediate aggregate particle dimension. Accordingly, if this dimension is smaller than the diagonal length of the square mesh/opening in a desired laboratory sieve, the particle passes through that given sieve. The average of measured size difference between the two systems for all the 14 aggregate sources was found to be less than 1% to verify that the new size VI used in E-UIAIA for estimating the sizes of aggregate particles gives very similar results to UIAIA system.

In summary, the findings from the comparison study on NCAT aggregate samples between the two imaging system showed that E-UIAIA and its image processing VIs for computing shape and size indices are accurate enough in terms of generating outputs that

are very close to UIAIA. In the next section, the effect of digitization error and natural color of the aggregates on angularity and surface texture measurements are presented.

Table 3.22 UIAIA and E-UIAIA Imaging Based Average Size for NCAT Aggregates

| Aggregate Sample | UIAIA | | | | E-UIAIA | | | | Measurement Difference (%) | | Ave. Diff. (%) |
| | Trial1 | | Trial2 | | Trial1 | | Trial2 | | | | |
	Ave.	Std. Dev	Ave.	Std. Dev	Ave.	Std. Dev	Ave.	Std. Dev	Trial1	Trial2	
Blacksburg 67	0.576	0.143	0.565	0.129	0.576	0.142	0.565	0.129	0.033	-0.068	-0.02
Blacksburg 78M	0.331	0.097	0.328	0.093	0.331	0.097	0.329	0.093	-0.163	-0.088	-0.13
Blain 1/2 crushed gravel	0.422	0.087	0.406	0.083	0.422	0.087	0.406	0.083	-0.043	-0.029	-0.04
Blain 3/4 crushed gravel	0.507	0.129	0.500	0.131	0.507	0.129	0.500	0.131	0.037	-0.025	0.01
Calera 67	0.558	0.188	0.547	0.176	0.558	0.188	0.547	0.176	-0.006	-0.046	-0.03
Calera 7	0.372	0.098	0.383	0.103	0.372	0.098	0.383	0.103	-0.061	-0.074	-0.07
Columbus 6	0.758	0.116	0.746	0.112	0.735	0.116	0.746	0.112	2.991	-0.013	1.49
Columbus 7	0.452	0.097	0.452	0.099	0.452	0.097	0.452	0.099	-0.010	-0.067	-0.04
Gadsdenslag 78	0.380	0.092	0.381	0.092	0.380	0.092	0.381	0.093	-0.009	0.032	0.01
Gilbertsville 57	0.660	0.173	0.657	0.172	0.660	0.173	0.657	0.172	0.040	-0.073	-0.02
Gordonville 78	0.411	0.104	0.417	0.108	0.411	0.104	0.417	0.108	-0.025	-0.022	-0.02
Jemison 1/2 crushed gravel	0.338	0.087	0.337	0.087	0.338	0.087	0.338	0.086	-0.088	-0.132	-0.11
Jemison 3/8 crushed gravel	0.337	0.091	0.336	0.091	0.337	0.091	0.336	0.091	-0.074	-0.084	-0.08
Lithia Springs 7	0.473	0.088	0.477	0.093	0.473	0.088	0.477	0.093	0.081	0.008	0.04
Average of Average Percentage Difference for Size Between UIAIA & E-UIAIA											*0.07*

3.3.3 Effect of Improved Illumination, Higher Spatial Resolution and Color Thresholding

In this section, the performances of UIAIA and E-UIAIA in differentiating between uncrushed and crushed aggregate particles with dark and bright colors are presented. Two important shape indices that are used in separating crushed versus uncrushed aggregate sources including angularity index and surface texture index are reported. Additionally, the variability of these shape indices as well as their corresponding separation parameters are demonstrated as indicators to compare the efficiency and repeatability of UIAIA and E-UIAIA imaging systems. The separation parameter between crushed and uncrushed aggregate

particle or S_{CU} for a desired shape index was developed by Pan [46] and defined according to Equation 3.7.

$$S_{cu} = \frac{\left| \mu_C - \mu_U \right|}{\sqrt{(SD_C - SD_U)}}$$ 3.7

where,

μ_C = Mean of the desired shape index distribution for crushed particle

μ_U = Mean of the desired shape index distribution for uncrushed particle

SD_C = Standard deviation of the desired shape index distribution for crushed particle

SD_U = Standard deviation of the desired shape index distribution for uncrushed particle

The average of shape index results and the separation parameters for the two systems are summarized in Table 3.23. Moreover, the images of these particles are shown in Figure 3.12.

| Bright crushed particle | Bright uncrushed particle |
| Dark crushed particle | Dark uncrushed particle |
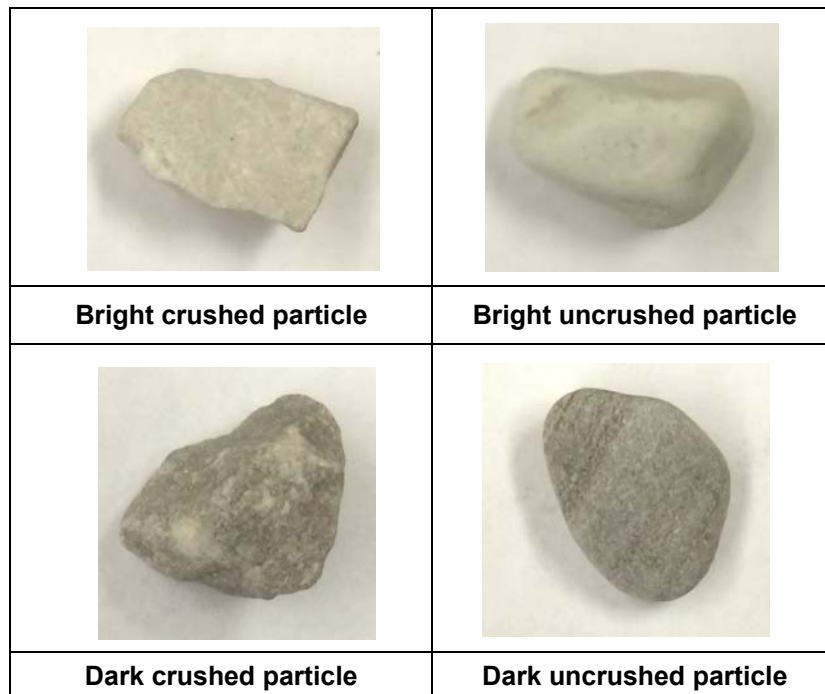
Figure 3.12 Crushed and Uncrushed Bright and Dark Colored Aggregate Particles

Only four aggregate particles including two uncrushed and two crushed with dark and bright colors were selected for this experiment in order to eliminate the effect of shape variability associated with aggregate sources. Each particle was scanned 10 times by both imaging systems with random positioning on the conveyor belt while the sitting surface of particles kept constant between different trials.

Table 3.23 UIAIA and E-UIAIA Imaging Based AI and STI for Crushed and Uncrushed Particles

Particle Color	UIAIA				S_{cu} (AI)
	Uncrushed		Crushed		
	Angularity Index	Std. Dev	Angularity Index	Std. Dev	
Dark	381	111	479	104	0.912
Bright	241	35	428	63	3.982
Particle Color	E-UIAIA				S_{cu} (AI)
	Uncrushed		Crushed		
	Angularity Index	Std. Dev	Angularity Index	Std. Dev	
Dark	115	7	385	52	14.15
Bright	205	20	394	40	6.68
Particle Color	UIAIA				S_{cu} (STI)
	Uncrushed		Crushed		
	Surface Texture Index	Std. Dev	Surface Texture Index	Std. Dev	
Dark	33.01	41.29	14.92	27.89	- 0.533
Bright	0.60	0.13	1.24	0.34	3.015
Particle Color	E-UIAIA				S_{cu} (STI)
	Uncrushed		Crushed		
	Surface Texture Index	Std. Dev	Surface Texture Index	Std. Dev	
Dark	0.63	0.09	1.44	0.31	4.798
Bright	0.59	0.07	1.21	0.18	5.530

Therefore, the sources of errors that were causing the variability of a shape index for an individual particle at each image acquisition trials were limited to a combination of digitization error, the position of particle on the image frame as well as the aggregate face coverage captured by front and side cameras.

-   *Discussion on imaging results for bright color particles*

The imaging results show that both imaging systems successfully differentiated between bright colored crushed versus uncrushed aggregate particles by their corresponding angularity and surface texture indices. A close match between two systems was observed regarding the average recorded surface texture index. Additionally, the observed standard deviation values were lower in uncrushed as opposed to crushed aggregate particles which is expected as of lower variability in more rounded and smoother particles. However, the standard deviation values for all cases achieved with E-UIAIA for both angularity index and surface texture index were lower than UIAIA. This finding shows the influence of more efficient illumination design as well as thresholding scheme that is used in E-UIAIA. These factors contribute to reduction of noise in generated binary images. Note that the average angularity index values recorded by E-UIAIA were 10-20% lower than those recorded by UIAIA. This result could be expected based on what was discussed earlier regarding the improved angularity VI used in E-UIAIA as well as the sources of errors during image acquisition process. Further, the separation parameter (S_{cu}) values computed with E-UIAIA were higher than those for UIAIA in case of both angularity and surface texture, which verifies the accuracy of the new system to efficiently differentiate between crushed and uncrushed aggregate particles. One way to show the variability of the measurements is through using box plots, which visually display differences between samples (see Figure 3.13).
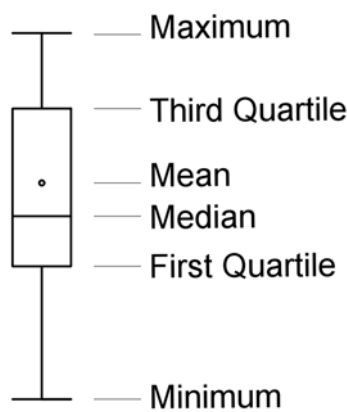
Figure 3.13 Different Components of a Typical Box Plot

To further demonstrate the variability of angularity index and surface texture measurements by these two imaging systems at different trials, the box plots associated with these measurements are shown in Figure 3.14. Note that the actual data points are also shown on the left side of each box plot. Accordingly, the box plots are visually showing how the variability is reduced and the associated errors are decreasing for both angularity and surface texture measurements from E-UIAIA in comparison to UIAIA.

Figure 3.14 Box Plots for Angularity and Surface Texture Measurements for Particles with Bright Colors Obtained by UIAIA and E-UIAIA Systems

- *Discussion on imaging results for dark color particles*

The imaging results show that the standard deviation values recorded by UIAIA for both angularity index and surface texture index are significantly higher than those achieved with E-UIAIA. The computed separation parameters (S_{cu}) for UIAIA were very low in case of angularity and even negative in case of surface texture which confirms the poor performance of this system in acquiring and processing the images of dark colored particles. Close investigation showed that a high noise level was observed in the binary images generated by UIAIA (see Figure 3.15). Note the poor performance of the automatic grayscale thresholding method used in UIAIA which is not capable of isolating the dark particle from a black background. The out of range average surface texture values recorded by UIAIA are clearly showing this shortcoming. According to Pan [46], the surface texture indices for different types of aggregate particles are generally reported in the range of less than 6.
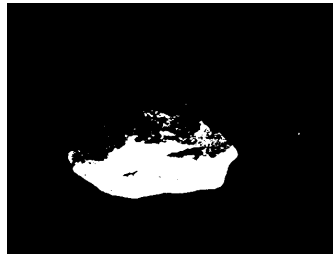
Figure 3.15 Poor Performance of Automatic Grayscale Thresholding in Processing the Image of a Dark Aggregate Particle in UIAIA

Table 3.23 indicates that E-UIAIA could successfully characterize both uncrushed and crushed dark aggregate particles and also differentiate these two particles with good separation parameters for both angularity and surface texture indices. To further demonstrate the variability of angularity index and surface texture measurements by both UIAIA and EUIAIA for different trials, the box plots associated with these measurements are shown in Figure 3.16. Note that the actual data points are also shown on the left side of each box plot for comparison. The box plots are showing how the variability is reduced and the associated errors are decreasing for both angularity and surface texture measurements from E-UIAIA in comparison to UIAIA for the dark particles.
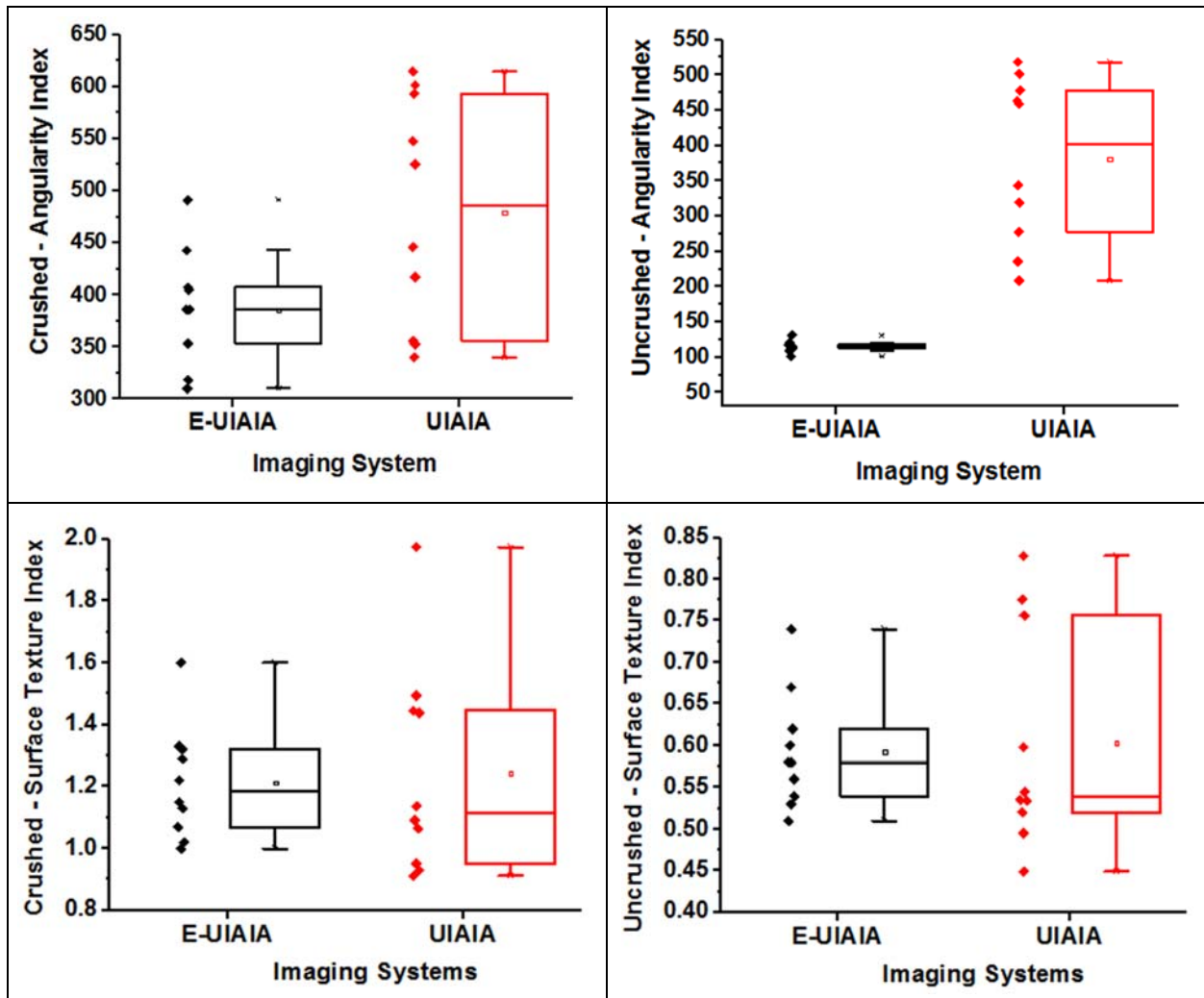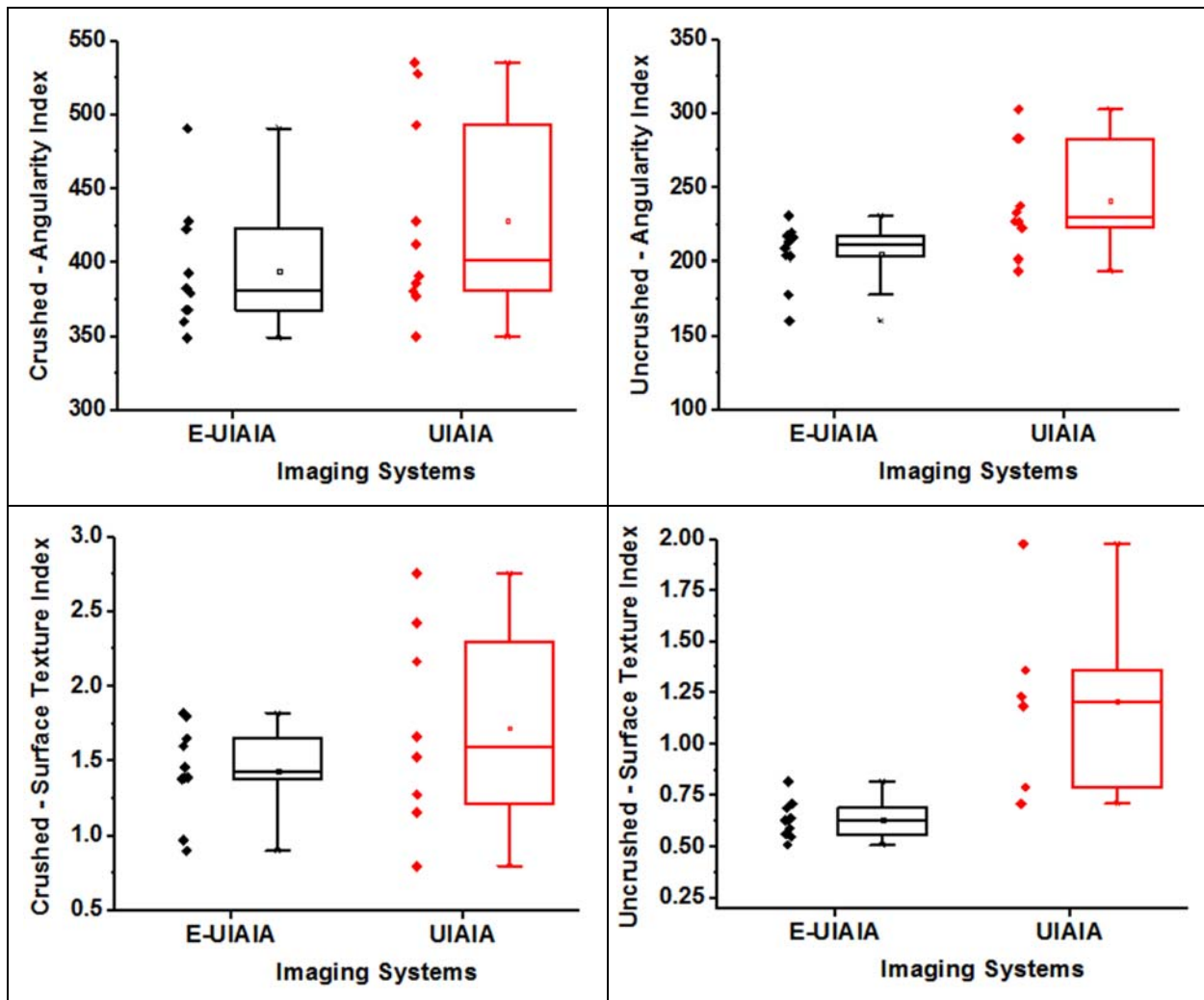
Figure 3.16 Box Plots for Angularity and Surface Texture Measurements for Particles with Dark Colors by UIAIA & E-UIAIA Systems

3.4 Summary

The development of E-UIAIA in terms of assembly of both hardware and software components was described in this chapter. Moreover, the advantages of an innovative HSI color thresholding method for separating the images of both dark and bright colored aggregate particles from a blue background was discussed. The new E-UIAIA was validated with different approaches including calibrating the system with calibration balls having different sizes at various special resolutions as well as comparing the shape indices results with UIAIA using a previously studied aggregate imaging database. Furthermore, the

performances of UIAIA and E-UIAIA systems in differentiating between dark and bright colored uncrushed and crushed aggregate particles were presented. In general, less than 1% difference was detected between two systems in measurements of surface texture index, flat and elongated ratio, size and volume for many different aggregate sources. Also, new angularity index and surface area VIs with fixed programming errors were incorporated into E-UIAIA. Consequently, 10-20% decrease in angularity index measurements and more accurate surface area results with E-UIAIA were obtained in comparison to UIAIA. As a result of improved hardware and software components designed in E-UIAIA, the variability of shape indices in terms of recorded standard deviation values decreased significantly. The applications of E-UIAIA in capturing the changes in size and shape properties during degradation of aggregate particles used in highway pavement and railroad ballast will be studied in the next two chapters of this dissertation.

CHAPTER 4:

PERFORMANCE OF E-UIAIA IN EVALUATING

DEGRADATION OF RAILROAD BALLAST USING

LA-ABRASION TESTING[1]

To evaluate degradation of aggregate materials for size and morphological properties, E-UIAIA can be used to quantify imaging based size and shape indices at different stages throughout the performance periods. For example, imaging based shape indices of aggregate particles are re-quantified after toughness/abrasion laboratory testing of these aggregate samples by measuring the changes in particle size distribution and the rate and magnitude of shape property. This chapter is divided into two parts. The first part presents findings from a comprehensive LA-Abrasion laboratory testing and image analyses performed on limestone and granite type railroad ballast materials. The material weight loss based on passing No.12 sieve as the LA-Abrasion degradation criterion is also related to the percentage of loss in angularity and surface texture of the particles. Based on the observations from the first part of this chapter and considering the ASTM C535 testing procedure, a new classification method is proposed later on. Accordingly, fourteen sources

---

[1] This chapter includes the results that are published in the following articles. The contribution of the co-authors is greatly appreciated.

1- **Moaveni, M.,** Qian, Y., Boler, H., and Tutumluer, E., "*Investigation of Ballast Degradation and Fouling Trends Using Image Analysis*", Proceedings of the Second International Conference on Railway Technology: Research, Development and Maintenance, April-2014, Corsica, France.

2- Qian, Y., Boler, H., **Moaveni, M.,** Tutumluer, E., Hashash, Y. M. A., Ghaboussi, J., "*Characterizing Ballast Degradation through Los Angeles Abrasion Test and Image Analysis*", Published in Transportation Research Record: Journal of the Transportation Research Board, No.2448, pp. 142-151, 2014, Washington DC, USA.

3- Wnek, M. A., Tutumluer, E., **Moaveni, M.,** Gehringer, E., "'*Investigation of Aggregate Properties Influencing Railroad Ballast Performance*", Published in Transportation Research Record: Journal of the Transportation Research Board, No.2374, pp. 180-189, 2013, Washington DC, USA.

of railroad ballast materials are classified using the imaging based shape properties obtained from the E-UIAIA.

4.1 LA-Abrasion Testing and Image Analyses on Granite and Limestone Ballast Materials

To better understand ballast performance associated with field usage and life cycle degradation due to particle abrasion and breakage, ballast particle size and shape properties at different LA-Abrasion degradation levels were identified using E-UIAIA and laboratory sieve analysis for two samples of 100% crushed granite and limestone. This section presents the sample preparation, testing procedure and imaging results for these two types of ballast materials.

4.1.1 Material Description, Laboratory Apparatus and Testing Procedure

The particle size distributions of the new clean samples of limestone and granite ballast materials followed the AREMA No.24 gradation band as illustrated in Figure 4.1.
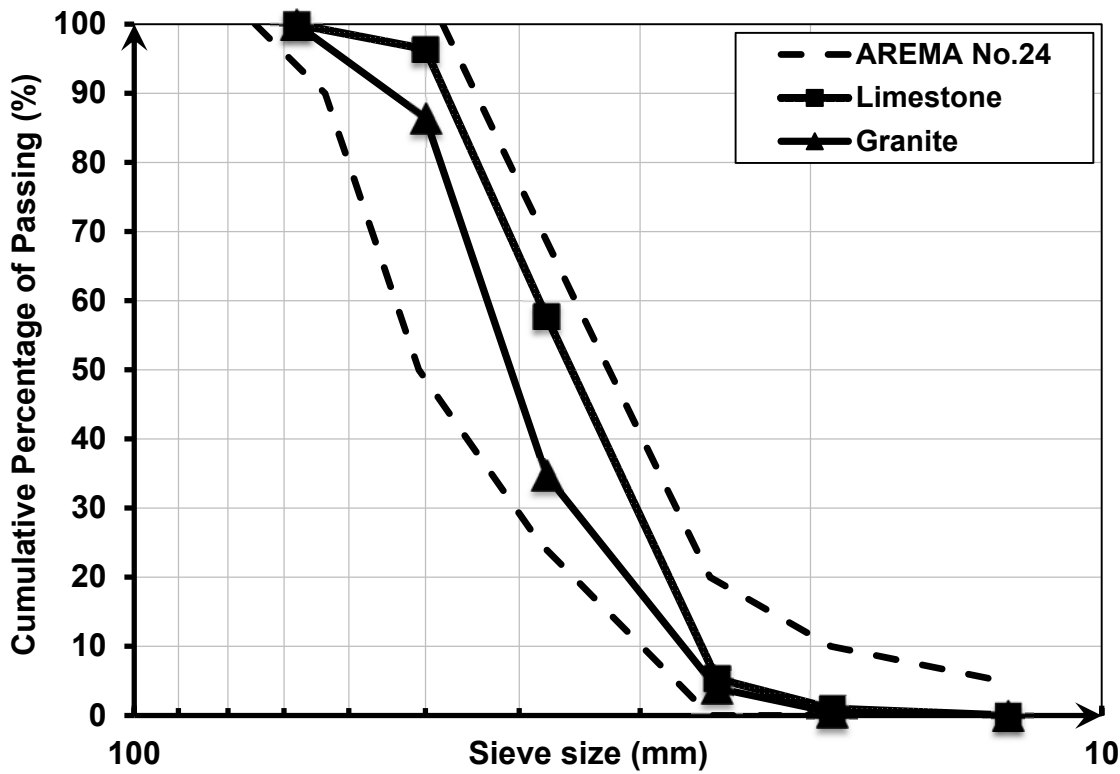

Figure 4.1 Particle Size Distributions for Limestone and Granite Ballast Materials

Twenty two pound (10 kilogram) samples of each virgin limestone and granite ballast materials were placed in the LA-Abrasion drum together with 12 steel balls (see Figure 4.2). The drum was set to rotate on the average 50 turns per minute and for each run the drum rotated 125 times for limestone and 250 times for granite for each stage of the LA-Abrasion testing. After finishing every set of turns, the drum was allowed to stand still for about 10 minutes to let dust settle down before the tested material was poured out. All particles above 1 in. (25.4 mm) sieve were also brushed to collect dust and fine material before sieving. The rest of the materials passing 1.0 in. (25.4 mm) sieve were carefully sieved using a DuraShake™ type rotation aggregate sifter so that loss of fine materials was minimized. In addition, aggregate particles larger than 3/8 in. (9.5 mm) sieve were hand collected to conduct image analysis using E-UIAIA. The outlined procedure was repeated every time on each sample until 1500 turns for limestone and 2125 turns for granite were reached.

According to Selig et al. [51], FI is the summation of the percentage by weight of ballast material passing the No.4 (4.75 mm) sieve and the percentage of material passing No.200 (0.075 mm) sieve. This index is commonly used by railroad industry to assess ballast fouling conditions. At the 1500 final drum turns for limestone and 2125 turns for granite, a FI value of 40 was reached to represent a heavily fouled ballast condition for each sample of the limestone and granite materials from the LA-Abrasion testing. Note that in-service ballast layers having such a FI value would require maintenance activities in the track.

Figure 4.2 LA-Abrasion Testing Apparatus and Sample with Steel Balls

The AI, STI and F&E Ratio indices of the particles were identified before starting the LA-Abrasion tests and after each run of the individual segment of the LA-Abrasion testing. The number of particles scanned at each LA-Abrasion segment are listed in Tables 4.1 and 4.2 for the limestone and granite samples, respectively.

Table 4.1 Number of Limestone Ballast Particles from Each Size Scanned with E-UIAIA

Number of LA-Abrasion Turns	Sieve Size						Total Number of Particles at each Drum Turns
	2 in.	1.5 in.	1 in.	0.75 in.	0.5 in.	0.375 in.	
	50 mm	37.5 mm	25 mm	19 mm	12.5 mm	9.5 mm	
0	2	29	85	19	11	0	146
125	1	21	85	32	66	58	263
250	0	20	86	35	77	72	290
375	0	18	79	44	78	71	290
500	0	18	74	50	78	76	296
625	0	18	74	46	78	81	297
750	0	17	71	45	75	100	308
875	0	17	71	45	75	79	287
1000	0	15	70	45	67	81	278
1125	0	15	70	44	68	66	263
1250	0	13	69	42	63	69	256
1375	0	13	68	42	55	69	247
1500	0	12	68	41	51	59	231

Table 4.2 Number of Granite Ballast Particles from Each Size Scanned with E-UIAIA

Number of LA-Abrasion Turns	Sieve Size						Total Number of Particles at each Drum Turns
	2 in.	1.5 in.	1 in.	0.75 in.	0.5 in.	0.375 in.	
	50 mm	37.5 mm	25 mm	19 mm	12.5 mm	9.5 mm	
0	7	37	64	19	8	0	135
250	3	29	65	44	65	51	257
500	2	28	58	48	94	70	300
750	2	28	58	46	102	66	302
1000	2	28	51	50	94	72	297
1250	2	27	49	49	90	69	286
1500	2	27	43	52	82	70	276
1750	2	27	37	52	77	57	252
2000	2	26	35	53	65	58	239
2125	2	25	37	49	55	67	235

Note that the same specimen was always tested in the LA-Abrasion drum, which required 12 individual runs for limestone and 9 runs for granite samples. Tables 4.1 and 4.2 show that for some of the passing sieve sizes, e.g., 0.5 in. (12.5 mm), the number of particles generated throughout the experiment increased first and then decreased later. Additional particles were created first when the larger sizes were broken down to generate particles and then, these 0.5 in. (12.5 mm) sized particles were broken into smaller sizes when the number of drum turns further increased. The number of particles retained on the 1.5 in. (37.5 mm) sieve did not change significantly since those particles did not break and not many new particles were created from larger sizes, e.g., particles retained on the 2 in. (50 mm) sieve size.

4.1.2 LA-Abrasion and Sieve Analysis Test Results

Figures 4.3 and 4.4 show the gradation curves and FI values for the new clean limestone and granite specimens as well as those degraded ones achieved after each run of the LA-Abrasion testing for up to 1,500 and 2,125 drum turns, respectively.
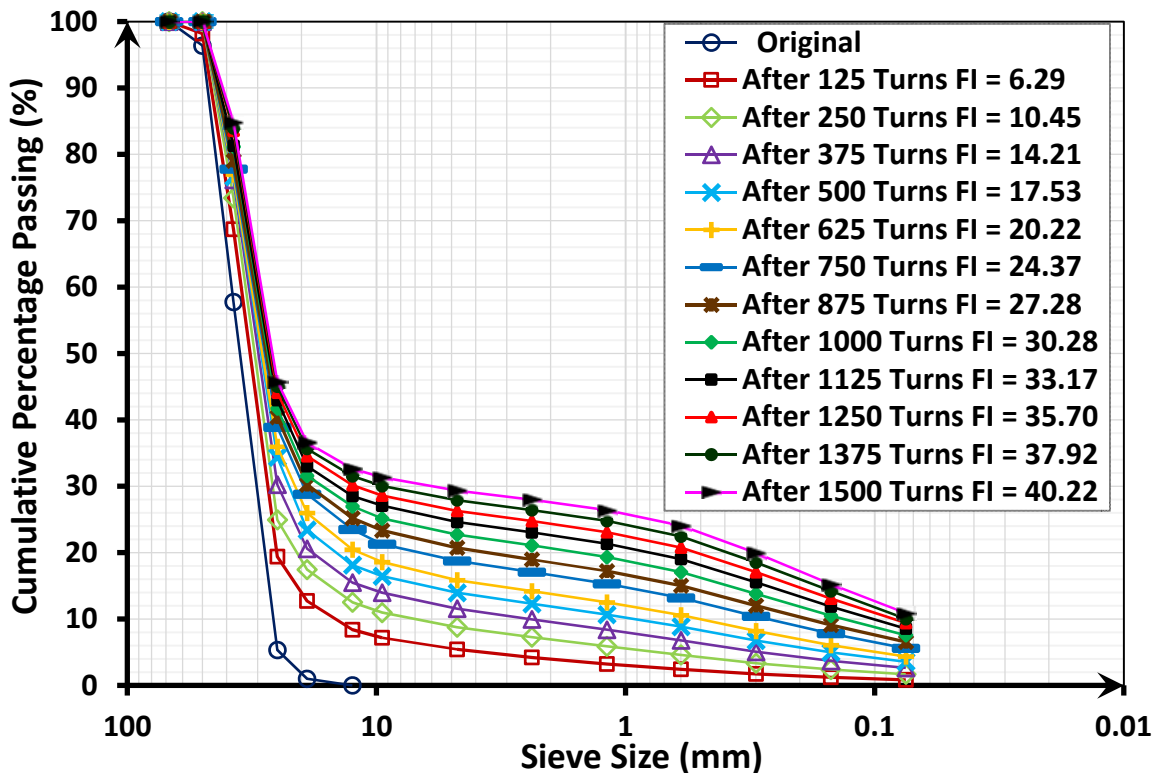

Figure 4.3 Limestone Gradation Curves at Different LA-Abrasion Drum Turns
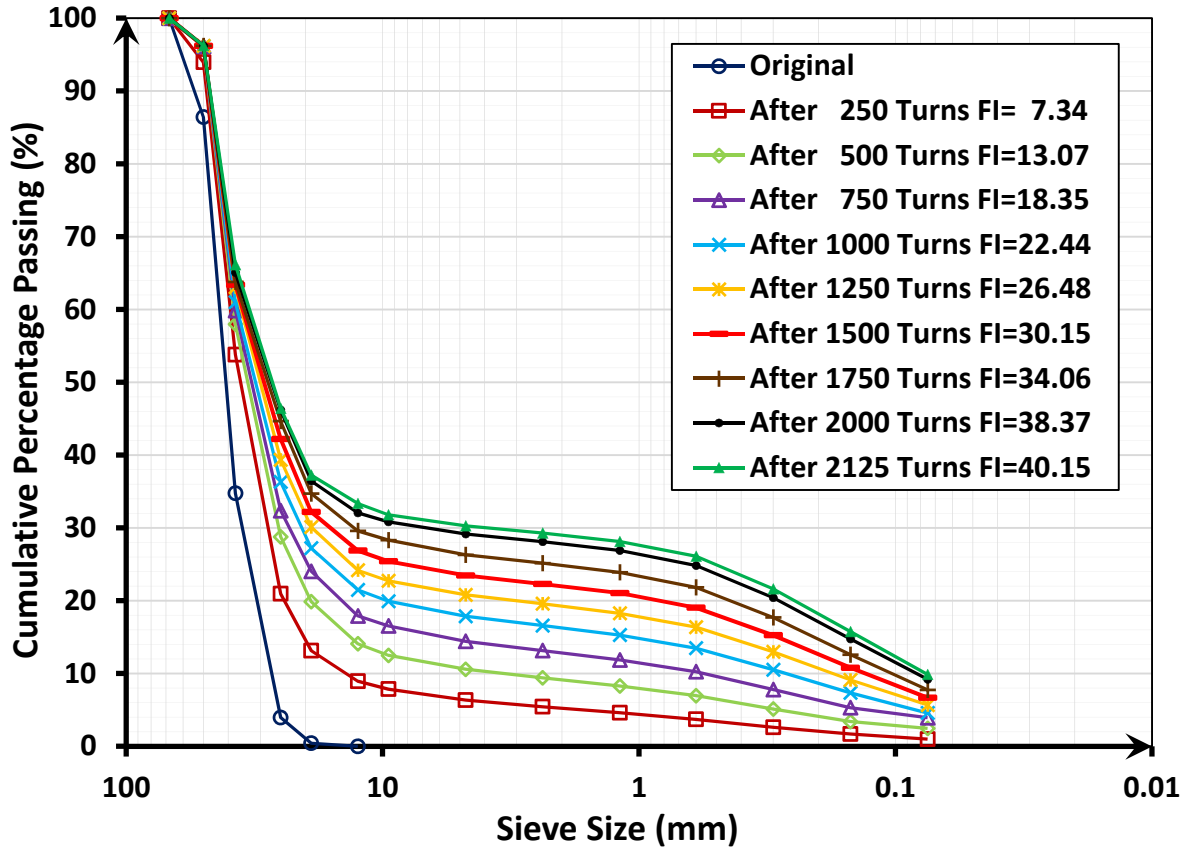
94

Figure 4.4 Granite Gradation Curves at Different LA-Abrasion Drum Turns

With the number of turns increasing in the LA-Abrasion test, ballast specimen changed gradually from "uniformly" graded to more "well" graded. No doubt, clean ballast material was more susceptible to abrading sharp corners and edges of the crushed particles. Interestingly, it was observed that breakage of the large sized particles mostly happened in the early stages of the experiment. With the number of turns increasing in the LA-Abrasion test, those particles that did not break due to the impact loads eventually became more rounded due to chipping corners and smoother textures due to abrasion of surfaces and edges. Note that according to ASTM C535, the weight loss of material passing No.12 sieve at 1000 LA-Abrasion drum turns is reported as the "LA-Abrasion Number" for the material. Figures 4.3 and 4.4 also show that the rate of degradation or the amount of shifts between the gradation curves decrease after 1000 drum turns for both limestone and granite ballast materials. This confirms that reporting the degradation level in terms of LA-Abrasion

Number at 1000 drum turns, which is recommended in ASTM C535, is a good indicator of the overall resistance of the material to degradation.

Boler et al. [34] conducted a study on a railroad ballast limestone material at different numbers of turns to study degradation trends. They also studied degradation at 100, 250, 400, 550, 700, and 1,000 drum turns and found that aggregates particles became somewhat well-graded after 400 drum turns in the LA-Abrasion testing machine. This point will be further discussed in this section from the perspective of change in imaging based particle shape indices.

By using equation 4.1, percent LA-Abrasion at different degradation levels can be newly defined. Note that according to ASTM C535, percent LA-Abrasion at 1,000 drum turns is called "LA-Abrasion Number". Accordingly, percent LA-Abrasion value calculated at different number of drum turns are reported in Table 4.3.

$$(Percent\ LA-Abrasion)_i = \frac{W_0 - R_i}{W_0} \times 100 \hspace{3cm} 4.1$$

where,

i = Number of drum turns;

W_0 = Initial dry weight of the sample prior to testing;

R_i = Cumulative weight of the material retained on No.12 (1.70 mm) sieve at i number of drum turns.

As expected, Table 4.3 shows that granite is more resistant to degradation since it needed 2,125 drum turns to reach a percent LA-Abrasion of about 30 while limestone reached the same percent LA-Abrasion after only 1,500 drum turns. Note that LA-Abrasion Numbers for limestone and granite are 21.45% and 16.04% respectively and are highlighted in Table 4.3. Gradation curves, fouling index and percent LA-Abrasion values indeed provide valuable information regarding the level of deterioration and resistance of ballast aggregate to degradation. However, the effect of change in the shape of the particles also needs to be captured to better understand the degradation mechanism.

Table 4.3 Percent LA-Abrasion and Fouling Index Values for Limestone and Granite Samples
Computed at Different Degradation Levels

Limestone			Granite		
Number of LA-Abrasion Drum Turns	Percent LA-Abrasion	Fouling Index (%)	Number of LA-Abrasion Drum Turns	Percent LA-Abrasion	Fouling Index (%)
0	0	0	0	0	0
125	3.2	6.29	250	4.75	7.34
250	6.31	10.45	500	8.84	13.07
375	9.02	14.21	750	12.56	18.35
500	11.48	17.53	1000	16.04*	22.44
625	13.92	20.22	1250	18.87	26.48
750	17.48	24.37	1500	21.98	30.15
875	19.42	27.28	1750	25.33	34.06
1000	21.45*	30.28	2000	28.08	38.37
1125	23.6	33.17	2125	29.35	40.15
1250	25.38	35.70			
1375	27.18	37.92			
1500	28.92	40.22			

*: LA-Abrasion Number according to ASTM C535

4.1.3 Imaging Based Particle Shape Property Results

Figures 4.5 to 4.7 present for the limestone ballast material average values of F&E Ratio, AI and STI, respectively. Additionally, Figures 4.8 to 4.10 present for the granite ballast material average values of F&E Ratio, AI and STI, respectively. The following trends could be observed from these figures:

1- For a certain particle size, decreasing trends for average AI and STI values were observed at higher degradation levels. This confirms that the particles with identical sizes tend to get smoother and more rounded during LA abrasion testing.

2- For a certain number of drum turns, the average AI and STI values generally increased as particle sizes decreased. This finding could be explained by the fact that smaller particles created from the breakage of larger particles initially have more crushed faces and thus they are more angular and rougher textured. On the

other hand, the larger particles that did not break often experienced abrasion only.

3- The average AI and STI values for all particle sizes decreased at higher degradation levels through LA-Abrasion testing.

4- The standard deviation levels (error bars in the bar charts) were proportional to the magnitudes of associated shape properties. In other words, at higher AI, STI and F&E Ratio values, higher standard deviations were observed.

5- The F&E Ratio results showed that LA-Abrasion testing did not change the form of the particles significantly.

6- At a certain degradation level, small particles of limestone gave higher AI and STI values in comparison to small particles of granite. This could be related to the different ways that particles break and abrade due to different mineralogical properties of limestone and granite. In other words, new and fresh surfaces generated after breakage were sharper and rougher in the limestone sample compared to granite sample.

7- Comparing the F&E Ratio values at different degradation levels between limestone and granite samples showed less variation of F&E Ratio in case of granite samples. This verifies the higher breakage susceptibility of limestone in comparison to granite.
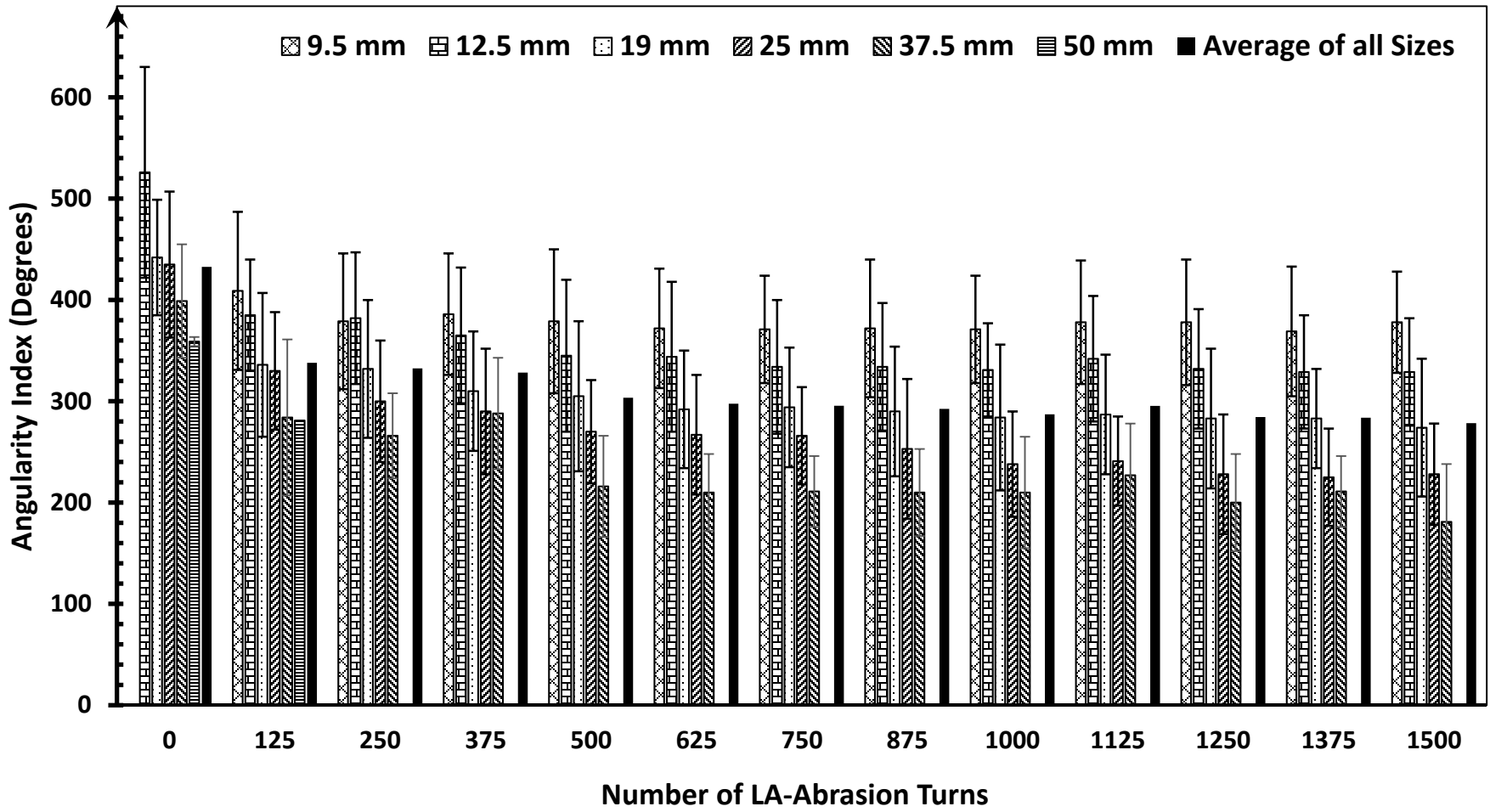
Figure 4.5 Average Angularity Index at Different Degradation Levels for Limestone Ballast

Figure 4.6 Average Surface Texture Index at Different Degradation Levels for Limestone Ballast

Figure 4.7 Average F&E Ratio at Different Degradation Levels for Limestone Ballast

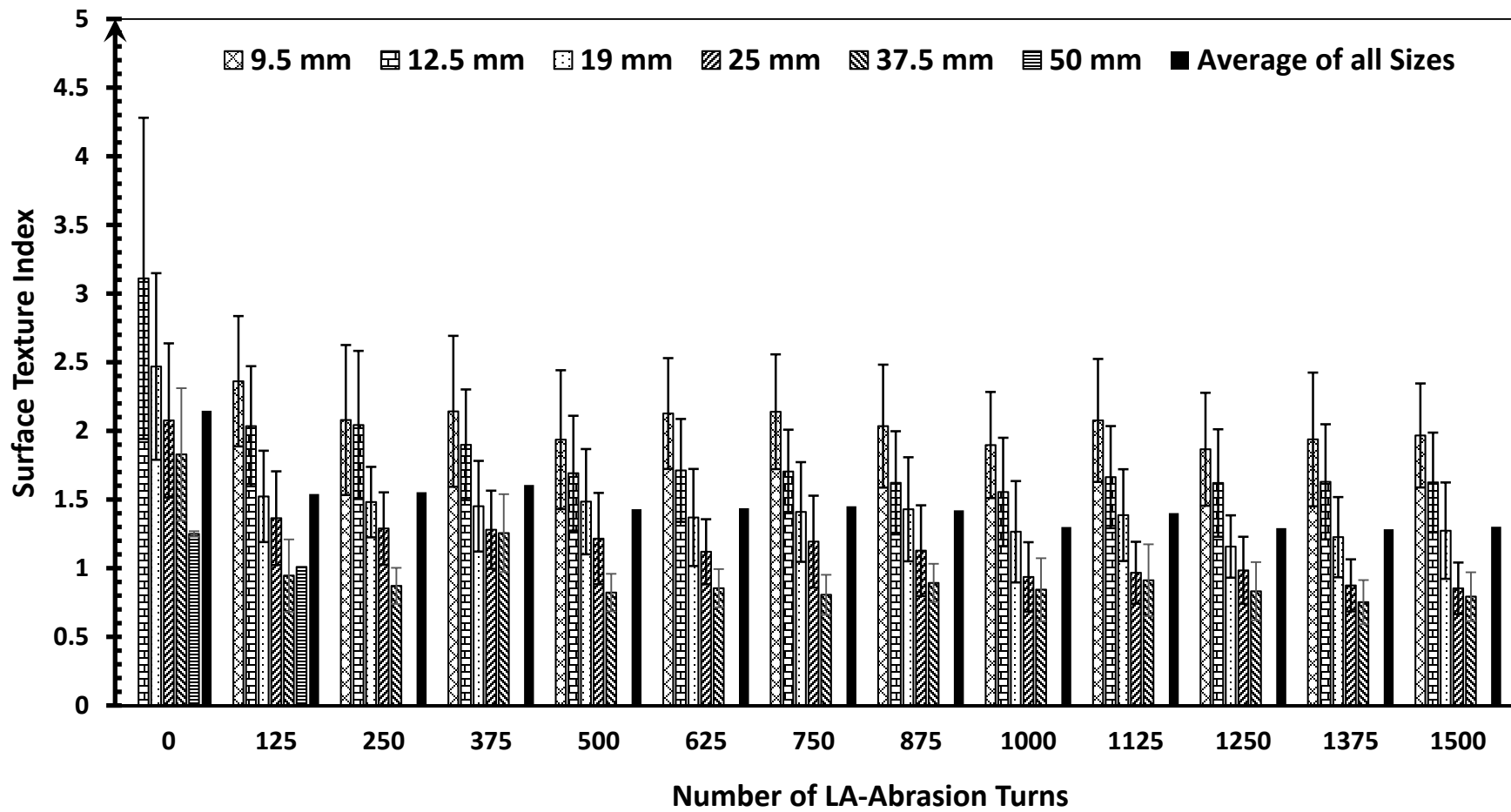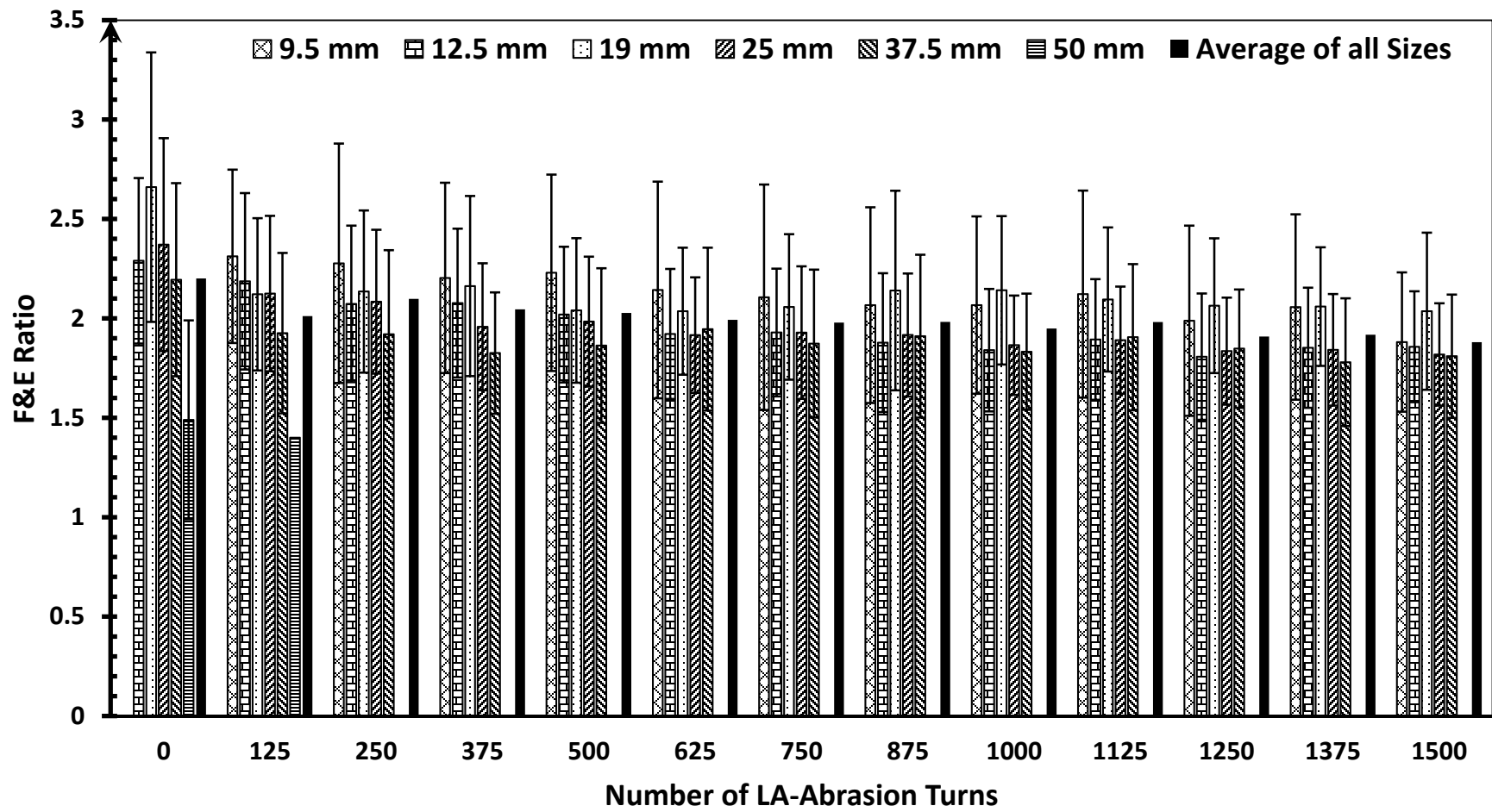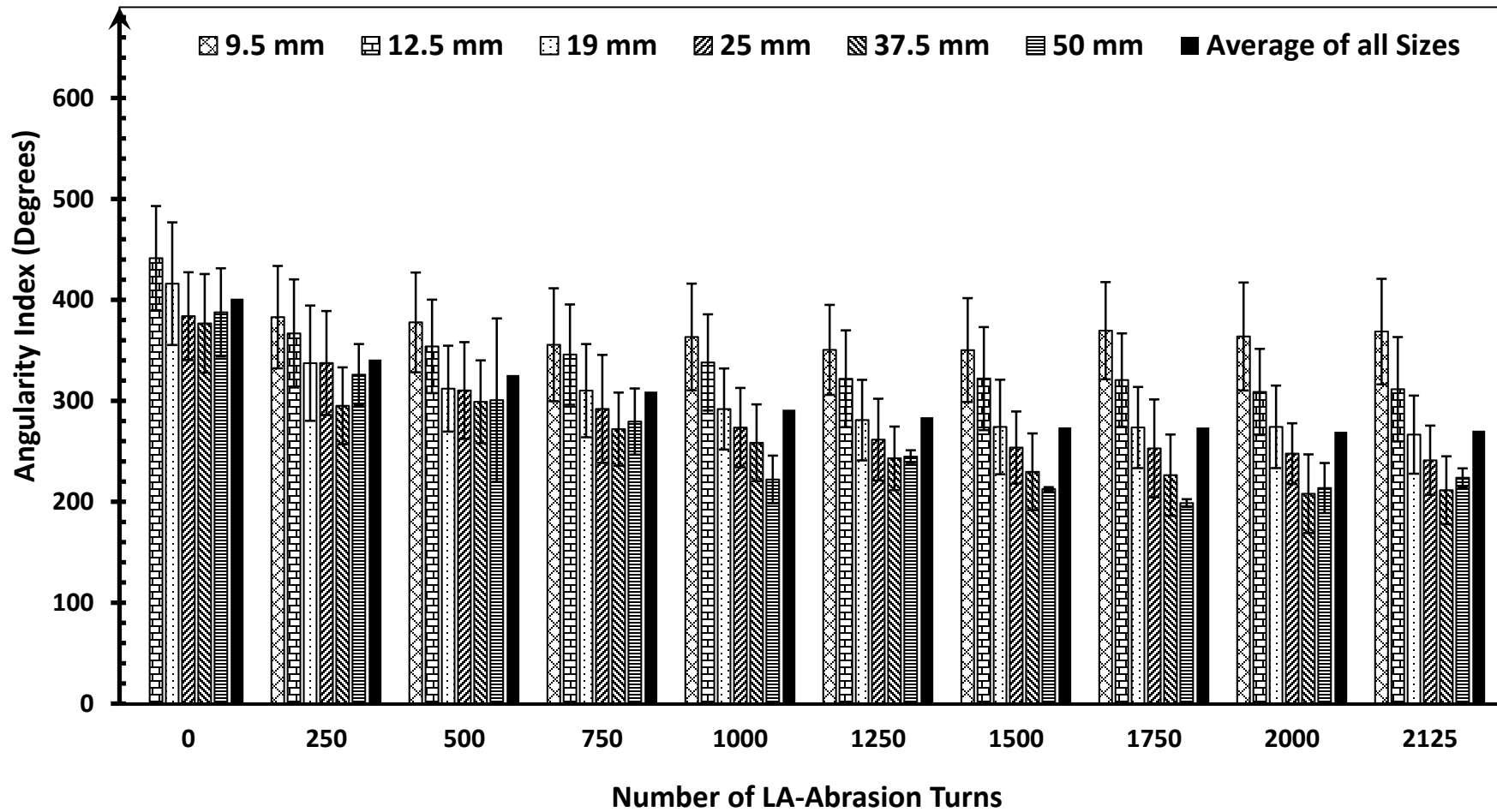Figure 4.8 Average Angularity Index at Different Degradation Levels for Granite Ballast
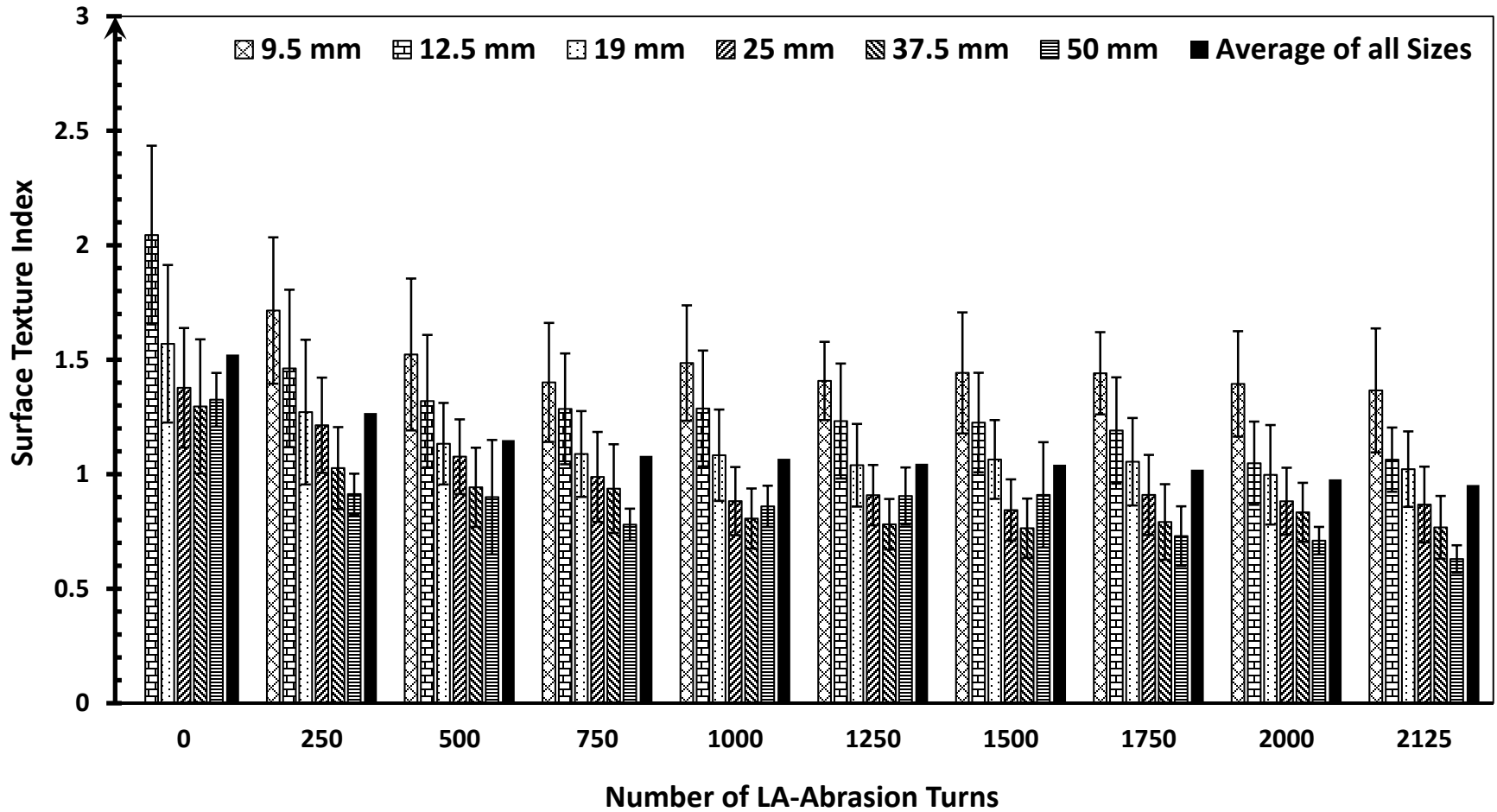
Figure 4.9 Average Surface Texture Index at Different Degradation Levels for Granite Ballast
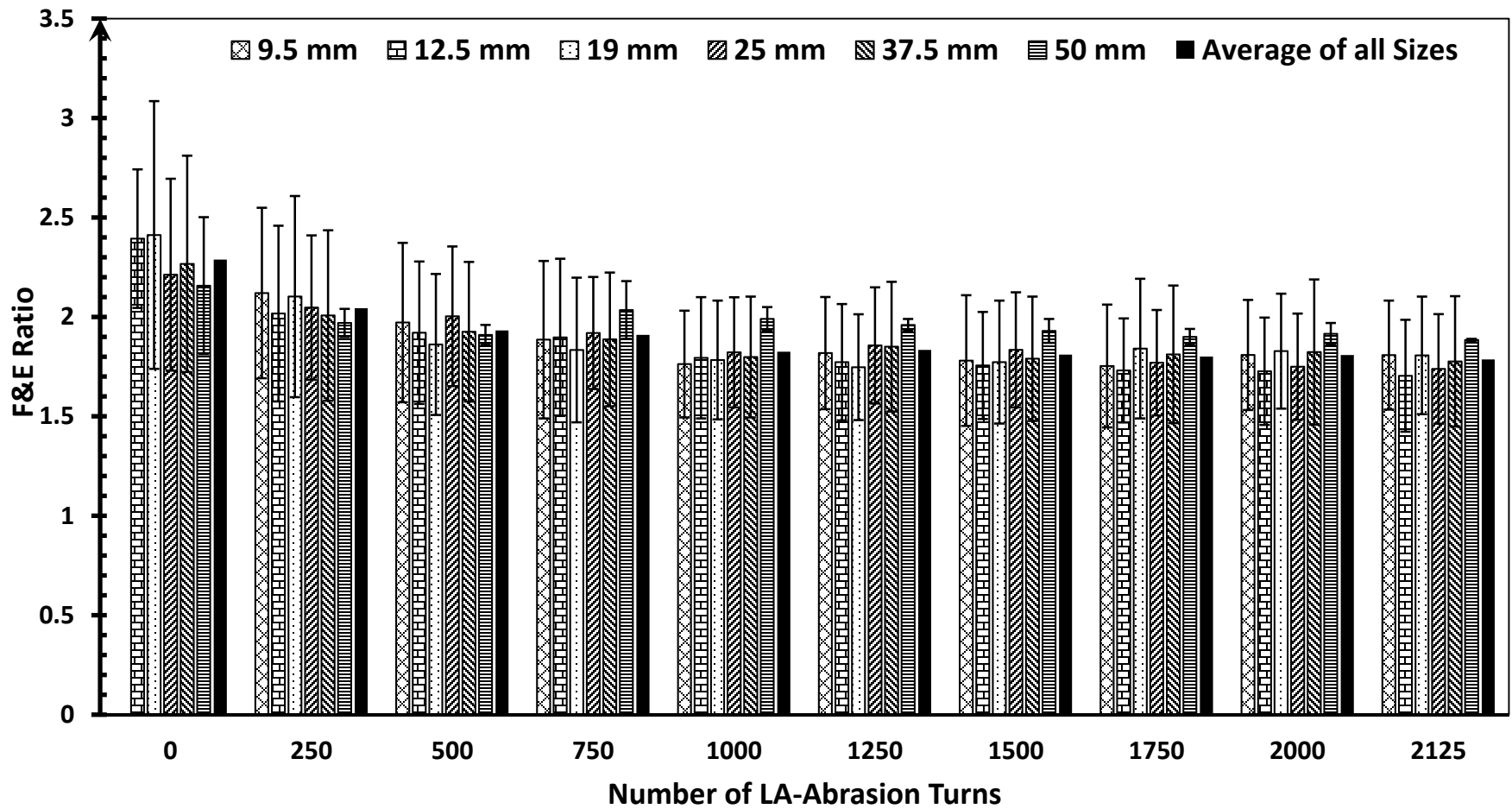
Figure 4.10 Average F&E Ratio at Different Degradation Levels for Granite Ballast

The distributions of F&E Ratio, AI and STI are presented for granite and limestone samples in Figures 4.11 to 4.16, respectively. These plots are different from the bar charts that are shown in Figures 4.5 to 4.10 because they include individual measurements of shape indices from particles. The shape property distribution curves clearly show the variability of shape indices captured by E-UIAIA at each degradation level.

In Figures 4.11 and 4.14 the gap between any two curves implies how much the AI changed between different numbers of drum turns. Clearly, the AI decreases at a slower rate when moving away from the original curve. Accordingly, the distribution curves tend to get closer to each other as they shift towards left, representing a higher number of drum turns. Note that the shift between the first two AI distribution curves is wider in case of limestone (see Figure 4.11) as opposed to granite (see Figure 4.14). This confirms how limestone is less resistant to abrasion particularly at the first stages of degradation. At 1500 drum turns for limestone, a wider shift was observed in the AI and STI distribution curves; see Figures 4.11 and 4.12, respectively. One observation is that relatively larger amounts of fine particles are accumulated at higher degradation levels. Towards the end, these fine particles might have remained on the surfaces of the particles to further decrease the captured AI and STI values. Note that different stages observed in the degradation behavior of limestone and granite samples will be discussed in the next section by using regression based statistical analysis.

Similarly, in Figures 4.12 and 4.15, the gap between any two curves is an indicator of how much STI changed between different numbers of drum turns. In general, both STI and AI distribution curves for granite are more uniform in comparison to those of the limestone. As expected, comparing the STI distribution curves for the limestone and granite shows that granite is more resistant to polishing at higher level of degradation as opposed to limestone.

Figures 4.13 and 4.16 present the F&E Ratio distributions for the limestone and granite samples, respectively. Unlike the AI and STI trends, the F&E Ratio distributions change from the initial wider range values to much narrower range values with increasing number of drum turns. This means that originally rounded particles generally tend to

converge to a certain shape and often become even more rounded; this is when most of the originally flat and elongated particles are broken due to abrasion and breakage.

Figure 4.11 Distributions of Angularity Index for all of Limestone Particles at Different Degradation Levels

Figure 4.12 Distributions of Surface Texture Index for all of Limestone Particles at Different Degradation Levels

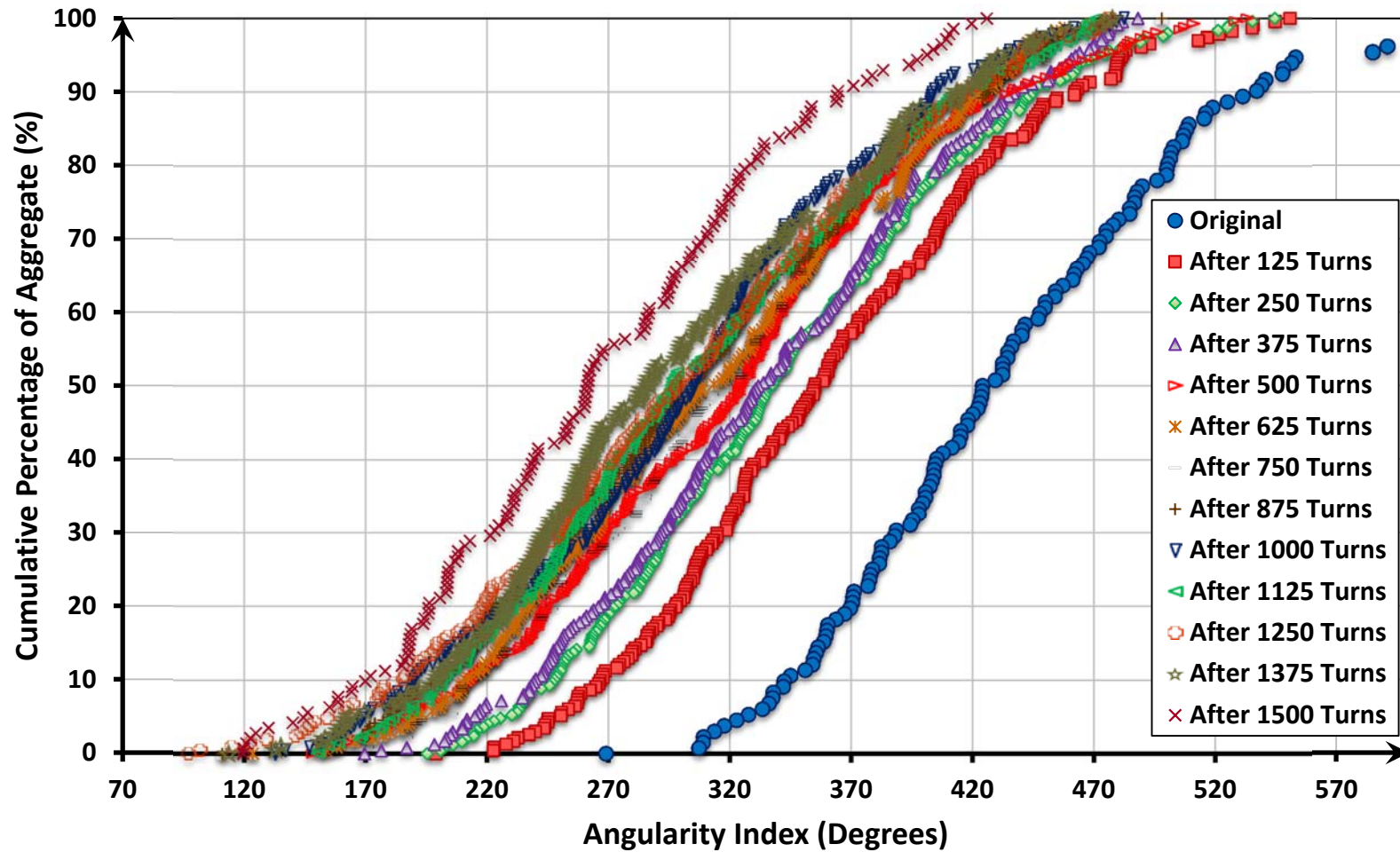Figure 4.13 Distributions of F&E Ratio for all of Limestone Particles at Different Degradation Levels

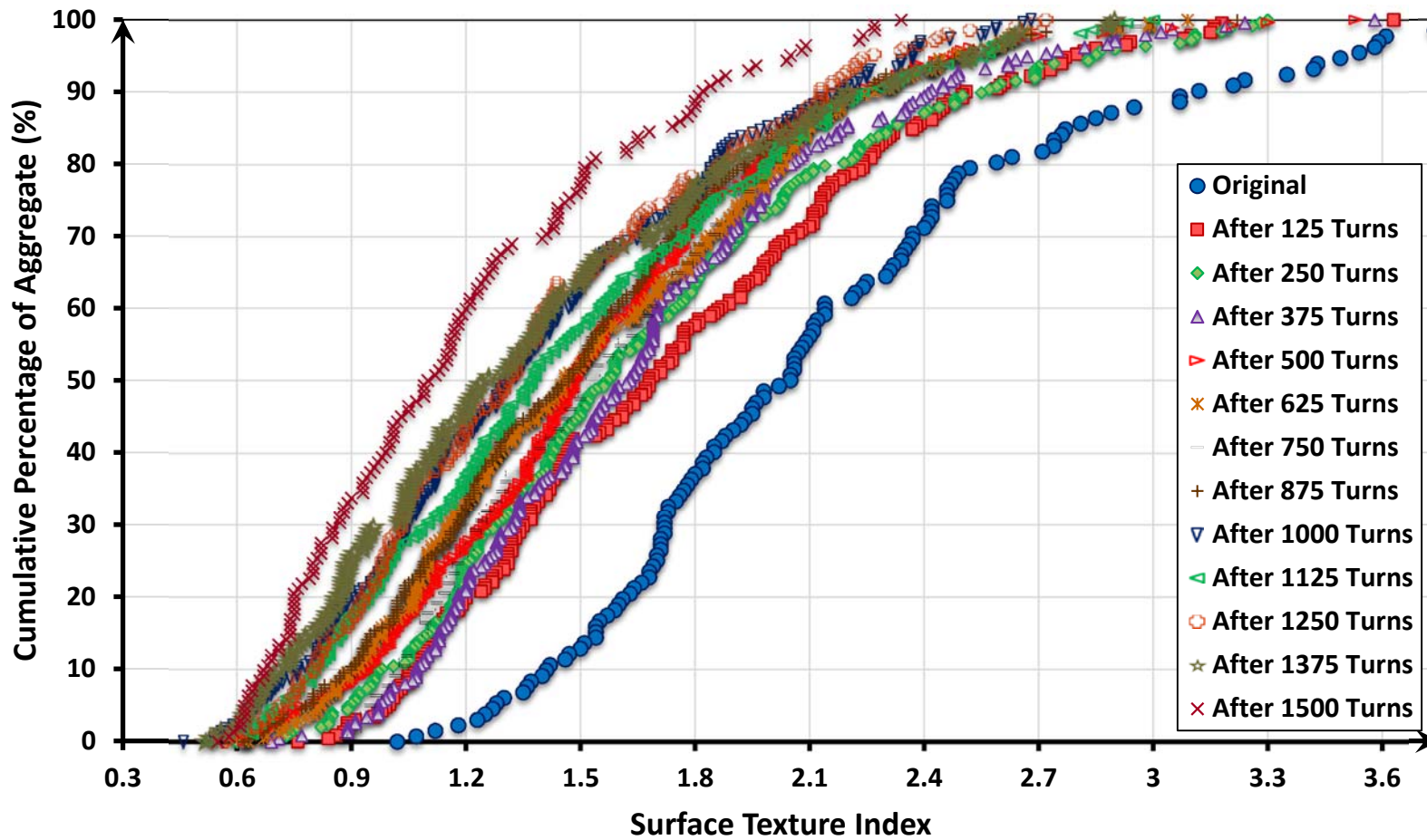Figure 4.14 Distributions of Angularity Index for all of Granite Particles at Different Degradation Levels
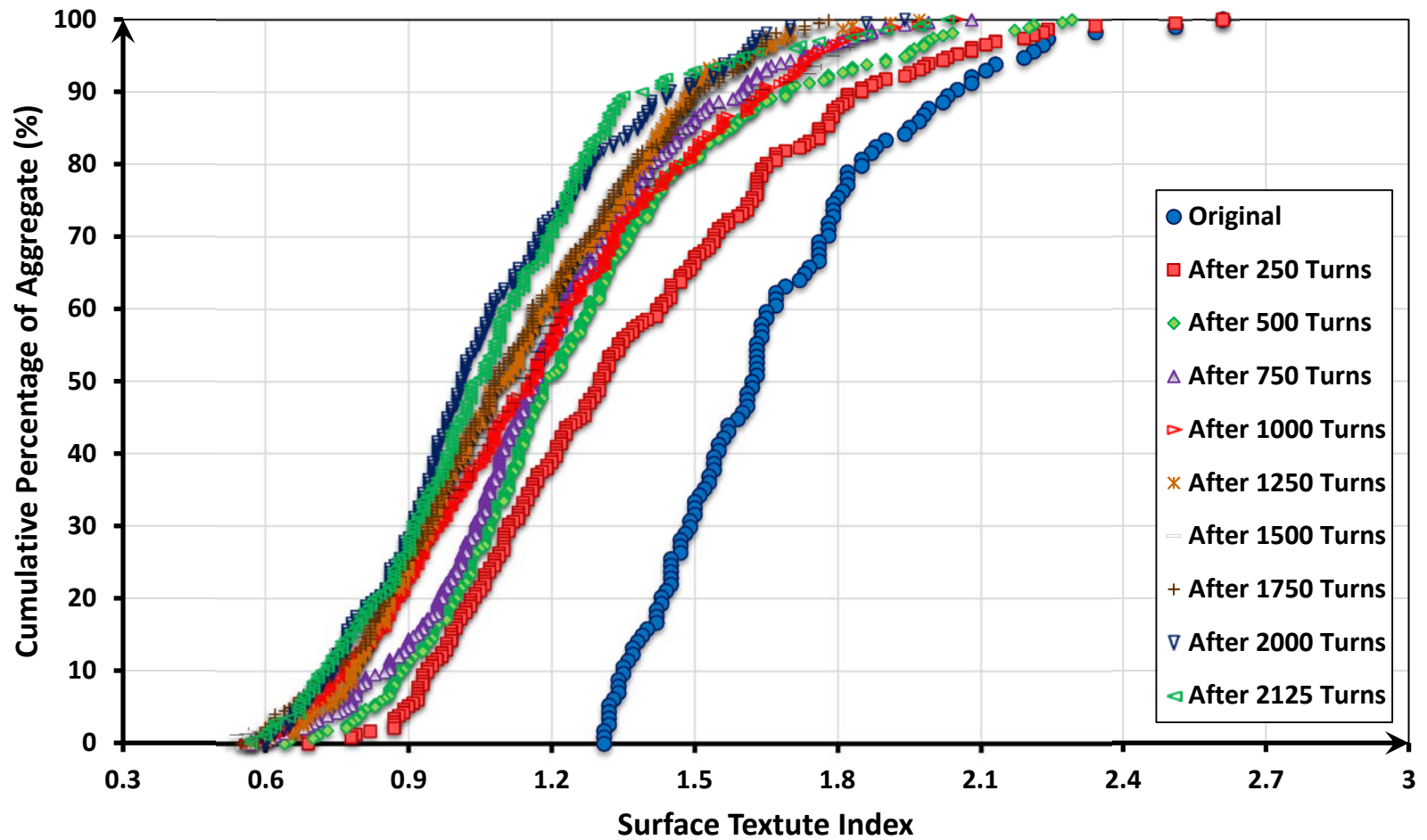
Figure 4.15 Distribution of Surface Texture Index for all of Granite Particles at Different Degradation Levels

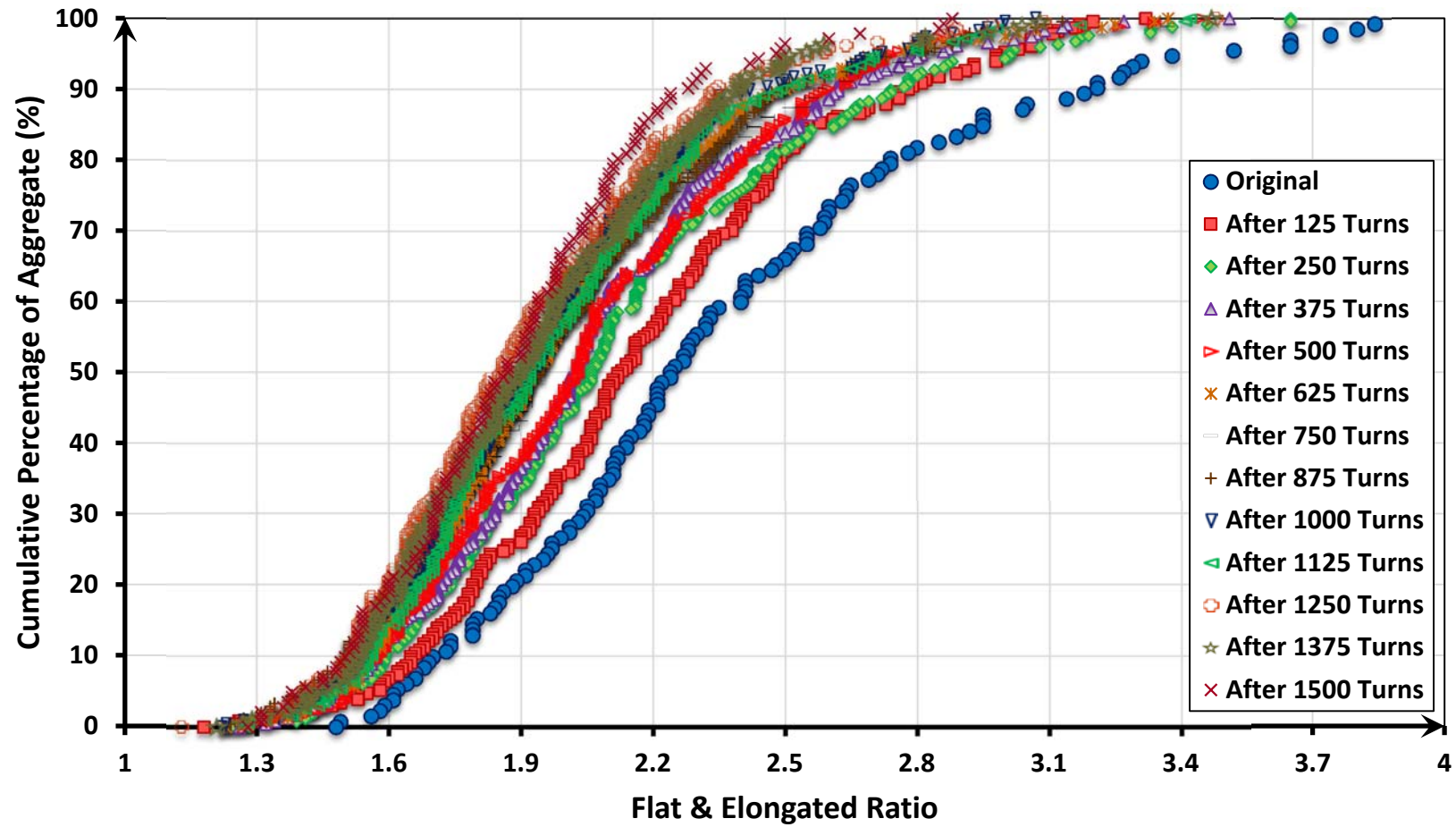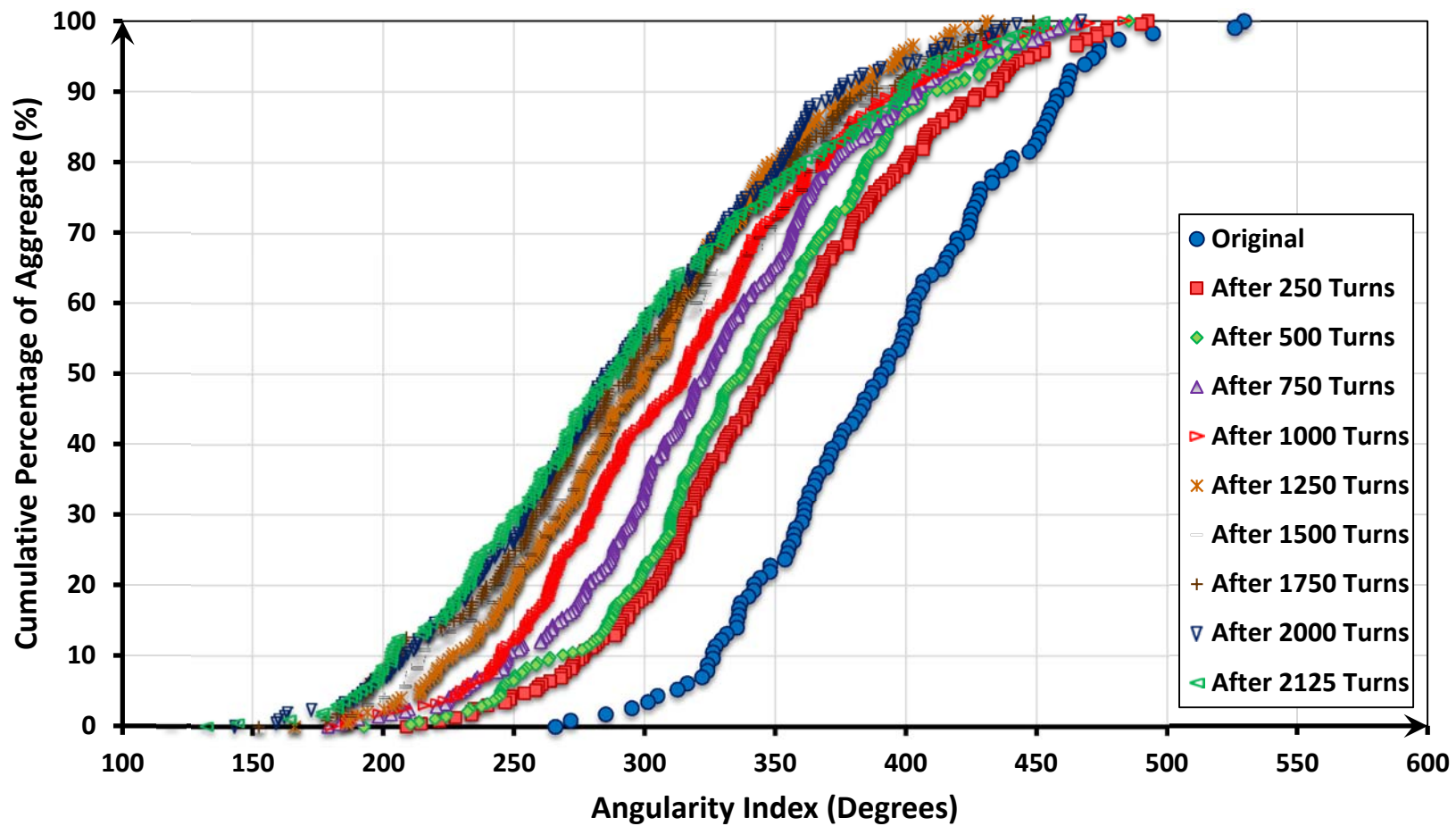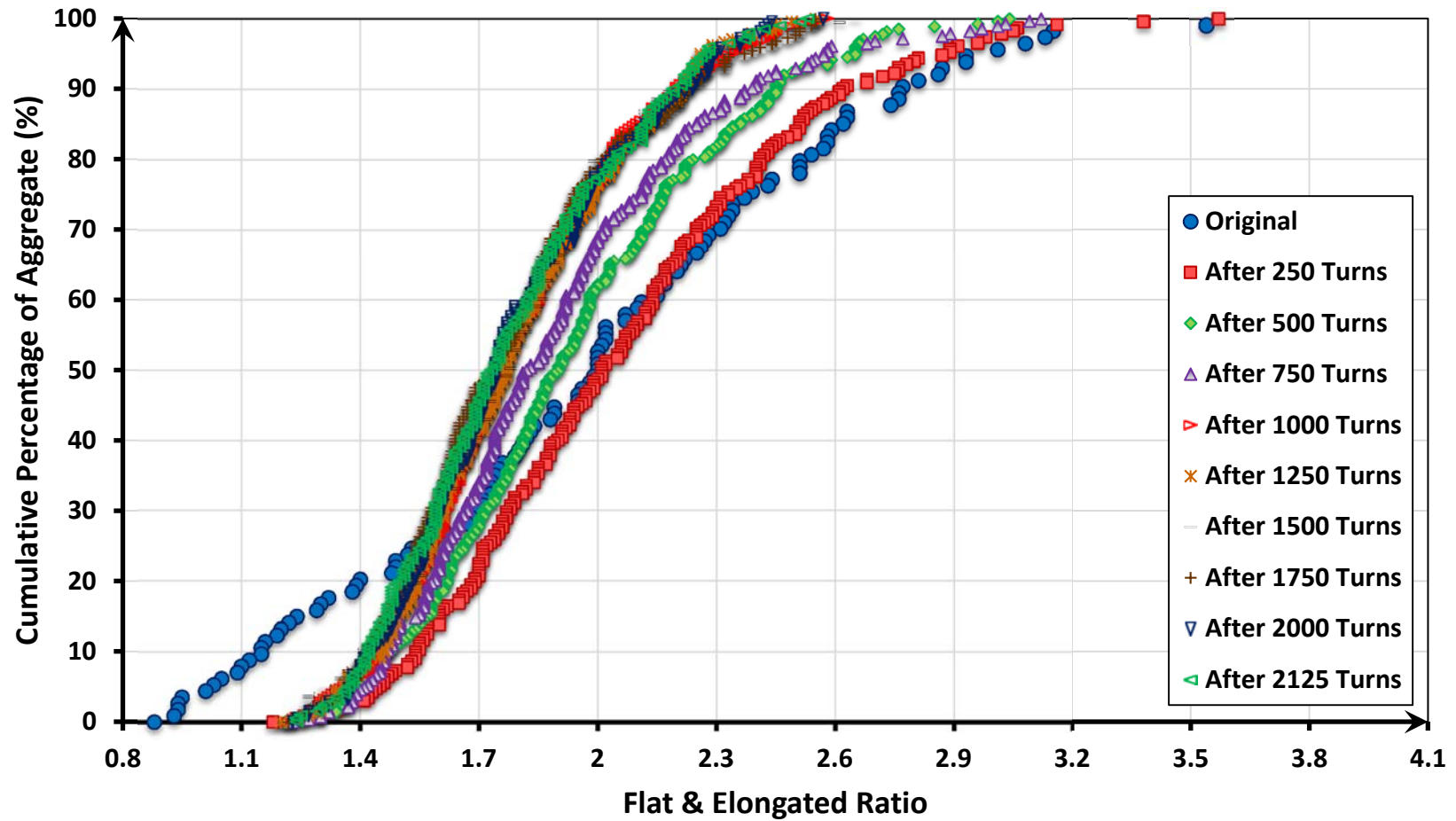Figure 4.16 Distributions of F&E Ratio for all of Granite Particles at Different Degradation Levels

4.1.4 Development of Imaging Based Degradation Models

In this section linear and nonlinear statistical regression methods were used to further analyze the degradation potentials of limestone and granite samples according to the changes in shape indices during LA-Abrasion testing. Figure 4.17 shows the linkage between percent LA-Abrasion value (see Table 4.3) and the percent loss in average AI at different stages of degradation. Linear regression equations are also presented in Figure 4.17. To indicate strong correlations, the coefficient of determination (R^2) values are computed as 0.88 for limestone and 0.92 for granite.
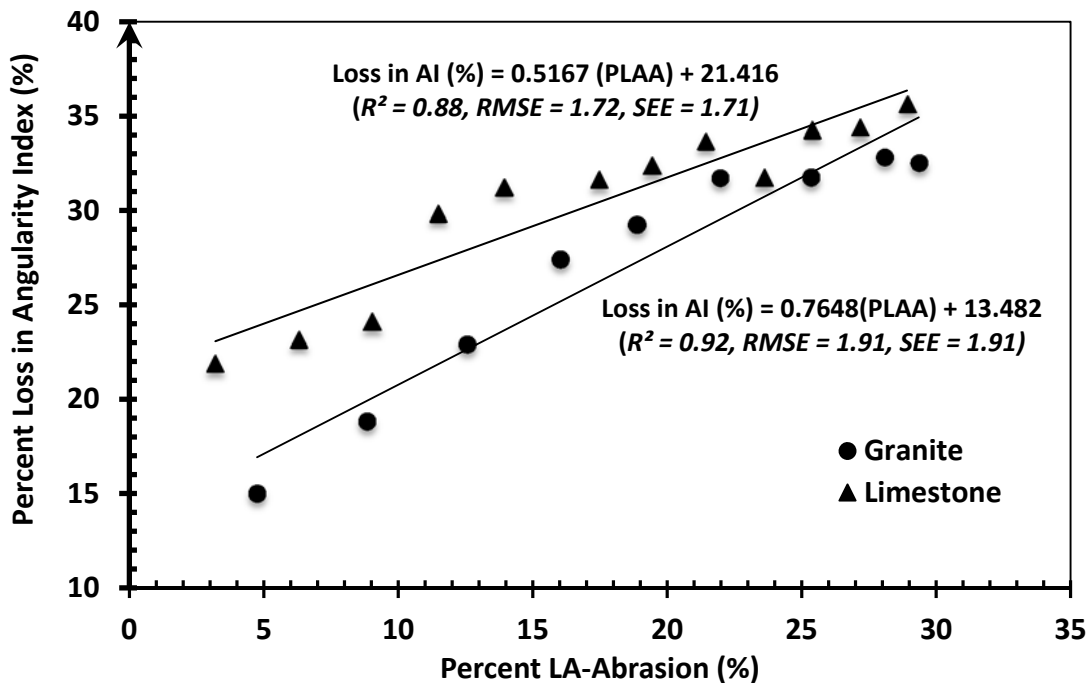
Figure 4.17 Linkages between Percent LA-Abrasion and Loss in AI for Limestone and Granite at different Degradation Levels

Similarly, Figure 4.18 presents a strong correlation between the loss in average STI values and the percent LA-Abrasion with a coefficient of determination R^2 of 0.81 for limestone and 0.90 for granite. Such trends confirm that there is a definite relationship between the imaging based shape indices and the results from LA-Abrasion testing, which is based on the loss in mass of material and the overall reduction in AI and STI of the aggregate particles.
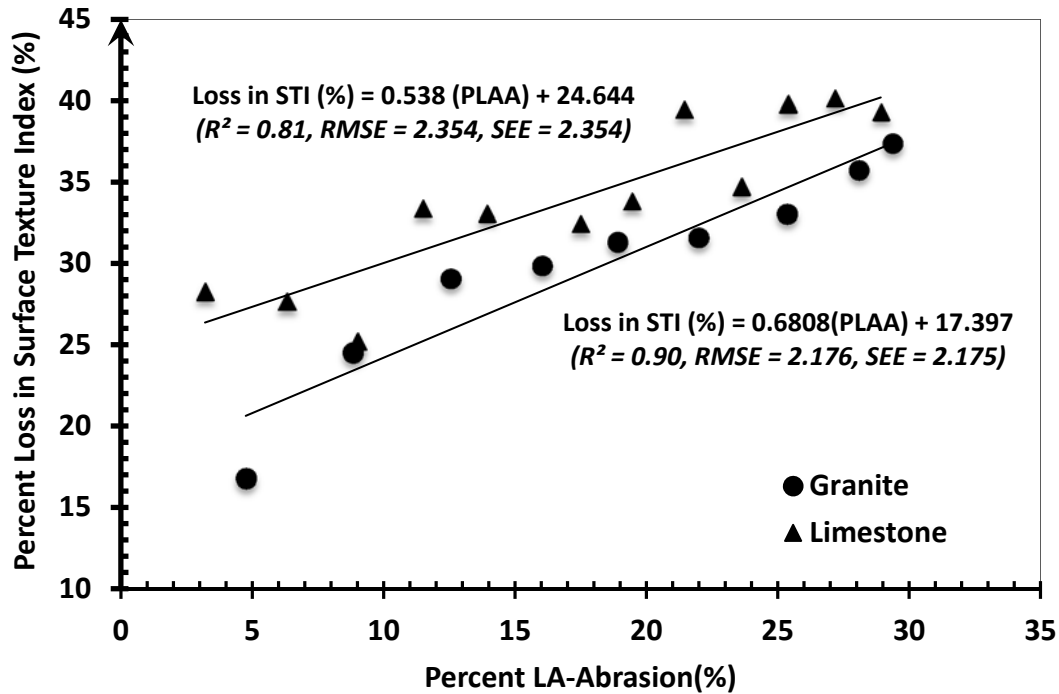
Figure 4.18 Linkages between Percent LA-Abrasion and Loss in STI for Limestone and Granite at different Degradation Levels

Average AI and STI results for limestone and granite quantified by E-UIAIA before LA-Abrasion testing and also at different degradation levels were used to calibrate a three parameter exponential model such as given in Equation 4.2. Mahmoud et al. [95] showed that this type of exponential expression was superior to other mathematical models in terms of describing the change in aggregate shape properties during degradation process.

$$Shape\ Index\ (AI\ or\ STI) = a + b \times e^{-c \times N} \qquad 4.2$$

where,

a, b, c = Model parameters related to initial, final and rate of change in Shape index;

N = Number of LA-Abrasion Turns.

Coefficient of determination (R^2) and Standard Error of Estimates (SEE) were used to assess the accuracy of the models in estimating the deterioration trends for AI and STI

114

during LA-Abrasion testing. Figures 4.19 to 4.22 present the regression analysis results and the fitted curves with their corresponding exponential equations to estimate the AI and STI at different degradation levels. Note that 13 data points for limestone and 10 data points for granite were available in this experiment to calibrate the full regression models. Since sample preparation and conducting several LA-Abrasion tests on one material is a time consuming and laborious process, it was decided to also evaluate the efficiency of exponential models using just 3 data points including shape properties obtained before and after LA-Abrasion testing at 500 and 1,000 turns. The fitted exponential models using three data points are marked with dotted line for comparison purposes with the full regression models.

Figure 4.19 Three Parameter Exponential Model to Estimate Angularity Index at Different LA-Abrasion Drum Turns for Limestone Ballast

Figure 4.20 Three Parameter Exponential Model to Estimate Surface Texture Index at Different LA-Abrasion Drum Turns for Limestone Ballast

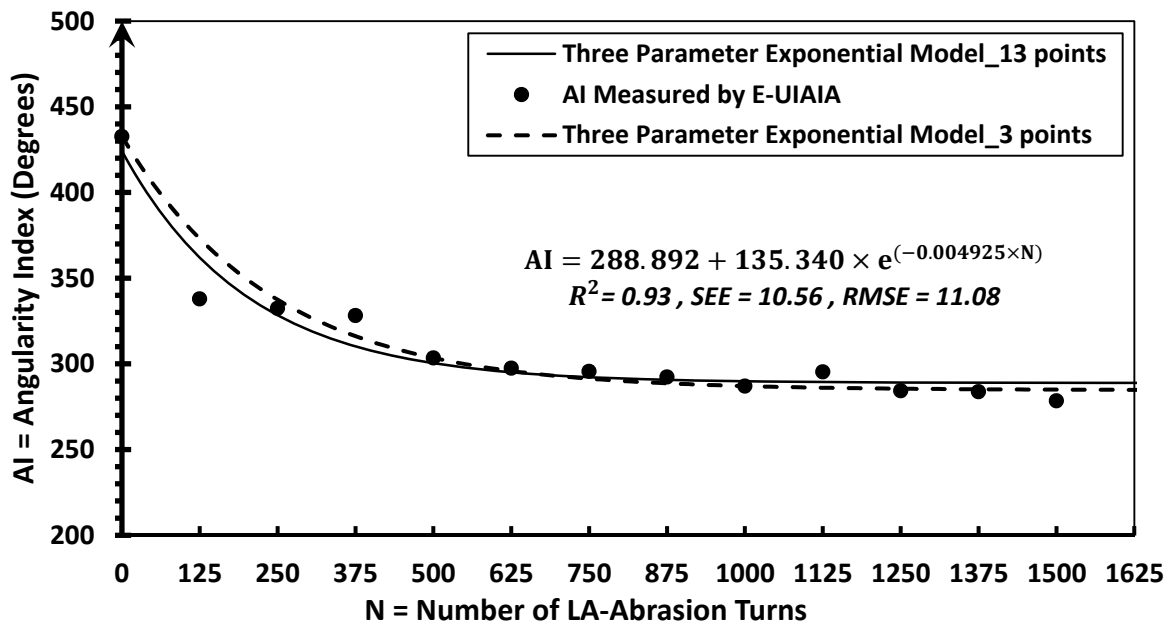$$STI = 1.372 + 0.727 \times e^{(-0.006381 \times N)}$$
$$R^2 = 0.85, SEE = 0.091, RMSE = 0.096$$
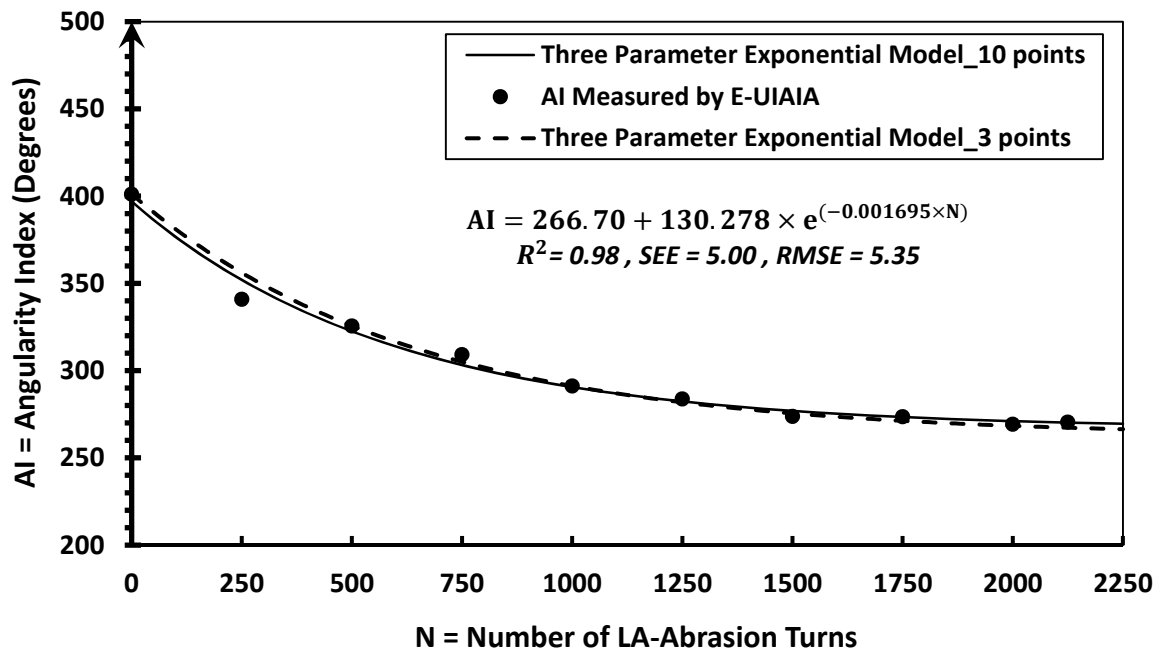
Figure 4.21 Three Parameter Exponential Model to Estimate Angularity Index at Different LA-Abrasion Drum Turns for Granite Ballast

$$AI = 266.70 + 130.278 \times e^{(-0.001695 \times N)}$$
$$R^2 = 0.98, SEE = 5.00, RMSE = 5.35$$

116

$$STI = 0.9955 + 0.5182 \times e^{(-0.002332 \times N)}$$
$$R^2 = 0.97 \,,\, SEE = 0.0254 \,,\, RMSE = 0.0274$$
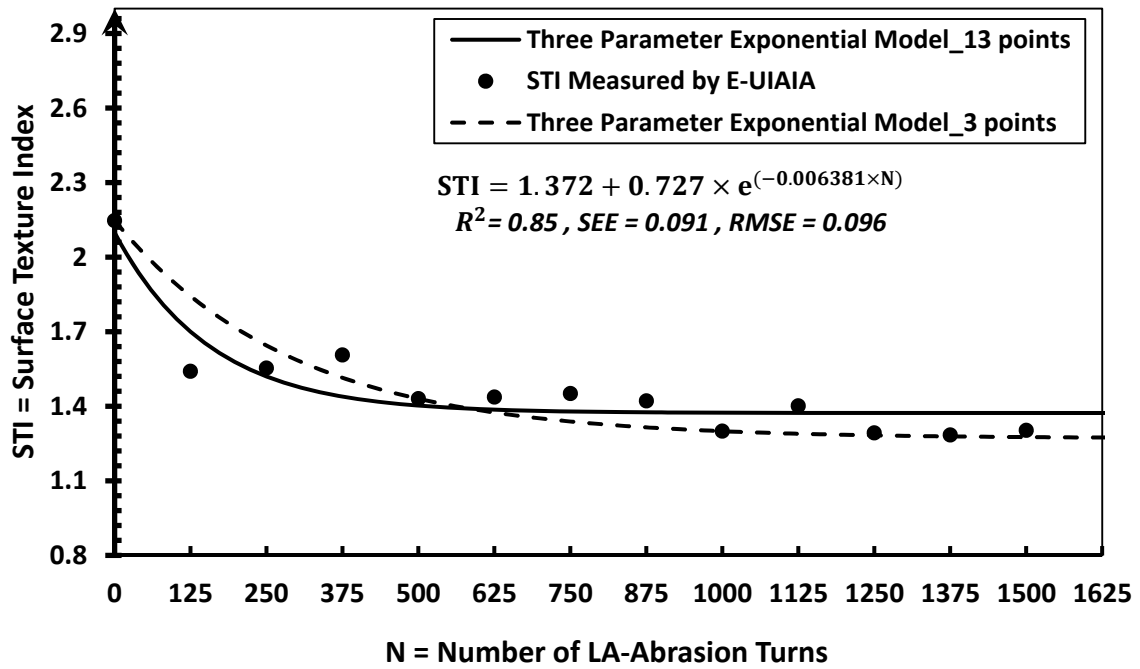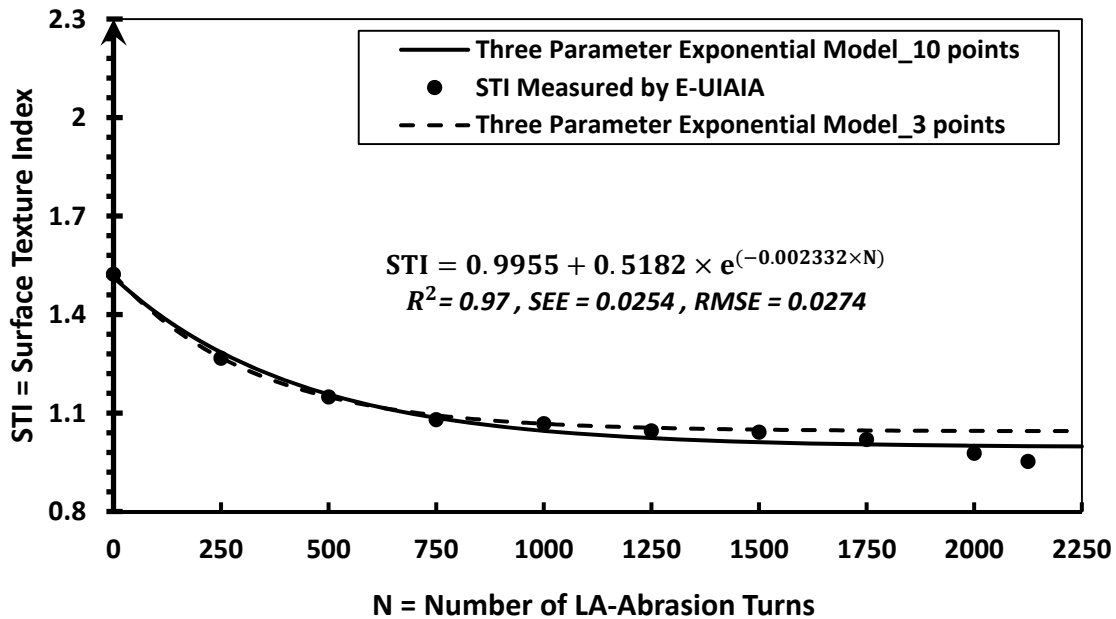
Figure 4.22 Three Parameter Exponential Model to Estimate Surface Texture Index at Different LA-Abrasion Drum Turns for Granite Ballast

In general high R^2 values were observed for the regression models developed for the limestone and granite samples. Three parameter exponential fitted curves showed that AI and STI deteriorated with a faster rate for limestone at initial stages of degradation in comparison to granite. Moreover, limestone reached a stable condition in terms of average AI and STI of all the particles at 1,000 LA-Abrasion turns. The fitted AI and STI deterioration curves for granite started to level off at around 1,000 turns and reached to a stable condition at 1,500 turns. It was also visually observed that the fitted models using three data points matched reasonably well with the full regression models. Considering the intensive laboratory work that is required to capture the full shape property data sets at different degradation levels for a desired ballast source, the accuracy of the three parameter models using three data sets sounds acceptable. Comparing the shape property deterioration curves between the limestone and granite samples, a three-stage behavior is observed in terms of rate of change in shape indices during LA-Abrasion testing. These three stages include: starting point, initial decrease with rapid rate and finally reaching a steady rate. The findings from this section confirmed that three parameter exponential regression modeling even

with three data points can be considered as an appropriate approach to characterize the deterioration trends of aggregates in terms of AI and STI indices measured by E-UIAIA.

4.2 LA-Abrasion Testing Combined with Imaging Results for Classifying Railroad Ballast

Fouteen sources of ballast are studied in this section. These ballast sources are currently used by Western freight railroad companies and were obtained from quarries all located west of the Mississippi river. The properties of these ballast sources including specific gravity and rock type are provided in Table 4.4

Table 4.4 Properties Including Specific Gravity and Rock Classification for Ballast Aggregate Sources

Ballast ID	Specific Gravity (G_S)	Rock Type
Ballast I	2.51	Trap Rock
Ballast II	2.41	Trap Rock
Ballast III	2.82	Trap Rock
Ballast IV	2.36	Trap Rock and Granitoid
Ballast V	2.74	Trap Rock
Ballast VI	2.94	Trap Rock
Ballast VII	2.33	Quartzite
Ballast VIII	2.46	Granitoid
Ballast IX	2.60	Trap Rock
Ballast X	2.32	Trap Rock
Ballast XI	2.29	Granitoid
Ballast XII	2.51	Trap Rock
Ballast XIII	2.32	Granitoid
Ballast XIV	2.60	Trap Rock

4.2.1 Laboratory Sieve Analysis and Imaging Results before LA-Abrasion Testing

The particle size distributions for these fourteen sources of ballast aggregate materials were determined according to ASTM C136. Each ballast aggregate was initially

weighed at dry condition, then was washed over a No.200 (0.075 mm) sieve and dried for 24 hours in the oven. Finally, the dry weight of the sample was determined to obtain the amount of material passing the No.200 (0.075 mm) sieve. The percentage passing amounts for each sieve size determined for all ballast sources are shown in Figure 4.23. As expected, the gradation curves confirmed that majority of the particle sizes in clean ballast were between 1 in. (25 mm) and 2 in. (50 mm). This information was used later to identify the required number of particles to scan from each size to obtain a representative imaging sample from each source. It needs to be noted that two samples from each ballast source were prepared and the average values of the two laboratory sieve analyses were reported.

E-UIAIA was used to quantify the shape indices of these ballast sources. Angularity index, surface texture index and F&E Ratio of the particles are presented in this section. These indices are later used in this chapter to investigate the degradation behavior of these ballast sources. Two samples were prepared from each ballast aggregate, with approximately 75 to 80 particles per sample to investigate the effect of random sampling on the imaging based shape indices. The number of particles for each sieve size were distributed proportional to the gradation of each ballast source and are presented in Table 4.5. In total more than 2,000 particles were scanned for all of the 14 ballast sources.

Note that very few particles with sizes less than 3/4 in. (19 mm) were selected for scanning since the majority of the particle sizes in clean ballast were between 1 in. (25 mm) and 2.5 in. (63 mm). The average imaging results for AI, STI and F&E Ratio for all the particle sizes from two random independent samples related to each source of ballast are presented in Figures 4.24 to 4.26.

According to Figure 4.24, in general a good match was observed for the AI values between sample 1 and sample 2 from each ballast source. Ballast XI had the highest AI value while Ballast III had the lowest angularity value. Sample 2 in ballast V and sample 1 in ballast XI showed relatively larger standard deviations in AI as opposed to sample 1 in ballast XII which showed lower standard deviation. Note that these ballast sources are all fully crushed particles and therefore, the AI for all the samples was above 330 which is comparable with AI values for a crushed particle reported in Table 3.23.
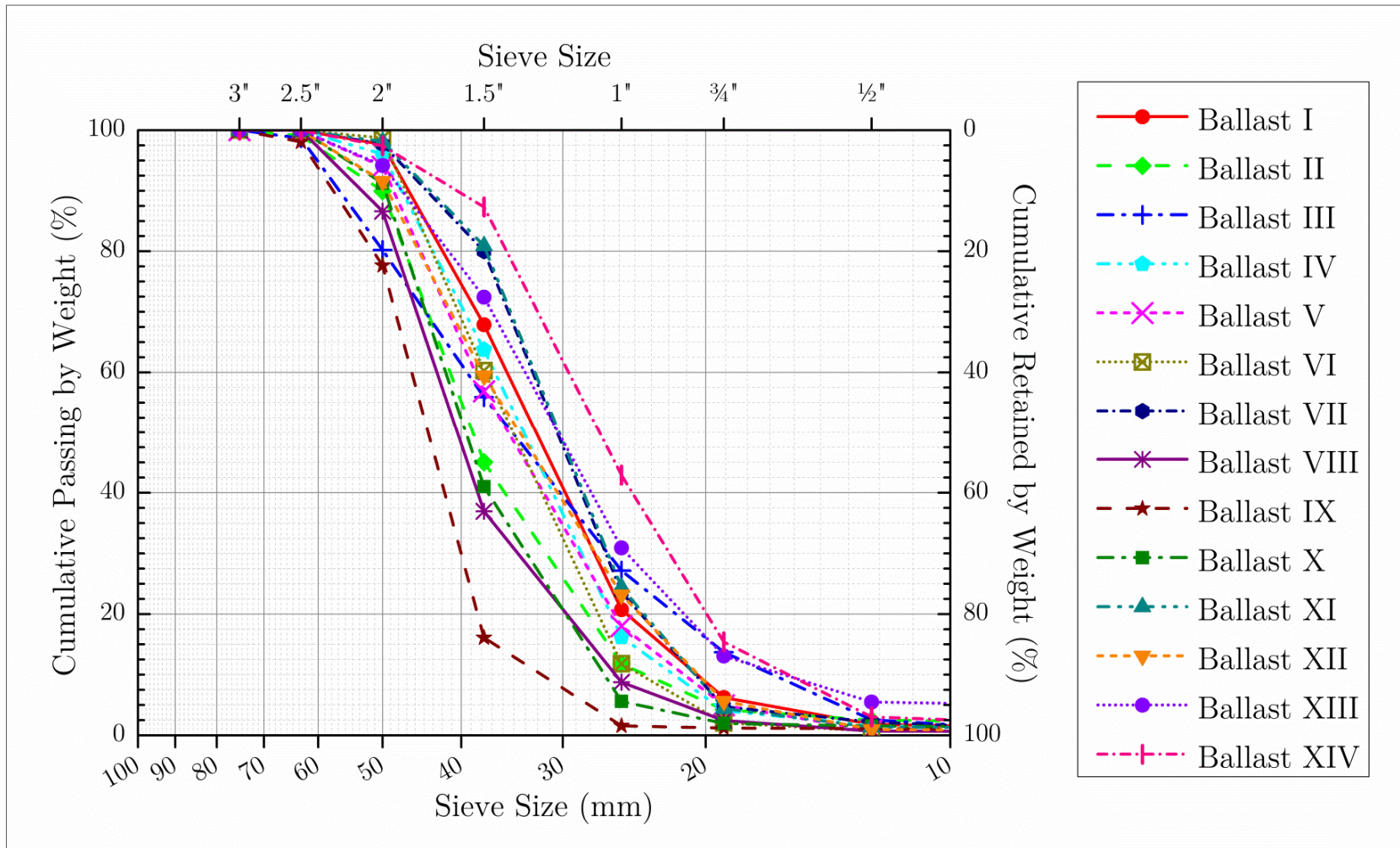
Figure 4.23 Particle Size Distributions for Fourteen Ballast Sources [9]

Table 4.5 Number of Particles Scanned with E-UIAIA for Each Sieve Size

Sieve Size (in.)	2.5	2	1.5	1	3/4	1/2	3/8	No.4	Total Number of Particles
Sieve Size (mm)	63	50	37.5	25.4	19	12.5	9.5	4.76	
Ballast I	0	2	23	36	11	4	1	1	78
Ballast II	1	7	34	25	6	2	1	1	77
Ballast III	1	14	19	22	11	9	1	1	78
Ballast IV	0	3	25	36	10	2	1	1	78
Ballast V	0	5	28	30	10	4	1	1	79
Ballast VI	0	2	14	43	15	2	1	1	78
Ballast VII	0	11	38	22	5	2	1	1	80
Ballast VIII	2	16	47	11	1	1	1	1	80
Ballast IX	0	7	38	27	3	1	1	1	78
Ballast X	0	2	13	43	15	3	1	1	78
Ballast XI	0	7	25	28	14	4	1	1	80
Ballast XII	0	5	17	32	14	6	1	1	76
Ballast XIII	0	2	8	34	21	10	1	1	77
Ballast XIV	0	1	29	37	8	2	0	1	78

Figure 4.25 shows that ballast XIV has the highest STI while ballast III was the source with the lowest STI. Relatively a good match was observed between STI measurements for sample 1 and sample 2 from each ballast source. Sample 2 in ballast V and sample 1 in ballast IX had the highest standard deviation values while sample 2 in ballast XI showed the lowest standard deviation. As was mentioned before, the particles in these ballast sources are fully crushed. Thus, the overall STI for all the sources was above 1 which verifies the STI measurements by E-UIAIA for a crushed particle reported in Table 3.23.

Based on the F&E Ratio results shown in Figure 4.26, ballast XIV showed the highest F&E Ratio while Ballast XI had the lowest F&E Ratio. In most of the ballast sources except ballast IV, ballast VII, ballast IX and ballast XIII a good match was observed in terms of F&E Ratio between sample 1 and sample 2. Additionally, ballast IV had the highest standard deviation while Ballast VI showed the lowest standard deviation for F&E Ratio.

Note that effects of the shape properties of these ballast sources on laboratory performance in terms of shear strength were also studied and can be found elsewhere [7].
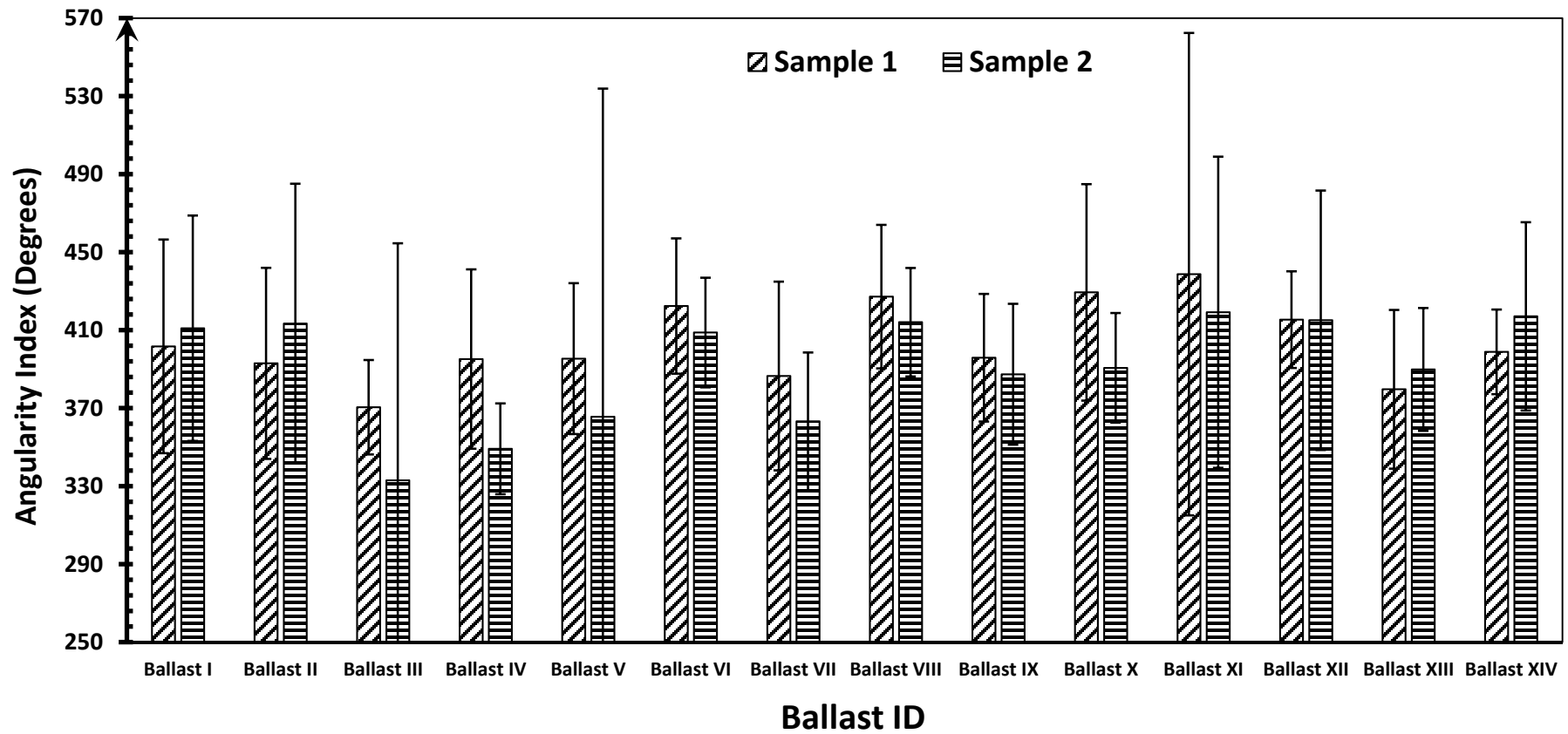
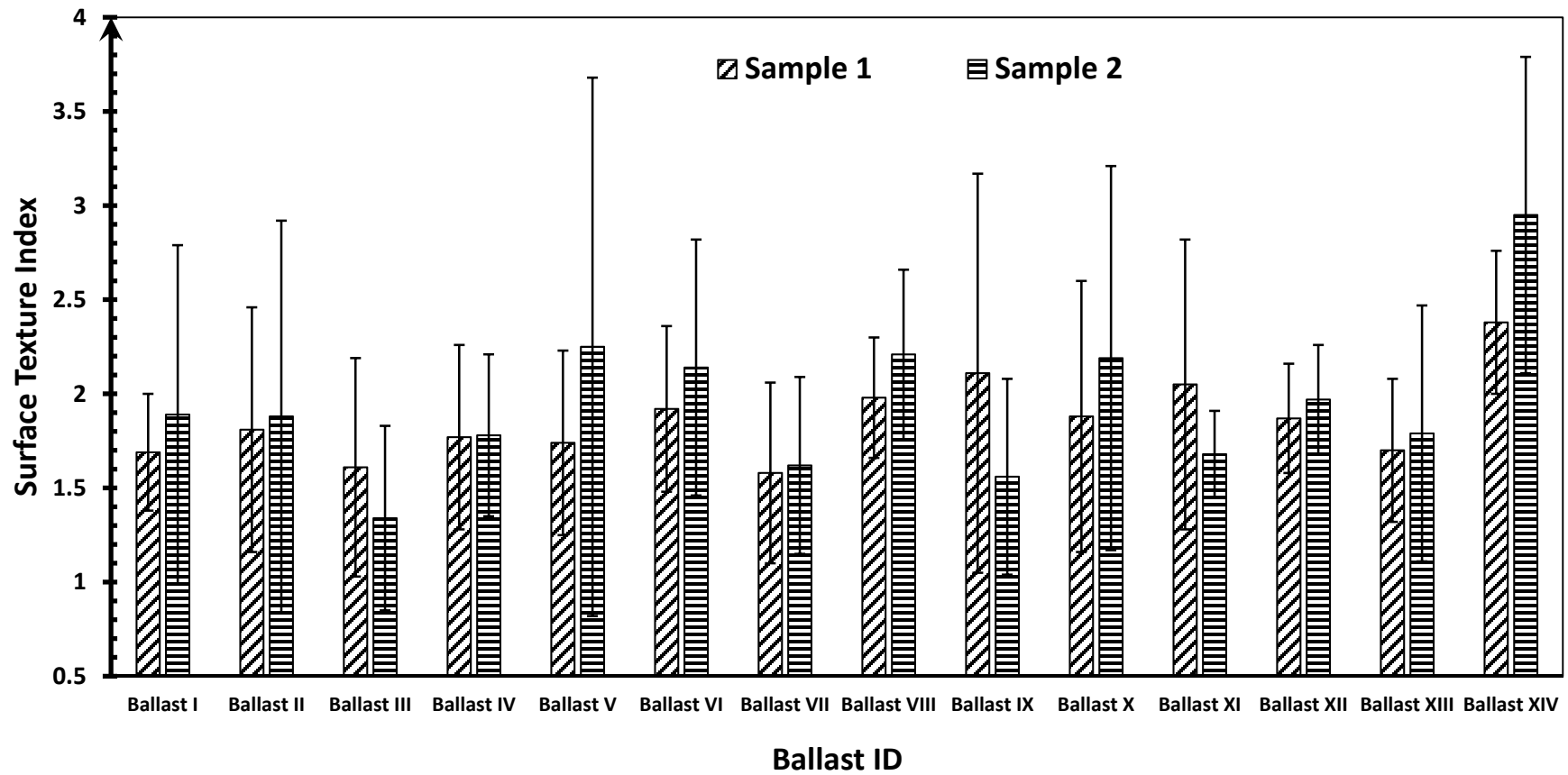Figure 4.24 Average Angularity Index Values for Samples 1 and 2 of 14 Ballast Sources

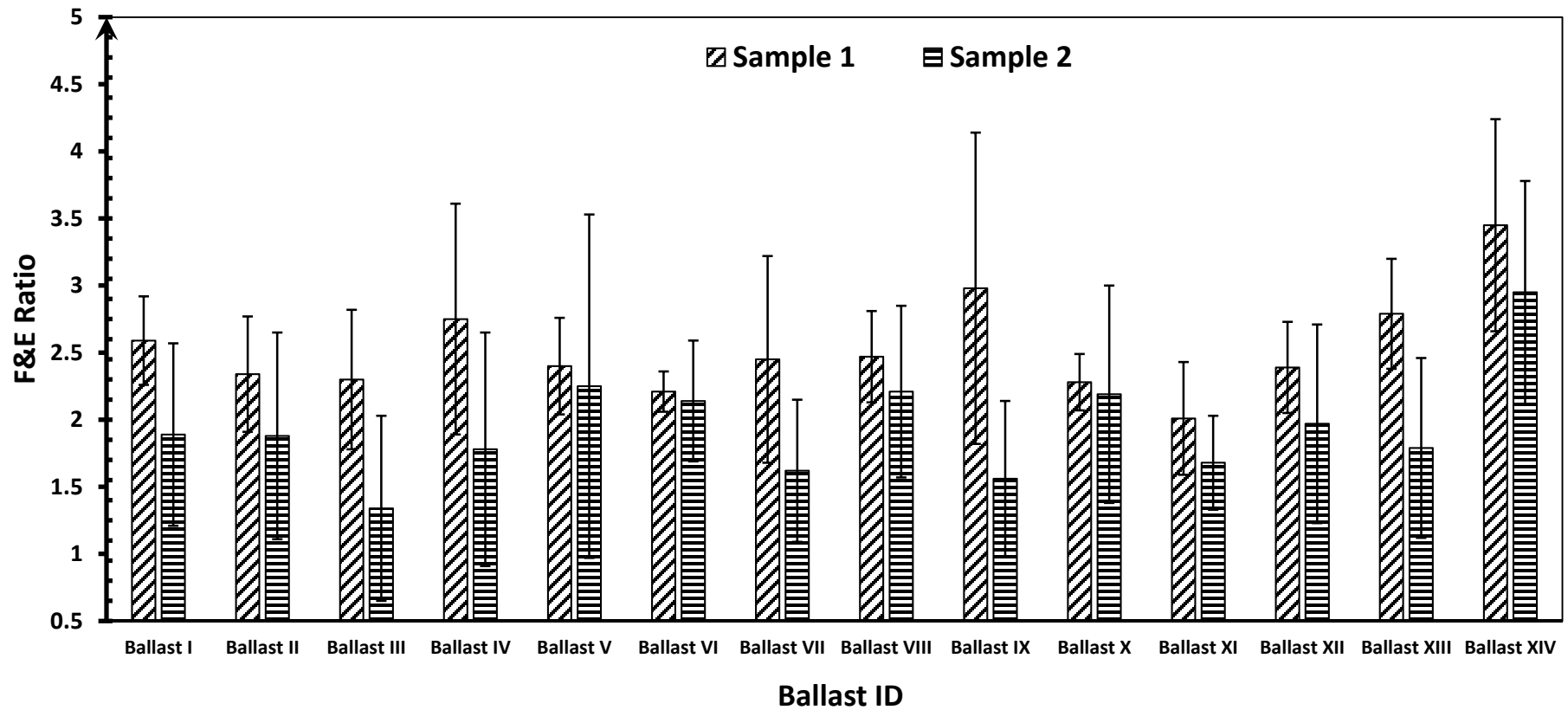Figure 4.25 Average Surface Texture Index Values for Samples 1 and 2 of 14 Ballast Sources

Figure 4.26 Average F&E Ratios for Samples 1 and 2 of 14 Ballast Sources

4.2.2 Laboratory Sieve Analysis and Imaging Results after LA-Abrasion Testing

LA-Abrasion laboratory testing was performed at 400 turns and 1,000 turns on these ballast sources according to ASTM C535 to study the effect of degradation determined by the changes in shape properties. The following steps were followed for the sample preparation and testing:

1- Prepare 11 lbs (5 kg) of 1 in. (25 mm) to 1.5 in. (37.5 mm) and 11 lbs (5 kg) of 1.5 in. (37.5 mm) to 2.0 in. (50 mm) aggregate samples for each ballast source;

2- Wash all the material to remove the fines passing No.200 (0.075 mm) sieve sticking to individual particles;

3- Dry the material in the oven for 24 hours;

4- Place prepared materials and 12 steel balls inside the LA-Abrasion drum;

5- Start the machine and allow it to rotate until it reaches the desired number of revolutions which is in this case 400 and 1,000;

6- Remove material from the drum. Locate and remove the 12 steel balls from the sample;

7- Determine the weight of the abraded aggregate sample before washing;

8- Thoroughly wash material over No.200 (0.075 mm) sieve to ensure all material finer than the No.200 (0.075 mm) sieve were washed away by gently screening the material on top of the sieve;

9- Place washed material in the oven for 24 hours to dry;

10- Remove material from oven and perform sieve analysis according to ASTM C136.

Note that ASTM C535 recommends 1,000 turns to determine the LA-Abrasion Number for ballast materials. Based on what was discussed before, 500 and 1,000 LA-Abrasion turns were selected in section 4.1 to capture the second and final stages of deterioration curves. Additionally, previous research by Boler et al. [31] recommended 400 and 1,000 turns as good break points to represent the changes in shape properties during LA-Abrasion degradation. Considering the large number of ballast sources studied, it was decided to determine the percent LA-Abrasion after 400 turns to efficiently capture the

initial degradation stage in each ballast source. Table 4.6 shows the percent LA-Abrasion for the 14 sources of ballast at 400 and 1,000 turns. (see Equation 4.1).

Table 4.6 Percent LA-Abrasion after 400 and 1,000 Drum Turns

Ballast Source	Number of LA-Abrasion Drum Turns	
	400	1,000
Ballast I	6.19	9.78
Ballast II	8.55	16.44
Ballast III	6.08	10.96
Ballast IV	6.41	13.65
Ballast V	4.02	8.80
Ballast VI	5.33	10.49
Ballast VII	5.95	15.20
Ballast VIII	6.24	9.01
Ballast IX	6.19	11.87
Ballast X	8.09	15.45
Ballast XI	8.90	18.48
Ballast XII	6.71	10.44
Ballast XIII	9.70	19.08
Ballast XIV	7.10	12.67

Note that for each set of LA-Abrasion testing a new sample was prepared. According to Table 4.6, at 400 drum turns ballast XI and ballast XIII had the highest percent LA-Abrasion while ballast V and ballast VI had the lowest percent LA-Abrasion. LA-Abrasion test results at 1,000 turns also showed that ballast XI and ballast XIII were the ballast sources with the highest susceptibility to degradation while ballast V and ballast VIII had the lowest percent LA-Abrasion. Note that ballast VI also did not show a significant amount of degradation at 1,000 turns in comparison to the other ballast sources.

After each LA-Abrasion test, all of the particles above No.4 (4.75 mm) sieve were scanned using E-UIAIA to identify AI, STI and F&E Ratio values. The average values for shape indices obtained after 400 and 1,000 LA-Abrasion turns were compared with their corresponding initial values before running LA-Abrasion testing. Note that because only 1.5 in. (37.5 mm) and 1 in. (25 mm) particles were used in LA-Abrasion testing, the imaging based shape properties are only compared to the shape properties of these particle sizes before LA-Abrasion testing. These imaging results and comparisons are shown in Figures 4.27 to 4.29.

Figure 4.27 indicates that AI values for all the ballast sources except ballast VI and ballast XII decreased at the higher level of degradation. As discussed in Chapter 2, the mineralogical properties including grain sizes and shapes of each rock source can influence the degradation and breakage mechanisms. By referring to Table 4.4, it was found that both ballast VI and ballast XII were trap rock. The loss in AI at 400 and 1,000 turns of LA-Abrasion was more significant in ballast III, ballast V and ballast XI. Later in this chapter these two parameters will be used to classify ballast sources in terms of their resistance to breakage and abrasion.

Figure 4.28 showed that STI values of the ballast sources except ballast IV, ballast VI, ballast VIII and ballast XII decreased at high degradation levels. Moreover, STI for ballast sources II, X and XIV decreased with a faster rate at higher degradation levels in comparison to the rest of the ballast sources. The percentage of loss in STI can be related to percent LA-Abrasion associated with each ballast source to evaluate the susceptibility of ballast breakage and polishing.

As shown in Figure 4.29, the F&E Ratio values for most of the ballast sources except ballast XIV did not change significantly at 400 and 1,000 LA-Abrasion turns. As discussed in section 4.1.3, this finding confirmed that LA-Abrasion testing do not extensively affect the form of the particles.

The imaging results that are shown in Figures 4.27 to 4.29 are based on the average value of each shape index. The full cumulative distribution plots associated with each shape property at different degradation levels for these fourteen ballast sources are provided in Appendix C of this dissertation. These plots are similar to those presented in Figures 4.11 to 4.16 in which individual measurement of each imaging based shape property is captured. These plots also show that by increasing the number of LA-Abrasion drum turns, the distribution curves of AI and STI shift toward the left which confirms their decreasing trends.

4.2.3 Imaging Based Degradation Models

Based on what was discussed in section 4.1.1, nonlinear regression method was used to calibrate three parameter exponential models using 3 data points to achieve AI and STI deterioration patterns. The model parameters for all the fourteen ballast sources are summarized in Table 4.7.
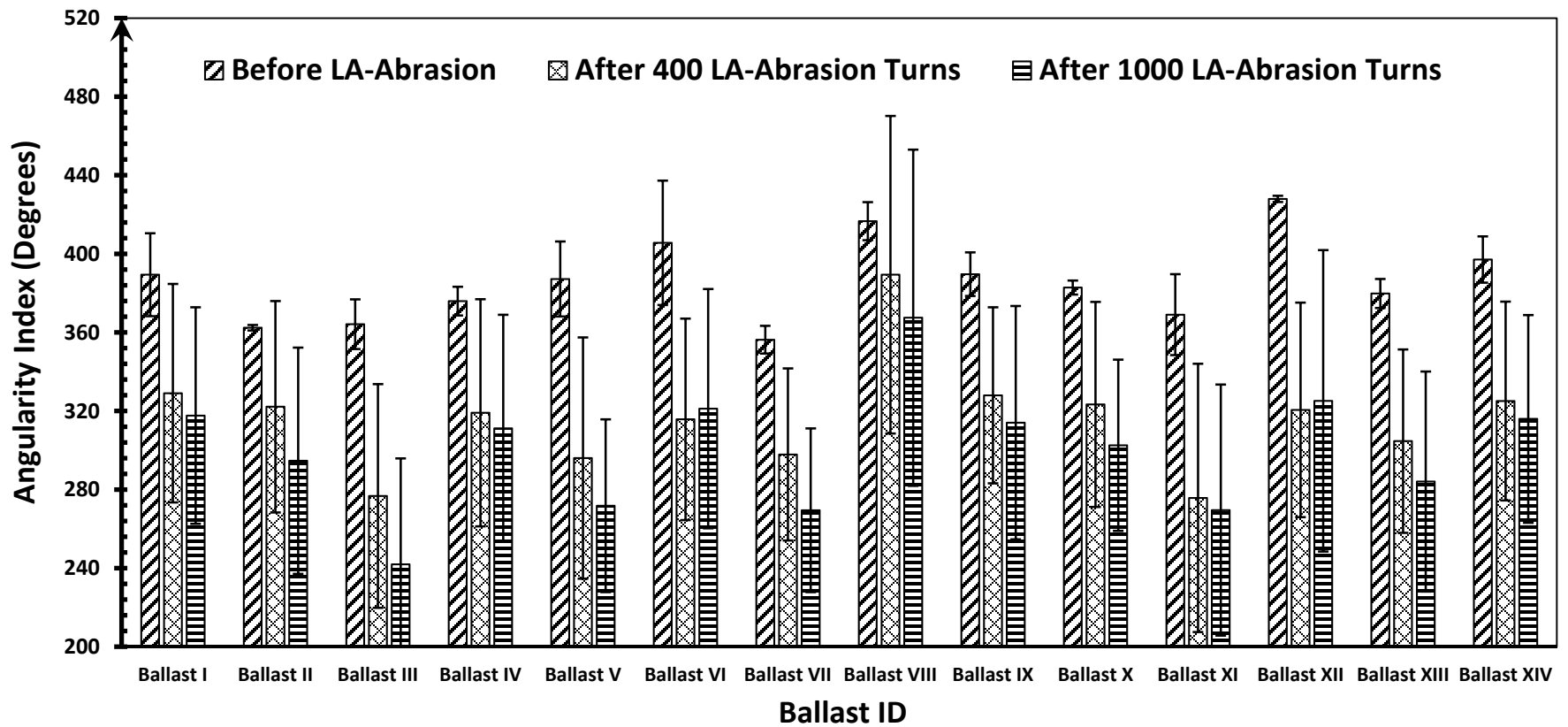
Figure 4.27 Average Angularity Index Values Before and After LA-Abrasion Testing for 14 Ballast Sources
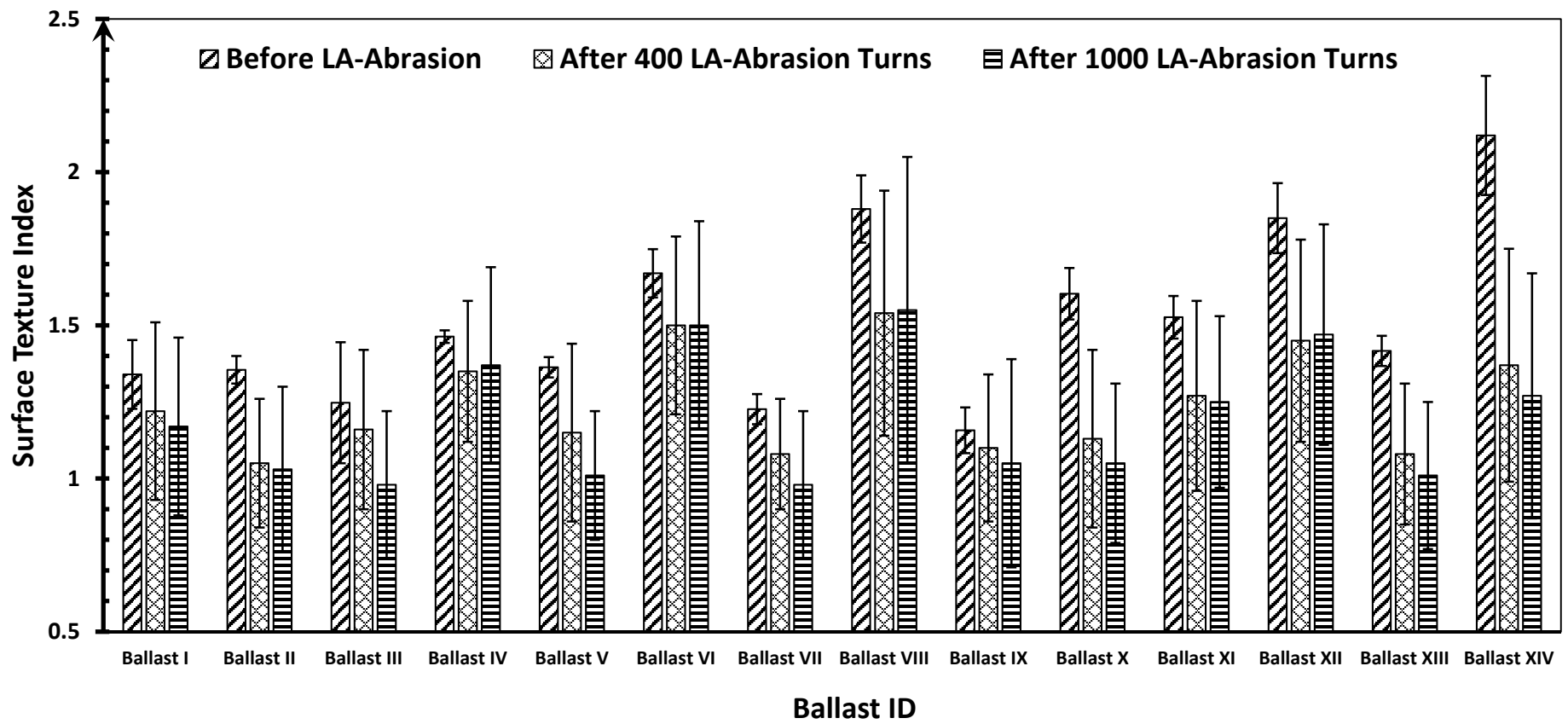
Figure 4.28 Average Surface Texture Index Values Before and After LA-Abrasion Testing for 14 Ballast Sources
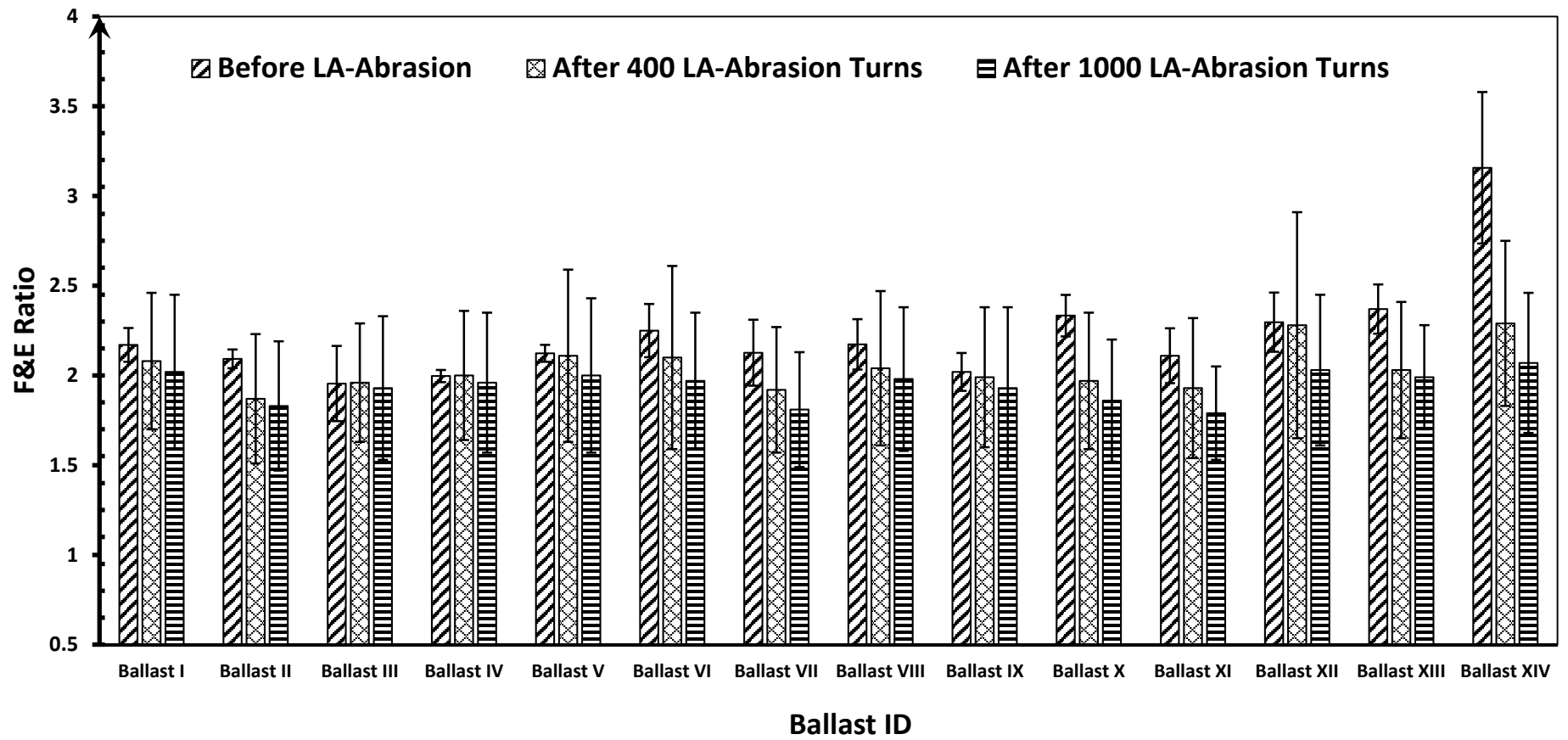
129

Figure 4.29 Average F&E Ratios Before and After LA-Abrasion Testing for 14 Ballast Sources

Table 4.7 Model Parameters for AI and STI Exponential Three Parameter Fitted Curves

Ballast ID	AI Degradation Model $AI = a + b \times e^{(c \times N)}$			STI Degradation Models $STI = a + b \times e^{(c \times N)}$		
	a	b	c	a	b	c
Ballast I	316.85	72.549	-0.004447	1.157	0.182	-0.002678
Ballast II	277.882	84.55	-0.001615	1.029	0.325	-0.006933
Ballast III	233.892	130.307	-0.002777	0.807	0.439	-0.000938
Ballast IV	310.825	64.141	-0.005158	1.36	0.103	-0.288839
Ballast V	268.772	118.461	-0.003667	0.931	0.432	-0.001701
Ballast VI	318.5	87.166	-0.290742	1.499	0.17	-0.020236
Ballast VII	260.278	96.055	-0.002343	0.919	0.307	-0.00162
Ballast VIII	348.411	68.221	-0.001274	1.545	0.335	-14.13891
Ballast IX	312.745	76.912	-0.004046	0.997	0.16	-0.001111
Ballast X	298.66	84.206	-0.003062	1.044	0.558	-0.004704
Ballast XI	269.499	99.566	-0.006901	1.249	0.277	-0.006521
Ballast XII	322.9	105.1	-0.065076	1.46	0.39	-0.112095
Ballast XIII	281.423	98.442	-0.003605	1.003	0.412	-0.00423
Ballast XIV	315.624	81.508	-0.00538	1.265	0.854	-0.005254

4.2.4 Classification of Ballast Sources by Imaging Results and LA-Abrasion Testing

Considering the LA-Abrasion and imaging results obtained by E-UIAIA, the ballast sources were classified into different zones in terms of their resistance to breakage, abrasion and polishing. The results of this classification are presented in Figures 4.30 and 4.31. According to Figure 4.30, it was observed that ballast sources I, IV, VI, VIII and XIV belong to low breakage and low abrasion zone while ballast sources VII, XI and ballast XIII were classified as sources with high breakage and high abrasion susceptibility. Similarly, Figure 4.31 shows that ballast I, III, IV, VI, VIII, IX and XII were classified as sources with low breakage and low polishing tendency while ballast sources VII, XI and XIII showed high breakage and high polishing susceptibility. Note that according to Table 4.4, the mineralogy of the majority of these fourteen ballast sources was identified as trap rock. Thus, it is interesting that the imaging based classification method could successfully differentiate ballast sources according to mineralogical origins. Those that were not trap rock, e.g., ballast sources VII, XI and XIII, were classified into separate zones. Figures 4.30 and 4.31 indicate that imaging results combined with LA-Abrasion testing can be used to better characterize the degradation behavior of different railroad ballast materials.
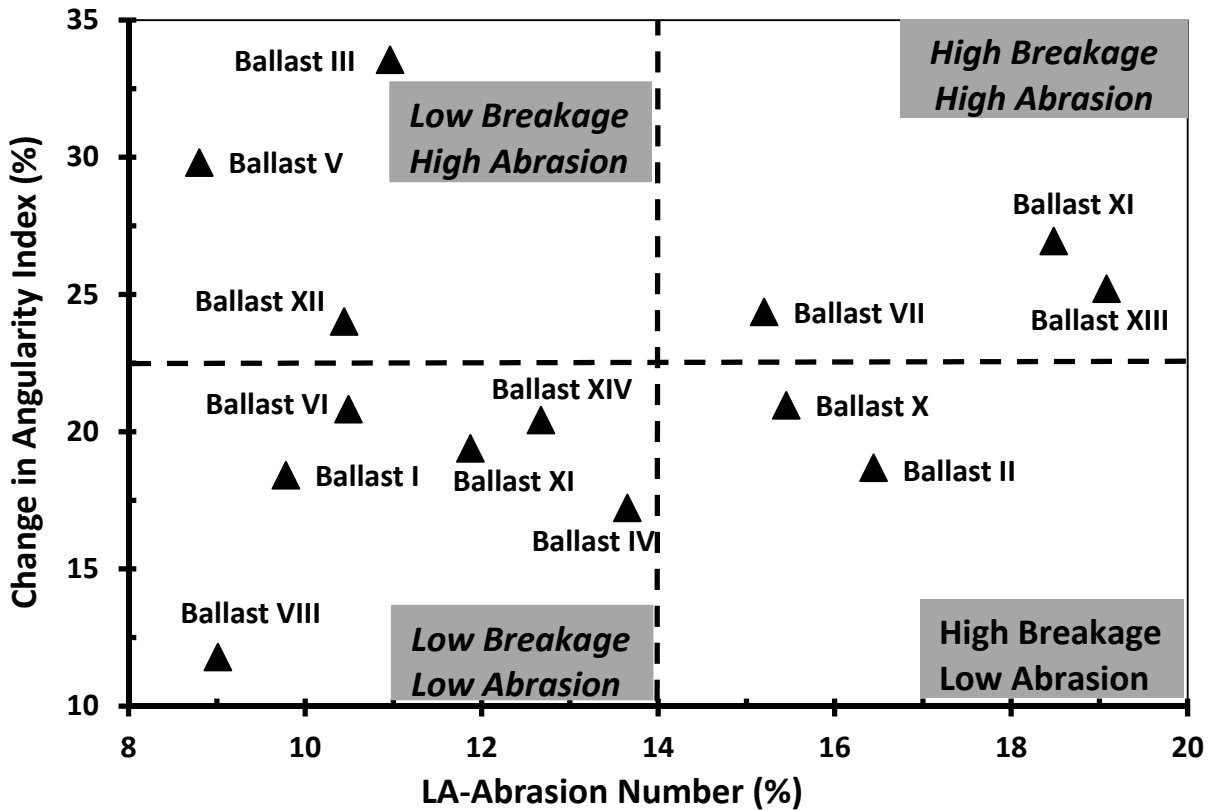
Figure 4.30 Angularity Classification of Ballast Sources Considering their Resistance to Breakage and Abrasion

4.3 Summary

In this chapter, the applicability of E-UIAIA in identifying the key shape indices for AI, STI and F&E Ratio of several railroad ballast materials was investigated. Additionally, the E-UIAIA was used to capture the degradation patterns in terms of changes in particle shapes caused by LA-Abrasion testing. The findings presented in this chapter showed that the changes in rate and magnitudes of shape properties of ballast particles can be adequately captured by an imaging-based approach. These imaging based shape indices combined with LA-Abrasion test results can be considered as an efficient alternative to measure the resistance of aggregate sources to degradation. Using the proposed approach described in this chapter, the aggregate sources were classified into different categories based on their resistance to breakage, abrasion and polishing.
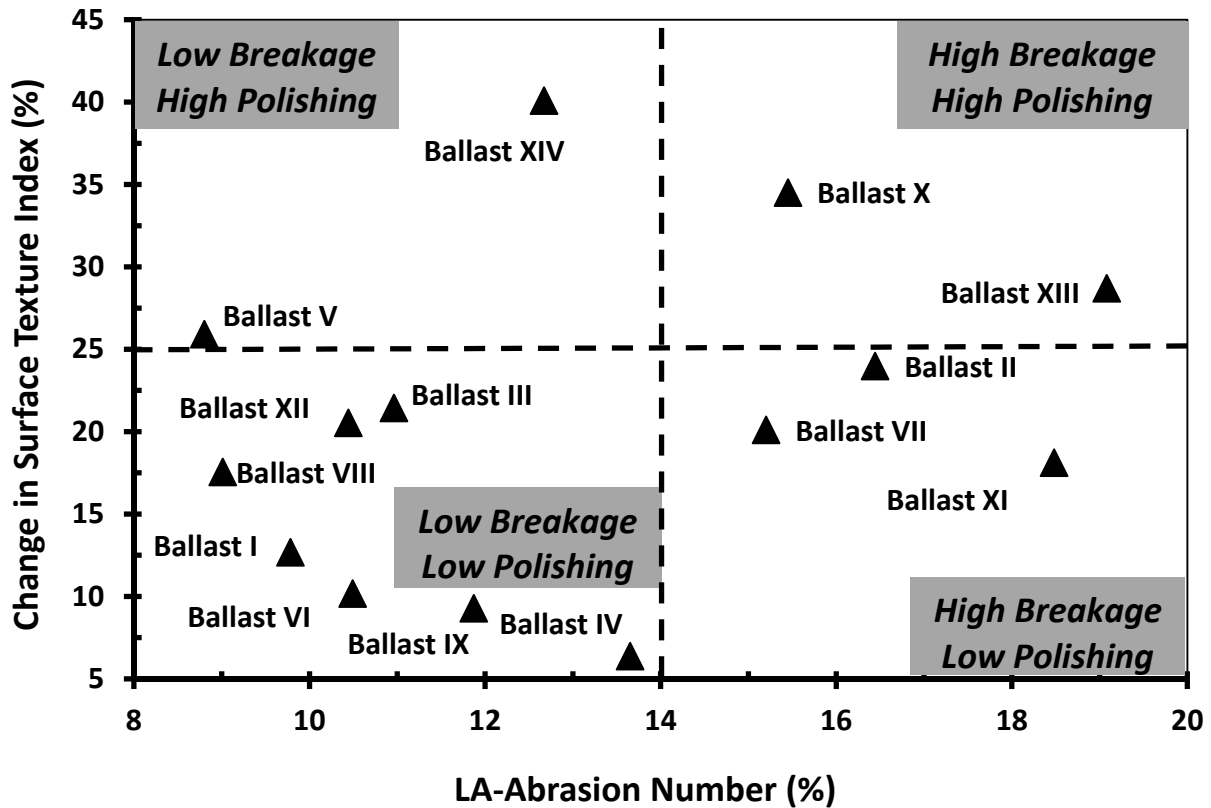
Figure 4.31 Surface Texture Classification of Ballast Sources Considering their Resistance to Breakage and Polishing

Nonlinear regression based three-parameter exponential models were developed and calibrated with full data sets as well as 3 data points obtained from LA-Abrasion testing. These models could capture reasonably well the degradation behavior of ballast sources in terms of their resistance to breakage, abrasion and polishing forces. This approach can be considered as a quality control based aggregate testing methodology to classify railroad ballast materials according to their degradation potentials.

CHAPTER 5:

PERFORMANCE OF E-UIAIA IN EVALUATING DEGRADATION OF HIGHWAY AGGREGATES USING MICRO-DEVAL TESTING[2]

5.1 Introduction

Under repeated traffic loading, aggregate particles in pavement courses are routinely subjected to degradation through attrition, impact, grinding and polishing type mechanisms, which result in altering their shape and size properties. The objective of this chapter is to demonstrate the effectiveness and applicability of implementing two advanced aggregate imaging systems, Enhanced University of Illinois Aggregate Image Analyzer (E-UIAIA) and second generation of Aggregate Imaging System (AIMS-II), in capturing changes in shape and size properties of aggregate particles caused by the breakage, abrasion and polishing actions. Micro-Deval (MD) apparatus was used in the laboratory to evaluate such field degradation/polishing resistance of eleven aggregate materials with different mineralogical properties collected from throughout the state of Illinois and neighboring states. These aggregate sources were commonly used in pavement construction as HMA surface friction courses.

The first research task established an aggregate database to include the initial size and shape properties of aggregates. Then, the magnitudes and rates of change in shape and

---

size properties caused by MD degradation were measured at different time intervals changing from 15 to 210 minutes. The second part is focused on a statistical evaluation of the results to develop prediction models for describing the degradation behavior of individual aggregate sources in terms of loss in AI and STI. Furthermore, material weight loss at different MD time intervals are also correlated with the percentage of change in shape properties in order to verify the applicability of imaging based methods in characterizing the resistance of aggregates to degradation.

5.2 Sample Preparation and Micro-Deval Testing Procedure

The aggregate materials were selected from a wide range of mineralogical properties and sampled from various quarries in different geographical regions in the state of Illinois and neighboring states. All the aggregate materials were washed, oven dried and sieved to obtain the particle sizes passing the ½ in. (12.5 mm) sieve and retained on the 3/8 in. (9.5 mm) sieve. Table 5.1 lists the types, designations and specific gravities of all aggregate materials tested.

Table 5.1 Aggregate Material Types, Designation and Geology

Aggregate ID	Aggregate Description	Geology	Specific Gravity* (Gs)
FP1	Limestone	Pennsylvanian/Bond/Millersvillle	2.695
FP2	Limestone	Mississippian/Salem	2.671
FP3	Limestone	Ordivician/Galena	2.629
FP4	Silurian Dolomite (reef formation)	Silurian/Racine	2.681
FP5	Silurian Dolomite	Silurian/Racine/Joliet	2.628
FP6	Crushed Gravel	Henry Formation, Wisconsinin Glacial Till	2.628
FP7	Chert Gravel	Maramec River Gravel, 99% Chert	2.500
FP8	Steel Slag	Steel Slag	3.448
FP9	ACBF Slag	Air-Cooled Blast Furnace Slag	2.403
FP10	Quartzite	Lower Proterozoic Quartzite (Baraboo Formation)	2.604
FP11	Sandstone	Mississippian/Rosiclare Sandstone	2.636
*Note: Specific gravity test was performed based on ASTM C127			

Aggregate resistance to degradation was measured based on the following steps:

1) Initial measurements of aggregate shape and size properties – Before Micro-Deval (BMD);
2) Filling the MD drum with 750 grams of aggregate materials;
3) Placing 5,000 grams of 9.5 mm diameter steel balls and 2 liters of water in the drum;
4) Subjecting the aggregate samples to the following target degradation times: 15, 30, 45, 60, 75, 90, 105, 180, and 210 minutes;
5) Washing the sample retaining on No. 16 (1.19 mm) sieve size and removing the steel balls;
6) Oven drying sample and checking gradation using sieves: No. 16 (1.19 mm), No. 8 (2.38 mm), No. 4 (4.76 mm), 3/8 in. (9.5 mm), ½ in. (12.7 mm);
7) Recording aggregate shape properties associated with each degradation time for the portion retained on 3/8 in. (9.5 mm) – After Micro-Deval (AMD).

Multiple aggregate samples from each source were used at different degradation times as opposed to using the same sample. Previous research by Mahmoud et al. [95] has shown the important effect of using single versus multiple aggregate samples. It was concluded that the two procedures would yield similar results. Additionally, using multiple aggregate samples ensures that consistent conditions in terms of initial gradation and aggregate weight would be followed for each set of MD tests.

5.3 Aggregate Image Acquisition and Processing

AIMS-II and E-UIAIA are the two advanced image analysis devices used in this chapter for measuring the morphological properties of aggregate particles at different MD stages. E-UIAIA and its associated aggregate image processing modules were described in detail in Chapters 2 and 3 of this dissertation. Additionally, a brief introduction was provided in chapter 2 regarding the first and second generations of AIMS. The software component of

AIMS-II includes an image processing algorithm that can compute the AI, STI, and F&E Ratio as well as sphericity of aggregate particles. A short summary describing the calculation process of individual shape indices computed by AIMS-II is provided here. In total, more than 26,000 aggregate particles were scanned using both systems to compile and establish the shape property database. Table 5.2 lists the number of aggregate particles scanned at each stage of degradation time. Note that the number of particles decreases with an increase in the degradation time since only the particles retained on 3/8 in. (9.5 mm) were image analyzed after each MD time.

Table 5.2 Number of Aggregate Particles Scanned after Each MD Degradation Time

MD Time (min.)	Aggregate ID										
	FP1	FP2	FP3	FP4	FP5	FP6	FP7	FP8	FP9*	FP10	FP11
0	362	396	361	358	566	559	433	275	478	429	415
15	357	341	356	363	434	378	401	271	-	395	331
30	330	306	323	329	341	272	409	266	374	367	289
45	305	322	280	335	276	263	397	256	-	360	262
60	289	281	255	312	209	221	392	261	-	348	235
75	294	297	227	283	165	224	393	258	281	354	212
90	264	244	225	286	158	214	383	237	-	375	183
105	244	258	219	290	128	188	399	253	251	341	170
180	201	204	189	246	61	128	393	219	169	325	138
210	199	176	146	216	34	119	375	225	124	321	107
Total	2845	2825	2581	3018	2372	2566	3975	2521	1677	3615	2342
*Note: Not enough material was available to run MD @ 15, 45, 60, and 90 minutes											

5.3.1 Aggregate Image Processing with AIMS-II

AIMS-II device consists of a computer-automated system, which includes a circular measurement tray. It is equipped with top and back lightings as well as an auto-focus camera unit. Aggregates are positioned on top of a circular tray which is fixed in x and y directions and the tray rotates to bring the particles inside the field of view of the camera. First, the images of the particles are captured for AI measurement and also the location of the particles

are recorded. During the second rotation, the camera returns back to the recorded location of each aggregate and is focused on the centroid of the particles to capture the texture images at higher spatial resolution [43, 44].

(1) Flat and Elongated Ratio (F&E Ratio) and Sphericity

Projections of a particle placed on the lighting table are captured by the camera in AIMS-II and used to generate the binary image. Eigenvector analysis [96] on the binary images identifies the major and minor axes of the particle. The third dimension or depth of particle is measured by determining the distance between the camera's lens and surface of particle relative the original location of the camera. The image processing algorithm sorts the three dimensions and identifies the maximum, minimum and intermediate particle sizes. Sphericity can be computed using Equation 5.1 [97].

$$Sphericity = \sqrt[3]{\frac{d_s \times d_I}{d_L^2}} \qquad\qquad 5.1$$

where,

d_L = Longest dimension;

d_I = Intermediate dimension;

d_s = Shortest dimension.

(2) Angularity

Gradient method is used as the image processing technique for angularity measurements. The gradient method starts by calculating the inclination of gradient vectors on particle boundary points from the x-axis (horizontal axis in an image). The average change in the inclination of the gradient vectors is considered as an indicator of angularity and can be calculated using Equation 5.2 [97].

$$Angularity = \frac{1}{\frac{N}{3} - 1} \sum_{i=1}^{N-3} |\theta_i - \theta_{i+3}| \qquad\qquad 5.2$$

138

where subscript i denotes the ith point on the boundary of a particle and N is the total number of points on the boundary. The average rather than the summation is considered in Equation 5.2 so that the angularity calculation is not biased by particle size. The step size used in calculating gradients is 3 since it minimizes the effect of noise created during image acquisition on the results [43].

(3) Surface Texture

Aggregate surface texture is measured using the wavelet technique. Texture details are identified in the horizontal, vertical, and diagonal directions in three separate images. Finally, the texture index at the desired decomposition level is considered as the arithmetic mean of the squared values of the wavelet coefficients for all three directions. Equation 5.3 is used for texture analysis [43, 97].

$$Surface\,Texture = \frac{1}{3N}\sum_{i=1}^{3}\sum_{j=1}^{N}\left[D_{ij}(x,y)\right]^{2} \qquad 5.3$$

where,

N = number of wavelet decomposition coefficients;

i = 1, 2, 3 for the three directions of texture;

j = wavelet coefficient index; and

D = wavelet coefficient.

5.4 Imaging Based Shape Degradation Models and Regression Analysis

Figures 5.1 through 5.4 present the average angularity and surface texture deterioration curves measured with both systems for all eleven aggregate materials at different MD degradation times. It should be noted that AIMS-II measures the angularity and surface texture in the scale of 0 to 10,000 and 0 to 1,000, respectively. However, angularity index and surface texture index values computed with E-UIAIA vary within the ranges of 0 to 720 and 0 to 6, respectively.
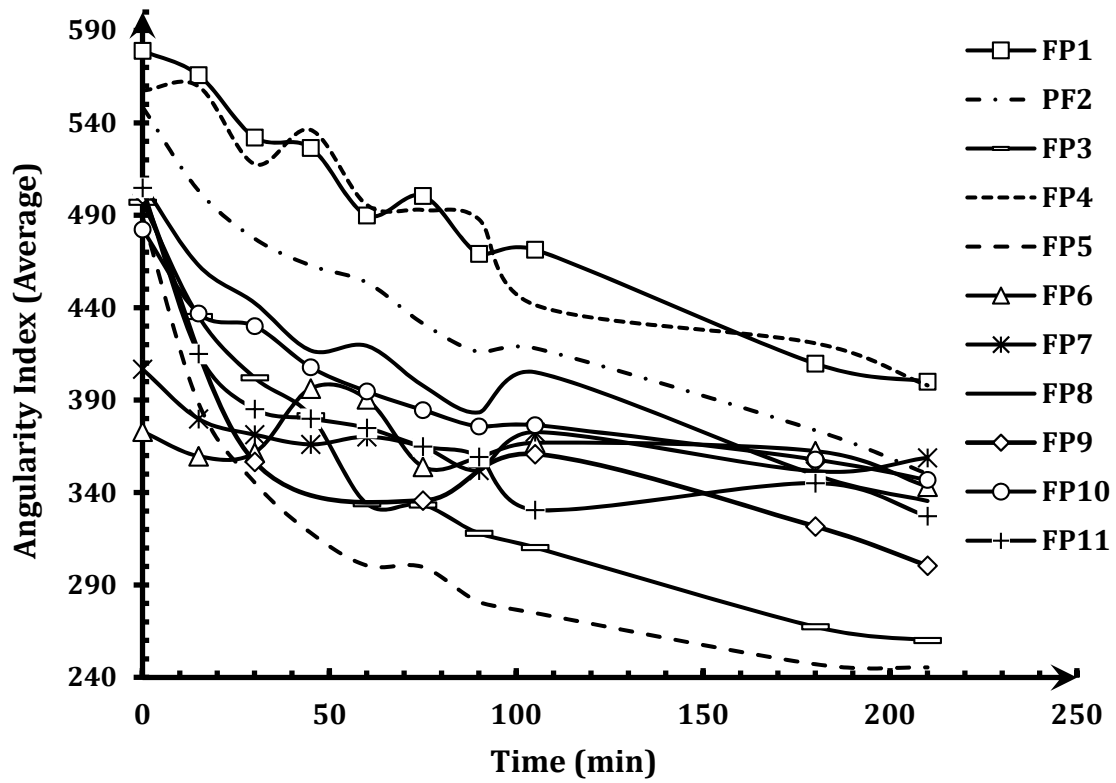
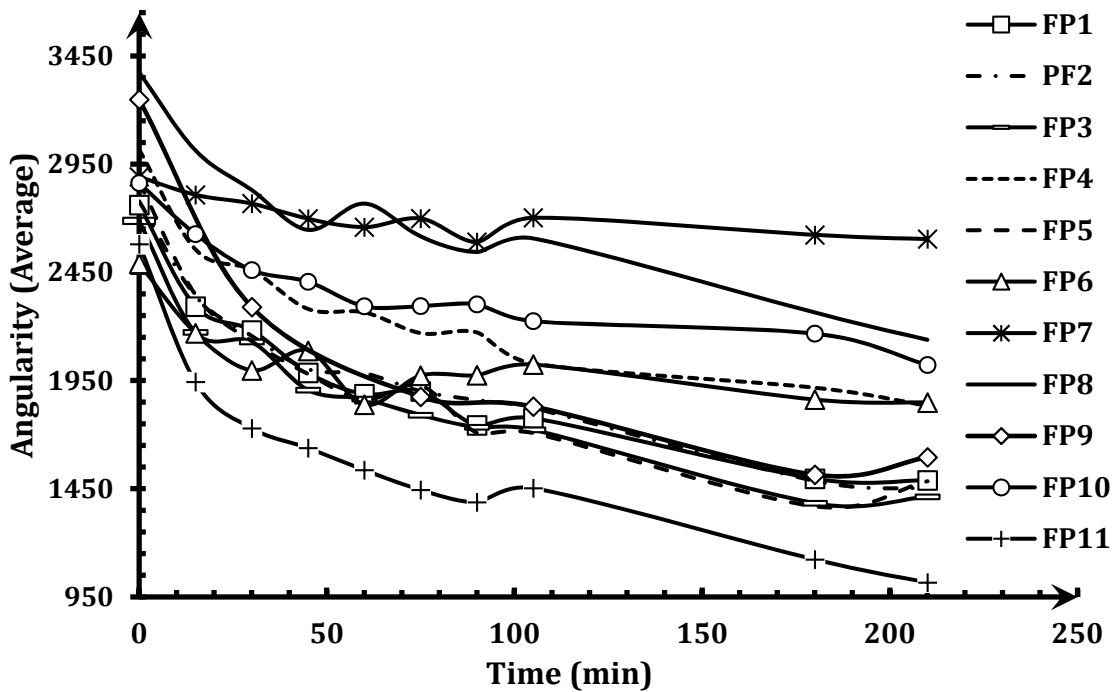Figure 5.1 Angularity Index with E-UIAIA at Different MD Degradation Times

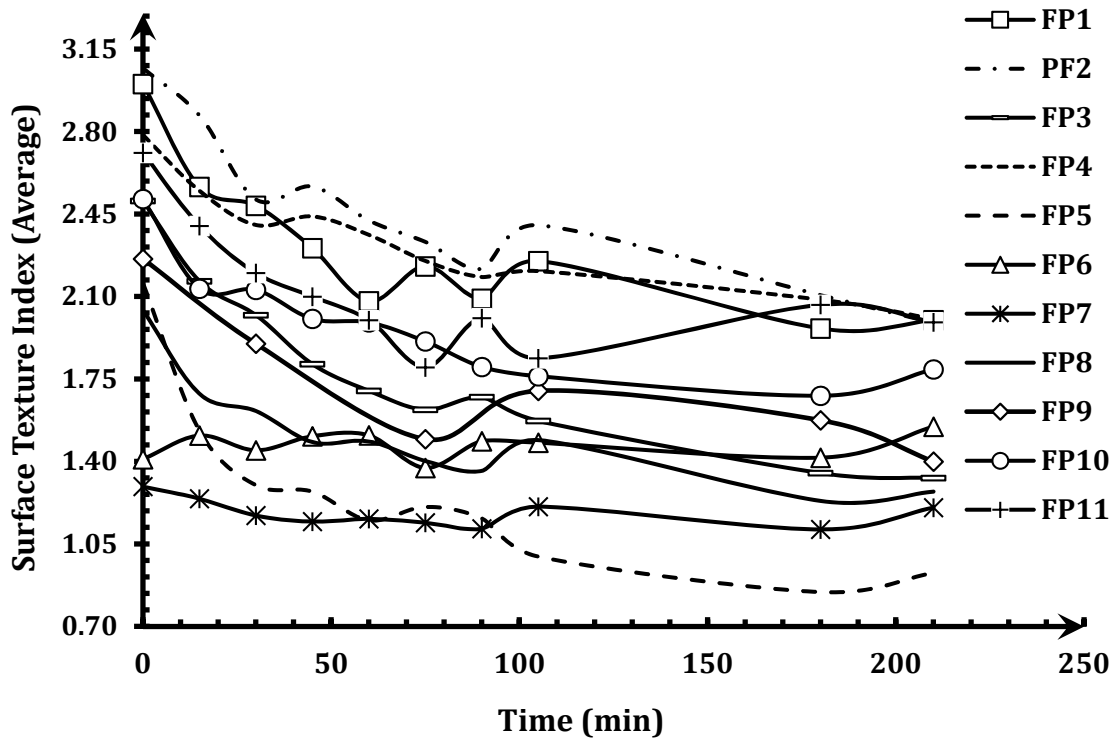Figure 5.2 Angularity Measurements with AIMS-II at Different MD Degradation Times

Figure 5.3 Surface Texture Index with E-UIAIA at Different MD Degradation Times
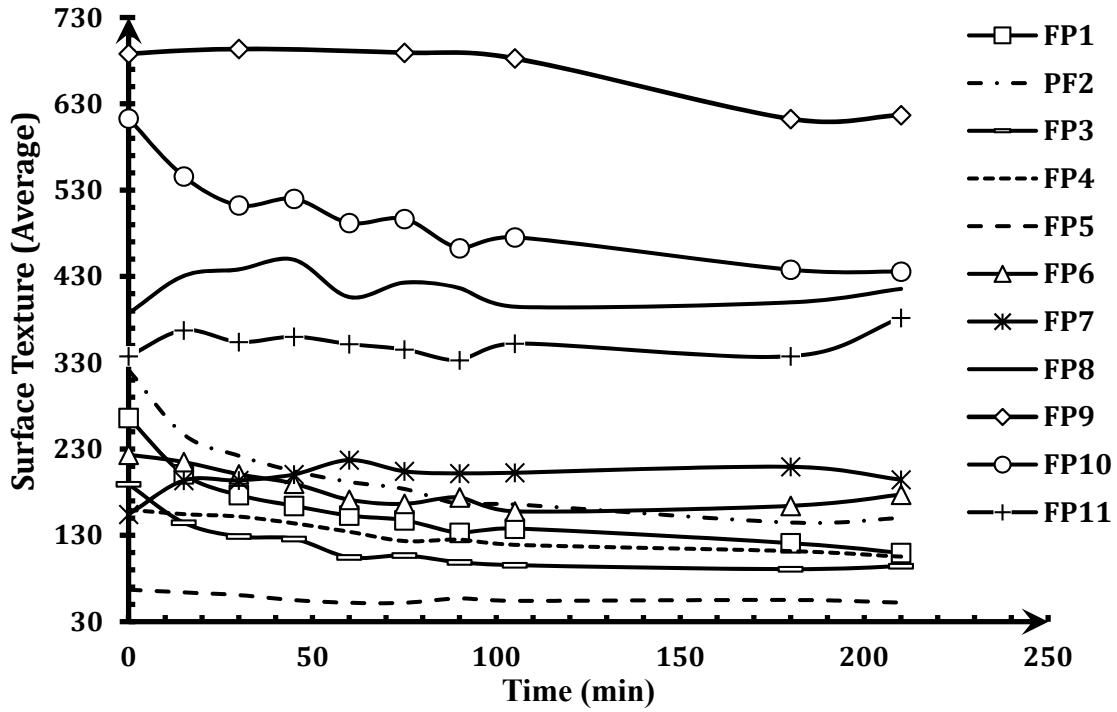

Figure 5.4 Surface Texture Measurements with AIMS-II at Different MD Degradation Times

141

Comparing angularity results determined from the two imaging systems in Figures 5.1 and 5.2, the overall trend of angularity decreasing with longer degradation time is indeed confirmed for all the aggregate sources. In general, the decrease rate in angularity slows down after 105 minutes degradation time. Both systems detected FP6 (crushed gravel) as the aggregate source with lowest initial angularity. However, AIMS-II reports FP8 as the most angular sample while E-UIAIA results show that FP1 has the highest initial angularity. Both systems detected fluctuating deterioration curve for FP6. This can be related to initially low angularity for this gravel source and increased angularity by the creation of sharp edges and corners after breakage during the MD process. In terms of angularity decrease rates, FP5 by E-UIAIA and FP9 by AIMS-II are the two aggregate materials that showed the most rapid decreases from 0 to 210 minutes of degradation.

Surface texture deterioration curves determined from the two imaging systems in Figures 5.3 and 5.4 also show a general initial decreasing trend for most of the aggregate sources. Overall, the rates of texture loss captured with both AIMS-II and E-UIAIA slow down significantly after 105 minutes of degradation time. FP2 detected by E-UIAIA and FP1 detected by AIMS-II are the aggregate sources with the highest initial surface texture. In general, more fluctuation is observed for the surface texture deterioration curves obtained from E-UIAIA. This can be related to the higher level of C.O.V (within laboratory) values in texture measurements in E-UIAIA in comparison to AIMS-II [44, 46]. According to AIMS-II results, FP8 and FP9 as steel slag aggregates do not lose texture overtime and tend to keep their initial texture. AIMS-II texture measurements more closely reflected historical data on aggregate frictional properties obtained by Illinois Department of Transportation (IDOT). Furthermore, FP7 or chert gravel was detected by E-UIAIA as an aggregate source with resistance to texture loss.

Figure 5.5 shows the F&E Ratio values at different degradation times quantified by E-UIAIA. It can be observed that F&E Ratio values for all the sources stayed within a constant range over time and different for most samples. The particle sizes are limited to one size in this study since the portion retained on the 3/8 in. (9.5 mm) sieve is separated and scanned after each MD time interval. Additionally, the abrasion and polishing rather than impact

142

forces are more intense during the MD process which results in less aggregate breakage. According to AIMS-II size measurements, the summation of percentage of particles that the ratio of their longest to shortest dimension are above 1:2 and 1:3 was recorded at a constant range between 45% to 75% for most of the aggregate sources after different MD time intervals.
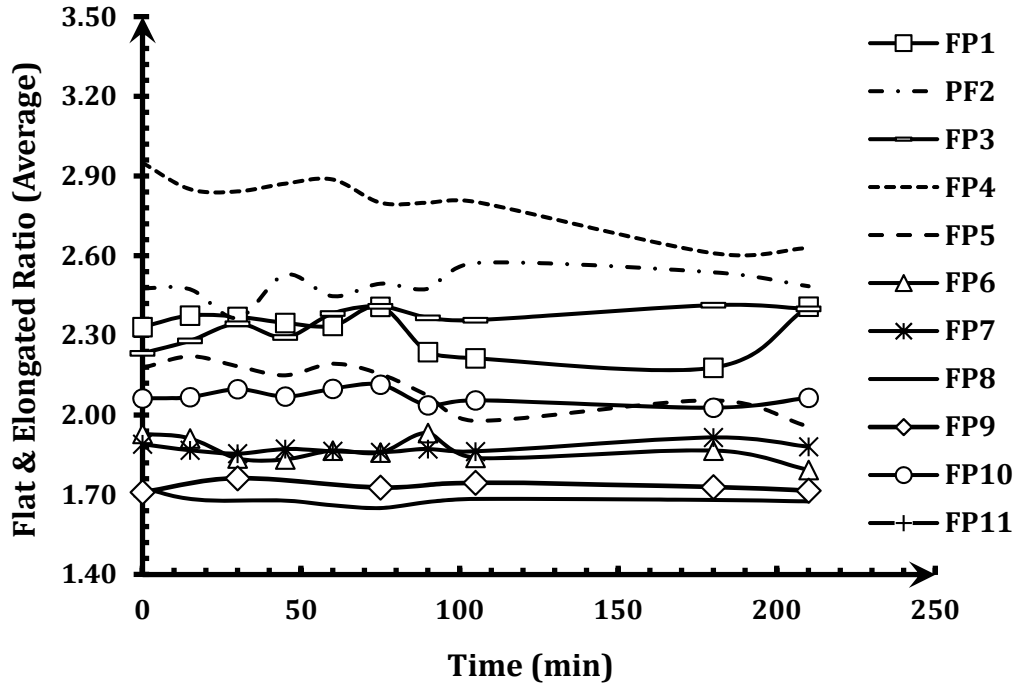

Figure 5.5 F&E Ratio Measurements with E-UIAIA at Different MD Degradation Times

Angularity and surface texture results quantified by the two imaging systems were used to calibrate a three-parameter exponential model given in Equation 5.4. Mahmoud et al. [95] showed that this type of an exponential expression was superior to other mathematical models in terms of describing the change in aggregate shape properties under MD degradation process.

$$Shape\ property\ (t) = a + b \times e^{-ct} \hspace{4cm} 5.4$$

where,

a, b, c = Model parameters related to initial and final values as well as rate of change in shape property;

t = Micro-Deval degradation time (minutes).

143

Standard Error of Estimates (SEE), coefficient of determination (R^2), and Root Mean Squared of Errors (RMSE) were also used to assess the accuracy of the three-parameter models in estimating the shape property. Tables 5.3 and 5.4 summarize the properties of the fitted models for the angularity loss for the two imaging systems E-UIAIA and AIMS-II, respectively.

Table 5.3 Angularity Loss Three parameters Exponential Model – E-UIAIA

Aggregate	Fitting parameters			Goodness of fit		
	a	b	c	SEE	R^2	RMSE
FP1	321.5	258.8	0.0057	8.61	0.98	9.2
FP2	329.9	208.4	0.0094	8.10	0.98	8.6
FP3	253.7	237.6	0.0152	7.94	0.99	8.5
FP4	278.9	286.4	0.0041	13.84	0.94	14.8
FP5	255.2	223.9	0.0276	10.96	0.98	137.2
FP6	371	-0.1	0.0265	14.47	0.28	15.5
FP7	360.2	45.1	0.0446	6.85	0.84	7.3
FP8	326.7	169.2	0.011	11.99	0.95	12.8
FP9	328.5	172.5	0.057	21.69	0.93	25.1
FP10	348.8	127.8	0.0169	5.61	0.98	6
FP11	343.1	153.8	0.037	13.53	0.94	14.4

Table 5.4 Angularity Loss Three-parameter Exponential Model – AIMS-II

Aggregate	Fitting parameters			Goodness of fit		
	a	b	c	SEE	R^2	RMSE
FP1	1492	1185	0.0174	72.73	0.968	77.7
FP2	1433	1232	0.014	86.24	0.957	92.2
FP3	1384	1189	0.0155	88.45	0.953	94.6
FP4	1877	1053	0.0185	71.69	0.962	76.6
FP5	1443	1331	0.0186	94.36	0.958	100.9
FP6	1924	560.6	0.0529	78.06	0.856	83.4
FP7	2618	274.4	0.0239	35.33	0.878	37.8
FP8	2112	1144	0.0114	103.00	0.924	110.1
FP9	1590	1635	0.0248	87.15	0.985	100.6
FP10	2098	730	0.019	52.53	0.957	56.2
FP11	1130	1323	0.0209	115.08	0.94	123

In general, the angularity loss models for both systems show high R^2 values in the range of 85% to 98%. Interestingly, the prediction model with the lowest R^2 values are for the FP6 aggregate source based on the measurements made with both systems. This can be related to the higher variability of particle shape or more breakage at different stages of MD degradation times. Surface texture loss model parameters are presented in Table 5.5 and 5.6.

Table 5.5 Surface Texture Loss Three-Parameter Exponential Model – E-UIAIA

Aggregate	Fitting parameters			Goodness of fit		
	a	b	c	SEE	R^2	RMSE
FP1	2.03	0.93	0.0285	0.092	0.92	0.098
FP2	2.02	1.01	0.0154	0.092	0.93	0.098
FP3	1.32	1.14	0.017	0.052	0.98	0.056
FP4	2	0.73	0.014	0.049	0.96	0.052
FP5	0.98	1.1	0.034	0.102	0.93	0.012
FP6	1.46	1.6 e-145	-1.576	0.050	0.25	0.054
FP7	1.152	0.148	0.054	0.035	0.66	0.038
FP8	1.3	0.68	0.026	0.070	0.92	0.074
FP9	1.5	0.8	0.0237	0.114	0.9	0.132
FP10	1.72	0.73	0.022	0.064	0.94	0.069
FP11	1.93	0.79	0.04	0.092	0.9	0.098

Table 5.6 Surface Texture Loss Three-Parameter Exponential Model – AIMS-II

Aggregate	Fitting parameters			Goodness of fit		
	a	b	c	SEE	R^2	RMSE
FP1	120.8	137.6	0.0266	8.27	0.97	8.8
FP2	151.1	162.1	0.0256	7.91	0.98	8.5
FP3	93.27	92.7	0.0304	4.88	0.98	5.2
FP4	97.16	65.95	0.0095	3.58	0.97	3.8
FP5	53.34	14.83	0.0341	2.32	0.83	2.5
FP6	164.7	64.5	0.0256	8.15	0.88	8.7
FP7	204.1	-49.39	0.0866	6.77	0.86	7.2
FP8	437.7	-16.49	-0.003	20.27	0.06	21.7
FP9	659.1	29.18	0.9935	40.63	0.1	46.9
FP10	436.8	161.8	0.0176	13.65	0.94	14.6
FP11	353.8	-16.31	2.413	15.02	0.12	16.1

The goodness of fit indicators for the two imaging systems are also included in the tables. The surface texture loss models based on the results from both systems show good R^2 values. The E-UIAIA prediction model for FP6 has the lowest R^2 value of 0.25 due to changes in gravel from smooth to rough texture due to breakage (see Table 5.5).

In addition, the models for FP8, FP9 and FP11 also have low R^2 values according to AIMS-II results (see Table 5.6). It should be noted that FP8 and FP9 are steel slag type aggregate and did not show texture loss behavior with AIMS-II. One possible reason for disagreement between the two systems regarding the texture loss behavior for these two types of steel slag can be related to the different texture definitions and methodologies used for image processing.

5.5 Aggregate Classification using Imaging and Micro-Deval Loss

Figures 5.6 to 5.9 show the percent changes in angularity and surface texture values measured with both systems against MD weight loss (passing No.16 sieve) after 105 minutes. These plots can be used to distinguish the effect of abrasion and polishing forces as well as impact, which result in the breakage of particles. The samples are classified into different categories in terms of level of resistance to abrasion, polishing and breakage. According to Figure 5.6 and Figure 5.8, AIMS-II and E-UIAIA systems have categorized FP3, FP5, FP9 and FP11 as the aggregate sources with high abrasion and high breakage characteristics. Interestingly, both imaging systems suggest FP6 with high breakage and low abrasion tendency. Moreover, both systems agree that FP7, FP8, and FP10 are in the region of low abrasion and low breakage. The rest of the samples are in the low breakage zone but at different abrasion zones associated with each system.

Based on Figure 5.7 and Figure 5.9, AIMS-II and E-UIAIA have differentiated the aggregate sources in terms of their polishing and breakage tendency but not in the same regions. Note that according to AIMS-II, the aggregate sources including FP7 and FP11 not only did not lose texture but also gained texture even at low breakage zones. The increase in FP7 texture is due to the removal of surficial polished layer within the first 15 minutes of MD polishing (see Figure 5.4) after which the surface texture was almost constant.
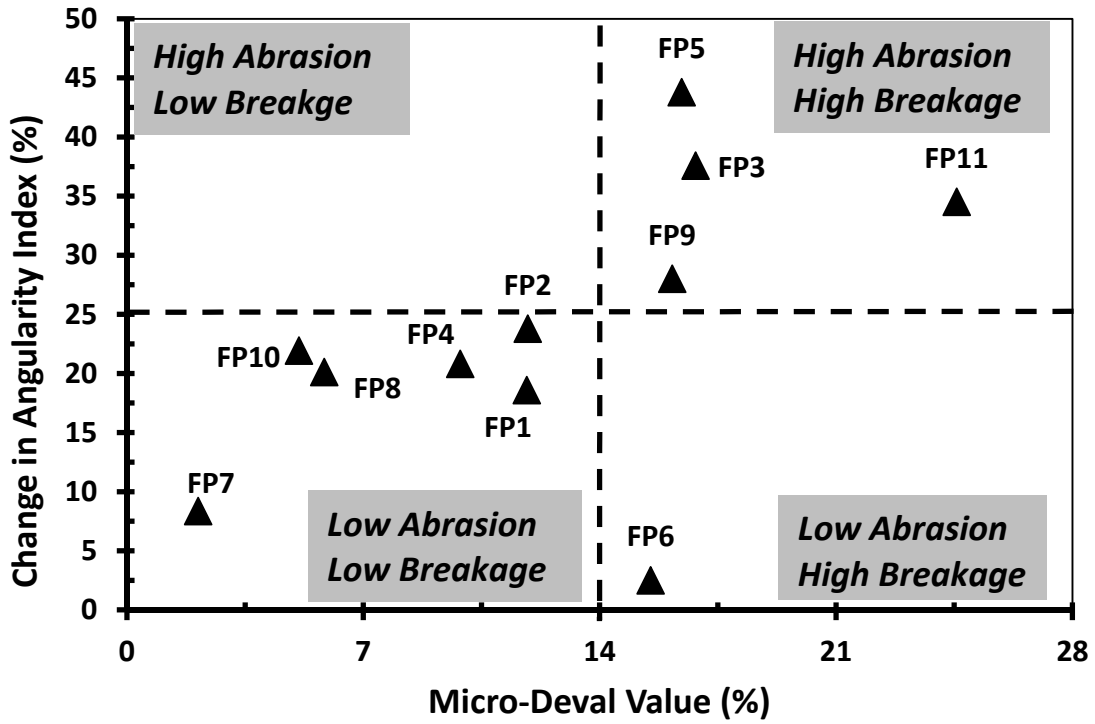
146

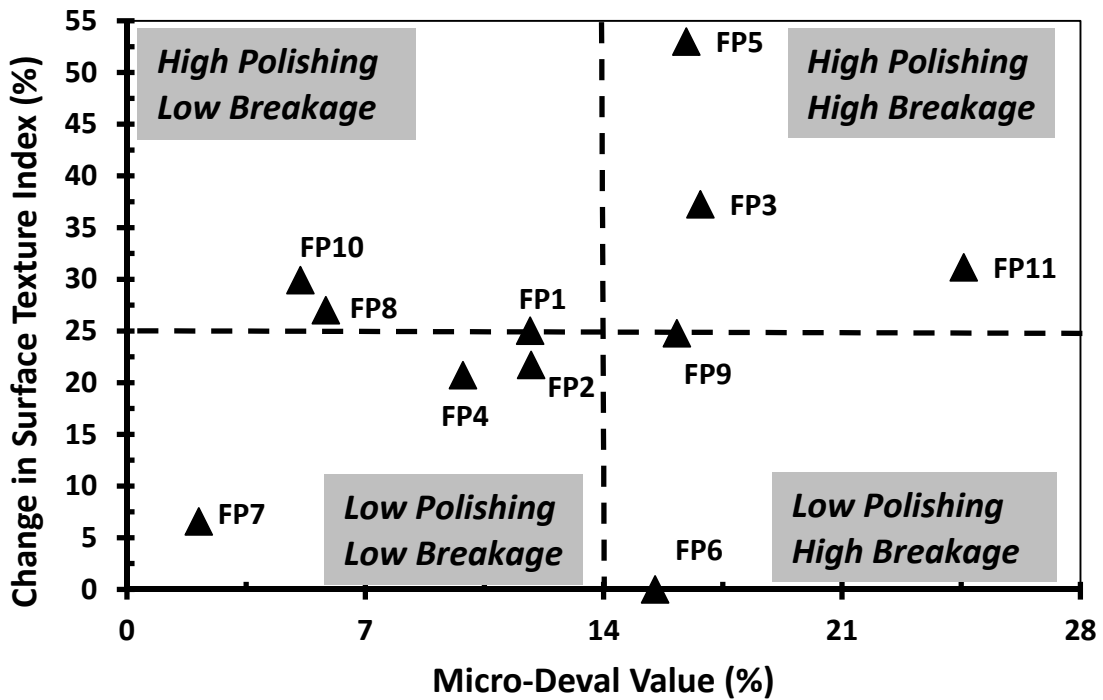Figure 5.6 Change in Angularity Index versus Micro-Deval Value (E-UIAIA)

Figure 5.7 Change in Surface Texture Index versus Micro-Deval Value (E-UIAIA)
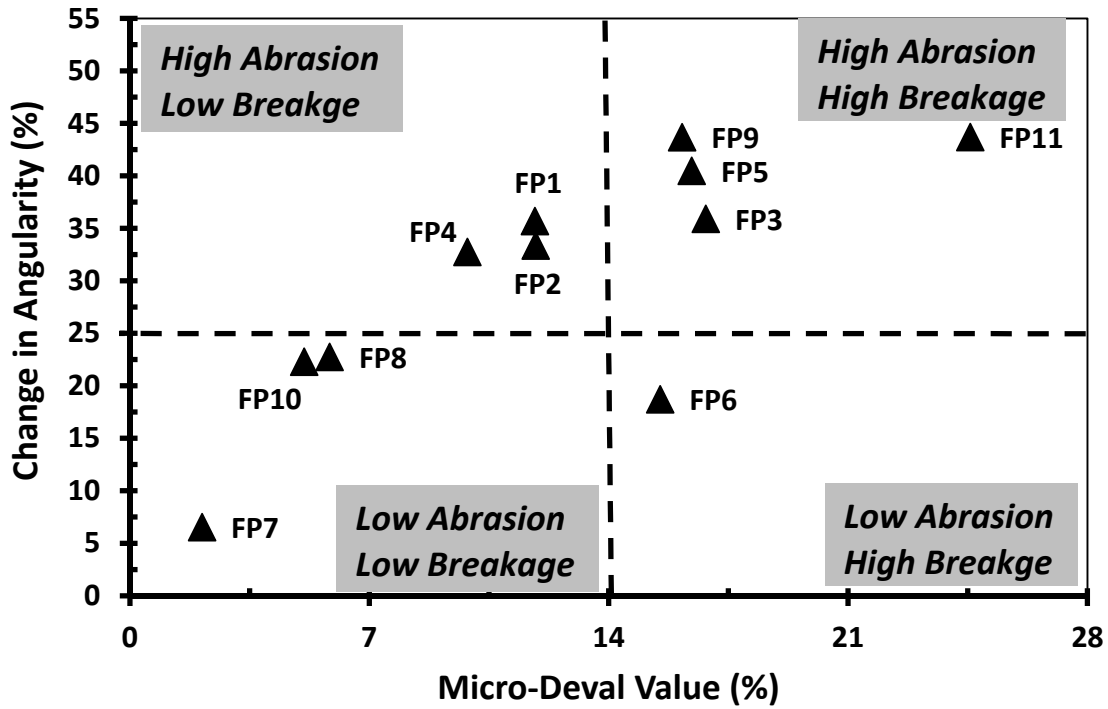
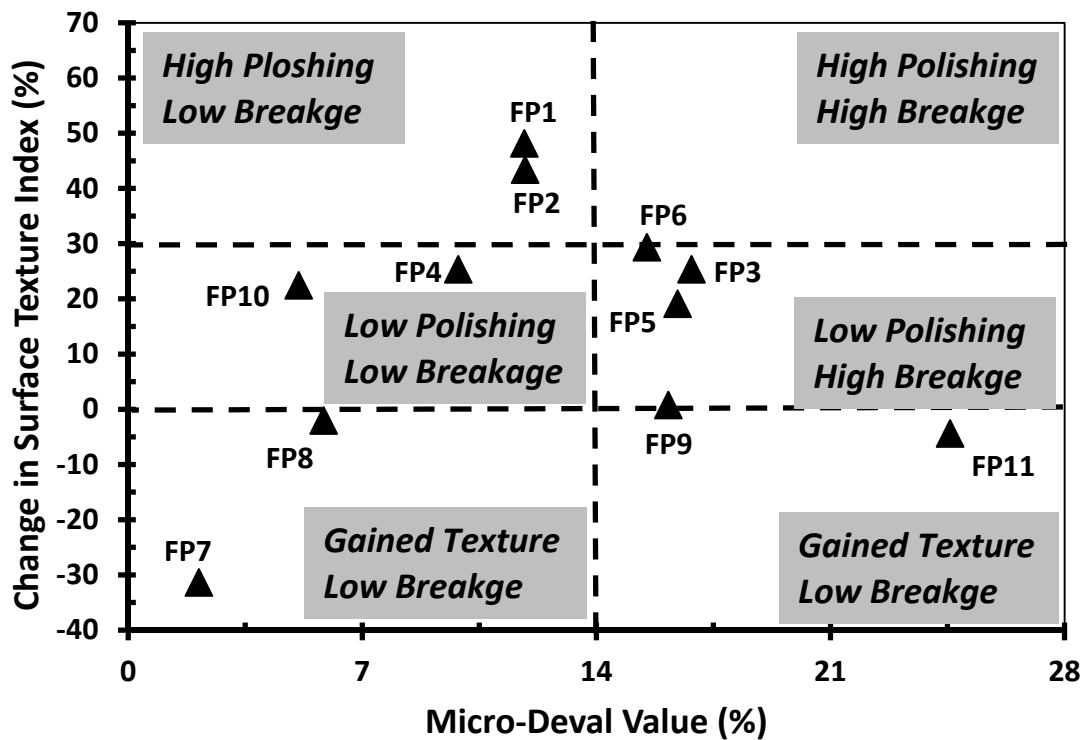Figure 5.8 Change in Angularity versus Micro-Deval Value (AIMS-II)

Figure 5.9 Change in Surface Texture versus Micro-Deval Value (AIMS-II)

Note that FP11 is a sandstone which continuously exposes new textured surface with polishing. Confirming with the surface texture deterioration curves in Figure 5.4, FP8 and FP9 do not loose texture in both high and low breakage zones.

5.6 Summary

In this chapter the feasibility and applicability of two advanced imaging systems, AIMS-II and E-UIAIA, to characterize the degradation behavior of aggregates from the perspective of change in shape properties was investigated. Both imaging systems were able to successfully identify aggregate shape property deterioration curves for angularity index, surface texture index and flat and elongated ratio with longer Micro-Deval (MD) degradation time. When these shape property losses were fitted to a three parameter exponential model, individual models developed for eleven aggregate materials achieved high values of coefficient of determination. These imaging based model parameters have the potential to be used for predicting the aggregate shape degradation behavior when a desired level of angularity or surface texture is required for field application.

The MD weight loss values were combined with the imaging based shape property results to evaluate the tendency to breakage, polishing and abrasion. The two systems similarly classified eleven types of aggregates into four categories in terms of resistance to breakage and abrasion. Considering the different texture definitions and image processing methods used in AIMS-II and E-UIAIA, classification for resistance to breakage and polishing based on surface texture values resulted in two different outcomes each associated with one imaging system. However, both systems were able to successfully differentiate between the aggregate sources and categorize them into separate regions based on their tendency to polishing and breakage.

CHAPTER 6:

CHARACTERIZATION OF SHAPE AND ASPHALT COATING
IN RECLAIMED ASPHALT PAVEMENT USING E-UIAIA[3]

6.1 Introduction

Considering limited sources of virgin aggregates and asphalt binder and the ever increasing material and construction costs, the utilization of Reclaimed Asphalt Pavement (RAP) as a recycled alternative in sustainable construction of highway pavements has increased significantly during the last two decades [98, 99, 100]. RAP is acquired through milling and processing deteriorated asphalt pavement layers. RAP particles can be agglomerations of smaller aggregates and binder and larger aggregates that are partially-coated with asphalt. RAP materials can be reused as recycled aggregates in unbound aggregate base/subbase layers [101]; new pavement layers consist of hot and warm mix asphalt [102] as well as concrete mixtures [103, 104, 105].

The common methods to produce RAP include hot recycling at the asphalt plant, hot in-place recycling, cold in-place recycling and full depth reclamation [106, 107, 108]. Milling machines scratch the pavement with milling teeth mounted on a drum and this impact tears and crushes the pavement layer into smaller size particles which creates uncoated surfaces around individual particles. RAP materials extracted from the roadway possess different properties corresponding to the source and type of virgin aggregate, binder content and the Performance Grade (PG) of the binder. RAP aggregates may have different particle shape

properties and asphalt coating percentages also depending on the crushing, fractionation and pulverizing processes.

According to NCHRP 452 report [109], the binder content and physical properties of RAP aggregates including the size distribution and particle shape, texture and angularity, need to be determined for their proper use in the desired mixture design. These factors also control the performance of RAP in terms of stiffness, crack resistance, modulus and deformation characteristics. When used in asphalt pavements, the aged binder in RAP can cause pavement cracking failure because of the increased stiffness and viscosity of the binder and decreased ductility [98]. This general expected increase in stiffness can lead to conservative design practices in terms of selection of costlier and softer asphalt binder grades and/or limiting the RAP content in a mixture [110]. When RAP contributes with a higher percentage of asphalt content than target designed value in the mix, it causes higher total achieved asphalt content in the mixture. Therefore, the mixture becomes soft and is prone to higher plastic deformation [99]. Conversely, if RAP contributes less asphalt than expected to the mixture, the final mix will have lower total asphalt content value which eventually makes the pavement susceptible to cracking, raveling and moisture damages [111]. Incorporation of RAP into cement-based materials alters the interface between cement matrix and RAP thereby affecting the bonding [105]. However, Huang et al. [112, 113] state that this asphalt coated aggregate might be useful in resisting the crack propagation along the interface which allows more energy to be dissipated. Recently, this finding has been confirmed by Brand et al. [103]

As clearly substantiated through the reviewed literature, accurate determination of asphalt coating percentages on the RAP particles is both needed as a quality indicator and at the same time, for the sustainable utilization of various RAP sources. Several standard methods such as centrifuge, vacuum or reflux extractor are currently used to measure the asphalt content in RAP (ASTM D6847, AASHTO T164). However, these techniques are time consuming, require expensive equipment and the solvents or chemicals used in the process can be hazardous to both the environment and the operators [114]. Additionally, the asphalt content values in RAP may not necessarily be an accurate representation of the existing

asphalt coating and film thickness on individual particles. The coating on RAP particles is a function of asphalt absorption by aggregate, particle size and shape, methods of milling/crushing during RAP production and resistance of virgin aggregate to breakage and/or degradation. A close look at the literature shows that limited research exists related to characterization of RAP particles in terms of particle shapes and the effect of asphalt coating on changing the shape properties. This can possibly be related to the lack of a standard procedure that can objectively and reliably quantify the shape properties of RAP particles rapidly and accurately.

This chapter describes the application of advanced image processing methods to determine asphalt coating percentage on RAP particles and investigates the changes in RAP aggregate size and shape properties influenced by the asphalt coating. The Enhanced University of Illinois Aggregate Image Analyzer (E-UIAIA) and its improved imaging-based shape and size indices, including Angularity Index (AI), Surface Texture Index (STI), Flat and Elongated Ratio (F&E Ratio) and Volume (V) are applied to characterize the morphological properties of RAP aggregates from six sources obtained from pavement surface courses in northern Illinois. Binary images of RAP materials generated by the E-UIAIA are used to develop an innovative computational algorithm to estimate the amount of asphalt coating on each RAP particle.

6.2 Objective and Scope

The primary objective of the research described in this chapter is developing a robust and accurate image processing algorithm to quantify the asphalt coating percentage on RAP particles. A combination of image processing and enhancement techniques, including histogram-based image thresholding, binary image morphology and arithmetic image operation are used to segment the asphalt coating from the RAP images captured by the E-UIAIA. The E-UIAIA is first used to determine the imaging-based size and shape indices of RAP aggregates from six sources in order to evaluate the influence of asphalt coating in altering these morphological properties. The imaging-based estimations of asphalt coating are then linked to the asphalt contents of RAP sources determined by the asphalt extraction method. Additionally, the total fracture energies of several concrete specimens made from

blending of these RAP sources and virgin aggregates are correlated to the imaging-based asphalt coating measurements.

6.3 Sample Preparation and RAP Image Acquisition

Six different RAP sources were used, all of which were obtained from highway pavement surface courses in northern Illinois. The pertinent details of the RAP sources and their properties are summarized in Table 6.1.

Table 6.1 Description and Properties of Six Illinois RAP Sources

	RAP 1	RAP 2	RAP 3	RAP 4	RAP 5	RAP 6
Aggregate Source Type	Dolomite			Dolomite and Steel Furnace Slag (SFS)		
RAP Description	Washed "clean" coarse fractionated RAP with few fines	Fractionated RAP with higher fines content		Fractionated RAP consisting of approximately one-third dolomite, one-third SFS, and one-third manufactured sand aggregates		
Initial Asphalt Content	5.4%	N/A	N/A	5.6%	5.4%	5.4%
Initial Asphalt Grade	PG 70-22	N/A	N/A	PG 76-22	PG 76-22	PG 76-22
RAP Asphalt Content	2.1%	3.3%	3.8%	3.6%	3.8%	3.9%
RAP Asphalt Grade	PG 88-22	N/A	N/A	PG 76*	PG 76*	PG 82-22

*Low temperature grade not determined

These RAP sources contained either dolomite or combination of dolomite and Steel Furnace Slag (SFS) aggregates. Additional details regarding these RAP sources can be found elsewhere [103, 104, 105]. While centrifuge extraction is more suitable and efficient for asphalt content determination, a rotary evaporator (ASTM D5404 and ASTM D6847) was used since it is more effective for asphalt extraction and binder characterization for its performance grade. The Dynamic Shear Rheometer (DSR) was used for the high temperature viscosity and elastic behavior of the binder (AASHTO T315) while the Bending Beam Rheometer (BBR) test was used to measure the low temperature stiffness and relaxation properties of the binder for low temperature cracking susceptibility (AASHTO T313). Since

the binder was already aged in the field, neither the Rolling Thin-Film Oven (RTFO) nor the Pressure Aging Vessel (PAV) was used for binder aging.

Table 6.2 lists the percent passing sieve sizes of the RAP aggregates from six sources. The majority of the particles from these sources were between 1/4 in. (6.35 mm) and 1/2 in. (12.5 mm) in size. Therefore, approximately 55 to 60 particles between these two sizes were randomly selected from each RAP source to be used in image acquisition stage (see Figure 6.1). Preliminary visual inspection of the particles, shown in Figure 6.1, revealed that in RAP 5 and 6 sources the asphalt coating coverages were in general higher when compared to RAP 1 and 2 sources. This observation will be verified later in this chapter using the developed imaging based approach.

Table 6.2 Particle Size Distributions of RAP Aggregates from Six Sources

Sieve Size	Percent Passing (%)					
	RAP 1	RAP 2	RAP 3	RAP 4	RAP 5	RAP 6
1 in. (25mm)	100.0	100.0	100.0	100.0	100.0	100.0
3/4 in. (19mm)	99.9	100.0	100.0	100.0	100.0	100.0
5/8 in. (16mm)	N/A	N/A	100.0	100.0	99.9	100.0
1/2 in. (12.5mm)	78.4	99.3	65.0	99.9	97.9	99.3
3/8 in. (9.5mm)	37.9	86.3	25.2	83.7	83.4	88.3
1/4 in. (6.35mm)	N/A	N/A	14.5	38.3	39.8	60.2
No.4 (4.75mm)	3.6	21.9	8.3	13.3	14.5	39.6
No.8 (2.36mm)	1.6	5.5	3.0	3.9	6.9	12.2
No.16 (1.18mm)	1.1	2.8	1.5	2.8	6.1	6.5
No.30 (0.6mm)	0.8	1.9	1.0	2.5	5.7	5.2
No.50 (0.3mm)	0.6	1.3	0.7	2.2	4.4	4.2
No.100 (0.15mm)	0.3	0.7	0.3	1.7	2.7	2.3
No.200 (0.075mm)	0.1	0.3	0.1	0.8	0.6	0.4

Initially, the top camera in E-UIAIA was used to capture three images associated with three different faces of RAP particles Before Asphalt Extraction (BAE). The advanced color thresholding scheme that was fully described in chapter 3 was utilized to generate the binary images of the aggregate particles. Using the blue background, different types of aggregates with various natural colors can be scanned and analyzed with this system.
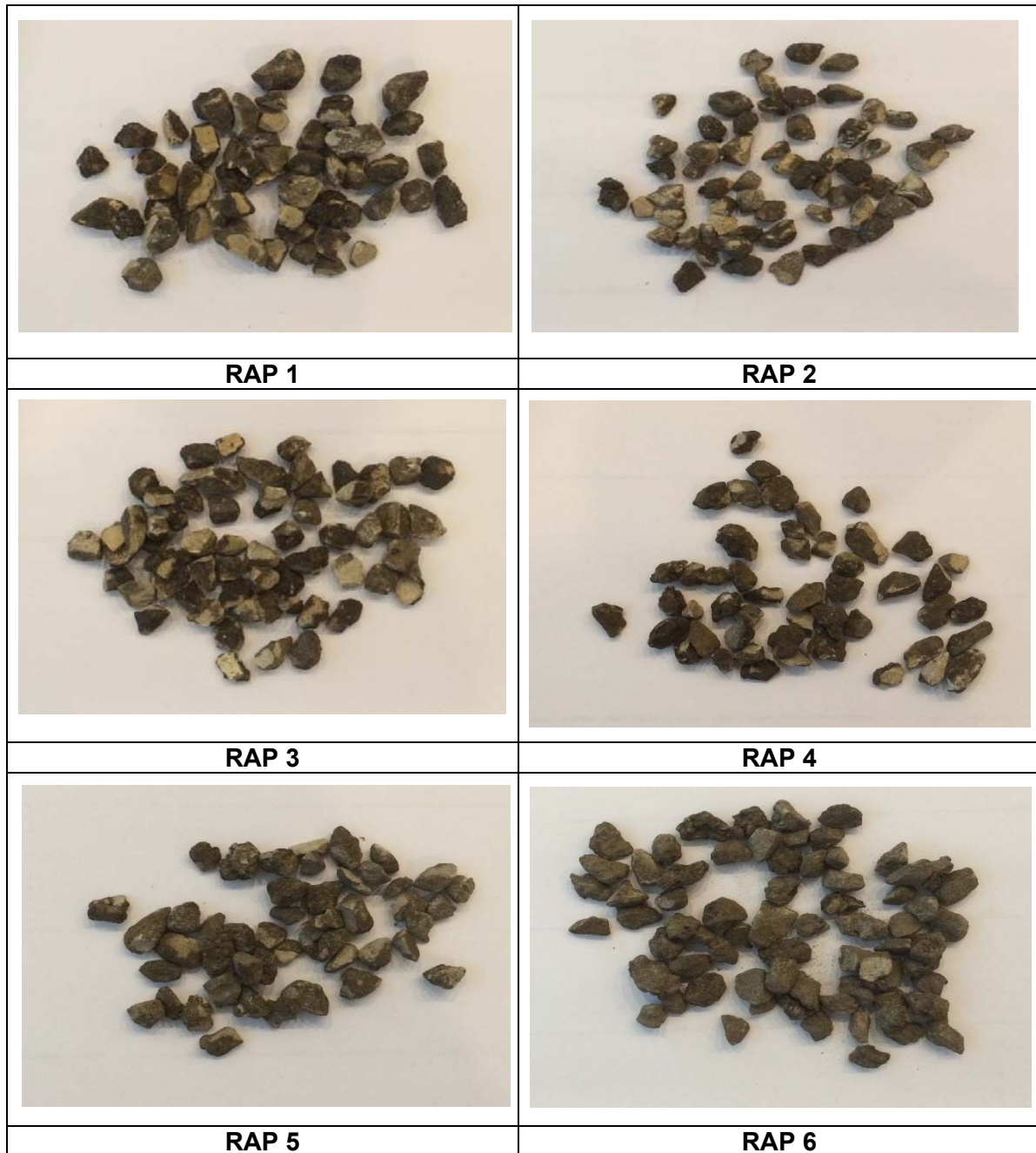
RAP 1	**RAP 2**
RAP 3	**RAP 4**
RAP 5	**RAP 6**

Figure 6.1 Particles from Six Sources of RAP Selected for Image Acquisition

Considering the size range of the RAP particles evaluated in this study, the E-UIAIA was calibrated at the spatial resolution of 330 pixels per inch (ppi) to acquire color RGB images with Portable Network Graphic (PNG) format. To study the effect of asphalt coating

155

on the size and shape properties of RAP aggregate particles, the asphalt binder was removed with methylene chloride from the particles that had been already scanned and examined. Finally, the image acquisition process was repeated on the RAP particles After Asphalt Extraction (AAE) to record the changes in the imaging based shape indices.

6.4 Description of Image Processing Procedure

As mentioned in chapter 3, one of the common challenges in segmenting an image into foreground and background is the determination of a proper threshold value. This happens when the background and the object have very similar pixel intensity values, which results in unimodal or multimodal shapes of image histograms [115]. Color plane decomposition into Hue (H), Saturation (S) and Intensity (I) channels is used in E-UIAIA to find the image representation with best contrast to facilitate the image thresholding.

After achieving the binary images of RAP, the imaging-based size and shape indices of the particles, including the average AI, STI, F&E Ratio and total volume, before and after asphalt extraction, were computed using their corresponding binary image processing modules incorporated in the E-UIAIA.

6.4.1 Image Processing Algorithm for Estimating Asphalt Coating in RAP

To segment the asphalt coating on RAP particles, a post image processing algorithm was developed in this chapter using the image processing toolkit available in MATLAB [116]. This algorithm initially calculates the mean of the corresponding grayscale version of each RAP image and applies it as a threshold value to detect the bright areas in the RAP image which is an indicator of "uncoated" regions of the particles. By subtracting this thresholded image from the binary image generated by the E-UIAIA and reducing the noises with binary morphological operators particularly "dilation" and "closing" [93], the coated areas of the RAP particles are segmented. Finally, the ratio of the coated surface area divided by the total surface area of RAP particle is then reported as the surface coating percentage. Figure 6.2 illustrates this procedure with an example of a RAP particle to demonstrate the methodology. (see Appendix D for further details)
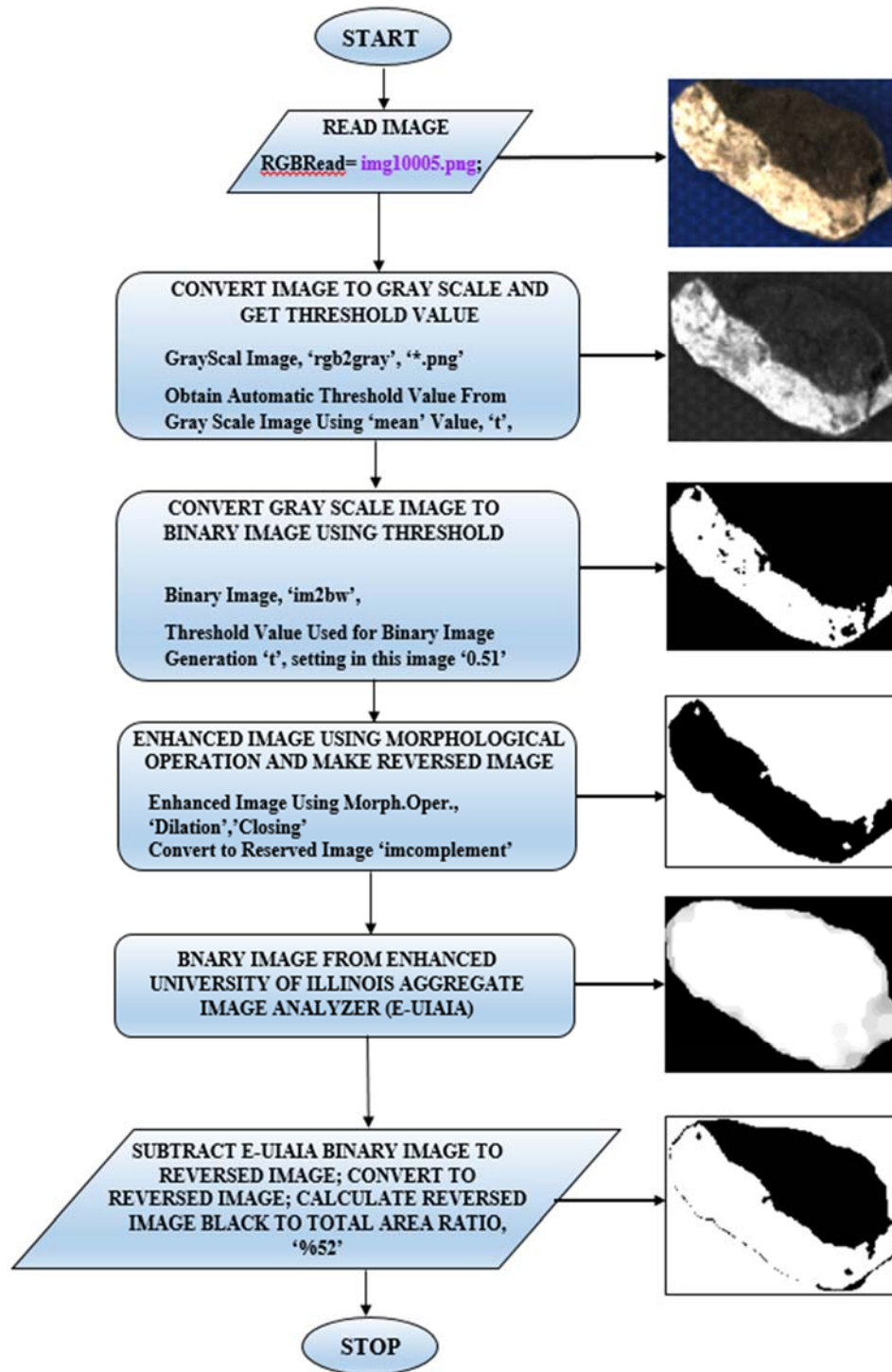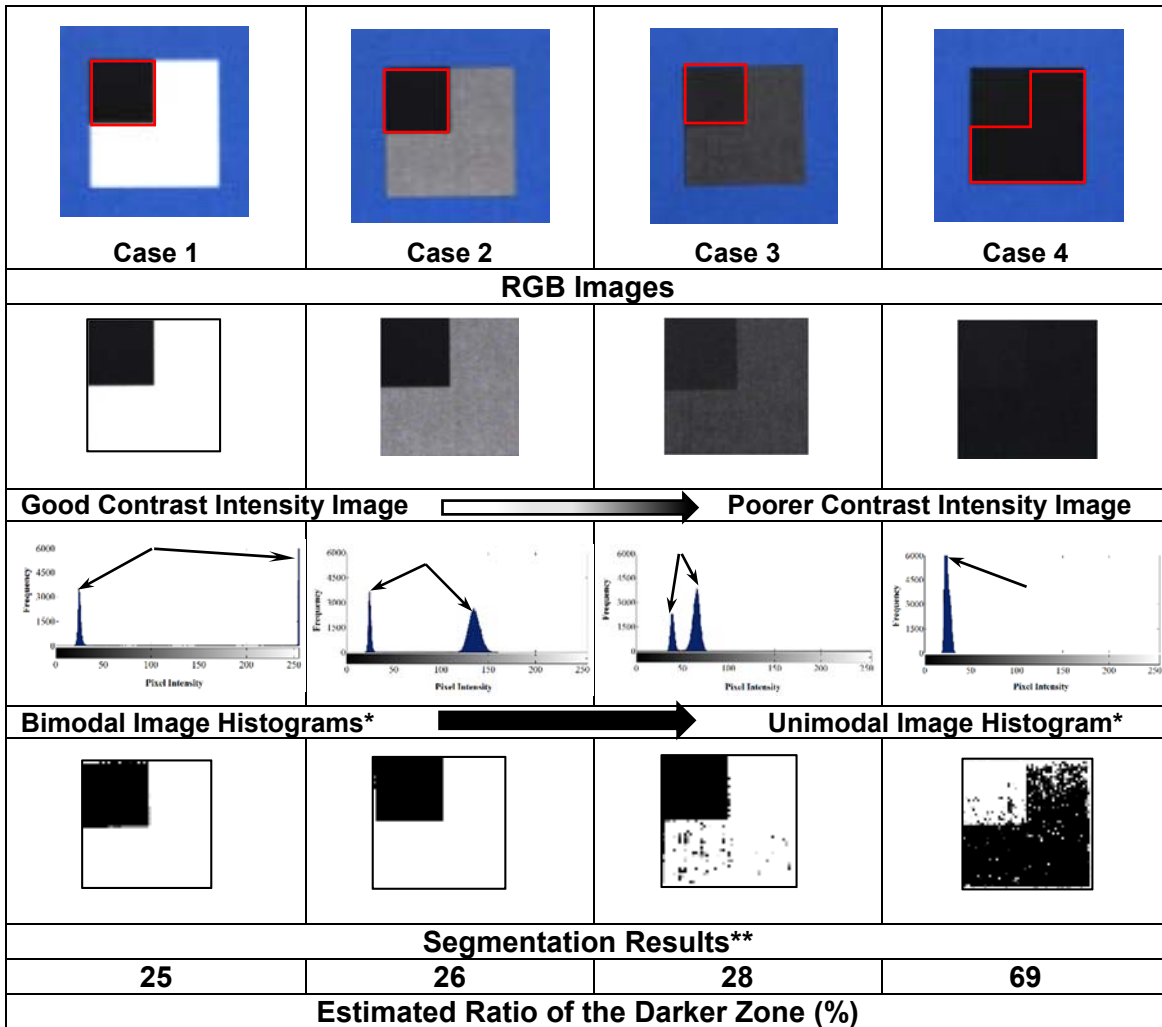
Figure 6.2 Flowchart of Algorithm Including MATLAB Commands and Numerical Output Values at Each Processing Step for Measuring Asphalt Coating on a RAP Particle

One of the original aggregate sources making up RAP 4, 5 and 6 sources, was SFS, which is typically darker in color than dolomite or limestone aggregates. Therefore, detecting the dark binder on these darker SFS RAP particles, where there is not necessarily sufficient contrast between the foreground and background, can be very challenging. Therefore, an experiment was conducted to evaluate the accuracy and robustness of the developed algorithm in terms of differentiating the asphalt binder from aggregates with different natural colors. As shown in Figure 6.3, several square shapes were prepared with certain known areas (25% for the first three squares and 75% for the last one) painted with darker color while assigning different gray shades to the remaining areas inside the squares. This method was used to validate the proposed method for segmentation and estimating the areas of the darker regions in the images. Figure 6.3 summarizes the results of this experiment as well as the image histograms corresponding to each image. The pixel intensity distribution plots show how the histograms change from a bi-modal shape in case of a high contrast image to a uni-modal shape for a poor contrast image. Accordingly, the error of the algorithm in terms of the level of noise in the binary images increased as the contrast level between the dark and bright zones in the image decreased. Aged asphalt binder might not be as dark or reflective as the fresh asphalt binder and for some sources of RAP the color of the aggregate can be even darker than the color of aged asphalt binder. Therefore, a preliminary visual inspection of the original aggregate source color of the RAP material is recommended prior to applying the proposed processing method. Nevertheless, the outcome of this experiment showed that the developed algorithm could estimate the areas of darker zones in all four images of square shapes with less than 10% error.

6.5 Imaging Results and Discussion

The average asphalt coating in percent and the imaging-based size and shape indices for the RAP aggregates from six sources are summarized in Figures 6.4 to 6.10 for the before (BAE) and after asphalt extraction (AAE) cases. The comparisons of the shape properties BAE and AAE results show that the asphalt coating caused an increase in the AI and STI of the particles and this effect on STI is more pronounced than on AI.

Case 1	Case 2	Case 3	Case 4
RGB Images			
Good Contrast Intensity Image ⟶		**Poorer Contrast Intensity Image**	
Bimodal Image Histograms* ⟶		**Unimodal Image Histogram***	
Segmentation Results**			
25	26	28	69
Estimated Ratio of the Darker Zone (%)			

*The arrows show each mode captured in image histogram.

**The red rectangles in images show the target darker zone.

Figure 6.3 Performance of the Algorithm for Detecting the Darker Zones - Different Cases Studied with Different Contrast Levels

This finding might be related to the shapes and thicknesses of agglomerations that are attached to RAP particles, which can create random sharper edges and rougher surface texture. The creation of the RAP particles through milling of the asphalt pavement likely contributed to the increased STI and AI. According to Figures 6.4 and 6.5, the recorded average AI varies from 407 to 444 and the average STI varies from 1.2 to 1.9 for the RAP particles from six sources BAE. These ranges more or less match the typical AI and STI values

159
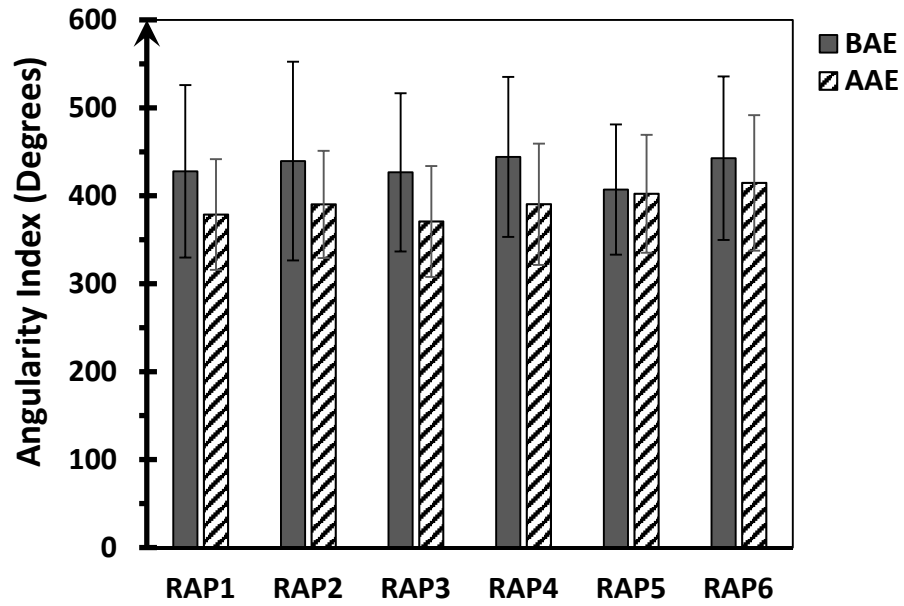
Figure 6.4 Average Angularity Index Before and After Asphalt Extraction
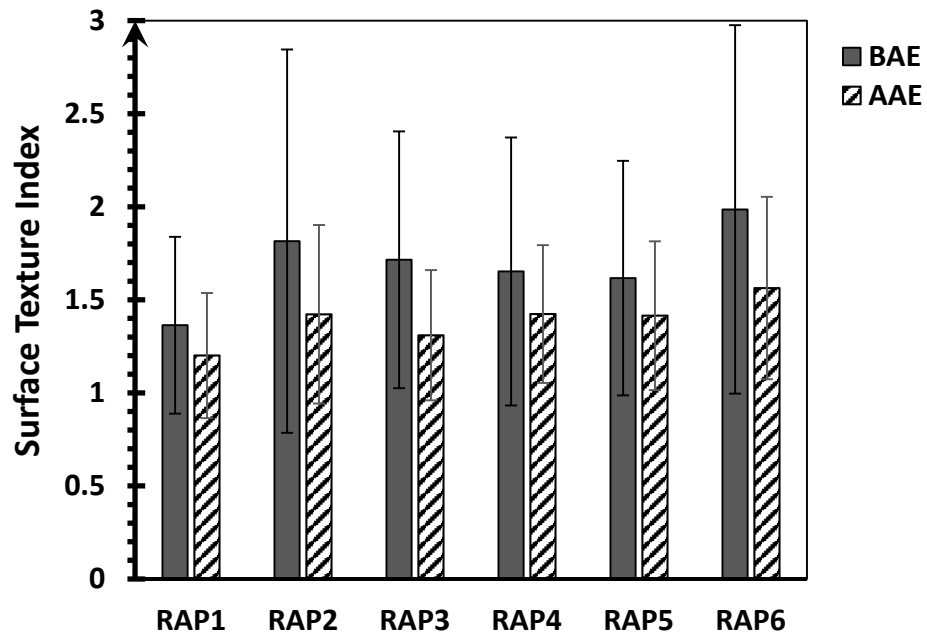
Figure 6.5 Average Surface Texture Index Before and After Asphalt Extraction
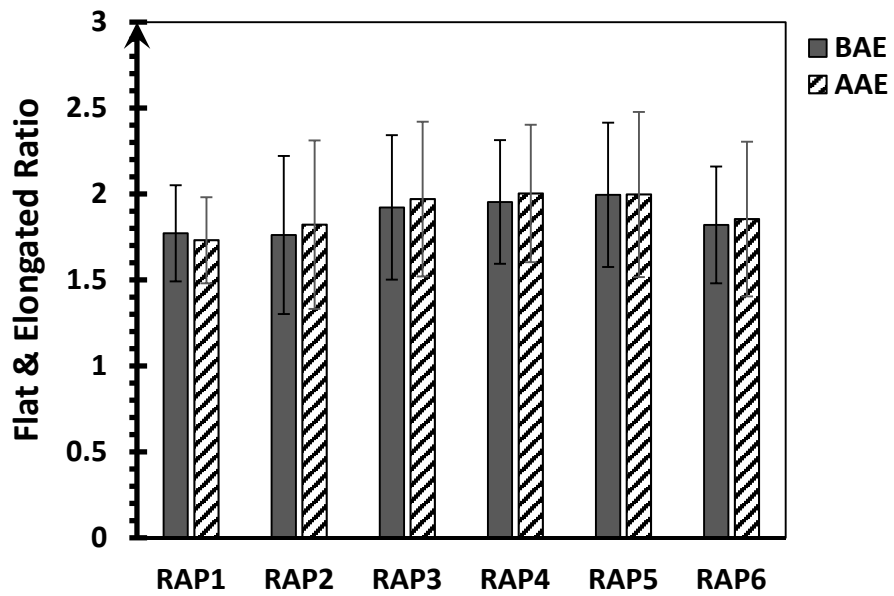
Figure 6.6 Average F&E Ratio Before and After Asphalt Extraction
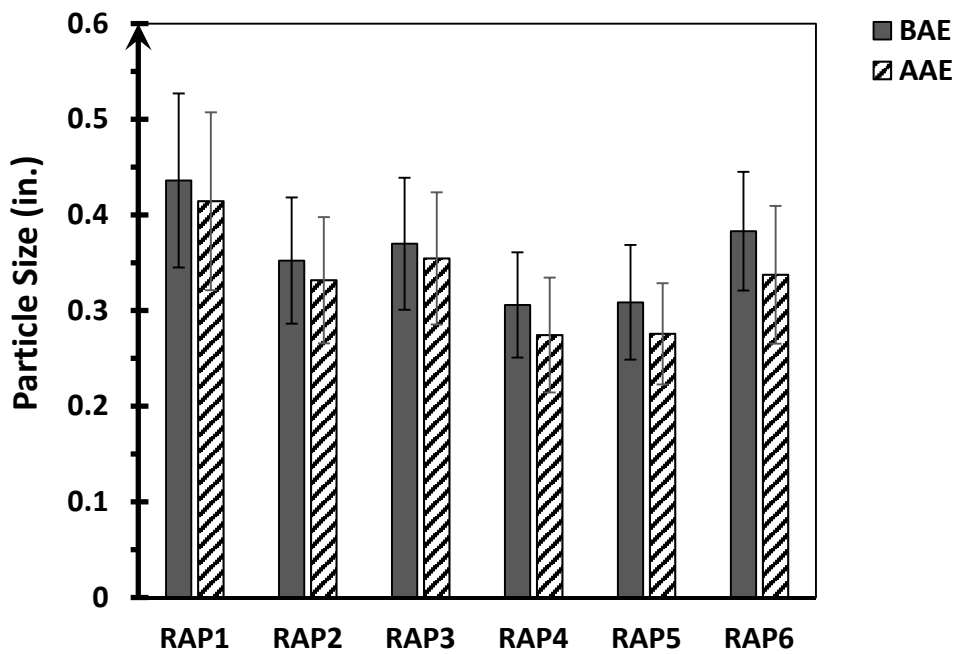
Figure 6.7 Average Particle Sizes Before and After Asphalt Extraction

161
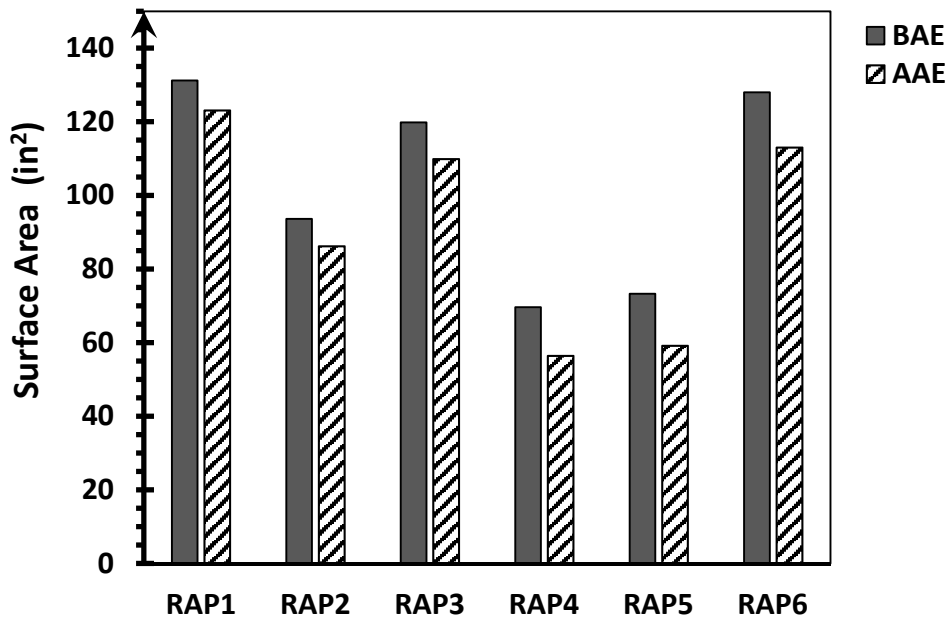
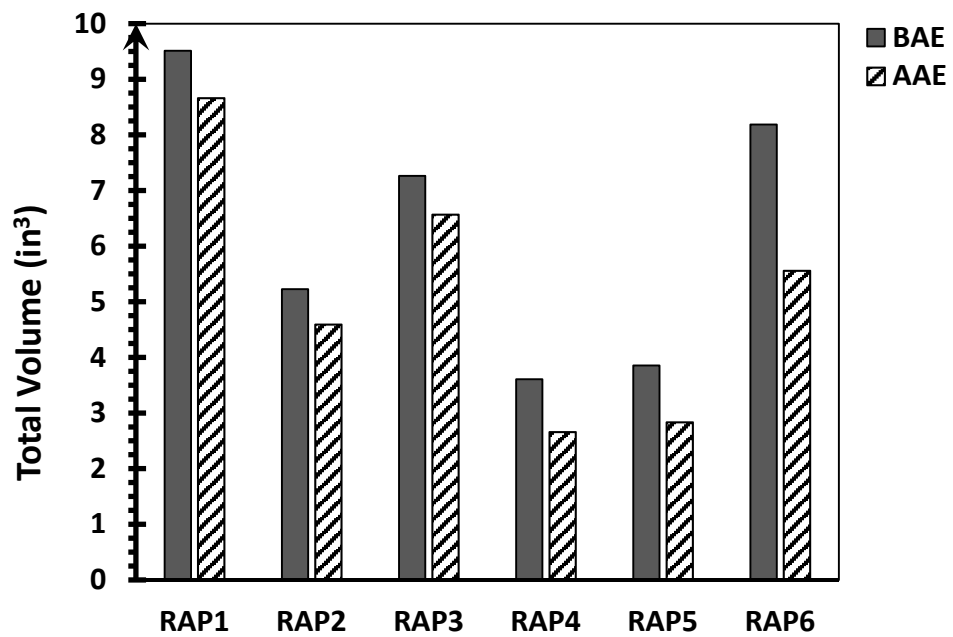Figure 6.8 Average Surface Area Before and After Asphalt Extraction

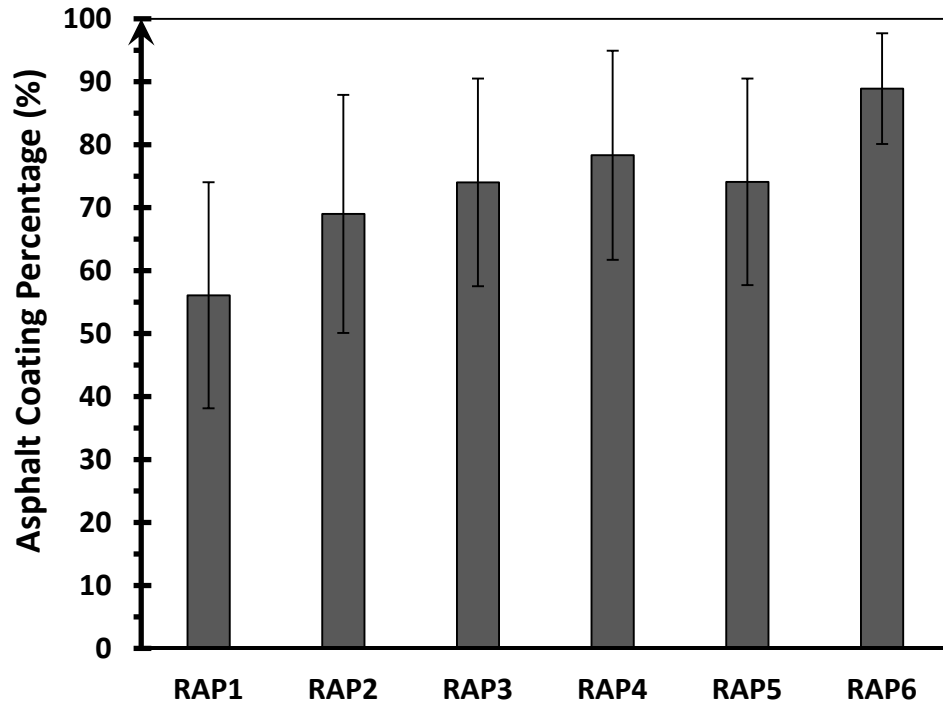Figure 6.9 Total Volume of Particles Before and After Asphalt Extraction

162

Figure 6.10 Average Asphalt Coating Percentages for RAP Sources

reported by Pan [46] for crushed limestone aggregates. The imaging results for the six sources of RAP determined between 56% and 89% of the RAP particles coated with asphalt. RAP 5 and 6 sources had higher asphalt coating percentages in comparison to RAP 1 and 2 sources, which was supported by the visual inspection of RAP sources in Figure 6.1.

The F&E Ratios of particles before and after asphalt extraction indicate that the asphalt coating did not significantly alter the shape of the particles. This confirms that aggregate did not degrade and break down and the overall flatness and elongation of the aggregate particles was not affected by the presence of the asphalt. However, the asphalt coating did increase the total volume of the particles. The magnitude of this increase is more or less related to the asphalt content and agglomerations on the RAP particles. As expected, the RAP particle sizes decreased after the asphalt binder was extracted from the surfaces of the particles.

A correlation was found to exist between the asphalt content of the RAP sources and the percent RAP coated as shown in Figure 6.11. RAP sources with about 4% asphalt content may have resulted in high coating percentages (~75-100%) for the RAP sources identified in this study. However, depending on the asphalt binder content and type, the source and type of the virgin aggregate and the milling and crushing process, the thickness and content of asphalt coating retained on a given RAP particle would vary. These factors may cause the trend in Figure 6.11 to be different for another RAP source or milling process. Additionally, the relationship established between the surface coating and the asphalt content might not stay linear for another RAP source or milling process.

RAP AC (%) = 0.0551 (Asphalt Coating) - 0.6288
(R² = 0.7691 , RMSE = 0.365 , SEE = 0.421)
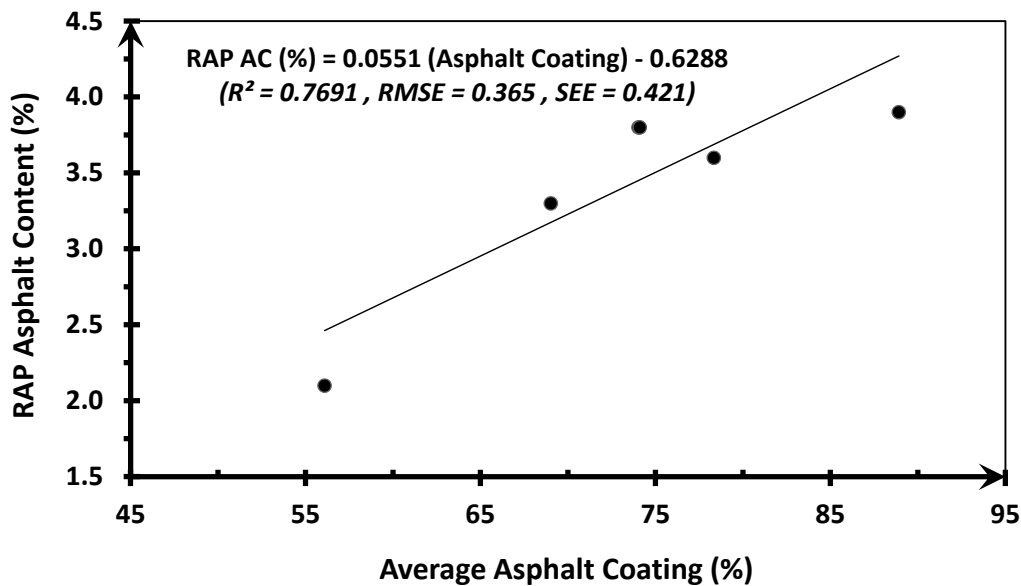
Figure 6.11 Relationship between the Measured RAP Asphalt Content and Estimated Imaging-based Average Asphalt Coating

6.5.1 Concrete Properties

Several research studies have been recently conducted using these RAP aggregates from six sources as a partial replacement of coarse aggregates in concrete [103, 104, 105]. It was initially hypothesized that percent of the RAP particle that is coated would correlate better to several hardened concrete properties than the RAP asphalt content. Note that a

strong correlation was not found between the percent coating of the RAP and the concrete strength and modulus properties. The presence of the SFS aggregates in RAP 4, 5 and 6 sources was found to affect the concrete properties particularly the concrete elastic modulus when compared to dolomite RAP (i.e. RAP 1, 2 and 3 sources) [104].

A strong correlation was found to exist between percent RAP coated and total fracture energy of the concrete [117] as seen in Figure 6.12. The percent RAP coated for a given source was multiplied by the percent RAP content in the concrete mixture, which was 20% to 50% by weight. A weaker linear correlation was found to exist between the total fracture energy and the normalized asphalt content of the RAP, which suggests that the percent RAP coating is a more critical parameter. Additional details on the concrete fracture properties can be referenced elsewhere [103, 105]. These concrete mixtures had total cementitious contents of 610-630 lb/yd^3 (362-374 kg/m^3) and a water-to-cementitious ratio of 0.37, yielding total fracture energies of 86 N/m (20% RAP 1 source), 106 N/m (35% RAP 1 source), 114 N/m (50% RAP 1 source) and 119 N/m (45% RAP 3 source). The asphalt coating on the RAP particle has been suggested to arrest crack propagation in cementitious materials [112, 113], which has been used to explain the fracture property findings for concrete with coarse RAP as the asphalt acts to dissipate energy. Therefore, it is not surprising that the percent coating of the RAP correlates well to the total fracture energy [103, 105, 118]. As more of the RAP particles are coated with asphalt, the fracture energy may increase but not without reducing the strength of the concrete.

6.6 Summary

The Enhanced University of Illinois Aggregate Image Analyzer (E-UIAIA) and its imaging-based morphological indices were used in this chapter to characterize the Reclaimed Asphalt Pavement (RAP) aggregate size and shape properties. In addition, an innovative binary image processing algorithm was developed to estimate the asphalt coating percentages on individual RAP particles. In total, around 400 particles from six sources of RAP obtained from pavement surface courses were studied to determine the average percent asphalt coating and its effect on the imaging-based particle size and shape properties before

and after asphalt extraction. The imaging results showed that there are some influences of asphalt coating on the RAP particles in altering the size and shape properties.
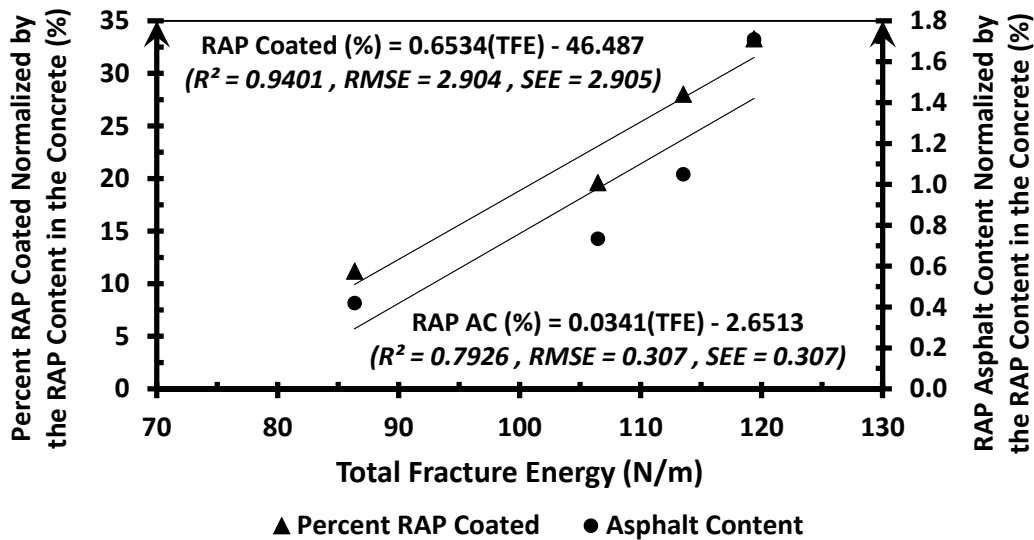

Figure 6.12 Total Fracture Energy of Concrete with Dolomite RAP Compared to the Percent Coating of the RAP and to the RAP Asphalt Content (Both Normalized by the RAP Content of the Concrete, which was 20% to 50%)

The described image processing methodology was validated based on the good results of the developed segmentation method on four case studies using variable contrast to detect the darker zones with predefined areas in images of square shapes. A correlation could be achieved between the estimated asphalt coating percentages and the RAP asphalt content values, which further verified the accuracy of the imaging approach. The developed method was also applied to examine linkages of percent coated RAP particles and concrete fracture energy from various concrete mixtures with different percentages of coarse RAP replacement. The analysis showed that a strong linear relationship existed between the average coated percentage of RAP particles normalized by the RAP content and the concrete fracture energy.

The summary findings of this chapter present an objective and fast alternative for state DOTs and practitioners to quantify the asphalt coating percentages as well as the size and shape properties of RAP materials used in highway construction.

166

CHAPTER 7:

IMAGE PROCESSING METHODS FOR EVALUATING AGGREGATE SHAPE PROPERTIES IN THE FIELD[4]

7.1 Introduction

Imaging technology has been shown in this dissertation to provide an objective and accurate measurement of aggregate particle size and shape properties in a rapid, reliable and automated fashion. However, this approach still has some difficulties including the need to sample aggregate particles in job sites/quarries and shipping to laboratory to image scan and process one at a time particles which makes the procedure tedious and time consuming. Consequently, there is a need to bring these advances in aggregate imaging to project sites and quarries for field implementation.

To analyze aggregate particle shape properties, one alternative is to apply digital image segmentation techniques to the 2D field-captured color images of aggregate samples. In computer vision, segmentation is the process of partitioning a digital image into multiple sets/classes of pixels ("superpixels"). Each segmented set/class should correspond to a well-defined object or a coherent region in the image. The segmentation results are commonly used to recognize regions and objects of interest in the scene. This aids in subsequent image analysis or annotation [119]. There are many approaches for image segmentation [120]; they are either completely automatic or are based, to different degrees, on user interaction.

Image segmentation techniques that combine a Markov Random Field (MRF) approach for modeling, graph cut for optimization and user interaction for enforcing hard constraints are known to be effective alternatives in many computer vision problems [121, 122]. Straightforward incorporation of user input into the formulation of segmentation problem is an important property that improves the performance of this approach. In this chapter, this methodology will be customized, validated and implemented to demonstrate image acquisition and processing for extraction and analyses of individual aggregate particle size and shape properties from 2D field images. The images of multi-aggregate samples will be captured using a Digital Single Lens Reflex (DSLR) camera. Note that in order to develop and implement refined aggregate material classes based on both aggregate gradation and shape, there is a need to quantify aggregate shape properties in the field at gravel pits, rock quarries and construction sites by means of rapid, automated and accurate measurements. Instead of being limited to capturing and processing images of aggregate particles one by one in the laboratory, this process can be replaced with a machine vision based faster process which will yield estimates of the shape property of a number of aggregate particles all together directly from color images. This chapter will also describe two case studies involving collected field images of railroad ballast samples as well as large size aggregate subgrade materials to demonstrate the effectiveness of the field imaging and segmentation approach. The extracted aggregate images are subsequently analyzed for size and shape properties through the use of binary image processing algorithms that are currently used in E-UIAIA.

7.2 Development of Field Collected Aggregate Image Processing

7.2.1 Introduction to Graph Theory

Graphs are mathematical structures used to represent relations between different objects. A graph consists of "vertices" or "nodes" and lines that are called "edges" or "links" which connect the vertices to each other. If a link connects two nodes, they are called "adjacent nodes". Also, the two nodes connected by a link are called "end nodes". The size of a graph is the number of its edges. A graph may be directed which means the edges have an arrow and

only can go in one direction. A graph can be valued or non-valued. In a valued graph, there are numbers attached to the lines that indicate the strength, intensity or quantity of the tie between the two desired nodes. As an example, Figure 7.1 shows a valued and non-directional graph with 5 nodes and 5 links. In this simple graph, each node represents a country and the values written close to each edge shows the amount of trade, in trillion dollars, between two adjacent countries [123].
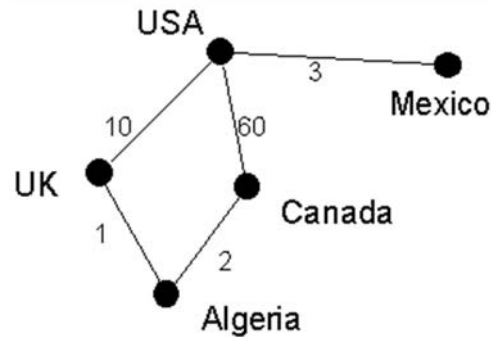

Figure 7.1 Representation of Trades, in Trillion Dollars, between Countries using a Graph with 5 Nodes and 5 Links [124]

7.2.2 Image Representation Using Graph Theory

In image processing using graphs, each digital image can be represented as an undirected graph. Basically, every pixel in the image can be viewed by a corresponding node in the graph. The edges in the graph can be assumed between the nodes with weights corresponding to how similar two adjacent pixels are in terms of a given feature or distance between them. Representing image processing problems with graphs makes it possible to take advantage of the available comprehensive literature related to optimization algorithms in graph theory to produce highly efficient solutions for vision problems [89, 125].

Figure 7.2 shows a valued graph with 16 nodes and 24 links representing a 4 × 4 pixels image. The edges in this graph connects neighboring pixels and possess weights that indicate the pixel similarities in terms of gray intensity. Therefore, neighboring pixels with much closer gray values will get higher weights values on their associated edges. In this example, the weights are distributed between 0 and 20 only for the purposes of demonstrating the concept. For example, if a link in the graph connects a white and a black

node (representing a white and a black pixel), the weight value assigned to that link will be 0. On the other hand, if a link connects two black nodes or two white nodes the weight value assigned to this link will be 20. Therefore, all the other links that connect each two adjacent nodes with different level of gray shades would get a weight value between 0 and 20. Further details about computing weights between pixels will be discussed later in this chapter.
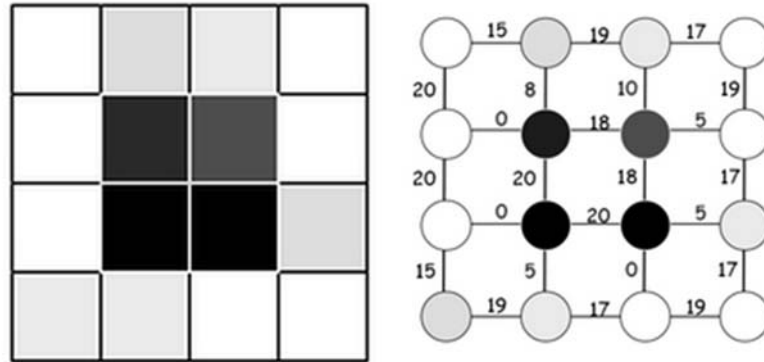

Figure 7.2 Representation of a 4×4 Grayscale Image with a Valued Graph with 16 Nodes and 24 links [126]

7.2.3 Minimum Cut and Maximum Flow Approach in Graph Cut

In a given a graph like $G = \{V, E, W\}$, V and E denotes the nodes and edges respectively. Also, W is the matrix of weights associated with each edge. A cut on this graph separates V into two subsets like K and L such that: $K \cup L = V$ and $K \cap L = \emptyset$.

In graph theory, a very commonly-used graph cut technique is called "minimum cut and maximum flow". In image segmentation problems where the goal is separating the foreground and background, often two additional nodes called terminal nodes or source (s) and sink (t) nodes are added to the graph model of the image [89].

Minimum s/t cut problem can be solved by finding a maximum flow from the source (s) to the sink (t). Generally speaking, "*maximum flow is the maximum amount of water that can be sent from the source to the sink by interpreting graph edges as directed pipes with capacities equal to edge weights. The theorem of Ford and Fulkerson states that a maximum flow from source (s) to sink (t) saturates a set of edges in the graph dividing the nodes into two disjoint portions {S, T} corresponding to a minimum cut. Thus, min-cut and max-flow*

problems are equivalent" [127]. This theorem is illustrated in a step by step example shown in Figure 7.3. In this example, a network is represented by a graph with 8 nodes and 10 links and we are looking for maximum flow and min cut from source to sink. The first number written next to each link is flow and the second number is the capacity of the link.
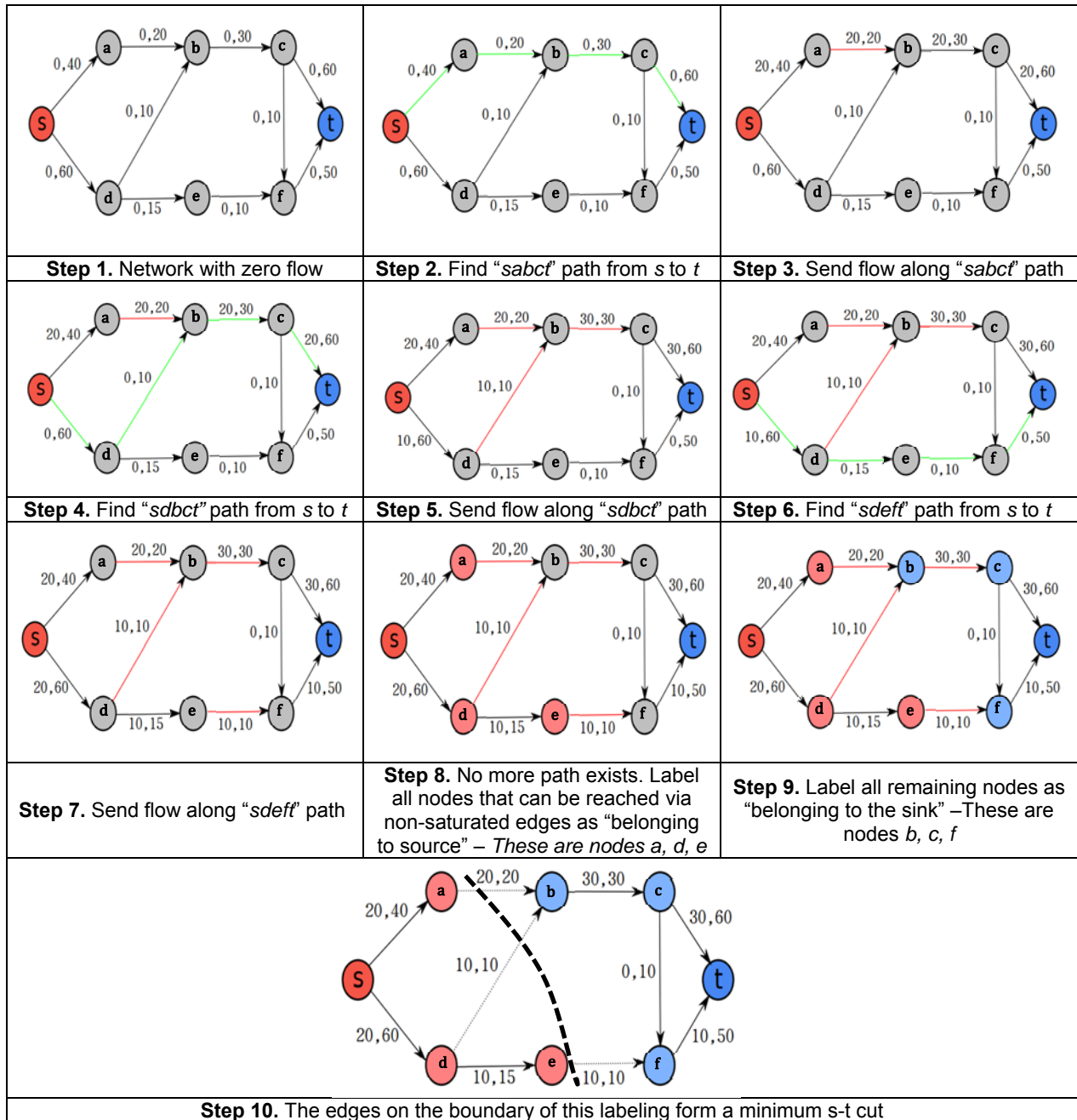

Step 1. Network with zero flow	**Step 2.** Find "*sabct*" path from *s* to *t*

Step 3. Send flow along "*sabct*" path

Step 4. Find "*sdbct*" path from *s* to *t*

Step 5. Send flow along "*sdbct*" path

Step 6. Find "*sdeft*" path from *s* to *t*

Step 7. Send flow along "*sdeft*" path

Step 8. No more path exists. Label all nodes that can be reached via non-saturated edges as "belonging to source" – *These are nodes a, d, e*

Step 9. Label all remaining nodes as "belonging to the sink" –These are nodes *b, c, f*

Step 10. The edges on the boundary of this labeling form a minimum s-t cut

Figure 7.3 Description of Maximum Flow and Minimum Cut Problem in a Graph [128]

171

Further information about optimization algorithms including Ford and Fulkerson method for finding the minimum cut in graphs can be found elsewhere [128].

7.2.4 Markov Random Field Image Modeling

The Markov Random Field (MRF) technique is widely used for pixel labeling problems in computer vision. When only two labels exist, they are labeled as "foreground" and "background". Pixels that belong to the foreground (object) are usually labeled as 1 while pixels that belong to background are labeled as 0.

The specific algorithm used in this chapter begins with the user drawing strokes on the images to select a small number of pixels for each label. In other words, the user interaction is needed to initially inspect the image and select a group of pixels belonging to background or foreground. The MRF is then invoked in order to learn and associate the foreground with a probability distribution of its pixel intensity. According to Equation 7.1, a Gaussian probability distribution function is used to model the intensity probability distribution of the selected pixels. A similar process is performed for the sampled background pixels. Then, given a new pixel in the image, the probabilities of the underlying intensity in each of the two probability models are evaluated.

$$p_k\left(x|\mu,\sigma\right)=\frac{1}{\sigma_k\sqrt{2\pi}}e^{-\frac{(x-\mu_k)^2}{2\sigma_k^2}}$$

7.1

where,

p_k (x|μ,σ) = The probability that the intensity of a desired pixel belonging to background for k=0 or foreground for k=1;

μ = Mean of the distribution associated with background or foreground;

σ = Standard deviation of the distribution associated with background or foreground.

The weights, therefore, at a pixel x, are two probability values P_0 (x) and P_1 (x) and are further discussed in detail in reference [122]. The algorithm continues by associating the image with a graph. An illustration of such graph that corresponds to an arbitrary 3×3 pixels image is given in Figure 7.4. Each pixel in Figure 7.4(a) corresponds to a node (pixel node)

in the graph shown in Figure 7.4(b). In addition to pixel node, the graph contains a pair of nodes corresponding to the background and the foreground/object labels. They are marked as node S and T. The horizontal edges (n-link) connect neighboring pixels while the vertical edges (t-link) connect each pixel node to the label nodes. In Figure 7.4, the weight of an edge is shown in proportion to the thickness of the link. Only neighboring pixels are connected; the weight of the edge, however, varies. In Figure 7.4, the user identifies pixel v as a background pixel. Therefore, pixel v is connected to the background by a very thick edge. Similarly, pixel p is marked by the user belonging to the object. In the absence of such user input e.g. pixel q, the terminal weights between this pixel and the foreground is W_q^f while its terminal weights with background is W_q^b. These weights can be calculated based on Equation 7.2 and 7.3 respectively.

$$W_q^f = \frac{p_1(q)}{p_0(q) + p_1(q)} \qquad\qquad 7.2$$

$$W_q^b = \frac{p_0(q)}{p_0(q) + p_1(q)} \qquad\qquad 7.3$$

The inspection of edges between label nodes and pixel nodes in Figure 7.4 shows that pixel q is more probable to be background while pixels w and r are more likely to belong to the object. The segmentation is then done via a graph-cut optimization technique. Note that edge weight between two arbitrary adjacent pixels such as q and r is dependent on the intensity as well as distance between these two pixels (see Equation 7.4).

(a) 3 X 3 image with user marking B (background) and O (object)	(d) Segmentation result (binary image)
(b) Graph representation for the image in part (a)	(c) The min cut on the graph
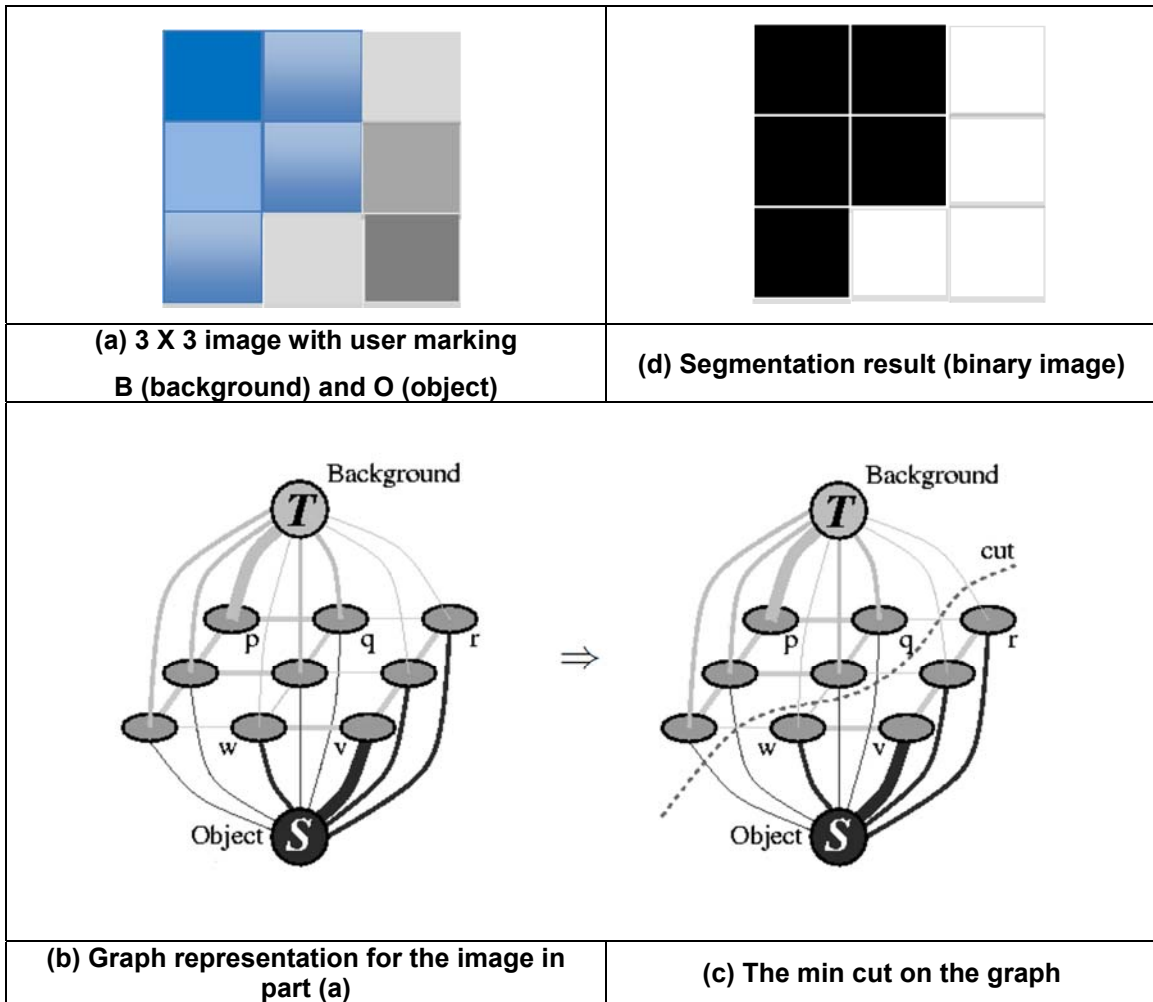
Figure 7.4 Illustration of the Graph-Cut Algorithm and MRF method

$$W_r^q = \exp(-\frac{R(q,r)}{\sigma_R}).\exp(-\frac{(q-r)^2}{\sigma w}) \qquad\qquad 7.4$$

where,

W_r^q = Edge weight between pixel q and r;

$R (q, r)$ = The distance between pixel q and r;

$(q-r)$ = The difference between the intensity of two adjacent pixels;

σ_R, σ_w = Segmentation tuning parameters (computed and converged through iterative procedure) [89].

174

In general, the algorithm tends to cut the edges with small weight while preserving edges with large weight. The result is shown in Figure 7.4(c) by the dotted line and the corresponding segmentation result is shown in Figure 7.4(d) in which the black pixels are the background and the white pixels are the object. Usually, the optimal graph cut is robust to contamination of the image by noise.

Naturally, the selection of this algorithm is guided by considering several factors, such as the color of the pixels in the aggregate images, to distinguish between foreground (particles) and background. The color of the foreground is to some extent uniform and at the same time distinct from the background. Additionally, enforcing neighborhood constraints ensures that the foreground particles are solid and their shape is not sensitive to acquisition noise. The user interface used in this paper is given in reference [129].

7.2.5 Binary Image Extraction Algorithm

Once the image is segmented into foreground and background regions, the connected components of the foreground need to be determined. Each such connected component is a single particle or a small cluster of particles. The algorithm examines each row in the image one by one and finds the intervals of foreground pixels and cluster intervals from adjacent rows. Each cluster is hence a connected component thus corresponds to a single particle. An illustration of the process is depicted in Figure 7.5. The related MATLAB code for binary image extraction algorithm can be found in Appendix E of this dissertation.

In Figure 7.5, aggregate particles with different natural colors were placed on the same blue belt used in E-UIAIA and their images were captured. A Canon EOS Rebel T1i DSLR camera with 15.1-megapixel resolution, Complementary Metal–Oxide–Semiconductor (CMOS) sensor technology and 18-55 mm lens was used. Note that these particles were also used in Chapter 3 to evaluate the automatic color thresholding scheme developed for E-UIAIA. In Figure 7.5, the performance of the segmentation results is only evaluated by visual inspection of the quality and the level of noise in the binary images associated with the particle color. This figure confirms the successful performance of the described graph cut image segmentation method and the binary particle extraction algorithm to detect aggregate particles with different natural colors.
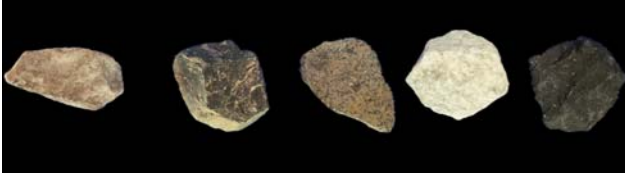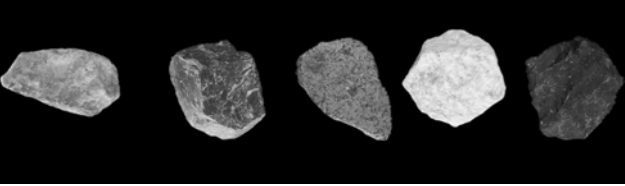
Aggregate image capturing	
Background and particle detection	
Grayscale image	
Thresholding	
Particle segmentation & extraction	

Figure 7.5 Illustration of Segmentation Technique for Particle Detection and Binary Image Generation

7.2.6 Validation of the Proposed Image Segmentation Algorithm

The validation study described in this section, only highlights the effect of using two different image segmentation approaches including graph cut segmentation versus histogram based thresholding on the final numerical values of the imaging based shape and size properties. Thus, E-UIAIA was used for image acquisition to eliminate the other sources of errors that are caused by the method of image capturing in field. These sources of errors include digitization error associated with using CCD versus DSLR camera type sensor technology, achieved spatial resolution in the field and the use of different type of blue

176

background such as a blue cardboard or a blue plastic sheet. Color images for the top views of calibration balls and aggregate particles were captured individually as well as in pairs. These images are shown in Figure 7.6. Note that these images have been captured at 200 pixels per inch (ppi) spatial resolution to ensure that there is enough room in the frame for both calibration ball and aggregate particle.
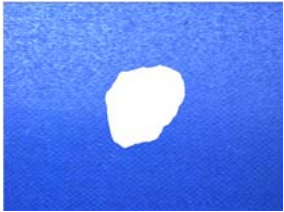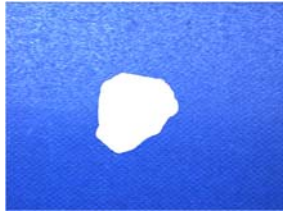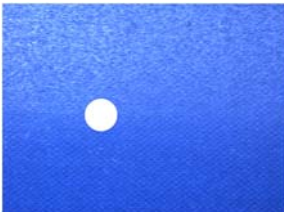

Figure 7.6 RGB Images of the Top Views of Calibration Balls and Aggregate Particles Captured Individually and in Pairs

The images containing only one particle or one calibration ball were segmented using histogram based thresholding method used in E-UIAIA and described in Chapter 3. However, the images containing both aggregate particle and a calibration ball together were processed

using the graph cut segmentation and particle extraction method. The resulting binary images using these two methods are shown in Figure 7.7.
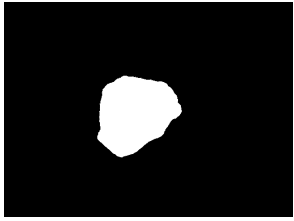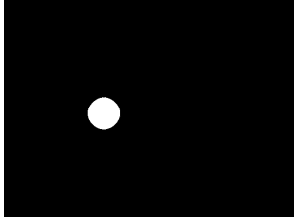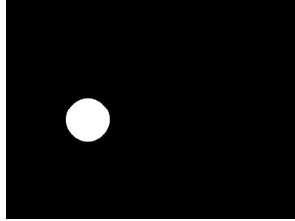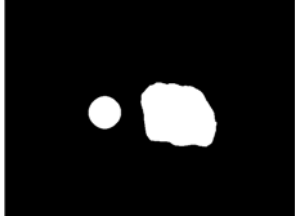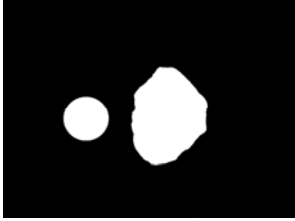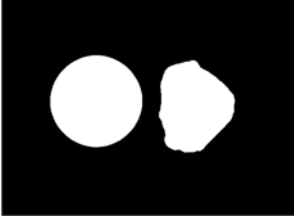
Binary image of aggregate particle and calibration ball in separate frames - Histogram based segmentation method used in E-UIAIA		
Aggregate No.1	Aggregate No.2	Aggregate No.3
0.75 in. calibration ball	1 in. calibration ball	2 in. calibration ball
Binary images of aggregate particle and calibration in the same frame – Graph cut segmentation method		
Aggregate No.1 and 0.75 in. calibration ball	Aggregate No.2 and 1 in. calibration ball	Aggregate No.3 and 2 in. calibration ball

Figure 7.7 Segmented Binary Images of Calibration Balls and Aggregate Particles Using Histogram Based and Graph Cut Segmentation Methods

Following both of the segmentation methods, the resulting binary images of particles and calibration balls were used to compute the shape and size properties using "analy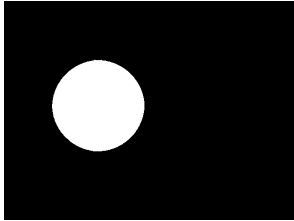ze image interface" function available in E-UIAIA (described in details in Chapter 3). Note that only one 2D top view image for each particle was captured and processed in this study to represent the field imaging process. Therefore, only size, angularity index, surface texture

index and flat and elongated ratio for each particle was computed. The results of shape and size indices associated with each segmentation method are presented in Figures 7.8 to 7.11.

According to Figure 7.8, both segmentation methods could measure the expected angularity index values close to zero for calibration balls of different sizes. Additionally, angularity index values associated with aggregate particles matched very well using the two different segmentation methods. Note that the numerical angularity values are provided for comparison purposes on top of each bar chart. The differences between the results were expected due to using two different segmentation approaches. In other words, few pixels might be categorized as background in one segmentation method while the exact same pixels may be segmented as part of the foreground in another method. Nevertheless, Figure 7.8 confirms that binary images resulting from graph cut segmentation are not significantly different from those binary images resulted from histogram based segmentation.

According to Figure 7.9, both of the segmentation methods could quantity the expected maximum dimension for calibration balls with different sizes. Additionally, maximum dimensions of aggregate particles measured, matched closely using the two different segmentation methods. Based on what was discussed in Chapter 2, E-UIAIA measures the maximum, minimum and the intermediate dimensions associated with three views of each particle. However, since only 2D top views of the particles were captured in the field, the intermediate and minimum dimensions were identical. Consequently, the maximum dimension was considered as the only indicator of the particles sizes in Figure 7.9. The same approach for measuring the particle size will be used later in this chapter to evaluate the sizes of the aggregate particles collected from the field.

Based on Figure 7.10, both of the segmentation methods could measure the expected flat and elongated ratio close to one for calibration balls with different sizes. Additionally, flat and elongated ratios of the aggregate particles were similar as predicted from the two different segmentation methods.

Figure 7.8 Angularity Index Values Quantified for Calibration Balls and Aggregate Particles Using Histogram Based and Graph Cut Segmentation Methods

Figure 7.9 Maximum Dimensions Quantified for Calibration Balls and Aggregate Particles Using Histogram Based and Graph Cut Segmentation Methods

Figure 7.10 Flat and Elongated Ratios Quantified for Calibration Balls and Aggregate Particles Using Histogram Based and Graph Cut Segmentation Methods
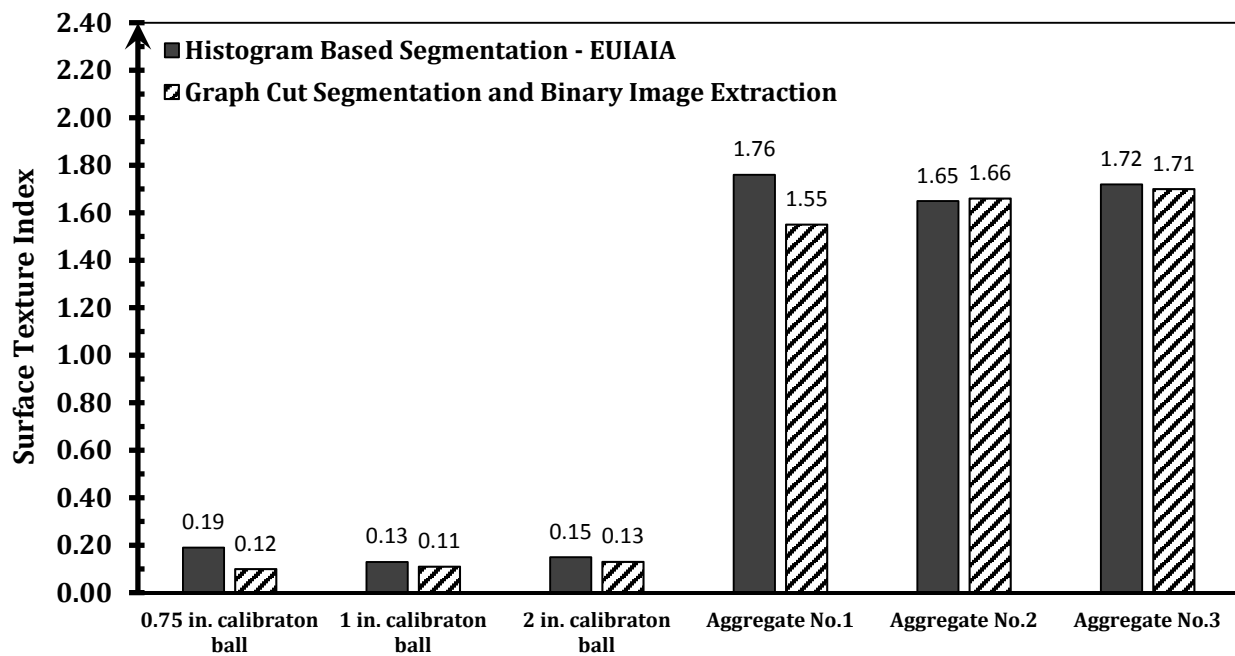
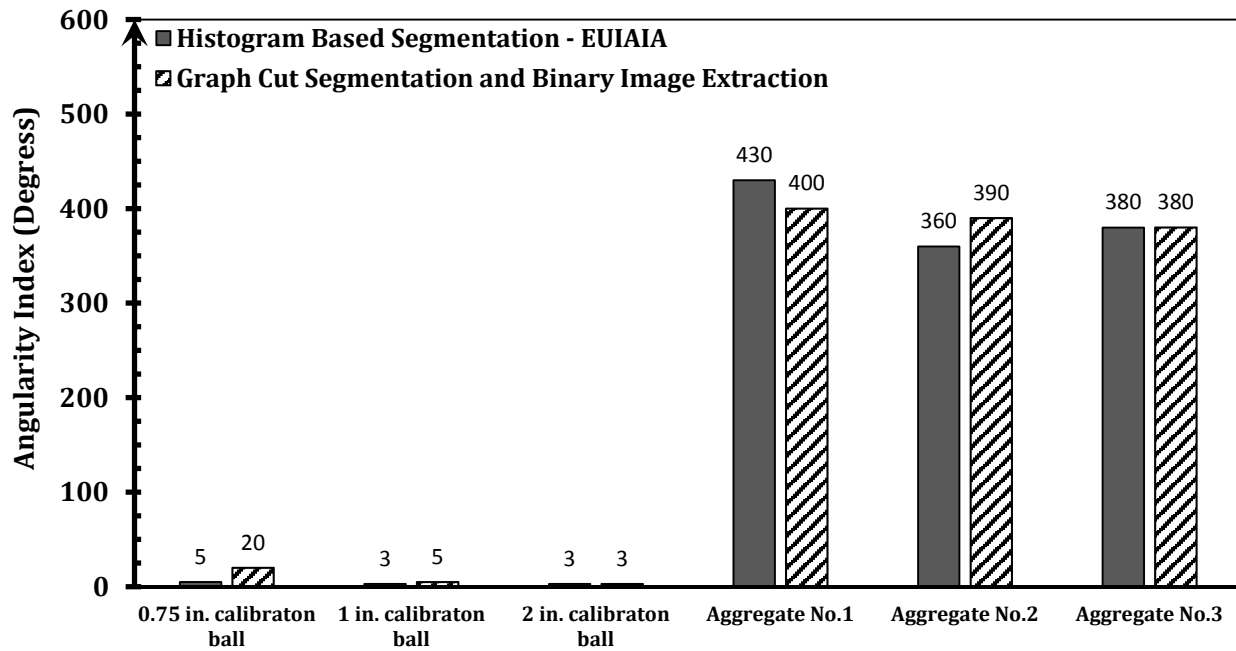Figure 7.11 Surface Texture Index Values Quantified for Calibration Balls and Aggregate Particles Using Histogram Based and Graph Cut Segmentation Methods

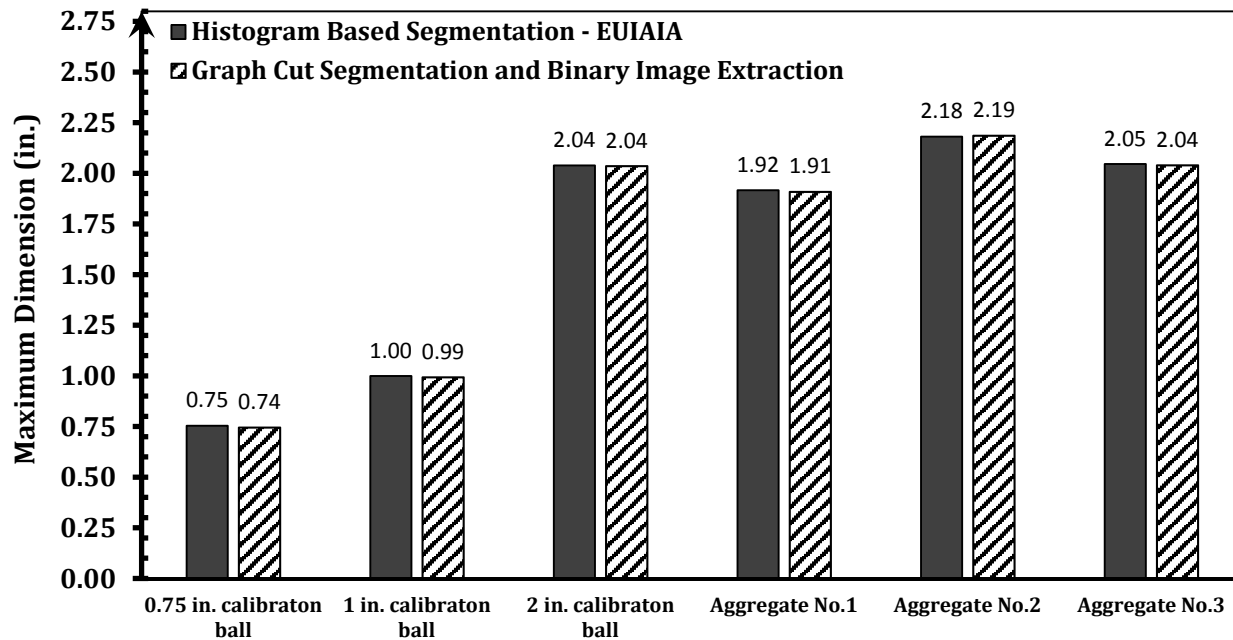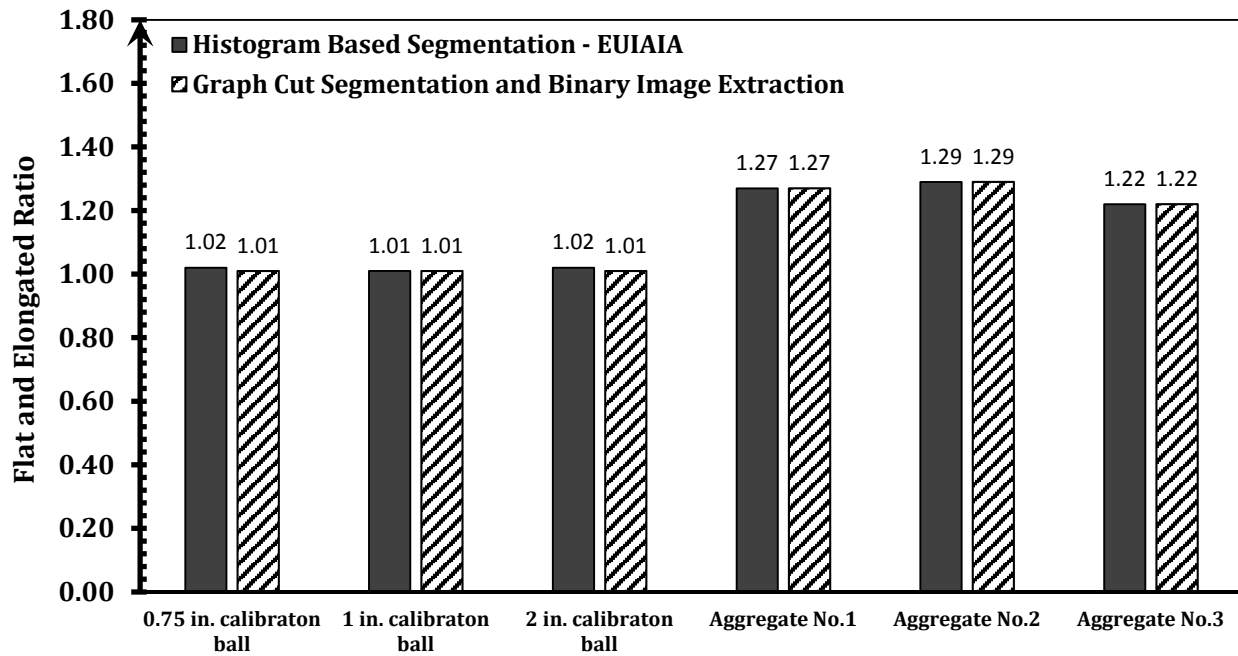Figure 7.11 shows that the measured surface texture indices for the calibration balls using the two segmentation methods are between 0.1 and 0.2. Referring to the surface texture index results for calibration balls in Chapter 2, the presented results in Figure 7.11 match reasonably well with the expected values. According to Figure 7.11, differences in texture index values were recorded as a result of using two different segmentation methods for the aggregate particles and calibration balls. This can be explained by the fact that surface texture index is computed based on applying cycles of erosion and dilation on a binary image. Therefore, errors associated with each segmentation method can affect the surface texture index results. Nevertheless, Figure 7.11 still shows a good match for the recorded surface texture index results associated with using two different segmentation methods.

7.3 Aggregate Image Acquisition Procedure with DSLR Camera in the Field

This section describes the procedure developed to capture images of aggregate particles in the field and perform the corresponding image processing techniques. Aggregate imaging kit was prepared for use in the field to capture the images of aggregates in job sites and quarries (see Figure 7.12).

Figure 7.12 Aggregate Imaging Kit Including DSLR Camera, Accessories, Tripod and Image Calibration Tools

Key elements in capturing the images of aggregate particles under ambient conditions include appropriate contrast between the background and the edge of the particles, proper exposure to avoid having any areas in the image that are overexposed, a specified resolution (pixels per inch) and elimination of any shadows caused by the sun or the camera's flash. These are seemed to be necessary conditions to successfully perform the segmentation procedure described. A Canon EOS Rebel T1i camera with 15.1-megapixel resolution with CMOS sensor technology and 18-55 mm lens was used.

Camera settings to achieve proper aggregate images are summarized in Table 7.1. Note that positioning the camera at 28 in. (711.2 mm) from the object and adjusting the focal length at 18 mm ensures that the images are captured with 215 pixel per inch spatial resolution.

Table 7.1 Developed Camera Settings for Field Imaging

DSLR Camera Setting Parameter	Value
Distance form camera lens to object	28 inches
Shutter speed	1/30 sec
Aperture	f/4
Light sensitivity	ISO-100
The focal length of the lens	18 mm

A step by step guideline was prepared for aggregate image acquisition in the field as follows:

1. Obtain aggregate particles from sampling location;
2. Spread particles out on blue screen-like cardboard or plastic sheet;
3. Make sure particles do not touch or overlap each other by providing enough spacing between the particles;
4. Add calibration ball into scene for determination of spatial resolution;
5. Adjust zoom lens to capture scene at predetermined spatial resolution of 215 pixels per inch (ppi) following the settings listed in Table 7.1;
6. Mount camera on tripod and use level to "flatten" camera view with respect to ground;

7. Adjust aperture setting for minimal lens distortion;

8. Provide adequate light (sun, lights, flash, etc.) to properly illuminate particles;

9. Prevent lighting from casting shadows on particle or from particles themselves;

10. Adjust focus (manual or auto);

11. Use triple exposure setting or "bracketing" option to capture three images, at one step above/below current setting;

12. Obtain new sample of aggregate from next sampling location;

13. Repeat imaging procedure.

The final camera setup for aggregate field imaging is shown in Figure 7.13.

Figure 7.13 Camera Setup for Aggregate Imaging with Blue Background in an Outdoor Setting (Left: Front View of Camera and Tripod, Right: Top View Camera Screen)

7.4 Case Study I – Railroad Ballast Field Imaging

Each year, a large portion of the US freight railroad operating budget to sustain the railway track system goes into maintenance and renewal of mineral aggregates used as track ballast. These large sized aggregates; with a maximum size of 3 in. (76 mm), are used as the ballast layer in the track substructure, which distributes the train load to the subgrade soil

and also provides drainage for the track with its uniform gradation. Unlike subbase/base layers in pavement structures, ballast aggregates tend to break down, powder and deteriorate under many repeated wheel loadings from heavy freight trains. This ballast degradation not only reduces particle sizes but also changes the physical shape properties of aggregate particles, resulting in accumulation of finer material causing ballast fouling. The intensity of the ballast degradation is a function of aggregate source properties, load levels as well as track geometry and environmental conditions. Fast and reliable field ballast assessment methods using machine vision and image processing techniques are needed to monitor changes in ballast properties.

To evaluate the performance of the field imaging and segmentation methods described in this chapter, aggregate samples were collected at different ballast depths from a mainline freight railroad in Mississippi. Figure 7.14(a) shows the aggregate samples collected at the surface (0 in.) as well as 8 in. (203 mm) and 16 in. (406 mm) ballast depths. Figure 7.14(b) is a photo of the sampling track location showing clean ballast on top and gradually fouling ballast with depth.

Figure 7.14(a) Aggregate Collected at the Surface or 0 in. (Left), 8 in. (Middle), and 16 in. (Right) Ballast Depths

Figure 7.14(b) Aggregate Sampling Track Location along a Mainline Freight Railroad in Mississippi (2 in. White Calibration Ball)

The shape properties of the ballast aggregate particles were measured using the field imaging/segmentation and the laboratory E-UIAIA methods described in this dissertation to

investigate the effects of train loading and the resulting ballast deterioration levels with depth. Table 7.2 summarizes the results of the morphological analyses with imaging based shape indices determined using both the E-UIAIA and the field imaging/graph cut segmentation techniques. It should be noted that 215 pixel per inch (ppi) resolution was used in scanning the aggregates by both methods. From Table 7.2, a comparison of the maximum aggregate dimensions and F&E ratios proves that both the field imaging/graph cut segmentation and the laboratory E-UIAIA methods agree quite well in determining aggregate particle sizes. Furthermore, good level of repeatability is observed with both methods from a comparison of trials 1 and 2 and the standard deviation values. The angularity index values determined by the field imaging/graph cut segmentation are consistently lower than those computed in the laboratory from the E-UIAIA image scanning and histogram based processing method. On the other hand, the surface texture index values are determined slightly higher using the field imaging/graph cut segmentation method. Since the camera sensor technologies, natural lighting conditions as well as blue background color shades vary considerably between two methods, it is conceivable that the pixel intensities of the captured aggregate images are not quite similar although the pixel calibrations are the same. In other words, digitization error can be considered as a factor for not achieving identical binary images by the two methods. Nevertheless, considering the ranges of angularity index and surface texture index values and the similar magnitudes of standard deviations, the results from the two methods are closely matching and quite acceptable for practical field applications.

It is interesting to note that both methods could successfully detect the gradual demise in the aggregate size with ballast depth due to degradation and particle breakdown under repeated train loading. This is with the understanding that old ballast, which is more degraded and broken down, is found in deeper sublayers. The particles sampled from the 8 in. (203 mm) depth have slightly higher F&E ratios as determined by the two methods.

Table 7.2 Ballast Aggregate Shape Indices Computed from E-UIAIA in the Laboratory and Field Imaging/Segmentation

Depth (in.)	No. of Particles	Angularity Index (degrees) Average	Std. Dev.	Max Dimension (in.) Average	Std. Dev.	F&E Ratio Average	Std. Dev.	Surface Texture Index Average	Std. Dev.
E-UIAIA – CCD Camera and Histogram Based Segmentation									
Trial 1									
0	34	420	112	2.19	0.55	1.37	0.16	1.44	0.63
8	54	438	116	1.29	0.37	1.42	0.20	1.8	0.64
16	42	432	108	0.96	0.33	1.38	0.24	1.91	0.56
E-UIAIA - CCD Camera and Histogram Based Segmentation									
Trial 2									
0	34	421	125	2.2	0.54	1.3	0.15	1.43	0.55
8	54	459	120	1.28	0.35	1.43	0.18	1.79	0.66
16	42	468	114	0.97	0.32	1.39	0.25	2.05	0.68
DSLR Camera and Graph Cut Segmentation									
Trial 1									
0	34	385	77	2.22	0.6	1.32	0.16	2.03	0.39
8	54	417	108	1.41	0.38	1.4	0.27	2.88	0.82
16	42	435	119	1.07	0.39	1.35	0.19	3.54	1.06
DSLR Camera and Graph Cut Segmentation									
Trial 2									
0	34	379	81.4	2.21	0.56	1.31	0.13	2.06	0.4
8	54	402	105	1.4	0.39	1.44	0.3	2.9	0.9
16	42	441	97	1.03	0.36	1.32	0.19	3.63	1.09

The F&E ratios also match closely between the two methods with the same pixel resolution used. For both methods, the measured angularity and surface texture indices indicate somewhat increasing trends with ballast depth, which can be explained with the size

reduction and breakage of older ballast under train loading. Interestingly, as the aggregate size gets smaller with depth, these more recently crushed particles at greater depths possess higher angularities and rougher surfaces.

7.5 Case Study II – Large Size Aggregate Subgrade Field Imaging

Aggregate Subgrade is a term used in the Illinois Department of Transportation (IDOT) Standard Specifications for road and bridge Construction [130] linked to furnishing, transporting and placing granular materials for subgrade improvement and subbase. The aggregate subgrade materials can be virgin aggregates, recycled materials such as crushed concrete and Reclaimed Asphalt Pavement (RAP) or combinations of both. They are often used for subgrade replacement and construction of granular subbase layers over soft, unstable Illinois subgrade soils for building pavement construction working platforms, which eventually become part of the pavement structure.

Recently, as part of ICT R27-124 research project, the field performances of different aggregate subgrade materials including sources of large size crushed concrete and primary crusher run aggregate were studied through accelerated testing of full-scale pavement sections at the University of Illinois. According to Table 7.3, due to expected large sizes of particles in these two aggregate sources, their size and shape properties could not be established through regular laboratory sieve analysis. Therefore, the aggregate field image acquisition and segmentation method described in this chapter was utilized to characterize the size and shape properties of the large particles retained on 3 in. (76 mm) sieve.

Five-gallon buckets were used for aggregate sampling from each source of aggregate. In each bucket, the particles with sizes above 3 in. (76 mm) were separated using the 3 in. (76 mm) sieve. Following the procedure described in section 7.3, the 2D top view images of particles were captured on a blue cardboard (see Figure 7.15).

Aggregate ID	Aggregate Type	Expected Sieve Size Range
CS01	Large Size Crushed Concrete	6 in. (152 mm) - No.200 (0.075 mm)
CS02	Primary Crusher Run Aggregate	6 in. (152 mm) – No.200 (0.075 mm)

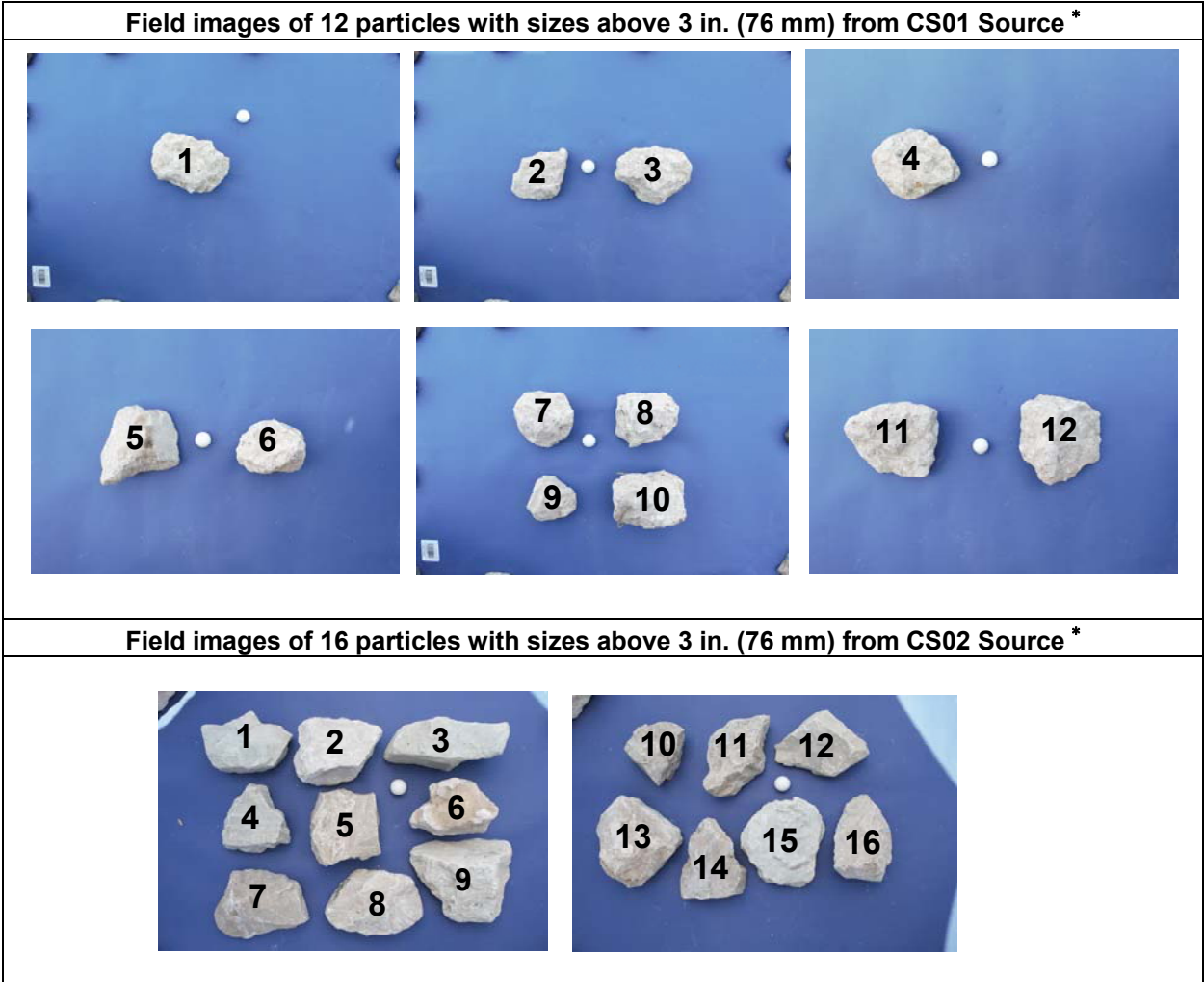

Figure 7.15 Left: Separating Large Particles with Sizes above 3 in. (76 mm)
Right: Image Acquisition in the Field with DSLR Camera and Blue Background

The captured color images of large size particles from CS01 and CS02 aggregate sources are presented in Figure 7.16. These color images were processed using the graph cut image segmentation and binary image extraction that was discussed in section 7.2. Note that in Figure 7.16, a number is assigned to each particle. These numbers will be later used in this section to track the particles and link them to their associated imaging based size and shape properties.

The shape and size properties related to CS01 and CS02 large size aggregate sources are listed in Table 7.4. In this table, the imaging based maximum dimensions of the particles obtained from the segmentation method are listed to indicate the large sizes of these aggregate sources. Additionally, it can be seen that the average angularity index and surface

texture index associated with CS01 are close to their corresponding values for CS02. This finding can be explained by the fact that both CS01 and CS02 are crushed aggregate sources; therefore, their angularity and surface texture indices should be more or less similar to each other.

Field images of 12 particles with sizes above 3 in. (76 mm) from CS01 Source *

Field images of 16 particles with sizes above 3 in. (76 mm) from CS02 Source *

* 1 in. (25.4 mm) calibration ball is shown in the images

Figure 7.16 Color Images Related to Top Views of Calibration Ball and Large Size Aggregates from CS01 and CS02 Sources

Table 7.4 Imaging Based Shape and Size Properties for CS01 and CS02 Large Size Aggregate Sources

Shape Properties for CS01 Large Size Aggregates				
Particle No.	Angularity Index (degrees)	Max Dimension (in.)	F&E Ratio	Surface Texture Index
1	490	5.26	1.40	1.61
2	530	4.52	1.35	2.34
3	510	5.09	1.31	1.83
4	410	5.14	1.25	1.49
5	510	5.22	1.22	1.68
6	210	4.05	1.33	1.62
7	290	4.10	1.07	1.44
8	640	4.61	1.29	204
9	310	3.40	1.14	1.77
10	510	5.47	1.39	2.88
11	420	4.66	1.28	1.47
12	470	5.44	1.07	1.49
Average	**441**	**4.74**	**1.25**	**1.80**
Shape Properties for CS02 Large Size Aggregates				
Particle No.	Angularity Index (degrees)	Max Dimension (in.)	F&E Ratio	Surface Texture Index
1	510	5.15	1.48	2.35
2	340	5.40	1.29	1.75
3	440	7.19	2.33	2.21
4	450	4.15	1.08	1.65
5	450	5.00	1.08	2.01
6	570	5.03	1.53	2.20
7	380	5.30	1.37	1.38
8	250	5.49	1.46	1.36
9	440	6.11	1.15	1.39
10	420	3.71	1.11	2.48
11	490	5.61	1.58	2.03
12	390	5.35	1.41	2.01
13	350	5.27	1.08	1.54
14	520	4.87	1.27	1.54
15	290	5.18	1.1	1.39
16	320	5.08	1.52	1.79
Average	**413**	**5.24**	**1.36**	**1.81**

7.6 Summary

Aggregate image processing using graph cut segmentation technique was described and used in this chapter to analyze the 2D images of aggregate samples captured by a commonly used DSLR camera in the field for extraction and analyses of individual aggregate particle size and shape properties. The segmented individual particle images were fed into the validated E-UIAIA image processing algorithms to compute particle size and shape properties using the imaging based indices of Flat and Elongated Ratio (F&E Ratio), Angularity Index (AI), and Surface Texture Index (STI).

The performances of the field imaging and segmentation methodologies were evaluated by means of two case studies involving field images of large size aggregate sources as well as railroad ballast samples collected from various ballast depths in a mainline freight railroad track. The results of ballast aggregate size and morphological analyses, i.e., the computed imaging based size and shape indices, using both the laboratory E-UIAIA and the field imaging/segmentation methods matched quite closely. Further, both methods could successfully detect the gradual decrease in the aggregate size due to higher degradation and particle breakdown with ballast depth as evidenced by higher AI and STI values measured at greater depths. In addition, the described field image acquisition and processing method was able to successfully detect the size and shape properties of large size aggregate sources.

These promising preliminary results therefore indicate that the methodology described in this chapter can be considered in the field to rapidly and reliably capture several aggregate particles in a single image so that individual particle size and shape properties can be analyzed. Additionally, both spatial property variability and property changes with layer depth and usage, i.e., property degradation in time, can be evaluated under service loading.

CHAPTER 8:

CONCLUSIONS AND RECOMMENDATIONS

The research study presented in this dissertation introduced innovative color image acquisition and segmentation techniques to identify size and shape properties of aggregate materials both in the laboratory and in the field. The development of new design as well as the manufacturing, calibration and validation of an Enhanced-University of Illinois Aggregate Image Analyzer (E-UIAIA) with many improvements over the first generation device was the first objective of this research. This also included the development of a binary image processing algorithm to estimate the percent asphalt coating on Reclaimed Asphalt Pavement (RAP) aggregate particles. The second objective of this study was to demonstrate the newly developed E-UIAIA for its effectiveness and improved aggregate image processing modules to characterize the morphological properties of different sources of aggregates with different natural colors and at different degradation levels from beginning to the end of their performance periods. These aggregate sources were used in the construction of railroad ballast in track systems and various layers in flexible pavements. The second objective was also included the development of an imaging based aggregate classification methodology to better quantify the resistance of aggregate sources to degradation. The third objective of this research was on the development, validation and implementation of a customized field aggregate image acquisition/processing technique which can be used to characterize shape and size properties of aggregate particles in the job sites and quarries.

8.1 Summary of Research Activities

The research activities described in this study can be divided into four major phases which focused on addressing the main objectives of this dissertation. In phase I, the different software and hardware components of the new E-UIAIA were designed and manufactured. An important task in this phase included the development of an advanced color image

thresholding algorithm to successfully acquire and segment images of aggregate particles even with dark natural colors when they are placed on a blue background. An image calibration interface was also developed and tested for precise measurements of particle sizes and shapes. The accuracy of the improved modules for computing the imaging based indices, i.e., angularity index, surface texture index, flat and elongated ratio, surface area and volume were validated using an available aggregate imaging database. The influence of the new image acquisition/thresholding technique on the variability of shape indices obtained for the same aggregate particles scanned with both the original and enhanced versions of UIAIA was also investigated.

In phase II of this research, E-UIAIA was used to fully capture the rate and magnitudes of changes in shape indices of aggregate samples degraded in the laboratory using commonly used testing procedures. The results from standard laboratory aggregate degradation tests including LA-Abrasion and Micro-Deval aggregate degradation tests were combined with an evaluation of the imaging based shape indices of the particles at different degradation levels. The described imaging based approach for evaluating degradation potentials of aggregates was used then to classify aggregate sources according to their resistance to abrasion, polishing and breakage.

In phase III, a post-processing aggregate image analyzer module was developed and validated using the image processing toolbox available in MATLAB. This module was used to estimate percent asphalt coating on the individual particles obtained from different sources of RAP aggregates. E-UIAIA was used to capture the images of RAP particles and generate their corresponding binary images. Using the binary images and the developed module, the average percentages of asphalt coating on the RAP particles were estimated and correlated to asphalt content values obtained by a laboratory asphalt extraction method. Additionally, the fracture energies of Portland cement concrete samples made from these RAP sources were also correlated to the imaging based percentages of asphalt coating on the particles.

Phase IV of this research had the research scope to practically bring the available aggregate imaging technology to the field job sites and aggregate quarries. A binary image extraction algorithm was developed to work with the graph cut image segmentation

approach. The proposed methodology was demonstrated to successfully process size and shape properties of aggregate particles from high resolution 2D digital images captured in the field. The developed aggregate field imaging procedure was evaluated using two case studies. In the first case study, the shape and size properties of railroad ballast samples collected from different depths of ballast layer of in-service track were identified. The second case study involved morphological characterization of large size aggregate sources used as aggregate subgrade materials in working platform and low volume flexible pavement construction.

8.2 Summary of Contributions and Research Findings

- The findings from Chapter 3 showed that the use of three high resolution CCD color cameras equipped with lenses having variable focal lengths improved the quality of the images for various aggregate sizes and shapes captured with E-UIAIA. Therefore, using the newly developed image acquisition and calibration interfaces, the images of aggregate particles for up to 3 in. (76 mm) railroad ballast aggregate sizes could be successfully quantified for size and shape indices. The final position of four LED lights controlled with dimmers resulted in images with the least amount of shadows around each particle. Additionally, the improved design of E-UIAIA made it smaller, portable, more efficient and easier to operate compared with the original UIAIA device.

- According to findings from Chapter 3, the developed fully automated color image thresholding algorithm could segment the images of aggregate particles from a blue background. Two innovative Look Up Tables (LUT) were developed to enhance the Hue (H) and Saturation (S) representations of color images. The corresponding binary image for each aggregate particle was successfully generated by applying a histogram based clustering threshold on the product of enhanced Saturation and Hue channels. The developed segmentation method showed excellent performance in generating binary images of aggregate particles with different sizes and natural colors. The color thresholding algorithm was also added to software image acquisition and calibration interfaces to assist the operator with automated and real time assessment of the segmentation results.

195

- As explained in detail in Chapter 3, the different binary image processing modules available in the original UIAIA device were debugged, updated and merged into a single module. This new module equipped with a user friendly interface was then used to simultaneously compute the size and shape indices for angularity, surface texture, volume and surface area from the three orthogonal views of an individual aggregate particle. Moreover, validation studies performed on E-UIAIA indicated that this imaging system could successfully identify the particle size and shape properties of several aggregate sources, e.g., differentiating between light and dark colored crushed and uncrushed aggregate particles.

- According to findings from Chapters 4 and 5, an imaging based approach was successfully established for aggregate morphology degradation analysis. In this method, the percentages of changes in shape indices of aggregate particles were measured with E-UIAIA at different degradation levels and compared to LA-Abrasion and Micro-Deval testing results. Using this method, fourteen sources of railroad ballast aggregates and eleven sources of crushed aggregate sources used in pavement surface friction courses were classified into different groups based on their resistance to abrasion, polishing and breakage. This method holds the potential to be included in standards for material testing and specifications for improved characterization of degradation properties of different aggregate sources.

- Based on findings from Chapter 6, an algorithm for computing the percentages of asphalt coating on RAP aggregates was developed. Arithmetic image operations and image thresholding techniques were utilized to segment the areas of the RAP particles coated with asphalt binder. This validated algorithm showed satisfactory performance in estimating the percentages of asphalt coating when applied to six different RAP aggregate sources. Furthermore, E-UIAIA was used to successfully capture how the asphalt coating on the surface could alter the morphological properties of aggregate particles. The imaging based percentages of asphalt coating were adequately correlated with the asphalt content values achieved using asphalt extraction methods.

- According to findings from Chapter 7, a field image acquisition and processing procedure was developed to quantify imaging based size and shape indices of aggregate particles in quarries and construction sites. This advanced image analysis and segmentation procedure combined a Markov Random Field (MRF) approach for image modeling, graph cut for optimization and user interaction for enforcing hard constraints, and was capable of detecting and extracting the images of several aggregate particles captured in a single frame using a Digital Single Lens Reflex (DSLR) camera. The developed aggregate field imaging procedure showed promising results in quantifying the particle sizes as well as angularity and surface texture indices of railroad ballast samples collected from in-service railroad track. Similarly, the procedure was capable of successfully identifying the size and shape properties used in pavement working platform construction.

8.3 Conclusions

Based on the findings from this dissertation the following conclusions can be made:
- Advanced image enhancements applied with customized Look Up Tables on Hue and Saturations channels of aggregate images could improve image thresholding results using clustering method in the newly developed E-UIAIA. This image processing approach showed excellent performance in segmentation of aggregates images with different colors placed on a blue background.
- Imaging based shape indices of aggregate particles evaluated at different degradation levels from Micro-Deval and LA-Abrasion testing were shown to provide an adequate quantification of degradation potentials of aggregate sources in terms of resistance to abrasion, polishing and breakage.
- Three-parameter statistical models successfully developed in this study could adequately capture changes in imaging based size and shape indices, i.e., degradation potentials of aggregate particles in terms of abrasion, polishing and breakage.
- E-UIAIA could successfully process the size and shape indices of RAP aggregate materials. By applying the developed advanced image processing techniques, i.e., digital image arithmetic operations, thresholding and noise reduction with binary morphology

analysis, percentages of asphalt coatings on different RAP aggregate sources could be adequately estimated.

- The laboratory developments in image acquisition and image processing of aggregate particles using E-UIAIA could be successfully implemented in field practices. The combination of advanced 2D image acquisition with DSLR camera and image segmentation with graph cut techniques produced comparable results to laboratory quantification of imaging based size and shape indices of individual particles and their aggregate morphology degradation patterns.

8.4 Research Limitations and Recommendations for Future Research

As discussed in Chapter 3, calibrating the cameras used in E-UIAIA at a target spatial resolution requires manual zooming and focusing of the lenses. This process can be tedious and time consuming because the camera lenses used in E-UIAIA do not have the auto-zoom and auto-focus feature. Therefore, no controller was implemented in the front panel of the image acquisition interface to digitally adjust the zoom and focus levels. Using auto-zoom and auto-focus lenses provide the opportunity for faster calibration of E-UIAIA as well as capturing the images of a single aggregate particle at different spatial resolutions. Therefore, multi-resolution analysis [131] on the aggregate images can be performed which potentially could result in the development of new and more efficient particle shape indices.

Although aggregate image acquisition and processing stages are fully automated in E-UIAIA, placing the aggregate particles on the conveyor belt is still manual and needs an operator. Therefore, designing and manufacturing an aggregate feeder system is highly recommended especially for commercialization purposes of E-UIAIA.

E-UIAIA uses three cameras to capture three orthogonal views of an aggregate particle. However, this system is still considered a semi-3D aggregate image analyzer. In other words, 2D binary image processing techniques are used on each orthogonal view and ultimately the analysis results from three views will be averaged to give the final particle index. Nevertheless, 3D image reconstruction and processing methods have the potential to be utilized for representation of a 3D model of the aggregate particles using their associated

three orthogonal views. These reconstructed 3D digital particles can be used in Discrete Element Modeling (DEM) programs to better consider the effect of particle shapes.

Considering the findings that were presented in Chapters 4 and 5, for each laboratory degradation test such as Micro-Deval and LA-Abrasion, a comprehensive repeatability and variability study is recommended to identify the type of statistical distribution as well as establishing the range and standard deviation for change in each individual shape property. These will assist in accurately determining the threshold limits with desired level of reliability in recognizing low, medium and high regions in terms of resistance to abrasion polishing and breakage for the available and commonly used aggregate material sources in each region. The field performance of aggregates used in bound/unbound layers in terms of strength, roughness, skid resistance and permanent deformation is required to be monitored over time to correlate with changes in particle shape properties obtained with different imaging results or laboratory degradation testing.

Imaging based methodology for efficient and objective estimation of the asphalt coating on RAP particles described in Chapter 6 has the potential to be further improved. This approach can be considered as an automated and machine vision based alternative to the current AASHTO T195, "Standard Method of Test for Determining Degree of Particle Coating of Bituminous-Aggregate Mixtures", which is a subjective method and mainly based on visual inspection of the aggregate particles. Additionally, machine vision technology and image processing methods can be utilized to evaluate the pavement surface condition in terms of levels of stripping or the loss of bond between aggregates and asphalt binder.

Future research related to morphological evaluation of aggregates in the field can be directed towards establishing more validation cases involving statistical analyses with different ranges of size and shape property indices for different types of aggregate using both the field image acquisition/segmentation and laboratory E-UIAIA methods. Additionally, field degradation trends of aggregate materials at different traffic levels can be captured during their service life using field imaging technology. Such system would automatically quantify the aggregate degradation trends and holds the potential to replace the prevailing subjective visual inspection and time consuming sampling and mechanical sieve analysis

practices. Ultimately, computer vision and image processing techniques can be combined with machine learning algorithms to develop degradation indices such as Imaging Based Fouling Index (IBFI) to represent different railroad ballast degradation levels and fouling conditions in the field.

Fitting well with sustainable engineering practices, further improvement and implementation of field aggregate imaging could provide mining industries and state and local transportation agencies with technologies for improved material specifications, aggregate quality control/quality assurance (QC/QA), optimized aggregate selection/utilization and associated significant economic benefits. The field aggregate imaging technology has the potential to be used by aggregate producers and/or state highway agencies for implementation in rock quarries and gravel mines supplying all the approved aggregate materials to highway agency projects throughout that country.

REFERENCES

[1]   Asphalt Institute, "Superpave Mix Design Series No.2 (SP-2)," 2001.

[2]   American Railway Engineering and Maintenance-of-Way Association (AREMA), "Manual for Railway Engineering (Volume1 - Track)," 2010.

[3]   Al-Rousan, T., Masad, E., Tutumluer, E., and Pan, T. , "Evaluation of Image Analysis Techniques for Quantifying Aggregate Shape Characteristics," *Journal of Construction and Building Materials,* vol. 21, pp. 978-990, 2007.

[4]   Wang, L., Sun, W., Lally, E. M., Wang, A., Druta, C., Tutumluer, E., "Application of LADAR in the Analysis of Aggregate Characteristics Report 724," Transportation Research Board, Washington, D.C., 2012.

[5]   Anochie-Boateng, J. K., Komba, J., Mvelase, G., "Three-dimensional laser scanning technique to quantify aggregate and ballast shape properties," *Journal of Construction and Building Materials,* vol. 43, pp. 389-398, 2013.

[6]   Kandhal, P. S. and Parker, J. F., "Aggregate Tests Related to Asphalt Concrete Performance in Pavements," National Cooperative Highway Research Program Report 405, Washington, D.C., 1998.

[7]   Meininger, R. C., "Aggregate Tests Related to Performance of Portland Cement Concrete Pavement," National Cooperative Highway Research Program Project 4-20, Washington, D.C., 1998.

[8]   Tutumluer, E. and Pan, T., "Aggregate Morphology Affecting Strength and Permanent Deformation Behavior of Unbound Aggregate Materials," *Journal of Materials in Civil Engineering,* vol. 20, no. 9, pp. 617-627, 2008.

[9]   Wnek, M .A., Tutumluer, E., Moaveni, M., Gehringer, E., "Investigation of Aggregate Properties Influencing Railroad Ballast Performance," *Journal of Transportation Research Board No.2374,* pp. 180-190, 2013.

[10]   Prowell, B. D., Zhang, Jingna,Brown, E. R., "Aggregate Properties and the Performane of Superpave-Designed Hot Mix Asphalt - NCHRP Report 539," National Cooperative Highway Research Program , Washington, D.C., 2005.

[11]   McLean, A.C., Gribble, C. D., Geology for Civil Engineers, E & FN Spon, Third Edition 2005.

[12]   Brown, R. H., Marek, C. R., "Effect of Crusher Operation on Corase Aggregate Shape," no. Publication#J96257, 1996.

[13]   Kojovic, T., "Crushing Aggregate: Shape and Control," Quarry Australia Magazine, Vol.3, No.6, 1995.

[14]   Barksdale, R. D., Pollard, C. O., Siegel, T., Moeller, S., "Evaluation of the Effect of Aggregate on Rutting and Fatigue of Asphalt," Technical Report FHWA-AG-92-8812, Atlanta, 1992.

[15]   Tutumluer, E., "Practices for Unbound Aggregate Pavement Layers," NCHRP Synthesis 445, Washington, D.C., 2013.

[16]   Perdomo, D., Button, J. W., "Identifying and Correcting Rut-Susceptible Asphalt Mixtures, Technical Report FHWA/TX-91/1121-2F," Texas Transportation Institute , 1991.

[17]   Dunford, A., "Friction and the Texture of Aggregate Particles Used in the Road Surface Course," University of Nottingham, 2013.

[18]   Thom, N. H., Brown, S. F., "The Effect of Grading and Density on the Mechanical Properties of a Crushed Dolomitic Limestone," in *Proceedings of the 14th ARRB Conference*, 1988.

[19]   Pavement interactive, 21 April 2011. [Online]. Available: http://www.pavementinteractive.org/article/flat-and-elongated-particles/. [Accessed 12 April 2014].

[20]   Davies, E. R., Computer and Machine Vision: Theory, Algorithms, Practicalities, Oxford: Elsevier, Fourth Edition 2012.

[21]   Trollhetta, "Advanced Image Analyses and Artificial Intelligence," Trollhetta AS, [Online]. Available: http://www.trollhetta.com/?page_id=52. [Accessed 15 Nov 2014].

[22]   Ioannis Brilakis, "Tracking Construction Site Resources with Machine Vision," Georgia School of Civil & Environmental Engineering, 3 10 2010. [Online]. Available: http://www.ce.gatech.edu/node/1801. [Accessed 4 May 2014].

[23]   Camargo, L. F. M., Resendiz, E., Hart, J. M., Edwards, J. R., Ahuja, N., Barkan, C. P. L., "Machine Vision Inspection of Railroad Track," Nextrans USDOT Region V Regional University Transportation Center, Urbana, 2011.

[24]   Gachet, P., Klubertanz, G., Vulliet, L., Laloui, L., "Interfacial Behavior of Unsaturated Soil with Small-scale Models and Use of Image Processing Techniques," *Geotechnical Testing Journal,* vol. 26, no. 1, pp. 1-10, 2003.

[25]   Masad, E., Al-Rousan, T., Button, J., Little, D., Tutumluer, E., "Test Methods for Characterizing Aggregate Shape, Texture, and Angularity," NCHRP Report 555 Transportation Research Board, Washington, D.C., 2007.

[26]   Tutumluer, E., Rao, C., and Stefanski, J. A., "Video Image Analysis of Aggregates," FHWA-IL-UI-278 Civil Engineering Studies UILU-ENG-2000-2015, Urbana, 2000.

[27]   Rao, C., Tutumluer, E., and Kim, I. T., "Quantification of Coarse Aggregate Angularity Based on Image Analysis," *Journal of Transportation Research Board No.1787,* pp. 117-124, 2002.

[28]   Pan, T., Tutumluer, E., and Anochie-Boateng, J., "Aggregate Morphology Affecting Resilient Behavior of Unbound Granular Materials," *Journal of Transportation Research Board No.1952,* pp. 12-20, 2006.

[29]   Xiao, Y., Tutumluer, E., "Best Value Granular Material for Road Foundations," Minnesota Department of Transportation Final Report MN/RC 2012-01, Minnesota, 2012.

[30]   Xiao, Y., Tutumluer, E., and Siekmeier, J., "Resilient Modulus Behavior Estimated from Aggregate Source Properties," in *In Proceedings of the GeoFrontiers Conference*, Dallas, 2011.

[31]   Rao, C., Development of 3-D Image Analysis Techniques to Determine Shape and Size Properties of Coarse Aggregate, Urbana: PhD Dissertation University of Illinois at Urbana-Champaign, 2001.

[32]   Deer, W. A., Howie, R. A., Zussman, J., Introduction to the Rock-Forming Minerals, Third ed., Mineralogical Society, 2013.

[33]   Sahoo, P. K., Soltani, S and Wong, A. K. C., A Survey of Thresholding Techniques, Computer Vision, Graphics, and Image Processing, vol. 41, 1988, pp. 233-260.

[34]   H. Boler, M. Wnek and E. Tutumluer, "Establishing Linkages between Ballast Degradation and Imaging Based Aggregate Particle Shape, Texture, and Angularity Indices," *Advances in Transportation Geotechnics,* vol. II, 2012.

[35]   Singh, D., Zaman, M., Commuri, S., "Effect of Production and Sample Preparation Methods on Aggregate Shape Parameters," *International Journal of Pavement Engineering No.2,* vol. 14, 2013.

[36]   Moaveni, M., Wang, S., Hart, J. M., Tutumluer, E., and Ahuja, N., "Evaluation of Aggregate Size and Shape by Means of Segmentation Techniques and Aggregate Image Processing Algorithms," *Journal of the Transportation Research Board No. 2335,* 2013.

[37]   Mc Daniel, R., Anderson, R. M., "Recommended Use of Reclaimed Asphalt Pavement in the Superpave Mix Design Method: Technician's Manual NCHRP Report 452," Transportation Research Board - National Research Academy, Washington, D.C., 2001.

[38]   Browne, C., Rauch, F. A., Hass, T. C., Kim, H., "Comparison Tests of Automated Equipment for Analyzing Aggregate Gradation," in *9th Annual Symposium of the International Center for Aggregates Research*, Austin, TX, 2001.

[39]   Tyler, W. S., *Particle Size and Shape Analyzers (CPA) - Product Brochure,* Mentor, OH, 2001.

[40]   "CPA Particle Size Analyzer and Particle Shape Analyzer," W.S. Tyler® Industrial Group, [Online]. Available: http://wstyler.com/particle-analysis/cpa-particle-size-and-shape-analyzer. [Accessed 15 November 2014].

[41]   Maerz, N. H., Zhou, W., "Flat and Elongated: Advances Using Digital Image Analysis," in *9th Annual Symposium of the International Center for Aggregates Research*, Austin, TX.

[42]   "Measuring the Size and Shape of Aggregates," Missouri University of Science and Technology, 14 November 2014. [Online]. Available: http://ge.mst.edu/gee/shape/.

[43]   Masad, E., "The Development of a Computer Controlled Image Analysis System," National Cooperative Highway Research Program NCHRP-IDEA Project 77 Final Report, Washington, D.C, 2003.

[44]   Gates, L., Masad, E., Pyle, R., Bushee, D., "Aggregate Imaging Measurement System 2 (AIMS2): Final Report FHWA-HIF-11-030," Washington, D.C..

[45]   Otsu, N., "A Threshold Selection Method from Gray-Level Histograms," *IEEE Transactions on Systems, Man, and Cybernetics,* vol. 9, no. 1, pp. 62-66, 1979.

[46]   Pan, T., Investigation of Coarse Aggregate Morphology Affecting Hot Mix Behavior Using Image Analysis, University of Illinois at Urbana-Champaign: PhD Dissertation, 2006.

[47]   Russ, J. C., The image Processing Handbook 3rd Edition, Boca Raton, FL: CRC Press, 1992.

[48]   T. T. E. Pan, "Imaging-based direct measurment of aggregate surface area and its application in asphalt mixture design," *International Journal of Pavement Engineering,* vol. 11, no. 5, pp. 415-428, 2010.

[49]   "LPX-60DS/600DS/1200DS 3D Laser Scanners," Roland DGA Corporation, 10 Nov 2014. [Online]. Available: http://rolanddga.com/products/scanners_new/lpx600/specifications.asp#subNav Top.

[50]   Komba, J. J., Anochie-Boateng, J. K., "Analytical and Laser Scanning Techniques to Determine Shape Properties of Aggregates," *Journal of Transportation Research Board No.2335*, pp. 60-71, 2013.

[51]   E. T. Selig and J. M. Waters, Track Geotechnology and Substructure, London: Telford, 1994.

[52]   Luce, A., Mahmoud, E., Masad, E., Chowdhury, A., "Relationship of Aggregate Microtexture to Asphalt Pavement Skid Resistance," *Journal of Testing and Evaluation ASTM,* vol. 35, no. 6, pp. 578-588, 2007.

[53]   Forster, S. W., "Pavement Microtexture and its Relation to Skid Resistance," *Journal of Transportation Research Board No.1215,* pp. 151-164, 1989.

[54]   H. Huang, Discrete Element Modeling of Railroad Ballast Using Imaging Based Aggregate Morphology Characterization PhD Dissertation, Urbana-Champaign: University of Illinois, 2010, pp. 3-5.

[55]   Uthus, L., Deformation Properties of Unbound Granular Aggregates PhD Dissertation, 2007: Norwegian University of Science and Technology, p. 41.

[56]   Han, X., Evaluation of ballast materials based on ballast particle characteristics and functions PhD Dissertation, University of Massachusetts in Amherst, 1998.

[57]   Quiroga, P. N., Fowler, D. W., "The Effects of Aggregate Characteristics on The Performance of Portland Cement Concrete," ICAR Research Report No. 104-1F, 2004.

[58]   Polat, R., Yadollahi, M. M., Sagsoz, A. E., Arasan, S., "The Correlation Between Aggregate Shape and Compressive Srength of Concrete: Digital Image Processing Approach," *International Journal of Structure and Civil Engineering Research,* vol. 2, no. 3, pp. 62-80, 2013.

[59]   Coree, B. J., Hislop, W. P., "A Laboratory Investigation into The Effects of Aggregate-Related Factors on Critical VMA in Asphalt Paving Mixture," Center for Transportation Research and Education Project 98-20 Iowa Department of Transportation, 2000.

[60]   Masad, E., Luce, A., Mahmoud, E., Chowdhury, A., "Relationship of Aggregate Texture to Asphalt Pavement Skid Resistance Using Iamge Analysis of Aggregate Shape Project 114," Transportation Research Board , Washington, D.C., 2007.

[61]   Tolppanen, P., 3D Characterization and Degradation Analysis of Rock Aggregates Doctoral Thesis, Royal Institute of Technology, Stockholm Sweden: Department of Civil and Environmental Engineering, 2001.

[62]   Moavenzadeh, F., Goetz, W. H., "Aggregate Degradation In Bituminous Mixtures: Technical Paper,," Publication FHWA/IN/JHRP-63/05 Joint Transportation Research Program, Indiana Department of Transportation and Purdue University, 1963.

[63]   Nurmikolu, A., Degradation and Frost Susceptibility of Crushed Rock Aggregates Used in Structural Layers of Railway Track Doctoral Thesis, Finland: Tampere University of Technology, 2005.

[64]   Page, G. C., Musselman, J. A. and Romano, D. C., "Effects of Aggregate Degradation on Air Voids of Structural Asphalt Mixture in Florida," *Journal of Transportation Research Board No.1583,* pp. 19-27, 1997.

[65]   Raymond, G. P., "Reinforced Ballast Behaviour Subjected to Repeated Load," *Geotextiles and Geomembranes,* vol. 20, pp. 39-61, 2002.

[66]   Pintner, R. M., Vinson, T. S. and Johnson, E. G. , "Nature of Fines Produced in Aggregate Processing," *ASCE Journal of Cold Regions Engineering,* vol. 1, no. 1, pp. 10-12, 1987.

[67]   Gatchalian, D., Masad, E., Chowdhury, A., and Little, D., "Characterization of Aggregate Resistance to Degradation in Stone Matrix Asphalt Mixtures," International Center for Aggregate Research, Report 204-1F, 2006.

[68]   Lynn, T., James, R. S., Wu, P. Y., Jared, D. M., "Effect of Aggregate Degradation on Volumetric Properties of Georgia's Hot-Mix-Asphalt," *Journal of Transportation Research Board No.1998,* pp. 123-131, 2007.

[69]   Alemu, A. Y., Survey of Railway Ballast Selection and Aspects of Modelling Techniques - Master Thesis, Stockholm: School of Architecture and the Built Environment, Royal Institute of Technology , 2011.

[70]   Selig, E. T., Boucher, D. L., "Abrasion Tests for Railroad Ballast," *American Society for Testing and Materials,* vol. 13, no. 4, pp. 301-311, 1990.

[71]   Saeed, A., Hall, J. W., Barker, W., "NCHRP Report 453: Performance-Related Tests of Aggregates for Use in Unbound Pavement Layers," Transportation Research Board, Washington, D.C., 2001.

[72]   Wu, Y., Parker, F., Kandhal, P.S., "Aggregate toughness/abrasion resistance and durability/soundness tests related to asphalt concrete performance in pavements," *Journal of Transportation Research Board No.1638,* pp. 85-93, 1998.

[73]   Folliard, K. J., Smith, K. D., "Aggregate Tests for Portland Cement Concrete Pavements: Review and Recommendations - Reseach Results Digest," Transportation Research Board, 2003.

[74]   Clifton, A. W., Klassen, M. J., Watters, B. R., "Production and Testing of Ballast," *Journal of Transportation Research Board No. 1131,* pp. 26-34, 1987.

[75]   Klassen, M. J., Clifton, A. W., Watters, B. R., "Track Evaluation and Ballast Performance Specification," *Journal of Transportation Research Board,* vol. 1131, pp. 35-44, 1987.

[76]   Raymond, G., Bathurst, R., "Repeated Load Response of Aggregate in Relation to Track Quality Index," *Canadian Geotechnical Journal,* vol. 4, no. 31, pp. 547-554, 1994.

[77]   Jain, R., Kasturi, R., Schunk, B.G., Machine Vision, McGraw-Hill, 1995.

[78]   Rouse, M, "machine vision," 1 Sep 2005. [Online]. Available: http://whatis.techtarget.com/definition/machine-vision. [Accessed 5 May 2014].

[79]   "Colour Image Processing," 1999. [Online]. Available: http://homepages.inf.ed.ac.uk/rbf/CVonline/LOCAL_COPIES/OWENS/LECT14/lecture12.html#gonzwoods.

[80]   "Color Physics," [Online]. Available: http://facweb.cs.depaul.edu/sgrais/Color%20Physics.htm.

[81]   "RGB Color Space - Color Space Conversion," [Online]. Available: http://www.blackice.com/colorspaceRGB.htm.

[82]   Bovik, A., The Essential Guide to Image Processing - Second Edition, Austin, TX: Department of Electrical and Computer Engineering, University of Texas, 2009.

[83]   Rotaru, C., Graf, T., Zhang, J., "Color image segmentation in HSI space for automotive applications," *Journal of Real-Time Image Processing,* vol. 3, no. 4, pp. 311-322, 2008.

[84]   Comaniciu, D., Meer, P., "Mean Shift: A Robust Approach toward Feature Space Analysis," *IEEE Trans. Pattern Analysis and Machine Intelligence,* vol. 24, no. 5, pp. 603-619, 2002.

[85]   Carson, C., Belongie, S., Greenspan, H., Malik, "Image Segmentation using Expectation-minimization and Its Application to Image Querying," *IEEE Trans. Pattern Analysis and Machine Intelligence,* vol. 24, no. 8, pp. 1026-1038, 2002.

[86]   Adams, R., Bischof, L., "Seeded Region Growing," *IEEE Trans, Pattern Analysis and Machine Intelligence,* vol. 16, no. 6, pp. 641-647, 1994.

[87]   Zabih, R., Kolmogorov, V., "Spatially Coherent Clustering Using Graph Cuts," in *In Proceedings of Computer Vision and Pattern Recognition (CVPR)*, Washington, D.C., 2004.

[88]   Shi, J., Malik, J., "Normalized Cuts and Image Segmentation,," *IEEE Trans Pattern Analysis and Machine Intelligence,* vol. 22, no. 8, pp. 888-905, 2000.

[89]   Eriksson, A. P., Barr, O., Astrom, K., *Image Segmentation Using Minimal Graph Cuts,* Sweden: Center for Mathemattical Science, Lund University.

[90]   National Instrument Corporation, *IMAQ Vision for LabVIEW User Manual,* 2003.

[91]   Relf, C. G., Image Acquisition and Processing with Lab View, CRC Press, 2004.

[92]   "2200 Series End Drive Conveyors," DORNER, 10 Sep 2014. [Online]. Available: http://www.dornerconveyors.com/Products/2X-Series-Conveyors/2200-Series/End-Drive-Conveyors.aspx.

[93]   Gonzalez, R.C., Woods, R. E., Eddins, S. L, Digital Image Processing Using Matlab, Tata McGraw Hill, 2010.

[94]   Mansurov, N., "What is Distortion?," [Online]. Available: http://photographylife.com/what-is-distortion. [Accessed 14 May 2014].

[95]   Mahmoud, E., Masad, E. , " Experimental Methods for the Evaluation of Aggregate Resistance to Polishing, Abrasion, and breakage," *Journal of Materials in Civil Engineering,* vol. 19, no. 11, 2007.

[96]   Fletcher, T., Chandan, C., Masad, E., Sivakumar, K., "Aggregate Imaging System (AIMS) for Characterizing the Shape of Fine and Coarse Aggregate," *Journal of Transportation Research Board No.1832*, pp. 67-77, 2003.

[97]   Al-Rousan, T., Masad, E., Myers, L., Speigelman, C., "New Technology for Shape Classification of Aggregates," *Transportation Research Record,* no. 1913, pp. 11-23, 2005.

[98]   A-Qadi, I. L., Elseifi, M. A., Carpenter, S. H., "Reclaimed Asphalt Pavement: A Literature Review," Illinois Center for Transportation, Springfield, 2007.

[99]   Howard, I. L., Cooley Jr., A. L., Doyle, J. D., "Laboratory Testing and Economic Analysis of High RAP Warm Mixed Asphalt," Mississippi Department of Transportation, Jackson, 2009.

[100]   Brock, J. D., Richmond, J. L., "Milling and Recycling," ASTEC, Chattanooga, 2007.

[101]   Scheartle, G. J., Edil, T., "Engineering Properties of Recycled Materials for Unbound Applications Task1A: Literature Review," University f Wisconsin-Madison, Madison, 2009.

[102]   Vavrik, W. R., Carpenter, S. H., Gillen, S., Behnke, J., Garrot, F., "Evaluation of Field Produced Hot Mix Asphalt (HMA) Mixtures with Fractionated Recycled Asphalt Pavement (RAP)," Illinois State Toll Highway Authority, 2008.

[103]   Brand, A. S., Amirkhanian, A. N., Roesler, J. R., " Flextural Capacity of Rigid Pavement Concrete Slabs with Recycled Aggregates. Report No. ICT-13-018," Illinois Center for Transportation, 2013.

[104]   Brand, A. S., Roesler, J. R., "Concrete with Steel Furnace Slag Fractionated Reclaimed Asphalt Pavement. Report No. ICT-14-015," Illinois Center for Transportation, 2014.

[105]   Brand, A. S., and Roesler, J. R., . 2014, "Ternary Concrete with Fractionated Reclaimed Asphalt Pavement," *ACI Materials Journal,* 2014, in press.

[106]   West, R. , "Reclaimed Asphalt Pavement Management: Best Practices," National Center for Asphalt Technology, Auburn, 2010.

[107]   Copeland, A. , "Reclaimed Asphalt Pavement in Asphalt Mixtures: State of the Practice," Turner-Fairbank Highway Research Center, McLean, 2011.

[108]   Knadhal, P. M., Mallick, R. B. , Pavement Recycling guidelines for State and Local Goverments-Participant's Refrence Book., Auburn: Naional Center for Asphalt Technology, 1997.

[109]   McDaniel, R., Anderson, R. M. , "Recommended Use of Reclaimed Asphalt Pavement in the Superpave Mix Design Method: Technician's Manual," National Academy Press, Washington, D.C., 2001.

[110]   Hill, B., Behnia, B., Buttlar, W.G., Reis, H. , "Evaluation of Warm Mix Asphalt Mixtures Contaning Reclaimed Asphalt Pavement Through Mechanical Performance Tests and an Acoustic Emission Approach," *Journal of Materials in Civil Engineering,* vol. 25, no. 12, pp. 1887-1897, 2013.

[111]   Shirodkar, P., Mehta, Y., Nolan, A., Sonpai, K., Norton, A., Tomlinson, C., Dubois, E., Sullivan, P. and Sauber, R. , "A study to Determine the Degree of Partial Blending of Reclaimed Asphalt Pavement (RAP) Binder for High RAP Hot Mix Asphalt," *Journal of Construction and Building Materials,* vol. 25, no. 1, pp. 150-155, 2011.

[112]   Huang, B., Shu, X., Burdette, E. G. , "Mechanical Properties of Concerete Contaning Recycled Asphalt Pavements," *Magazine of Concrete Research,* vol. 58, no. 5, pp. 313-320, 2006.

[113]   Huang, B., Shu, X., Li, G., "Laboratory Investigation of Portland Cement Concrete Containing Recycled Asphalt Pavements," *Cement and Concrete Research,* vol. 35, no. 10, pp. 2008-2013, 2005.

[114]   Garcia, H. C., Tia, M., Roque, R., Choubane, B., "Alternative Solvent for Reducing Health and Environmnetal Hazards in Extracting Asphalt: An Evaluation," *Journal of Transportation Research Board,* vol. 1712, pp. 79-85, 2007.

[115]   Raju, P. D. R., Neelima, G. , "Image Segmentation by Using Histogram Thresholding," *IJCSET,* vol. 2, no. 1, pp. 776-779, 2012.

[116]   *MATLAB and Image Processing Toolbox,* Natick, Massachusetts: The MathWorks, Inc., 2013.

[117]   Hillerborg, A. , "The Theoretical Basis of a Method to Determine the Fracture Energy Gf of Concrete," *Materials and Structures,* vol. 18, no. 4, pp. 291-296, 1985.

[118]   Brand, A. S., Amirkhanian, A. N., Roesler, J. R., "Flextural Capacity of Full-Depth and Two-Lift Concrete Slabs with Recycled Aggregates," *Journal of Transportation Research Board,* 2014.

[119]   Shapiro, L. G., Stockman, G. C., Computer Vision, New Jersey: Prentice Hall, 2001, pp. 279-281.

[120]   Akbas, E., Generation and Analysis of Segmentation Trees for Natural Images, PhD Dissertation, University of Illinois at Urbana Champaign, 2011, pp. 9-11.

[121]   Li, S.Z., "Markov Random Field Models in Computer Vision," in *In Proceedings of the European Conference on Computer Vision*, Stockholm, Sweden, 1994.

[122]   Boykov, Y. Y, Jolly, M. P. , "Interactive Graph Cuts for Optimal Boundary & Region Segmentation of Objects in N-D Images," in *In Proceedings of International Conference on Computer Vision*, Vancouver, 2001.

[123]   Lin, C. K., Hsu, L. H., Graph Theory and Interconnection Networks, CRC Press, 2008, pp. 1-20.

[124]   "Introduction to Graph Theory," [Online]. Available: http://www.analytictech.com/networks/graphtheory.htm. [Accessed 15 March 2015].

[125]   Lézoray, O., Grady, L., Image Processing and Analysis with Graph: Theory and Practice, Boca Raton, FL: CRC Press, Taylor & Francis Group, 2012.

[126]   Jepson, A., "Introduction to Image Segmentation," University of Toronto, 16 August 2010. [Online]. Available: http://www.cs.toronto.edu/~jepson/researchISeg.html#pub. [Accessed 10 Nov 2014].

[127]   Sinha, S. N., "Graph Cut Algorithms in Vision, Graphics and Machine Learning An Integrative Paper," University of North Carolina , Chapel Hill, 2008.

[128]   Schroeder, J., Pires Guedes, A., Duarte Jr., E. P., "Computing the Minimum Cut and Maximum Flow of Undirected Graphs," Federal University of Paran´a, 2004.

[129]   "nEo iMaging," [Online]. Available: http://www.neoimaging.cn/en/. [Accessed 15 April 2014].

[130]   "Standard Specification for Road and Bridge Construction," Illinois Department of Transportation (IDOT), 2012.

[131]   Vujovic, I., Multiresolution Approach to Processing Images for Different Applications, New York: Springer, 2015.

APPENDIX A

WIRING DIAGRAM FOR E-UIAIA
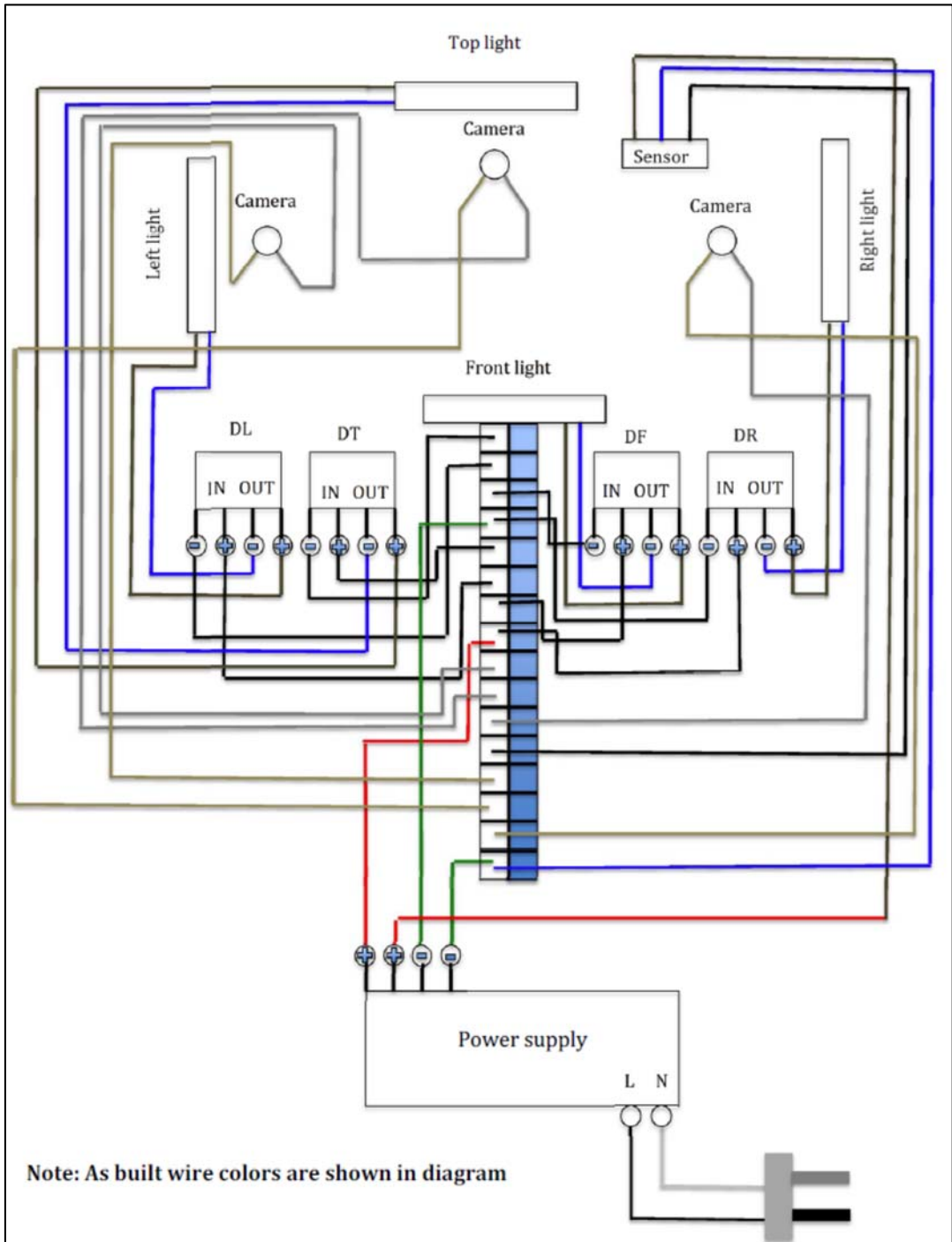
Figure A.1 Wiring Diagram for E-UIAIA

APPENDIX B

LABVIEW VIs FOR COMPUTING AGGREGATE SHAPE

PROPERTIES IN E-UIAIA
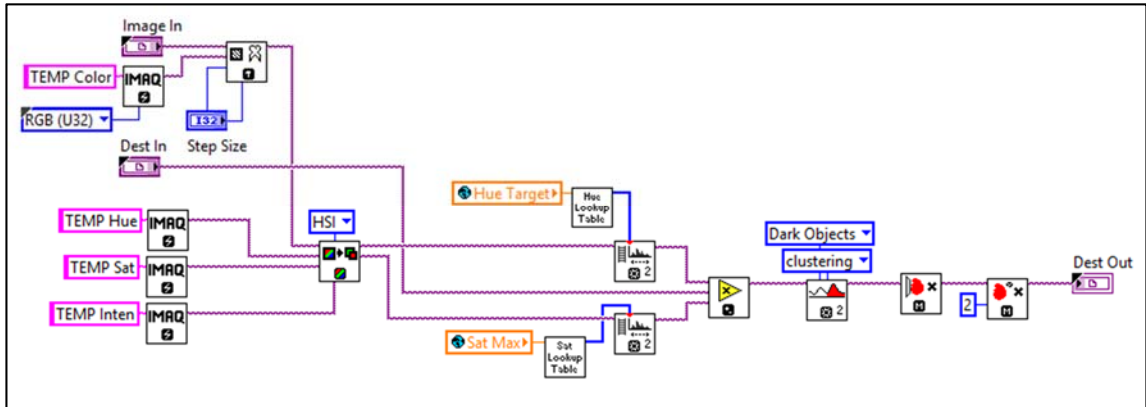
Figure B.1 Threshold Color Image
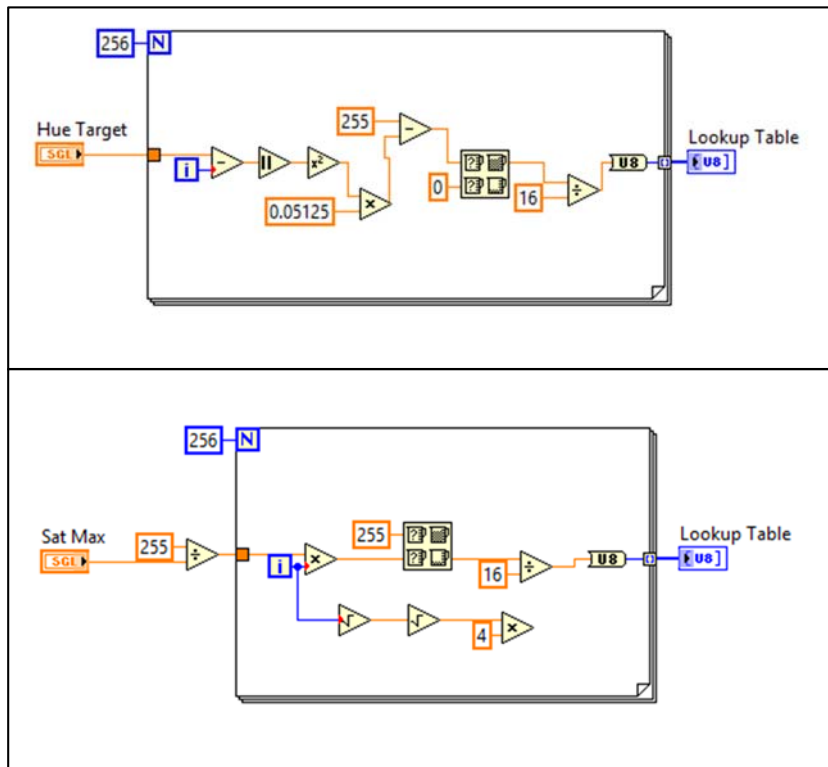
Figure B.2 Hue and Saturation Look Up Table
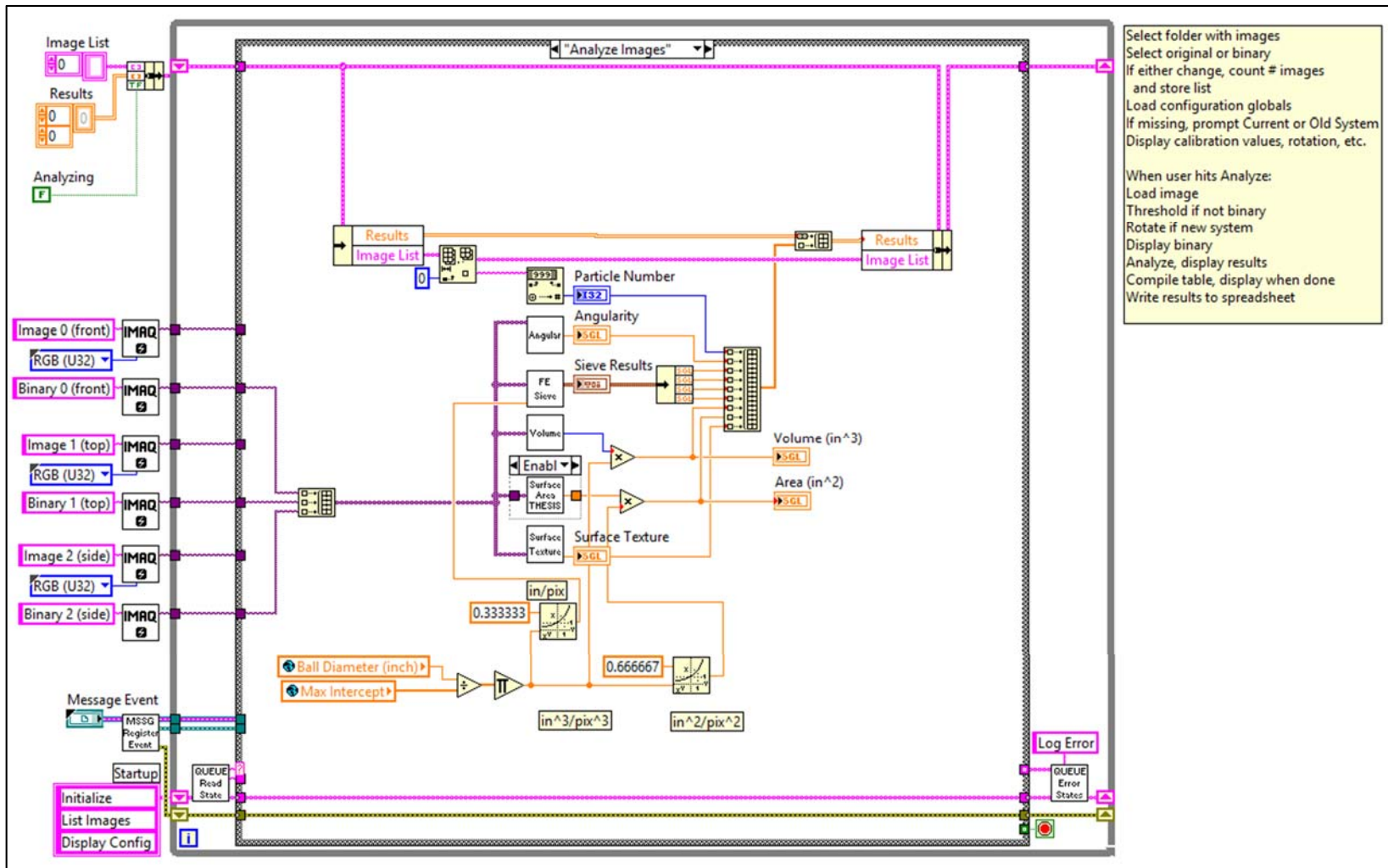
Figure B.3 Central Module to Analyze Images and Compute Particle Shape Properties

APPENDIX C

DISTRIBUTION CURVES FOR SHAPE PROPERTIES OF RAILROAD BALLAST BEFORE AND AFTER LA-ABRASION TESTING
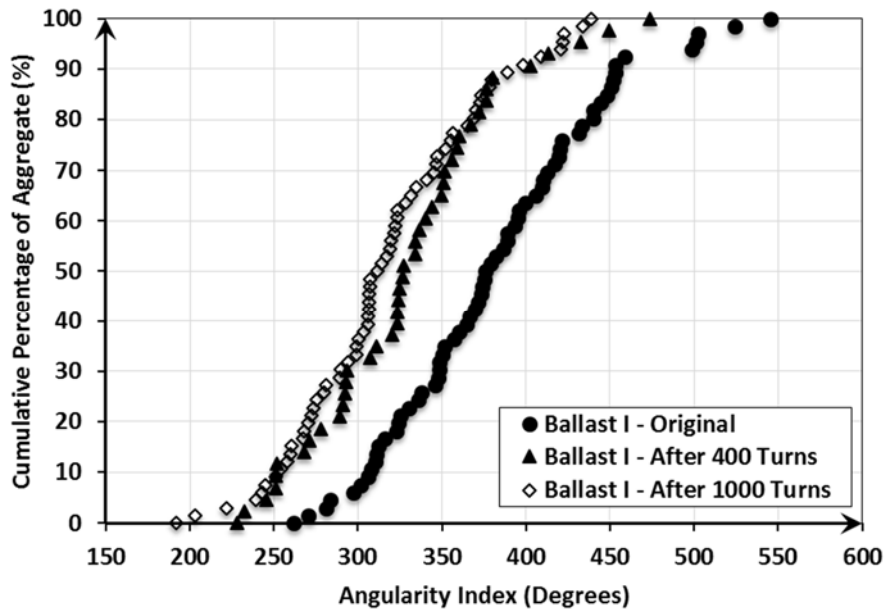
Figure C.1 Angularity Index at Different Degradation Levels for Ballast I
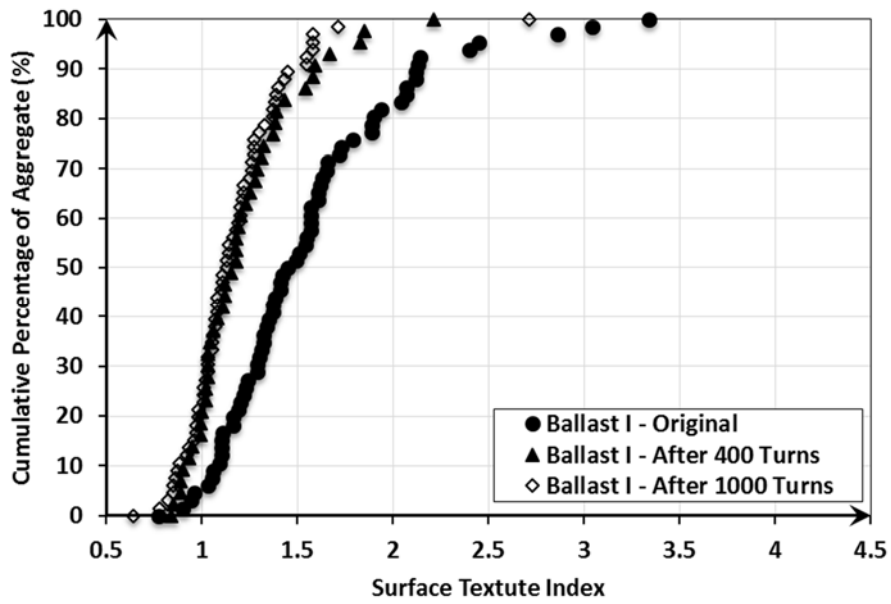
Figure C.2 Surface Texture Index at Different Degradation Levels for Ballast I
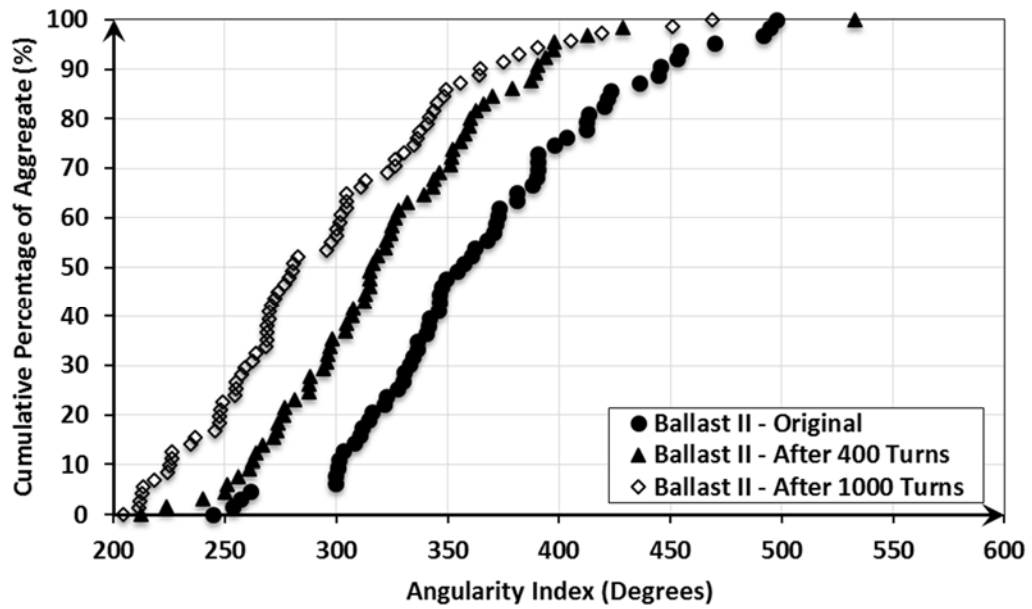
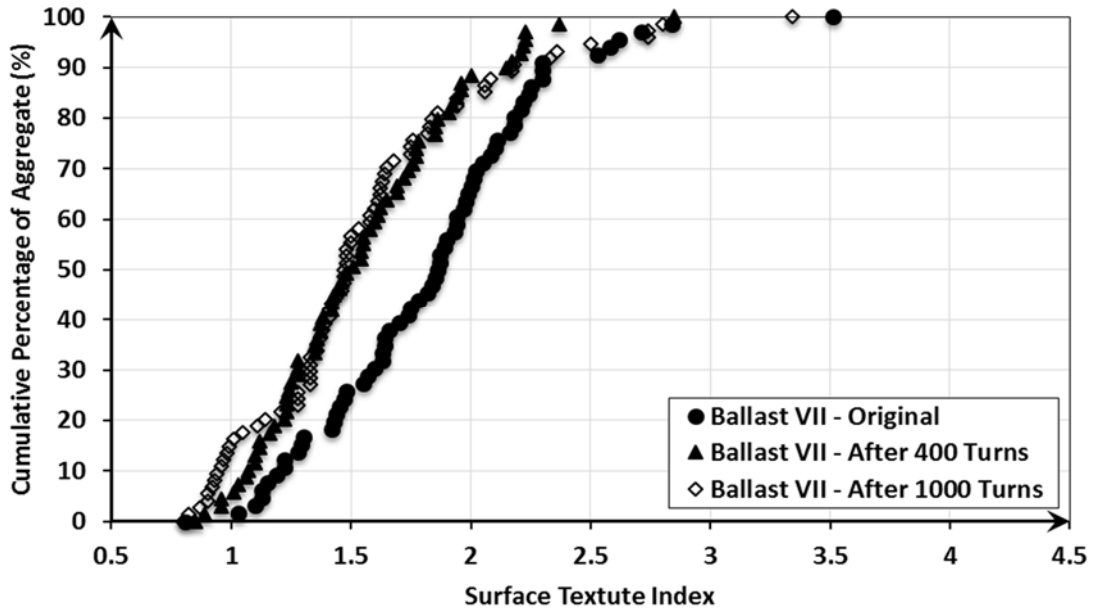Figure C.3 Angularity Index at Different Degradation Levels for Ballast II
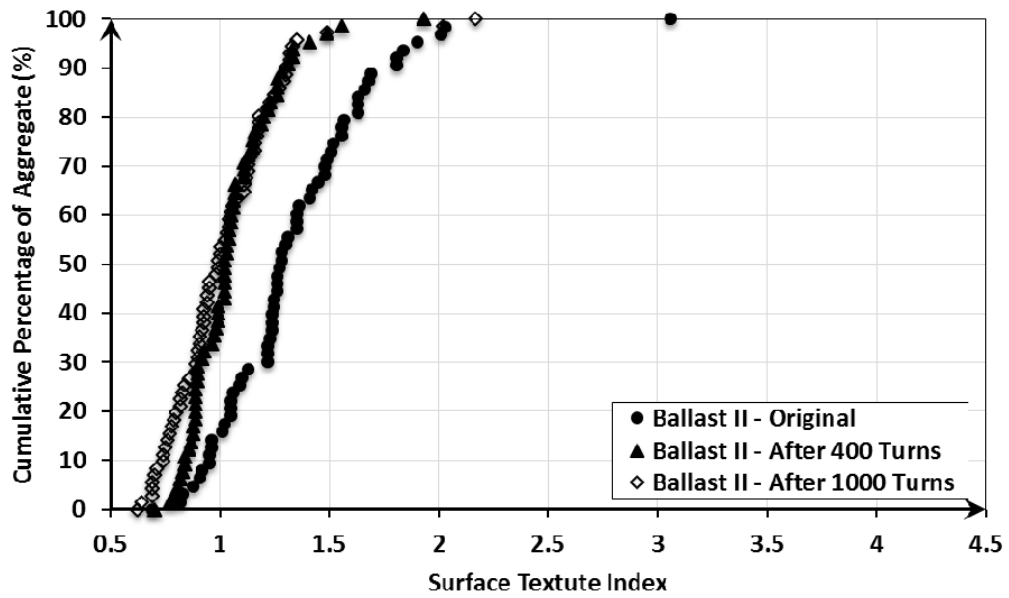
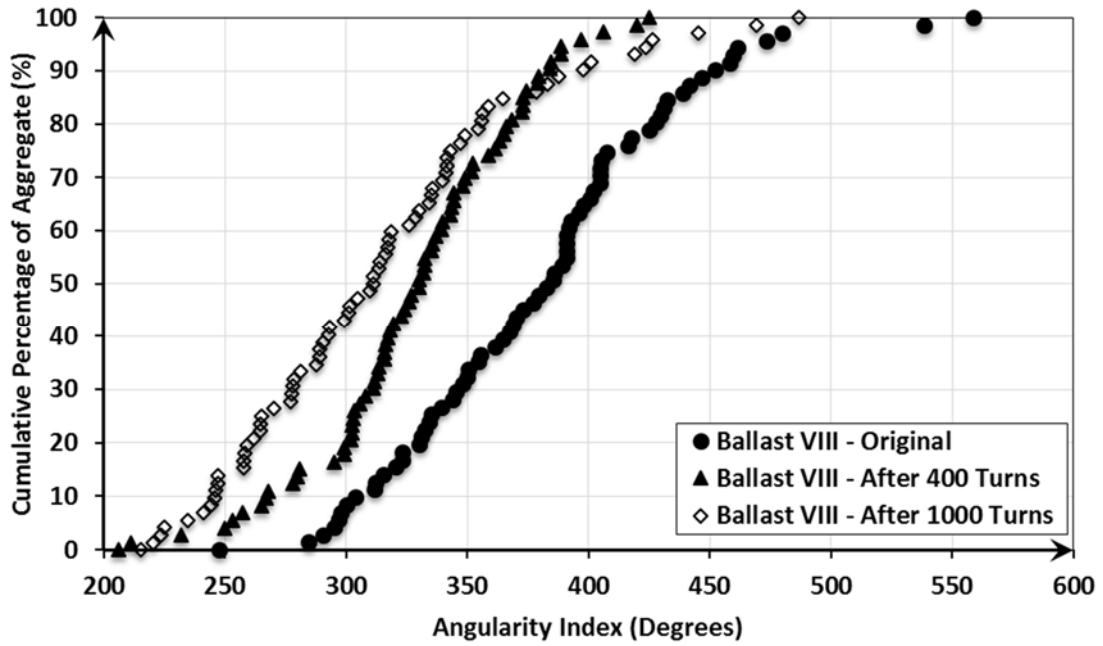Figure C.4 Surface Texture Index at Different Degradation Levels for Ballast II
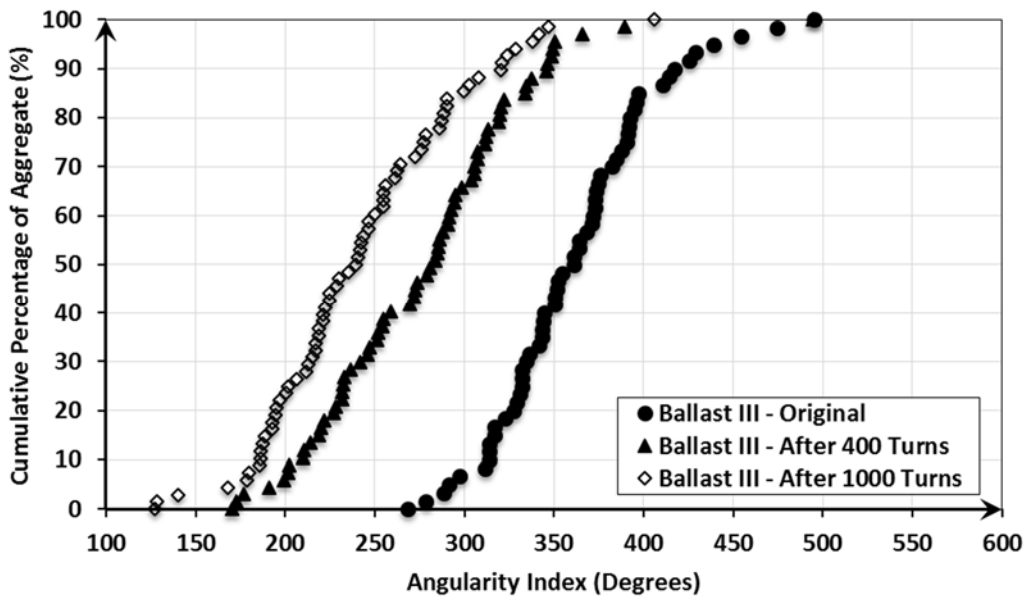
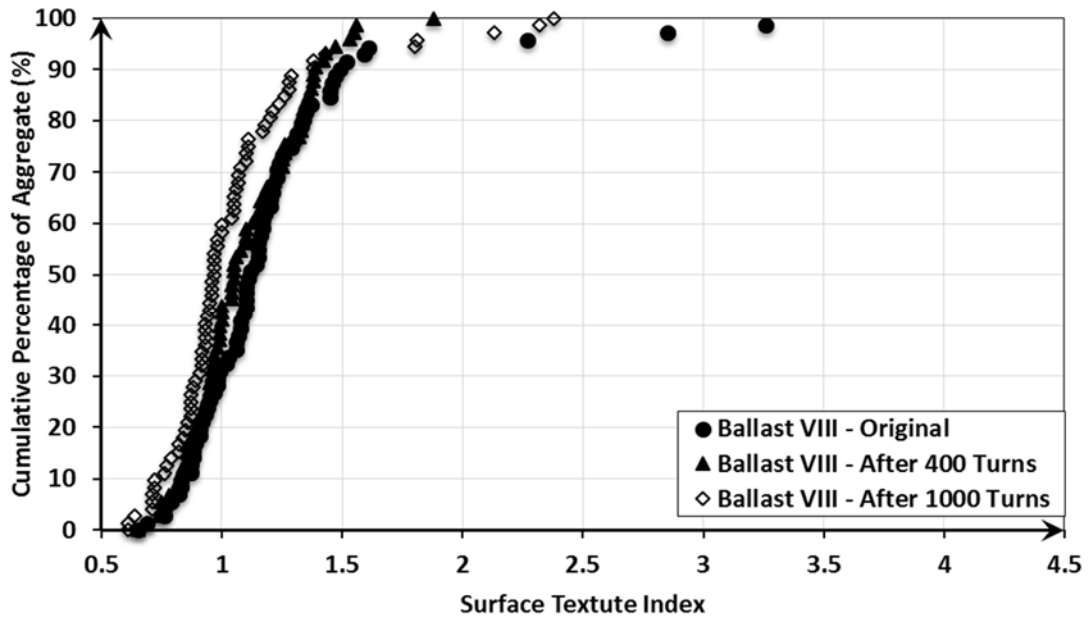Figure C.5 Angularity Index at Different Degradation Levels for Ballast III
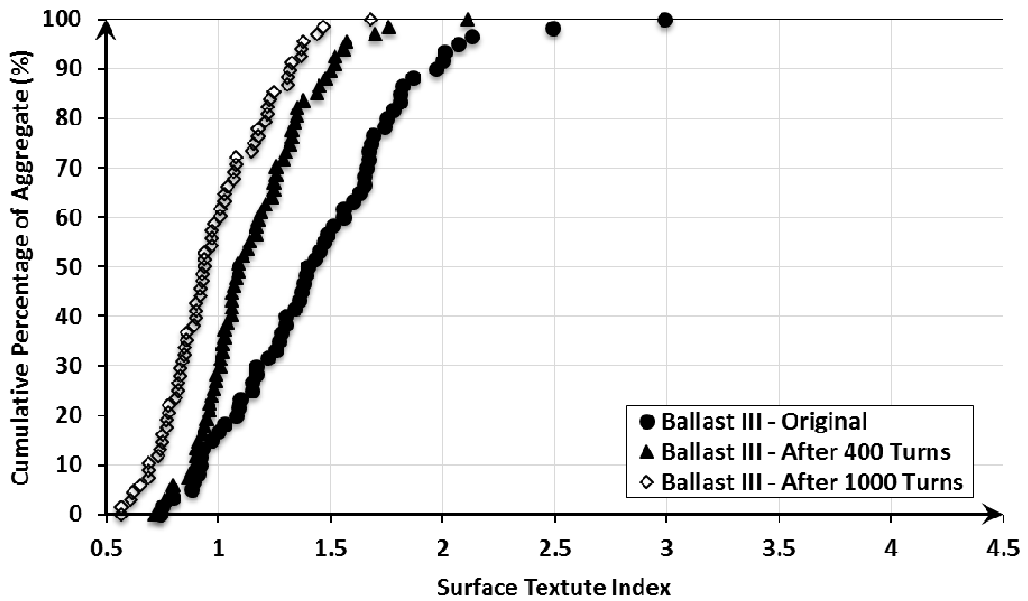
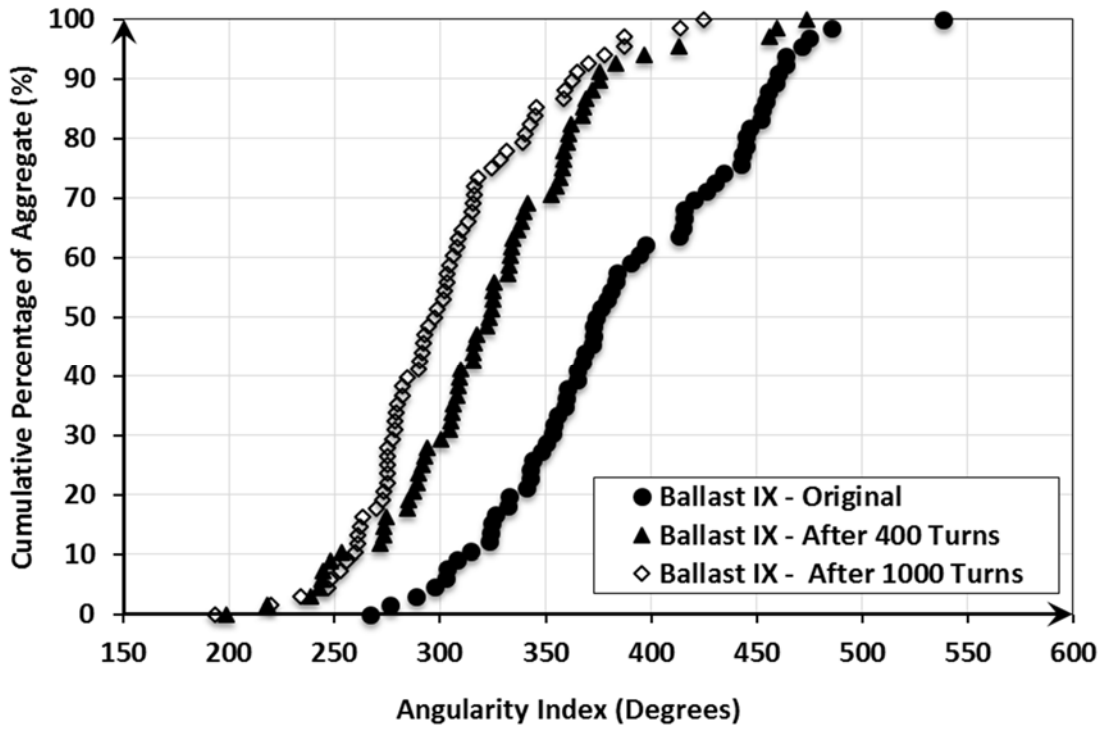Figure C.6 Surface Texture Index at Different Degradation Levels for Ballast III
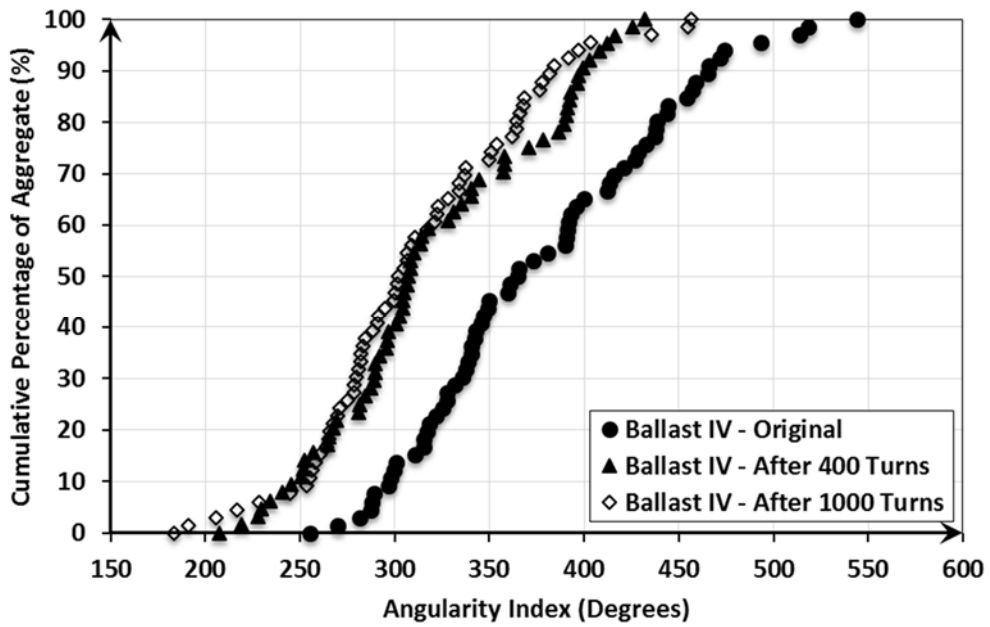
Figure C.7 Angularity Index at Different Degradation Levels for Ballast IV
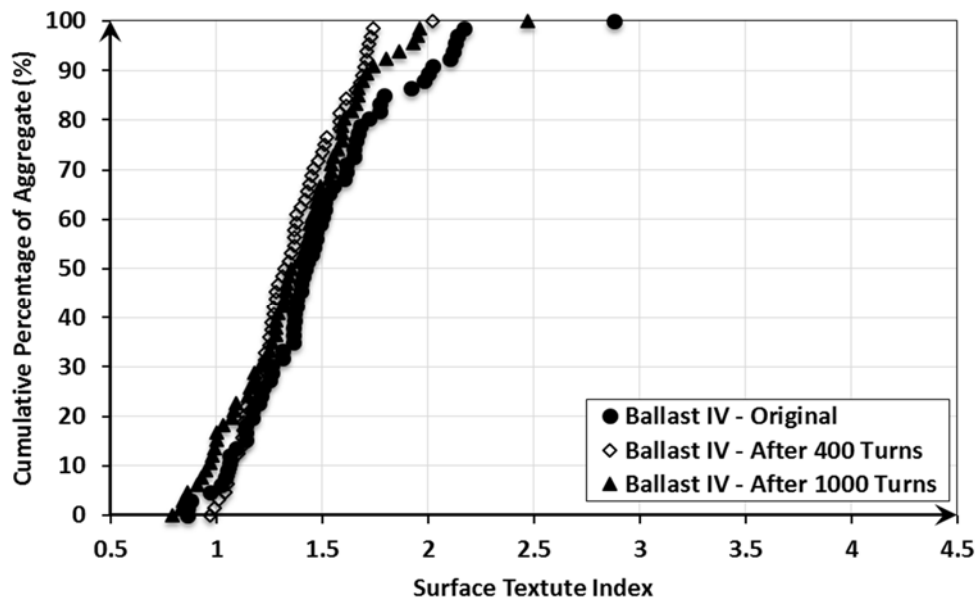
Figure C.8 Surface Texture Index at Different Degradation Levels for Ballast IV
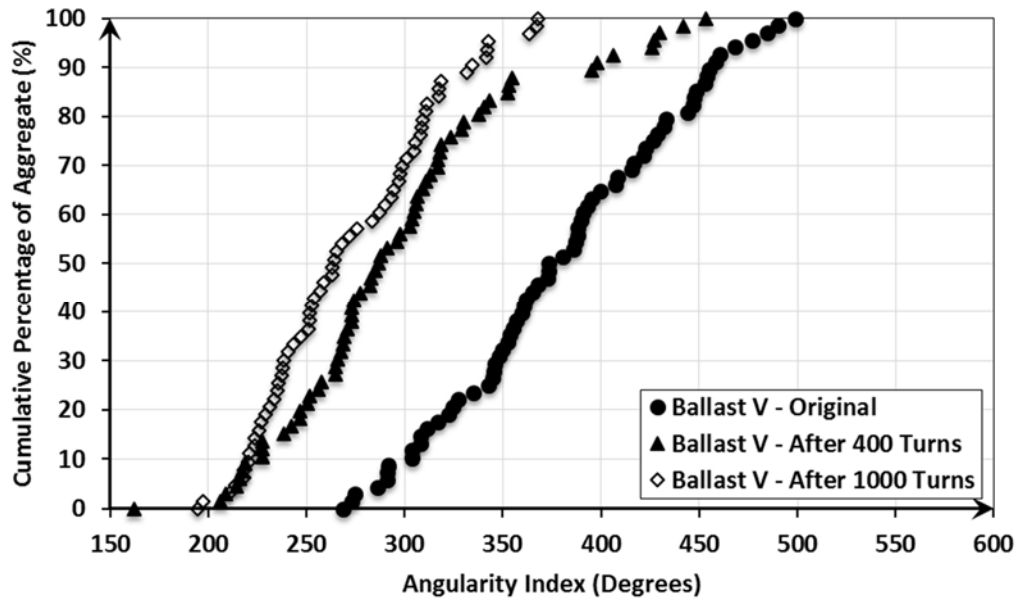
Figure C.9 Angularity Index at Different Degradation Levels for Ballast V
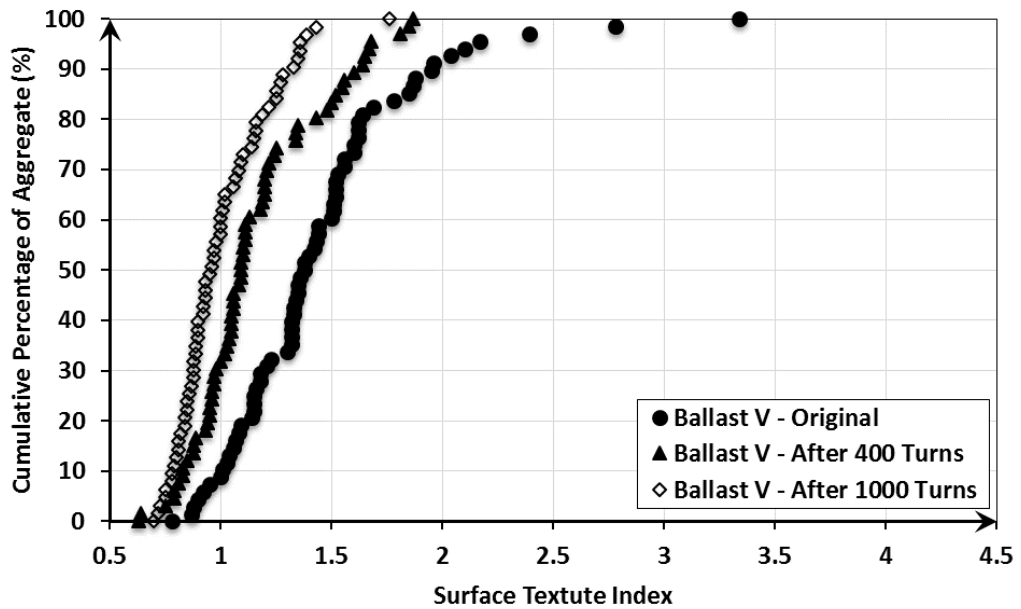
Figure C.10 Surface Texture Index at Different Degradation Levels for Ballast V
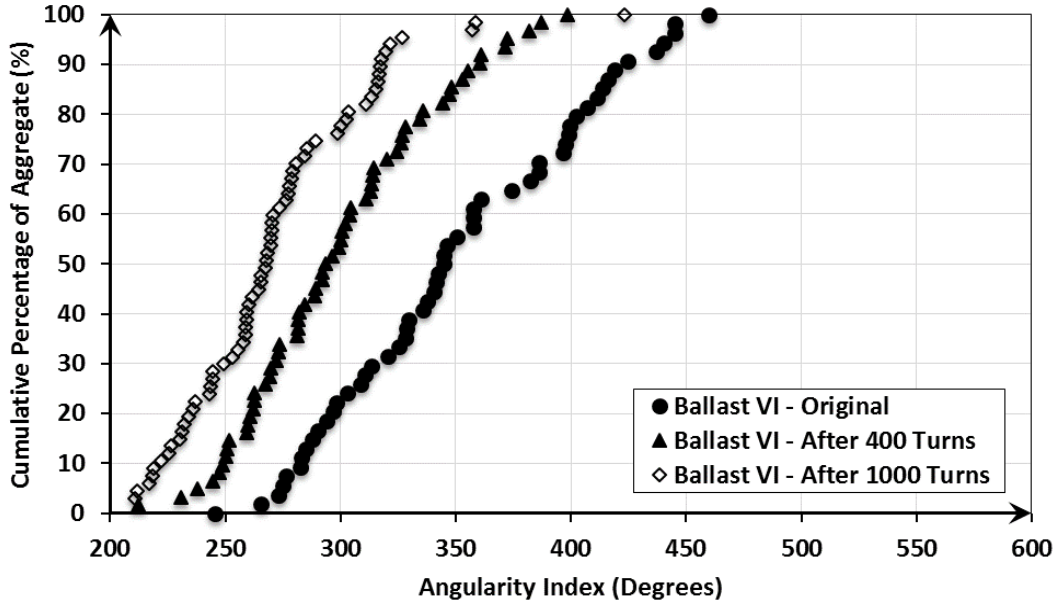
Figure C.11 Angularity Index at Different Degradation Levels for Ballast VI
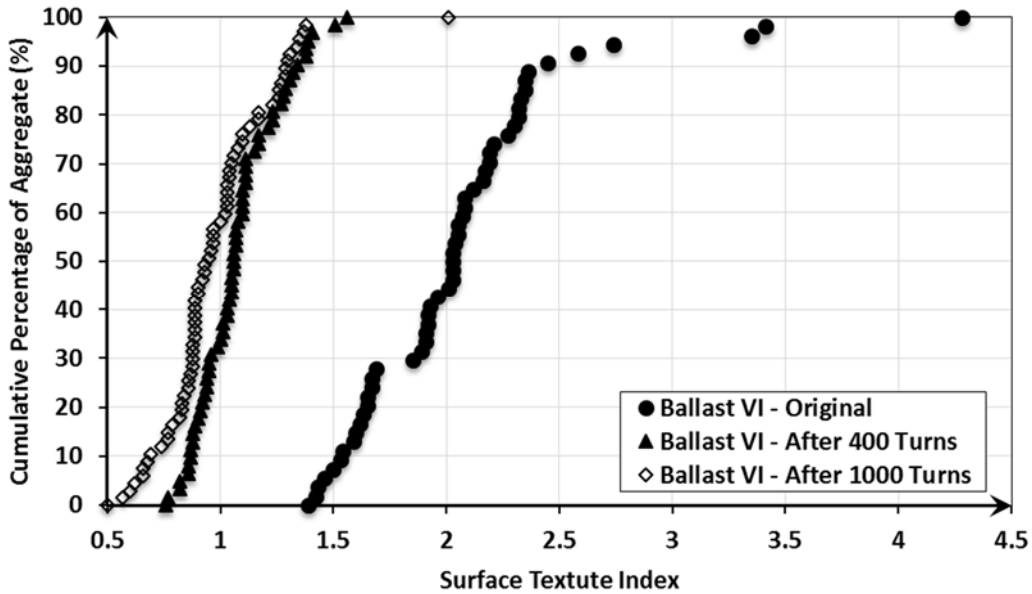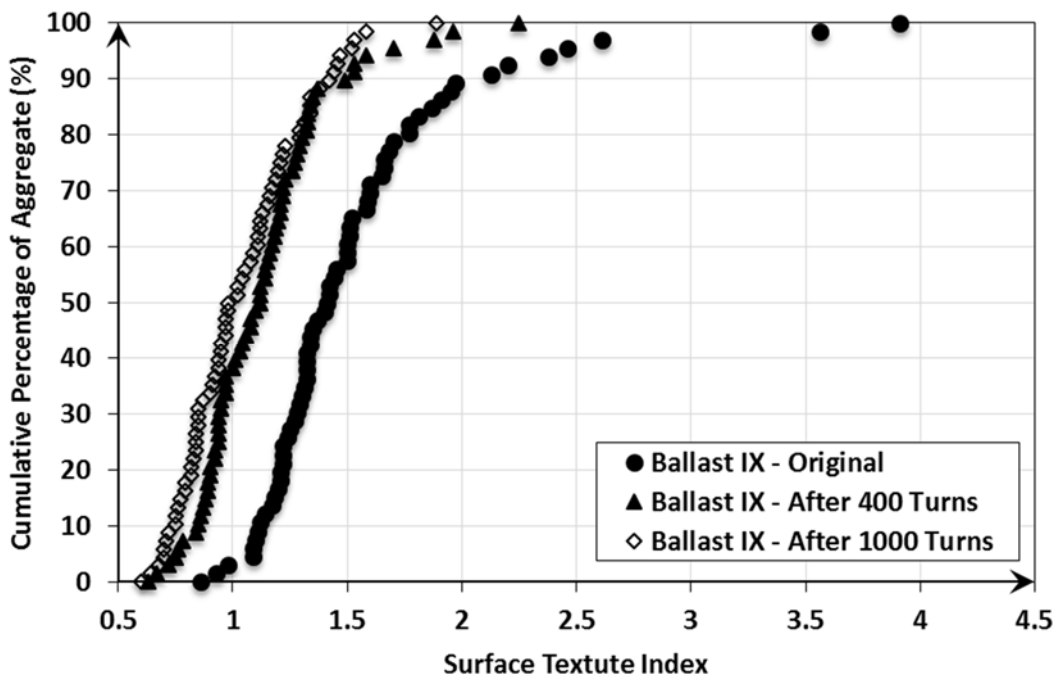

Figure C.12 Surface Texture Index at Different Degradation Levels for Ballast VI
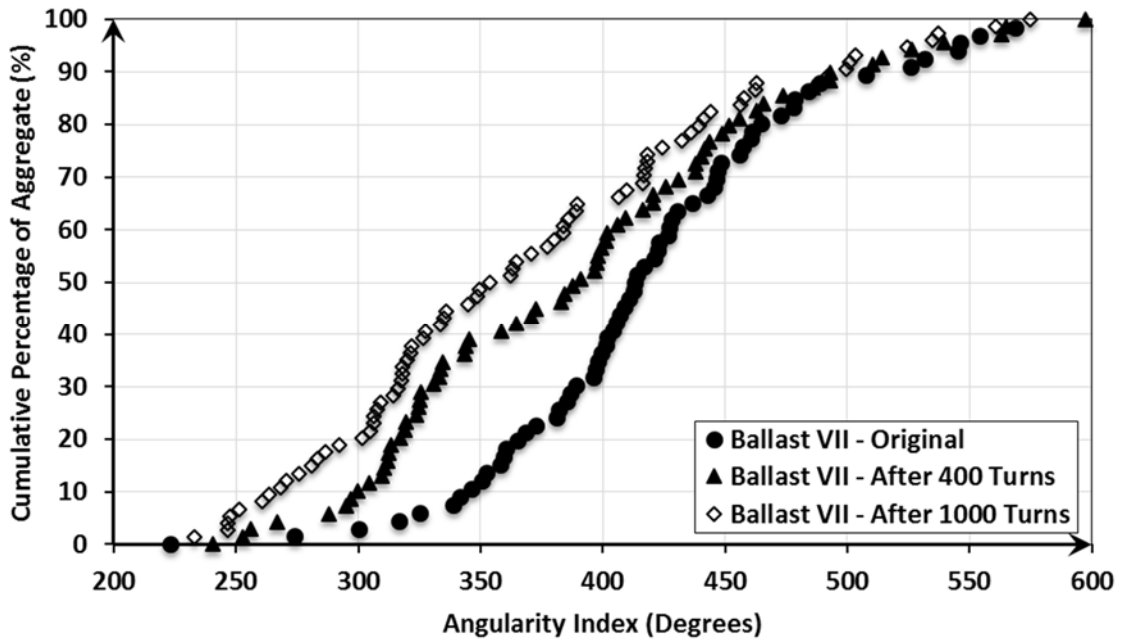
Figure C.13 Angularity Index at Different Degradation Levels for Ballast VII

Figure C.14 Surface Texture Index at Different Degradation Levels for Ballast VII

Figure C.15 Angularity Index at Different Degradation Levels for Ballast VIII

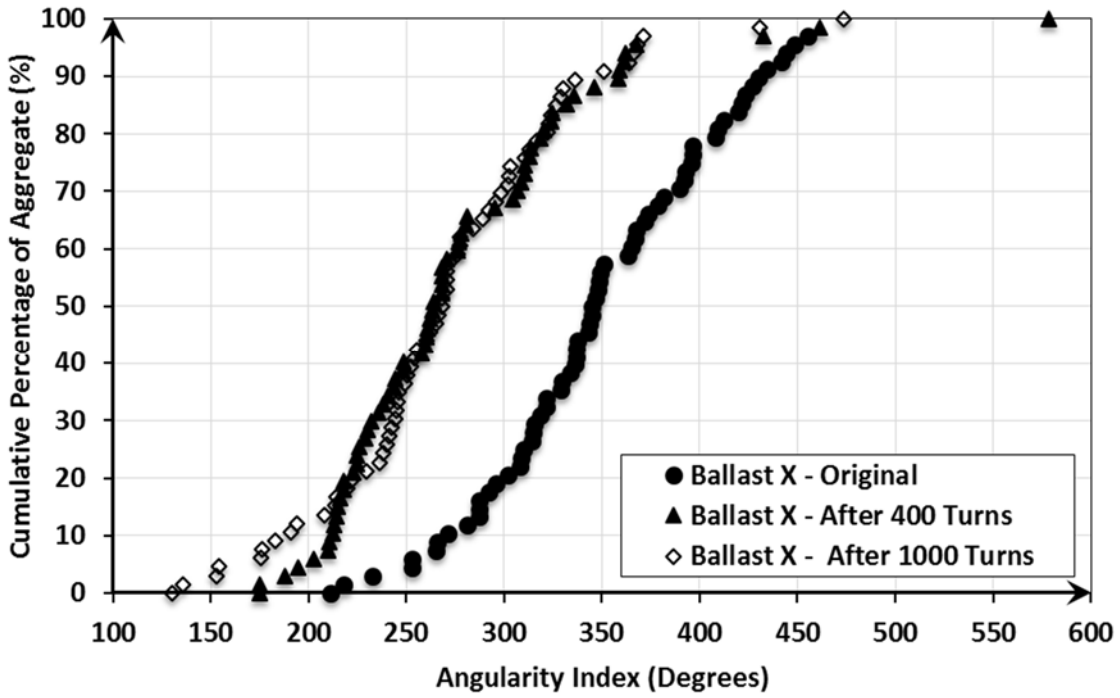Figure C.16 Surface Texture Index at Different Degradation Levels for Ballast VIII

Figure C.17 Angularity Index at Different Degradation Levels for Ballast IX

Figure C.18 Surface Texture Index at Different Degradation Levels for Ballast IX

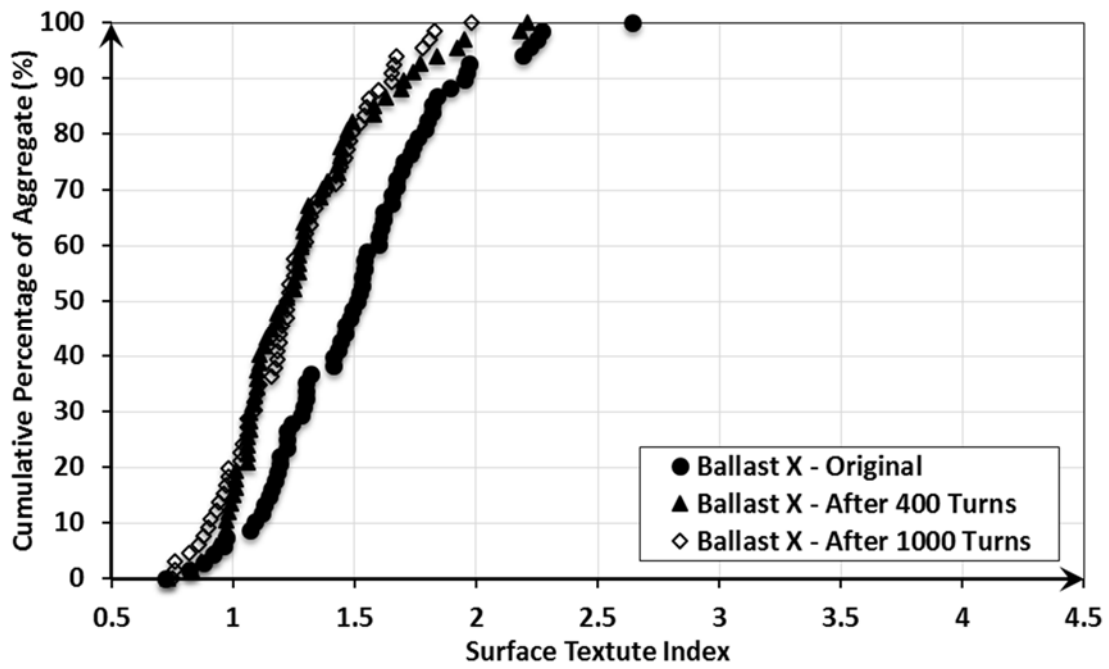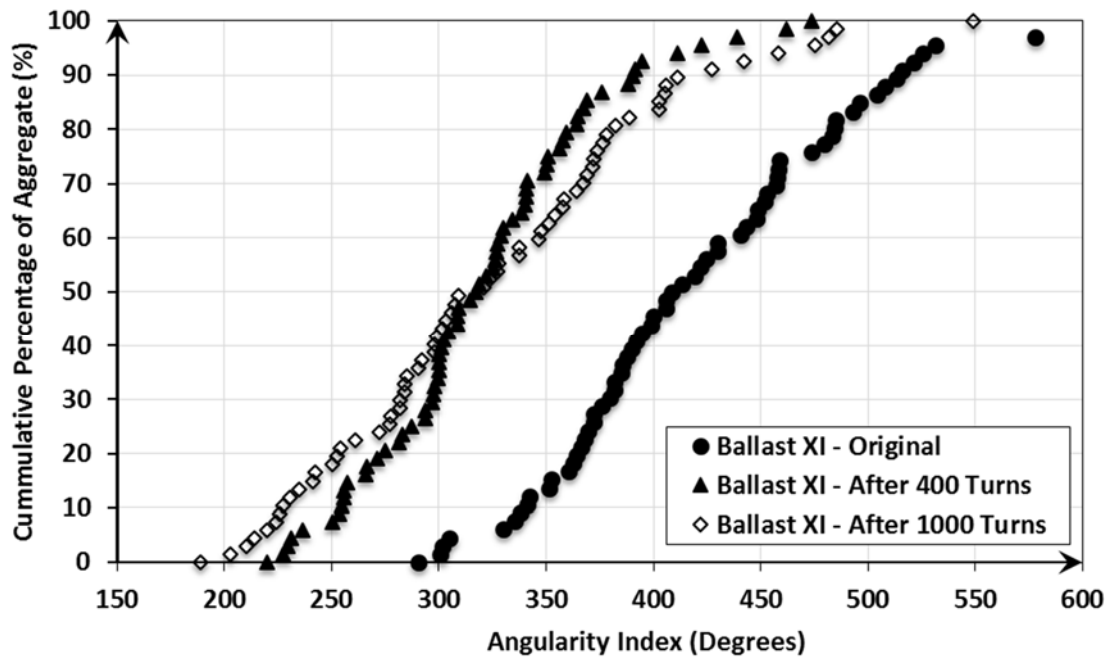**Figure C.19 Angularity Index at Different Degradation Levels for Ballast X**

Figure C.20 Surface Texture Index at Different Degradation Levels for Ballast X

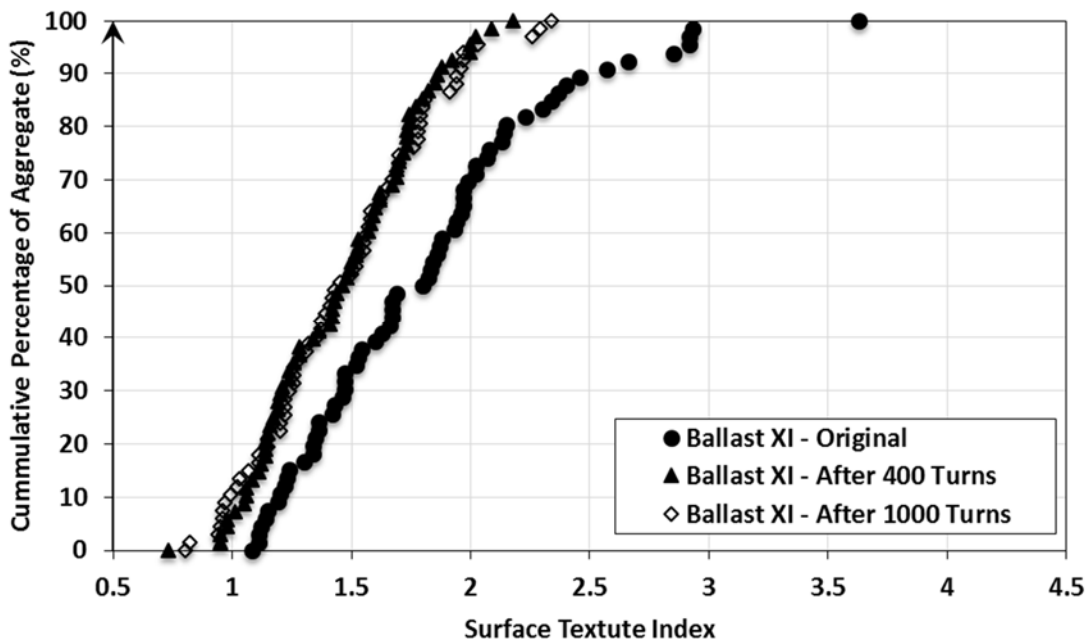Figure C.21 Angularity Index at Different Degradation Levels for Ballast XI

Figure C.22 Surface Texture Index at Different Degradation Levels for Ballast XI
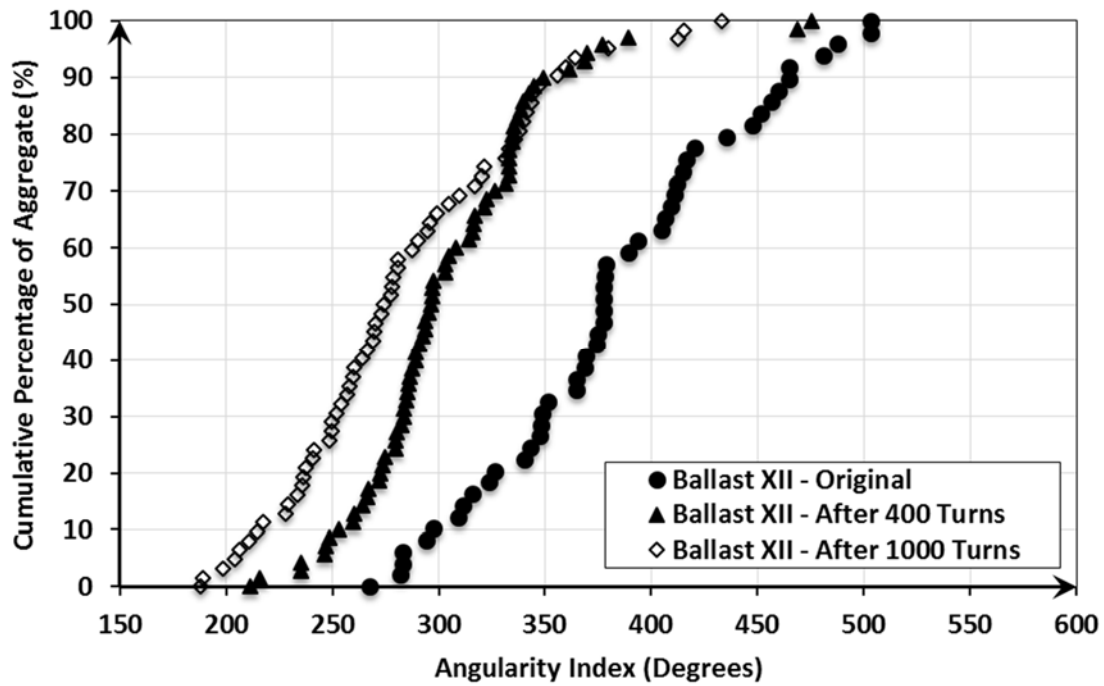
Figure C.23 Angularity Index at Different Degradation Levels for Ballast XII

Figure C.24 Surface Texture Index at Different Degradation Levels for Ballast XII

Figure C.25 Angularity Index at Different Degradation Levels for Ballast XIII
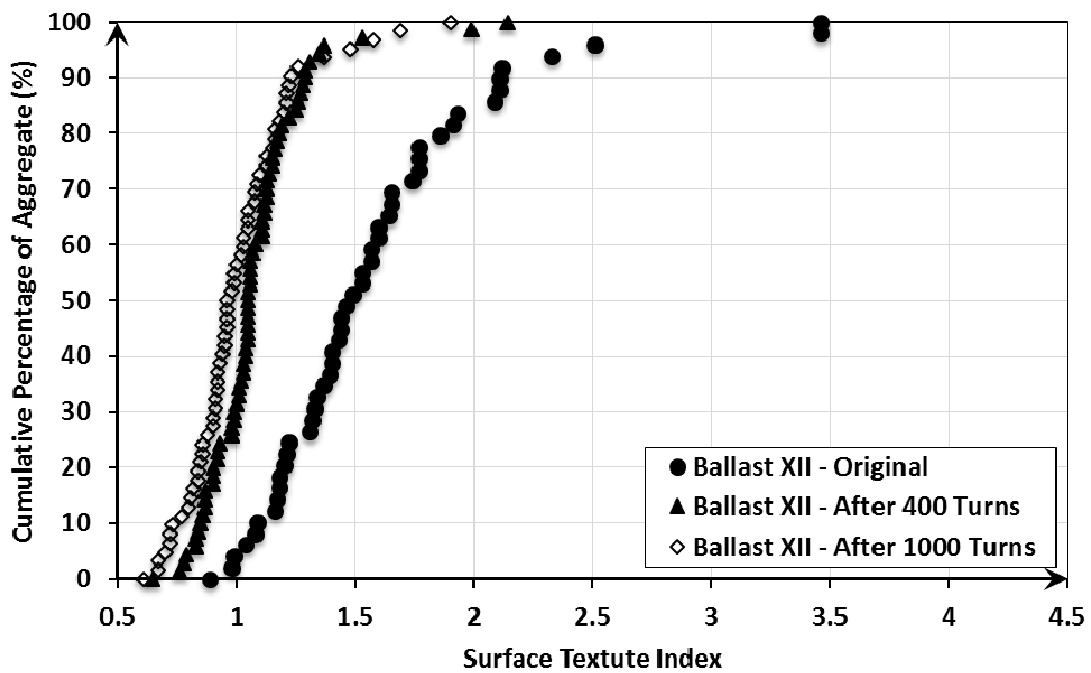

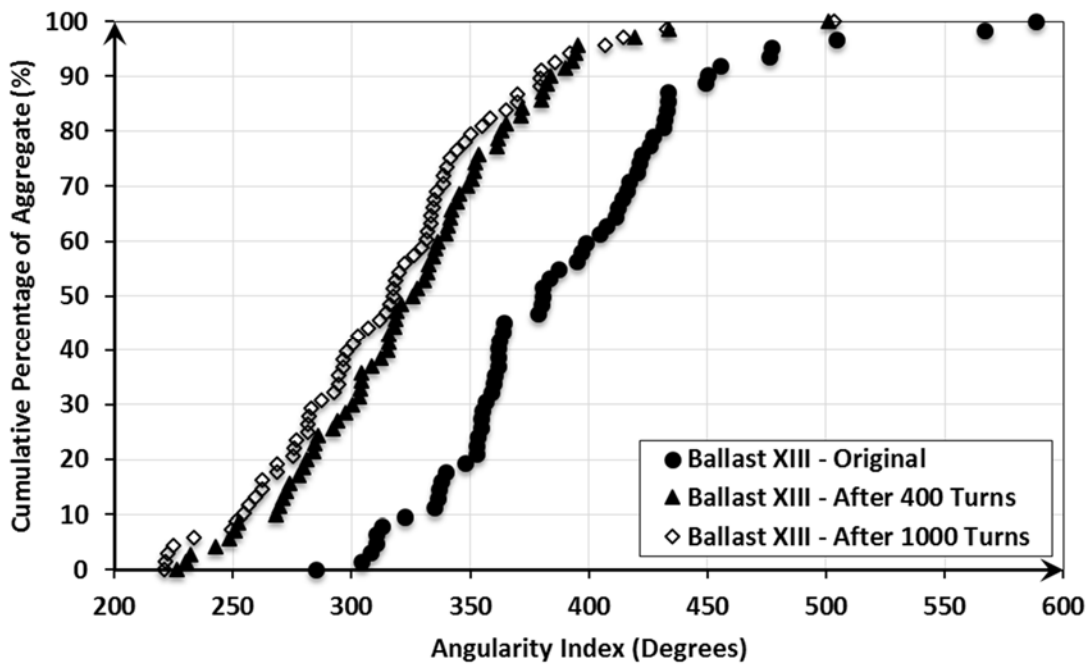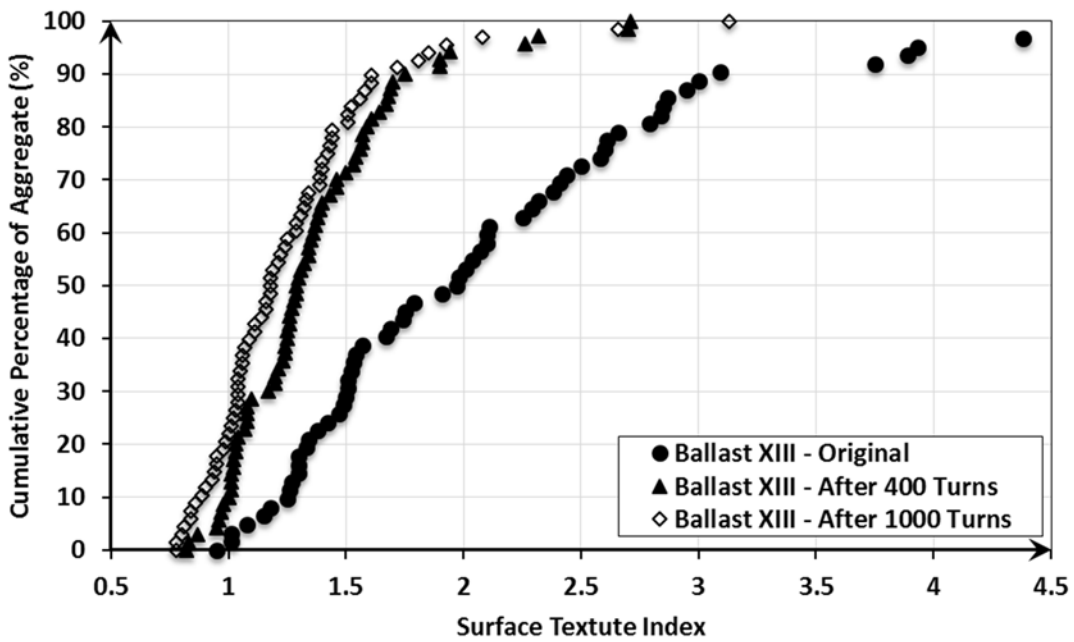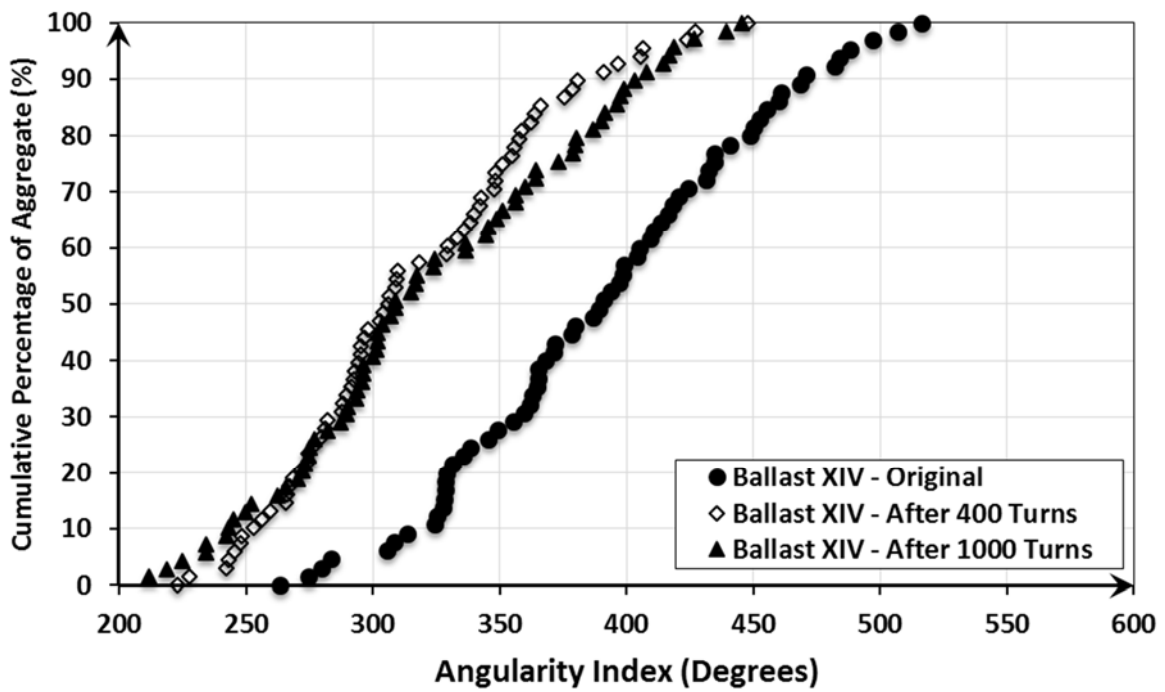**Figure C.26 Surface Texture Index at Different Degradation Levels for Ballast XIII**

Figure C.27 Angularity Index at Different Degradation Levels for Ballast XIV
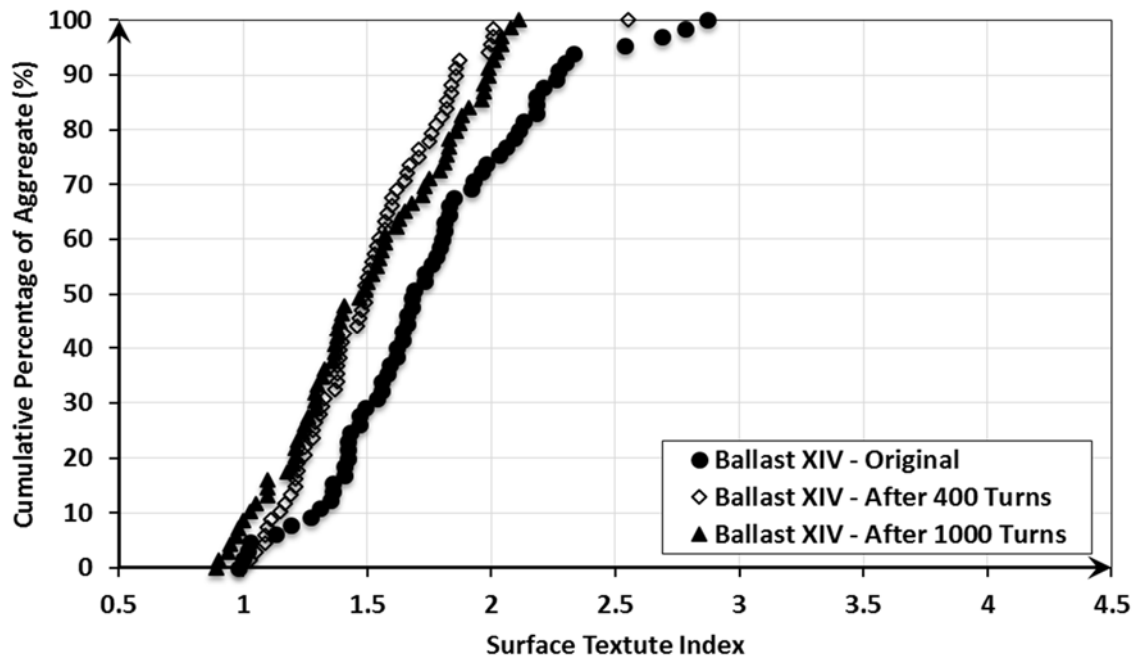

Figure C.26 Surface Texture Index at Different Degradation Levels for Ballast XIV

APPENDIX D

MATLAB CODE FOR COMPUTING ASPHALT COATING ON

RECLAIMED ASPHALT PAVEMENT (RAP) AGGREGATE

PARTICLES

```matlab
I = imread('img.png');
figure,imshow(I);
img=rgb2gray(I);
t = mean2(img) * 0.01; %User interaction
e=im2bw(img,t);
figure,imshow(e)


se = strel('disk',2);
bw=imdilate(e,se);
figure,imshow(bw)
bwx=imclose(bw,se);
figure,imshow(bwx)
K=bwareaopen(bwx,150); %User interaction
figure,imshow(K)
bw1=imcomplement(K);
figure,imshow(bw1)


m=imread('timg.png');
Lg=logical(m); %m is the tresholded image from E-UIAIA
x=Lg-K;
figure,imshow(x)
se = strel('disk',2);
x=imclose(x,se);
figure,imshow(x)
x2=imcomplement(x);
figure,imshow(x2)



f2=bwlabel(x);
A1=regionprops(f2,'Area');
grain_areas1 = [A1.Area];
toparea1=sum(grain_areas1(:));

f3=bwlabel(x2);
A2=regionprops(f3,'Area');
grain_areas2 = [A2.Area];
toparea2=sum(grain_areas2(:));

if  toparea1>toparea2
    A = toparea2;
    wholearea = bwarea(m);
FRAPUNCOATED=((wholearea-A)/wholearea)*100

else
    A = toparea1;
    wholearea = bwarea(m);
FRAPCOATED=(A/wholearea)*100
end
```

APPENDIX E

MATLAB CODE FOR BINARY AGGREGATE IMAGE

EXTRACTION IN THE FIELD

```matlab
img = imread('img.jpg');
figure; imshow(img);
[RN, CN, CH] = size(img);
if CH == 3
    img = rgb2gray(img);
end
figure; imshow(img);
rockID = zeros(RN,CN);
BW = im2bw(img, 0.05);
figure; imshow(BW);
%+++++++++++++++++++++++++++++++++++++++++++++++++++++++++++++++++++++++
% create intervals
filter = [-1 1];
intervals2 = {};
EG = [];
for i = 1:RN
    EG(i,:) = conv(double(BW(i,:)),filter,'same');
    lows = find(EG(i,:)==-1);
    highs = find(EG(i,:)==1);
    if size(lows,2)== 0 lows = 0; end
    if size(highs,2)== 0 highs = 0; end
    intervals2 = [intervals2; lows' highs'];
end
%%
%+++++++++++++++++++++++++++++++++++++++++++++++++++++++++++++++++++++++
overlapID = {};
intervals = intervals2;
rockIdx = 0;
rockID = zeros(RN,CN);

for i = 1:RN
    % no intervals, a black line
    if (intervals{i}(1) == [0,0])
        continue;
    elseif rockIdx == 0 %initialization, first non-zero line
%        rockIdx = rockIdx + 1;
            currentLine = [];
            currentLine = intervals{i};
            for j = 1:size(currentLine,1)
            % for the segms in the first line, each segm gets an ID
                rockIdx = rockIdx + 1;
                rockID(i,currentLine(j,1)+1:currentLine(j,2)) = rockIdx;
            end
        else      % look for the overlapping interval and get its rockID
            lastLine = intervals{i-1,1};
            currentLine = intervals{i,1};

            neighID = 0;
            for j = 1:size(currentLine,1)
                neighN = 0;
                AA = currentLine(j,1);
                BB = currentLine(j,2);
                mergeInt = [];
                if neighID ~= 0 %start from previous overlapping
                    k = neighID;
                else
```

237

```matlab
                    k = 1;
                end
                while(k <= size(lastLine,1))
                    CC = lastLine(k,1);
                    DD = lastLine(k,2);
                    if neighN == 0 && (BB < CC || AA > DD)
                        k = k+1;
                        continue;  %no overlap

                    elseif neighN == 0 && ~(BB < CC || AA > DD) %find the
first overlap interval
                        interID = rockID(i-1,lastLine(k,2));
                        rockID(i,currentLine(j,1)+1:currentLine(j,2)) =
interID;
                        neighID = k;
                        neighN = neighN + 1;
                        k = k + 1;
                        mergeInt = [mergeInt interID];
                    elseif neighN ~= 0 && (BB < CC || AA > DD) %no additional
overlap
                        break;
                    elseif neighN ~= 0 && ~(BB < CC || AA > DD) %need to
merge
                        neighN = neighN + 1;
                        neighID = k;
                        interID = rockID(i-1,lastLine(k,2));
                        rockID(rockID == interID)=
rockID(i,currentLine(j,2));
                        k = k + 1;
                        mergeInt = [mergeInt interID];
                    end
                end
                if neighN == 0 %didn't find any interval
                    rockIdx = rockIdx + 1;
                    rockID(i,currentLine(j,1)+1:currentLine(j,2)) = rockIdx;
                    mergeInt = [mergeInt rockIdx];
                end
                if ~isempty(mergeInt)
                    overlapID = [overlapID; mergeInt];
                end
            end
    end
end
% Mask out the single rock according to the rockID
realrockID = [];
rockBW = {};
rockIMG = {};
nRocks = max(max(rockID));
for i = 1:nRocks
    rockMask = BW;
    sz = size(find(rockID == i),1);
    if sz > 100
        realrockID = [realrockID; i sz];
    end
end
figure; imshow(rockID,[]);
```

```matlab
[Y,I] = sort(realrockID(:,2),'descend');
srtRockID = realrockID(I,:);
%+++++++++++++++++++++++++++++++++++++++++++++++++++++++++++++++++++
stat = [];
for i = 1:size(srtRockID,1)
        rockMask = BW;
        currentID = srtRockID(i,1);
        rockMask(find(rockID ~= currentID)) = 0;
        [rows,cols] = find(rockID == currentID);
        A = max(min(rows)- 1, 1);
        B = min(max(rows)+ 1, RN);
        H = max(rows) - min(rows)+ 1;
        C = max(min(cols)- 1, 1);
        D = min(max(cols)+ 1, CN);
        L = max(cols)- min(cols) + 1;
        singleMask = rockMask(A:B,C:D);
        rockimg = double(img(A:B,C:D)).*double(singleMask);
        singRock = double(img).*double(rockMask);
        imwrite(singleMask,['img_m',int2str(i),'.jpg']);
        imwrite(uint8(rockimg),['img_r',int2str(i),'.jpg']);
        stat = [stat; i L H];
end
```